Effective nonlinear interactions in circuit QED and optomechanical setups

Inauguraldissertation

zur Erlangung der Würde eines Doktors der Philosophie
vorgelegt der Philosophisch-Naturwissenschaftlichen
Fakultät der Universität Basel

von

Samuel Aldana

aus Vuisternens-devant-Romont (FR), Schweiz

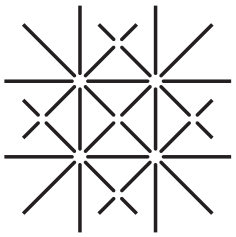

Basel, 2014

Namensnennung-Keine kommerzielle Nutzung-Keine Bearbeitung 3.0 Schweiz
(CC BY-NC-ND 3.0 CH)

Sie dürfen: **Teilen** — den Inhalt kopieren, verbreiten und zugänglich machen

Unter den folgenden Bedingungen:

Namensnennung — Sie müssen den Namen des Autors/Rechteinhabers in der von ihm festgelegten Weise nennen.

Keine kommerzielle Nutzung — Sie dürfen diesen Inhalt nicht für kommerzielle Zwecke nutzen.

Keine Bearbeitung erlaubt — Sie dürfen diesen Inhalt nicht bearbeiten, abwandeln oder in anderer Weise verändern.

Wobei gilt:

- **Verzichtserklärung —** Jede der vorgenannten Bedingungen kann **aufgehoben** werden, sofern Sie die ausdrückliche Einwilligung des Rechteinhabers dazu erhalten.
- **Public Domain (gemeinfreie oder nicht-schützbare Inhalte) —** Soweit das Werk, der Inhalt oder irgendein Teil davon zur Public Domain der jeweiligen Rechtsordnung gehört, wird dieser Status von der Lizenz in keiner Weise berührt.
- **Sonstige Rechte —** Die Lizenz hat keinerlei Einfluss auf die folgenden Rechte:
    - Die Rechte, die jedermann wegen der Schranken des Urheberrechts oder aufgrund gesetzlicher Erlaubnisse zustehen (in einigen Ländern als grundsätzliche Doktrin des **fair use** bekannt);
    - Die **Persönlichkeitsrechte** des Urhebers;
    - Rechte anderer Personen, entweder am Lizenzgegenstand selber oder bezüglich seiner Verwendung, zum Beispiel für **Werbung** oder Privatsphärenschutz.
- **Hinweis —** Bei jeder Nutzung oder Verbreitung müssen Sie anderen alle Lizenzbedingungen mitteilen, die für diesen Inhalt gelten. Am einfachsten ist es, an entsprechender Stelle einen Link auf diese Seite einzubinden.

Quelle: http://creativecommons.org/licenses/by-nc-nd/3.0/ch/ Datum: 12.11.2013

Genehmigt von der Philosophisch-Naturwissenschaftlichen Fakultät auf Antrag von

Prof. Dr. Christoph Bruder

Prof. Dr. Klaus Mølmer

Basel, den 25. März 2014

Prof. Dr. Jörg Schibler, Dekan

Summary

In this thesis, we study two different physical systems, namely superconducting circuits and optomechanical cavities.

In the first part of the thesis, we study superconducting qubits and resonators and their potential to implement quantum information processing tasks. We propose a circuit quantum electrodynamics realization of a protocol to generate a Greenberger-Horne-Zeilinger (GHZ) state for transmon qubits homogeneously coupled to a microwave cavity in the dispersive limit. We derive an effective Hamiltonian with pairwise qubit exchange interactions of the XY type that can be globally controlled. Starting from a separable initial state, these interactions allow to generate a multi-qubit GHZ state within a time that does not depend on the number of qubits. We discuss how to probe the non-local nature and the genuine multipartite entanglement of the generated state. Finally, we investigate the stability of the proposed scheme to inhomogeneities in the physical parameters and the weak anharmonicity of transmon qubits.

In the second part of the thesis, we study optomechanical systems in which the position of a mechanical resonator modulates the resonance frequency of an optical cavity. The resulting radiation-pressure interaction is intrinsically nonlinear and can be used to implement strong Kerr nonlinearities and an effective interaction between photons. We investigate the optical bistability of such a system. The steady-state mean-field equation of the optical mode is identical to the one for a Kerr medium, and thus we expect it to have the same characteristic behavior with a lower, a middle, and an upper branch. However, the presence of position fluctuations of the mechanical resonator leads to a new feature: the upper branch will become unstable at sufficiently strong driving in certain parameter regimes. We identify the appropriate parameter regime for the upper branch to be stable, and we confirm, by numerical investigation of the quantum steady state, that the mechanical mode indeed acts as a Kerr nonlinearity for the optical mode in the low-temperature limit. This equivalence of the optomechanical system and the Kerr medium will be important for future applications of cavity optomechanics in quantum nonlinear optics and quantum information science.

Acknowledgments

This thesis would never have been possible without the support, the assistance, the ideas and the friendship of numerous people, to who I would like to express my appreciation. First and foremost, I would like to express my deep gratitude to my advisor Christoph Bruder for accepting me as a PhD student and giving me the opportunity to work on interesting research topics. I really enjoyed his kindliness and availability for discussions and benefited a lot from his experience, knowledge, and insightful comments.

During the course of this research, I have been fortunate to work with Ying-Dan Wang and Andreas Nunnenkamp. Ying-Dan introduced me to the field of quantum information and I am grateful for her helpful comments and suggestions. I owe much to Andreas, whose constant input, far from being noisy or quantum, had a great impact on my working dynamics. I would like to thank him for his contagious enthusiasm and for sharing with me his profound knowledge of optomechanical systems. Moreover, I am deeply indebted to him for the valuable comments and careful proof-reading of this thesis.

The condensed matter theory group, headed by Christoph Bruder and Daniel Loss, has provided a very pleasant working atmosphere. I particularly enjoyed the stimulating discussions, both scientific and otherwise, with my office-mates Christoph Orth, Grégory Strübi, Andreas Wagner, and Stefan Walter. I also would like to thank all the current and former members I had the chance to met during my four years in Basel: Daniel Becker, Stefano Chesi, Gerson Ferreira, Jan Fischer, Suhas Gangadharaiah, Patrick Hofer, Kevin van Hoogdalem, Adrian Hutter, Jelena Klinovaja, Christoph Klöffel, Viktoriia Kornich, Axel Lode, Franziska Maier, Tobias Meng, Simon Nigg, Jennifer Nussbaum, Fabio Pedrocchi, Diego Rainis, Hugo Ribeiro, Maximilian Rinck, Beat Röthlisberger, Arijit Saha, Manuel Schmidt, Thomas Schmidt, Peter Stano, Dimitrije Stepanenko, Vladimir Stojanovic, Constantin Schrade, Rakesh Tiwari, Luka Trifunovic, Mircea Trif, Talitha Weiss, James Wootton, Robert Zak, Robert Zielke, and Alexander Zyuzin.

Last but not least, it impossible to record how grateful I am to Aline. I can only hardly imagine how I could have completed this thesis without her love, encouragement, and unconditional support. Finally, I would like to thank my daughter Malorie. She was a constant source of wonder during the last two years and often I found myself envying her steep learning curve.

Contents

Chapter 1

Introduction

The advent of quantum mechanics revolutionized our understanding of physical reality, explaining many phenomena arising at the smallest scales. In the first place, researchers devoted themselves to test its validity, never disproved to date, in a wide range of situations. Progressively, the scope of quantum mechanics was extended to almost all branches of physics. Major developments in the fields of condensed-matter physics and quantum optics for instance were accompanied by numerous technological advances. Over the last decades, the focus of experimental activities moved from the verification of quantum effects, to the manipulation of the quantum state of systems with a few degrees of freedom.

Nowadays, available experimental techniques allow researchers to control individual quantum systems such as an atom inside an optical cavity, an ion trapped in an electric field, an electron spin in a quantum dot, or an artificial atom (e.g., a superconducting quantum bit) in a superconducting circuit. Recently, even macroscopic mechanical resonators have been cooled to their quantum mechanical ground state. These tremendous achievements have also gradually changed the way we consider quantum mechanics. An ever growing part of the scientific community rapidly started to explore which potential applications could take advantage of both the richness of quantum theory and this novel experimental situation. In particular, sensing and information processing are two prominent examples of tasks that might benefit from the remarkable and intriguing properties of quantum devices whose state can be reliably controlled and manipulated.

The main feature of quantum mechanics that would make quantum information processing devices reach outstanding performance is undeniably the fundamental principle of superposition. Also, the quantum state of several coupled subsystems can exhibit correlations that are much richer and very different from those classically allowed. In this case the state of the whole system is said to be entangled. While the complexity of composite quantum systems can be very challenging at the mathematical level, it simultaneously enables new applications in the domain of information science.

Information is physical, even in classical devices, in the sense that it is always encoded in the state of a particular system. The processing, the storage, and the communication of information are intrinsically physical processes. Thanks to the richness of quantum correlations, encoding information in systems whose quantum state can be coherently manipulated can enhance the capabilities or the performance of information processing devices. For instance, entanglement enables the realization of totally secure quantum communication schemes without any classical counterpart and certain quantum algorithms provide exponential computational speedup over classical ones.

In the domain of metrology, quantum effects come into play when we consider the

ultimate limitations that any sensing device will unavoidably face. To extract quantitative information about the state of a system we must interact with it. Some limitations on the measurement sensitivity might arise from the noisy nature of almost any apparatus, i.e., uncontrolled degrees of freedom spoiling the measurement record. Such technical noise sources can in principle be eliminated and an ultimate limit on the measurement performance finds its origin in the intrinsic random nature of quantum mechanics, quantum fluctuations.

An important prediction of quantum mechanics is that, during the course of a measurement, the imprecision of the record and the disturbance of the measured system – the back-action – are intimately related and cannot be arbitrarily and simultaneously lowered. In practice, reaching such ultimate sensitivity where the only remaining source of noise is of quantum-mechanical origin is not a trivial task. Another consequence of quantum theory is that there measurement situations where preparing the meter in a non-classical state can help to reach a better sensitivity.

In this thesis we study two different types of physical systems, namely superconducting quantum circuits and optomechanical cavities. During the past decade and a half, these systems have attracted a lot of attention as promising platforms for quantum technologies. Superconducting circuits have been used to realize a solid-state version of cavity quantum electrodynamics, where atoms and cavity are replaced by electrically-controlled integrated elements. This architecture is a candidate to implement some of the elementary components and functionalities required to perform quantum computations. Cavity optomechanics explores the effects of the radiation-pressure interaction between light confined inside optical resonators and mechanical oscillators. Optomechanical cavities were originally studied in the context of interferometric gravitational-wave detectors and this research helped to understand the implications of quantum mechanics in the measurement process. More recently, a large assortment of micro-fabricated devices have demonstrated the potential of optomechanical systems for sensing applications as well as for quantum information processing tasks such as quantum information storage.

1.1 Quantum information processing

Quantum systems whose components together as well as their mutual interactions can be accurately controlled might achieve several useful tasks:

- Quantum computation: the execution of quantum algorithms on a register of qubits to obtain the solution to some computational problem [Nielsen00, Bennett00, Ladd10]. It has been shown that some computational tasks can be carried out more rapidly, in terms of computational steps, when using quantum algorithms rather than classical ones. The two most celebrated examples are probably Shor's factoring algorithm [Shor97], which provides exponential speedup over any known classical algorithm, and Groover's search algorithm [Grover97], whose speedup is quadratic.

- Quantum communication: the reliable transfer of quantum information between two parties. This task has two major aspects. First, protocols of quantum key distribution and quantum cryptography enable the transmission of secret information in a fully secure way [Bennett84, Ekert91, Gisin02, Gisin07, Scarani09]. Quantum key distribution is actually the first quantum information task to reach the status of a commercially available technology [ID Quantique, a Geneva-based company]. A

second important aspect of quantum communication tasks is the transfer of a qubit of information between two physically different platforms, allowing different modules in a quantum information processor to communicate [Kimble08].

- Quantum simulation: the simulation of complex quantum systems, in particular strongly-correlated systems, where numerical or analytical solutions are only approximate and unsatisfactory [Feynman82, Buluta09, Cirac12].

The two types of systems we will discuss throughout this thesis find direct applications in the first and second items on this list. Superconducting circuits are a promising platform for quantum computing, realizing so far an integrated all-electrical version of a small qubit register on which simple algorithms have been implemented [Devoret13]. A new generation of micro-fabricated optomechanical devices [Kippenberg08, Aspelmeyer13, Meystre13] might find applications both in the context of quantum communication and quantum computing. They are potential candidates to interface different quantum information encoding platforms [Hill12, Andrews14] and to store quantum information [Verhagen12, Palomaki13a]. For the purposes of quantum computing with photons, optical resonators with large optomechanical coupling could implement optical nonlinearities at the single-photon level [Nunnenkamp11, Rabl11] and nondestructive single-photon detection [Ludwig12].

1.1.1 Basic requirements

A physical system designed to be used as a quantum computer should satisfy stringent conditions. In short, logical information is encoded in the amplitudes of well-defined basis states of the quantum system. In the case of a collection of (effective) two-level systems, we usually talk about the qubit register. The execution of a quantum algorithm requires the ability to initialize the qubit register in a predefined state, to control its Hamiltonian while letting it evolve coherently, and finally to measure its state.

The core part of a quantum algorithm is the unitary transformation one needs to apply on the qubit register. It has been shown that a finite set of single and two-qubit operations is sufficient and can be used to effectively perform any possible operation that is relevant for quantum computing. The most common example of such a universal set of quantum gates is composed of the single-qubit Hadamard gate H, phase gate S, and $\pi/8$ gate T together with the two-qubit CNOT gate. If we denote the two logical states of a qubit by

$$|0\rangle = \begin{pmatrix} 1 \\ 0 \end{pmatrix}, \qquad |1\rangle = \begin{pmatrix} 0 \\ 1 \end{pmatrix}, \tag{1.1}$$

these gates can be conveniently expressed as

$$H = \frac{1}{\sqrt{2}} \begin{pmatrix} 1 & 1 \\ 1 & -1 \end{pmatrix}, \qquad S = \begin{pmatrix} 1 & 0 \\ 0 & i \end{pmatrix}, \qquad T = \begin{pmatrix} 1 & 0 \\ 0 & e^{i\pi/4} \end{pmatrix}, \tag{1.2}$$

$$\mathrm{CNOT} = \begin{pmatrix} 1 & 0 & 0 & 0 \\ 0 & 1 & 0 & 0 \\ 0 & 0 & 0 & 1 \\ 0 & 0 & 1 & 0 \end{pmatrix} \tag{1.3}$$

where the two two-qubit computational basis is given by $(|00\rangle, |01\rangle, |10\rangle, |11\rangle)$. Even if any unitary transformation acting on the qubit register can be reduced, to arbitrary accuracy,

to a finite sequence of gates from such a universal set [Williams11], it is generally preferable if an overcomplete set of gates is available. This is particularly true if the decomposition of an algorithm requires a large number of simple gates, since decoherence unavoidably sets in. In any physical implementation, the qubit register will never be completely isolated from its environment and the interaction with uncontrolled degrees of freedom causes qubit relaxation and dephasing, introducing errors in the computation.

To circumvent the effect of decoherence, a crucial innovation was the development of quantum error correction (QEC) methods [Shor95, Steane96, Knill97]. They rely on the possibility to encode one qubit of information, the logical qubit, in the state of several physical qubits. Single-qubit errors on a physical qubit, such as bit or phase flips, could be detected with the help of so-called error syndromes. The latter are non-demolition measurements of multi-qubit observables that detect if the encoded state was corrupted. Their outcomes indicate the correcting gate that must be applied to restore the state of the physical qubits prior to the error. The use of QEC schemes in principle allows the total calculation time on a quantum computer to be longer than the decoherence time of its physical subcomponents. However, the implementation of QEC methods, essential for fault-tolerant quantum computation [Preskill98], requires high gate fidelities at the level of the physical qubit. An often cited threshold for the required error rate of single and two-qubit quantum gates is 10^{-4} [DiVincenzo00]. This translates to the condition that each gate must be performed within a time that is typically 10'000 times shorter than the decoherence time of the qubit.

Another more pragmatic approach to limit the effect of decoherence is to have available a larger set of simpler multi-qubit gates. Experimentally, single-qubit gates are rarely the main issue and can be performed by rather fast local manipulation only, provided sufficient control parameters are accessible and can be tuned in situ. Controlled two-qubit gates are more problematic, because they require an (effective) interaction between the qubits. The time required for such operations is inversely proportional to the interaction strength and is the main limiting factor on how many quantum gates can be applied before decoherence sets in. The application of successive controlled two-qubit gates are in particular needed for the creation of entanglement among many qubits. These entangled states are an essential resource for any quantum information processing tasks, and their generation has been the subject of intense experimental efforts.

1.1.2 Implementing a quantum information processor

Many different physical platforms are considered as potential candidates for the implementation of a small register of qubits that can be accurately controlled and manipulated. Among these, superconducting circuits have been used to successfully realize a solid-state version of cavity quantum electrodynamics [Haroche06, Raimond01, Mabuchi02] in the microwave domain, where artificial atoms – the superconducting qubits – couple to a common microwave resonator. External control lines allow to control the frequency of the qubits in situ while the resonator acts as a quantum bus mediating qubit-qubit interactions by virtual excitations, making possible the implementation of two-qubit gates. The microwave resonator plays additional roles: it serves as a filter to protect the qubits against the surrounding electromagnetic environment, improving its coherence properties, and can carry microwave pulses that perform single-qubit operations. This technology has reached a quite mature stage and the latest achievements suggest that experiments with superconducting qubits could implement simplified QEC schemes in a not so distant

future [Devoret13], first steps towards this goal having already been reported [Reed12].

Another possibility that is currently pursued to realize a quantum information processor is to use optical networks, where qubits are encoded with photons [O'Brien07]. An important requirement for photonic quantum information processing is the ability to implement nonlinear interactions between photons, which are crucial for the realization of two-qubit gates. These interactions can in principle be obtained with optical media exhibiting large Kerr nonlinearities [Milburn89], but in practice their implementation turned out to be very challenging. A major breakthrough was made by Knill, Laflamme, and Milburn who showed that probabilistic two-qubit gates could be realized with *linear* optical elements, single-photon sources and detectors only, using additional ancilla qubits and post-selection [Knill01]. This approach sounds particularly promising but its non-deterministic nature could prevent an implementation in its original form. Possible improvements of this scheme have been explored that make use of quantum teleportation protocols to enhance the success probability of two-qubit gates (see e.g. [Kok07, O'Brien09] and references therein). Despite these conceptual advances, the implementation of effective photon-photon coupling is still highly desirable. In particular, it was realized that even small nonlinearities – not large enough to realize deterministic two-qubit gates – can still offer potential benefits in the context of photonic quantum computing [Nemoto04, Barrett05, Munro05].

Like a medium with an optical nonlinearity, optomechanical systems could find application for the realization of photonic two-qubit gates. By coupling the motion of a mechanical resonator to the light field inside an optical cavity, the resulting optomechanical interaction is intrinsically nonlinear. While in most experiments this radiation-pressure interaction is in general fairly weak, the progress in the design and the fabrication of such devices and the most recent accomplishment suggests that they may soon make a significant step towards the implementation of single-photon nonlinearity [Safavi-Naeini12, Chan12]. In the future, optomechanical devices might offer an alternative to other potential approaches that are pursued to implement effective photon-photon interactions, such as cavity QED setups using single atoms [Turchette95, Rauschenbeutel99, Birnbaum05] or photonic crystal nanocavities [Yoshie04, Hennessy07].

Optomechanical systems could play an important role as interfaces between different quantum information platforms. An important functionality that is thought to be realizable with such devices is the transfer of a quantum state of light from the optical to the microwave domain or vice versa [McGee13]. A first proof-of-principle experiment has been reported recently with a setup consisting of two optical and microwave resonators, each one coupling to a common mechanical element via the radiation-pressure interaction [Andrews14]. The ability to transfer quantum information from one physical platform to another is also an important functionality with clear applications for the storage of quantum information. Lately, a major breakthrough was the demonstration of coherent coupling between a mechanical degree of freedom and an optical mode. This allowed to realize the transfer and retrieval, after some time, of the state of a light field into a mechanical mode that was previously cooled to its ground state [Palomaki13a, Verhagen12].

1.2 Quantum metrology

Any measurement device unavoidably faces some limitations on how small a signal can still be detected. Real experimental outcomes are subject to noise sources that can mask the signal. Noise of technical and thermal origin can be avoided with appropriate control or cooling techniques, but sensitive measurements are ultimately limited by a type of noise

that find its roots in quantum fluctuations.

Interferometric sensing is a situation where non-classical states find direct applications and could help to achieve a better measurement sensitivity when some resources, such as signal integration time, are limited. To illustrate this capability of non-classical states in the measurement process, we will first consider the situation where a light field is used to monitor the position of an object.

1.2.1 Quantum noise and quantum limits

Before specifying how systems with quantum correlations might be useful for measurement tasks, it seems appropriate to first exemplify the consequences of quantum mechanics in the measurement process. For this purpose, we consider the most relevant example of a measurement in the field of optomechanics: the interferometric detection of gravitational waves. It is the precise understanding of the implications of quantum mechanics in the measurement process that helped developing practical tools for the observation of this fundamental effect.

The existence of gravitational waves was predicted by general relativity but still lacks direct experimental evidence. These are tiny perturbations of the space-time curvature, due to violent astrophysical events, traveling through space at the speed of light and causing tidal forces on matter. Due to their extremely weak amplitudes, measuring them is a formidable task and requires very stringent experimental conditions. The initial approach that is still currently pursued consists in continuously measuring the displacement of large test masses forming the end mirrors in a L-shaped interferometer.[1] In short, a light beam is divided by a first beam splitter (input port), propagates along two different optical paths, is recombined by a second beam splitter. The accumulated phase shift contains information about the length difference between the two arms of the interferometer and can be measured with balanced detection of the two output modes.

The phase sensitivity of such a measurement device is ultimately limited by the effects of quantum noise. The Heisenberg uncertainty relation sets a lower threshold on the achievable precision in the ideal case where the whole setup is at zero temperature, i.e., all sources of thermal fluctuations influencing the position of the test masses and the statistics of the light field have been eliminated. The laser shot noise and the mirrors' zero-point motion, both intrinsically quantum features, introduce noise in the measurement outcome.

When the laser light entering the interferometer is in a coherent state, the so-called shot-noise limit, sometimes also referred to as standard quantum limit, applies to the phase sensitivity. The electromagnetic field can be decomposed in two quadrature components – the in-phase and out-of-phase amplitudes of the electromagnetic wave – usually called amplitude and phase quadratures of the field. A coherent state is a quantum state of the light which most closely resembles a classical field. In such a state, both amplitude and phase quadrature uncertainties are identical and equal to those of the vacuum: their product reaches the lowest possible value according to the Heisenberg uncertainty principle. The phase sensitivity of an interferometer scales as $1/\sqrt{N}$, where N is the average photon number of the coherent light state.

The imprecision noise could then be reduced by raising the input power. At some point, the shot-noise of the light exerts some back-action on the end mirror that limits the overall sensitivity at higher input power. Such a limitation actually arises in any situation where one tries to measure an observable that does not commute with itself at

[1] For instance, LIGO and VIRGO operate Michelson interferometers with Fabry-Pérot arms.

different times, like the position of a mechanical resonator. More precisely, this trade-off between imprecision and back-action noise applies to any linear measurement scheme, i.e., that couples linearly the measured observable and an observable of the meter. By raising the system-meter coupling, the imprecision noise is reduced, but the back-action noise is increased. As a consequence, there is an optimal coupling at which the overall noise is minimal. In the case of interferometric position measurements, the back-action of the light on the mechanical motion is called radiation-pressure shot-noise.[2]

Caves suggested that a light source exhibiting a particular type of non-classical property, named squeezing, might allow to reach a better phase sensitivity [Caves80a, Caves81], a possibility that was further investigated and verified [Bondurant84]. A squeezed state of light has reduced fluctuations in one of its quadratures. If it has less noise in one quadrature than a coherent state, the other quadrature exhibits larger fluctuations to satisfy the Heisenberg uncertainty relation. When phase-squeezed light is fed into an interferometer, the phase sensitivity is increased compared to the case of a coherent state with the same average photon number N. This was a major breakthrough as the total power needed to achieve a given phase-sensitivity is reduced and allows to limit the back-action of the radiation-pressure shot noise. Using a squeezed state, the limit on the phase sensitivity scales as $1/N$ large input power and is known as the Heisenberg limit. While the $1/\sqrt{N}$ scaling of the standard quantum limit relates to the use of coherent light, or more generally to the use of a classical resource, the $1/N$ scaling of the Heisenberg limit is the quantum limit.

1.2.2 Sensing applications of optomechanical devices

The generation of squeezed light requires a nonlinear optical medium. Such nonlinearities can be obtained effectively, with atoms in a cavity for instance [Slusher85], or with materials exhibiting bulk optical nonlinearities [Wu86]. As we have seen, squeezed light is useful for displacement sensing. Conversely, it has been suggested early on that optomechanical systems could themselves act as effective Kerr nonlinear media and used for the generation of squeezed light [Fabre94, Mancini94, Corbitt06]. This has recently become an experimental reality as three very different types of optomechanical devices have shown this effect [Brooks12, Safavi-Naeini13, Purdy13b].

The optomechanical interaction makes possible to use the influence of the light field to control the mechanical motion. A prominent example is the development of cavity-assisted cooling techniques [Mancini98, Marquardt07, Wilson-Rae07, Genes08b]. In a series of experiments, exquisite control made possible to cool mechanical degrees of freedom into their ground state [Teufel11a, Chan11]. More generally, feedback and cooling techniques have attracted much attention, especially because of their important implications in the domain of ultra-sensitive force detection [Teufel09, Abbott09b, Winger11, Krause12, Cohen13, Iwasawa13]. The optomechanical interaction could also allow the preparation of non-classical states of a mechanical object. For instance, the ability to generate a mechanical squeezed state with position uncertainty below the level of vacuum fluctuations could lead to enhanced sensitivity when detecting small displacements [Mari09].

Finally, particularly relevant in the context of cavity optomechanics are so-called quantum non-demolition measurements, suggested early on by Braginsky [Braginsky80]. Such measurements can be realized when the Hamiltonian of the measured system commutes

[2] Even though it has been predicted for more than thirty years, the first experimental evidence of radiation-pressure shot noise on a macroscopic object was reported only recently [Purdy13a]

with the system observable. Since the system observable is a constant of motion, a repetition of the measurement produces the same outcome, hence the term quantum nondemolition. At first sight, the optomechanical interaction should forbid this type of measurement for the position of mechanical resonator. However, the position of an harmonic oscillator commutes with itself at stroboscopic times, allowing to measure a single quadrature of the mechanical motion while the radiation-pressure back-action only affects the other quadrature [Clerk08]. A first proof-of-principle experiment was realized with an optomechanical device operating in the microwave domain [Hertzberg10]. Conversely, these devices could take advantage of the fact that the radiation-pressure interaction is intrinsically nonlinear and couples to the light intensity. By monitoring the mechanical displacement, one could perform a quantum non-demolition detection of the light intensity [Pinard95]. If the optomechanical interaction is strong enough, such a measurement scheme could implement nondestructive single-photon detection [Ludwig12].

1.2.3 Role of quantum correlations

As discussed above, squeezed states represent a particular type of non-classical states that are useful for optical interferometry. We now try to show how, in general, states exhibiting quantum correlations might be useful in the context of metrology. For this purpose, we briefly introduce a general measurement scheme which both highlights the benefits from using highly entangled states and applies to interferometric sensing in a broad sense. We emphasize that the following discussion involves simplified arguments. It is inspired by Ref. [Giovannetti06], in which a more rigorous treatment can be found.

We model a measurement outcome as the estimation of some parameter λ, obtained by preparing some system – the probe – in the state $|\psi\rangle$, letting it evolve under the influence of some unitary operator $\hat{U}$, and finally measuring an observable $\hat{O}$. The information about the parameter λ is contained in the evolution of the state $|\psi\rangle$ and this effect is captured by a unitary operator of the form $\hat{U} = \exp(-i\lambda\hat{A})$, where $\hat{A}$ is a known Hermitian operator $\hat{A} = \sum_i a_i |a_i\rangle\langle a_i|$. Assuming the probe is initially in the state $|\psi\rangle = \sum_i \psi_i |a_i\rangle$, by measuring the observable $\hat{O}$ (which must satisfy $[\hat{A}, \hat{O}] \neq 0$) one obtains

$$\langle \hat{O} \rangle = \langle \psi | e^{i\lambda\hat{A}} \hat{O} e^{-i\lambda\hat{A}} | \psi \rangle = \sum_{i,j} e^{i\lambda(a_j - a_i)} \psi_j^* \psi_i \langle a_j | \hat{O} | a_i \rangle. \tag{1.4}$$

The uncertainty on the parameter λ can be estimated from $\Delta\lambda = \Delta O \left| \frac{d\langle \hat{O} \rangle}{d\lambda} \right|^{-1}$, where ΔO denotes the uncertainty of the operator $\hat{O}$ evaluated in the final probe state $\hat{U}|\psi\rangle$.

Repeating the measurement N times or using N independent probes that share only classical correlations is formally equivalent and can be described with a fully separable probe state $|\Psi_R\rangle$ and a measurement of $\hat{O}_R$ given by

$$|\Psi_R\rangle = \bigotimes_{k=1}^{N} |\psi\rangle_k, \qquad \hat{O}_R = \bigoplus_{k=1}^{N} \hat{O}_k. \tag{1.5}$$

According to estimation theory, we have

$$\Delta\lambda_R = \frac{\Delta O_R}{|d\langle \hat{O}_R \rangle / d\lambda|} = \frac{1}{\sqrt{N}} \frac{\Delta O}{|d\langle \hat{O} \rangle / d\lambda|}. \tag{1.6}$$

This relation spells out the error scaling when estimating a parameter with N repeated measurements. Using the Heisenberg uncertainty relation and the fact that $|\langle [\hat{A}, \hat{O}] \rangle| =$

$|d\langle\hat{O}\rangle/d\lambda|$, the error $\Delta\lambda_R$ can be related to ΔA, the spread of the operator $\hat{A}$ in the initial state $|\psi\rangle$,

$$\Delta\lambda_R \geq \frac{1}{2\sqrt{N}\Delta A}. \tag{1.7}$$

The minimal error on the parameter λ is obtained by preparing all the probes in the state $(|a_M\rangle + |a_m\rangle)/\sqrt{2}$, where a_m and a_M are the respective smallest and largest eigenvalues of the operator $\hat{A}$, such that the value $\Delta A = (a_M - a_m)/2$ is maximized. To saturate the inequality (1.7) an appropriate observable would be for instance $\hat{O} = |a_m\rangle\langle a_M| + |a_M\rangle\langle a_m|$, yielding $\langle\hat{O}\rangle = \cos\lambda(a_M - a_n)$ and $\Delta O = |\sin\lambda(a_M - a_m)|$. In this case we have

$$\Delta\lambda_R = \frac{1}{\sqrt{N}(a_M - a_n)}. \tag{1.8}$$

This $1/\sqrt{N}$ scaling of the minimal error is sometimes called standard quantum limit.

Now we consider the situation where the same resource is available, i.e., N probes undergoing an evolution given by the unitary operator $\hat{U}^{\otimes N}$, but we allow for a measurement of the observable $\hat{O}_N = \hat{O}^{\otimes N}$, acting separately on the probes, and a highly entangled state of the N probes.

$$|\Psi_N\rangle = \frac{1}{\sqrt{2}}\left(\bigotimes_{k=1}^{N}|a_M\rangle_k + \bigotimes_{k=1}^{N}|a_m\rangle_k\right). \tag{1.9}$$

Since $\langle\hat{O}_N\rangle = \cos N\lambda(a_M - a_m)$ and $\Delta O_N = |\sin N\lambda(a_M - a_n)|$, we obtain

$$\Delta\lambda_N = \frac{1}{N(a_M - a_n)}, \tag{1.10}$$

and the minimum error is reduced by a factor $\sqrt{N}$. The above relation for the minimal error and the N^{-1} scaling express the so-called Heisenberg limit.

A practical application of this formalism is optical interferometry. In particular, it applies to the situation where one tries to detect a difference in the length of two optical paths. In this case, the quantity that one tries to measure is the accumulated phase shift φ that photons acquire by passing through the interferometer. Denoting by $\hat{a}_{1,2}$ the annihilation operators associated with the two paths of the photons, the unitary operator is $\hat{U} = e^{-i\varphi\hat{A}}$, where $\hat{A} = \hat{a}_1^\dagger\hat{a}_1 - \hat{a}_2^\dagger\hat{a}_2$. Single photons entering the interferometer after having passed through a first beam splitter are described by the state $|\psi\rangle = (|1,0\rangle + |0,1\rangle)/\sqrt{2}$. An appropriate observable is, for instance, $\hat{O} = \hat{b}_1^\dagger\hat{b}_1 - \hat{b}_2^\dagger\hat{b}_2$, where $\hat{b}_{1,2} = (\hat{a}_1 \pm \hat{a}_2)/\sqrt{2}$ are the output mode operators after the two beams have been recombined on a second beam splitter. This form of the observable describes balanced photo-detection and leads to $\langle\hat{O}\rangle = \cos\varphi$. Accordingly, when N single photons passing through the interferometer are measured, the corresponding phase uncertainty is $\Delta\varphi = 1/\sqrt{N}$. We recover the shot-noise limit that applies to coherent states in optical interferometry. This emphasizes the classical nature of a coherent light beam in the sense that it can be regarded as a stream of independent photons, i.e., sharing only classical correlations, passing through the interferometer and acting as N uncorrelated probes. To reach the Heisenberg limit, one would need to introduce quantum correlations between the photons, i.e., prepare them in a highly entangled N00N state $|\Psi\rangle = (|N,0\rangle + |0,N\rangle)/\sqrt{2}$.

Another situation where an improvement of the sensitivity could be achieved by resorting to highly entangled states of two-level systems is the case of frequency or time

measurements [Bollinger96, Huelga97]. For instance, atomic clocks are based on interferometric sensing. Schematically, one prepares a two-level system in the ground state $|\downarrow\rangle$, applies a $\pi/2$-pulse to create a superposition $(|\downarrow\rangle + |\uparrow\rangle)/\sqrt{2}$ of the ground and excited state $|\uparrow\rangle$, and applies a second $\pi/2$-pulse after some time t. One can infer the elapsed time between the two pulses by measuring the probability that the final state is $|\downarrow\rangle$, given by $p_\downarrow = \cos^2(\omega t/2)$ where ω is the known transition frequency between the ground and excited states. If one starts from the maximally entangled state $(|\downarrow \ldots \downarrow\rangle + |\uparrow \ldots \uparrow\rangle)/\sqrt{2}$, the sensitivity can be increased by a factor $\sqrt{N}$, where N is the number of entangled two-level systems.

1.3 Thesis overview

This thesis is organized as follows. In Chapter 2, we review the basic features of superconducting circuits and how they are used to engineer qubits, based on nonlinear Josephson junction elements, as well as microwave transmission lines and resonators. We explain why these systems can effectively be described with a few electromagnetic degrees of freedoms at low temperatures. In particular, we discuss the properties of superconducting charge qubits and how they can be strongly coupled to a microwave resonator, realizing an integrated and electrically-controlled version of cavity quantum electrodynamics (QED). Finally, we mention the most significant achievements that have been experimentally demonstrated within this approach.

Entangled states are important for several tasks of quantum information processing, such as fault-tolerant quantum computing or quantum secret sharing. In Chapter 3, we present a one-step deterministic procedure to generate Greenberger-Horne-Zeilinger (GHZ) states in the standard circuit QED architecture. We consider the case of superconducting transmon qubits coupled to a single mode of a transmission line resonator. In the dispersive regime, an effective pairwise qubit interaction allows to produce, starting from a separable state, a GHZ state in a time that does not depend on the number of qubits. This scheme implements an idea of Mølmer and Sørensen that was originally proposed to entangle trapped ions [Mølmer99]. We discuss a way to confirm the genuine multi-qubit entangled nature of the generated GHZ states with an entanglement witness relying on the Bell-Mermin operator. The consequences of undesirable effects, such as inhomogeneous qubit-resonator coupling or the weak anharmonicity of transmon qubits, are studied and quantified.

Chapter 4 introduces the prototypical model of cavity optomechanics and several of its realizations. We present the basic principles of the radiation-pressure force and how it couples the light field inside a cavity to the motion of a mechanical object. The important parameters and their relevance for certain applications are discussed and a brief overview of the model phenomenology is given. A survey of recent implementations, based on standard optical Fabry-Pérot cavities, whispering gallery modes, photonic crystals, and superconducting microwave resonators is provided. Finally, typical parameter regimes and promising features achieved with these respective implementations are summarized.

The optomechanical interaction, being intrinsically nonlinear, might potentially be used to create and manipulate non-classical states of the optical mode. It was, for instance, realized that the radiation-pressure interaction might produce an effective photon-photon interaction, allowing to exhibit quantum effects such as photon antibunching [Kronwald13] or photon blockade [Rabl11]. Chapter 5 is dedicated to the comparison between a generic optomechanical system and an optical cavity filled with a Kerr medium. These two systems

are investigated with regards to optical bistability. The steady-state mean-field equations of an optomechanical system are well-known to be equivalent to those of a Kerr medium, with three possible solutions in certain regimes. However, the optomechanical system, due to position fluctuations of the mechanical resonator, exhibits a richer stability diagram; the upper branch can become unstable at high driving power. We identify the parameters that indicate in which regime the mechanical mode effectively acts a Kerr nonlinearity for the optical mode.

Chapter 2

Quantum electrodynamics with superconducting circuits

Superconducting circuits provide a promising solid-state platform to perform quantum information processing tasks. In the present chapter, we provide the basic ingredients to understand how these circuits can realize a solid-state version of cavity quantum electrodynamics (QED). We describe how superconducting resonators and qubits are physically implemented, coupled, and controlled. We also discuss how realistic experimental conditions affect the coherence of such systems.

As mentioned in the introduction, physical quantum systems tailored to be used as the fundamental building blocks of a quantum information processor – the quantum bits – and to implement logical operations – quantum gates – should satisfy some essential requirements.

A single ideal qubit has two well-defined accessible energy levels, defining the logical states of the qubit. The preparation of a single qubit in any desired linear superposition of the two logical states is a first condition, for instance by initialization in a predefined state and subsequent application of a single-qubit gate. Secondly, we need the ability to perform a minimal set of logical operations – a universal set of quantum gates – on any pair of qubits, while preserving the quantum coherence between them. Finally, an accurate readout of the state of the qubits has to be possible. These minimal but restrictive conditions, which form the first five DiVincenzo criteria [DiVincenzo00], have set a list of experimental goals and stages to be achieved for the successful realization of quantum computing devices.

Over the last nearly two decades, several research groups have been working on demonstrating the potential of integrated quantum circuits to perform these operations and the progress so far is impressive. The first stage was the design and the characterization of a single physical qubit, followed by the demonstration of single-qubit operations or quantum gates. The circuit QED architecture, where multiple charge qubits are capacitively coupled to a common microwave resonator, was a major breakthrough [Wallraff04]. Initially, this architecture allowed to perform two-qubit gates, but was rapidly further improved and made possible the execution of simple quantum algorithms on three qubits [DiCarlo10, Fedorov12, Reed12]. Another remarkable achievement was the realization of quantum non-demolition (QND) measurements of the state of superconducting qubits, a crucial experimental step before envisioning the implementation of simplified quantum error correction (QEC) schemes. According to Ref. [Devoret13], proof-of-principle demon-

strations of QEC algorithms, that is the storage of a single bit of quantum information into a small register of qubits for a time that is significantly longer than the decoherence time of its physical sub-components, represent the next experimental challenge.

2.1 Superconducting circuits in the quantum regime

At first sight, it is not obvious why a superconducting qubit made out of $N \sim 10^9 - 10^{12}$ atoms behaves like a quantum-mechanical object with only one or few relevant quantized degrees of freedom. How can a flux qubit be in a coherent superposition of two states with supercurrents, made of $2N$ electrons, flowing in opposite direction? How can a charge qubit be in a superposition of states with precisely N and $N+1$ Cooper pair?

The answer to these questions requires a quick look at the underlying physical mechanisms allowing us to quantize the relevant degrees of freedom of superconducting circuits. The first effect, superconductivity, explains how we can neglect many electronic degrees of freedom in these circuits. The second one, Coulomb interaction, prevents the appearance of undesired collective excitations of the superconducting electrons. In short, superconductivity is at the origin of currents that flow without dissipation and also provides a straightforward solution to the problem of decoherence. The strong Coulomb repulsion lifts collective excitations known as bulk plasmons up to optical frequencies. Another interpretation is that these effects gap both the single-particle and plasmon excitations, freezing them into their quantum mechanical ground state at low temperatures. In the following two sections, we briefly discuss these effects and the consequence for superconducting circuits.

2.1.1 Superconductivity

A detailed description of the microscopic theory of superconductivity is beyond the scope of this thesis and can be found in standard condensed-matter textbooks [Tinkham96, Marder10]. We only review briefly the phenomenological properties of conventional BCS superconductors such as aluminum or niobium, used in most of the experiments.

The BCS theory predicts how an effective phonon-mediated attractive interaction between the electrons causes the formation of a condensate of electrons pairs near the Fermi level, the Cooper pairs [Cooper56, Bardeen57]. As a result of this condensation, an energy gap of $2\Delta_{\mathrm{SC}}$ opens in the single-particle density of states around the Fermi level, which means that $2\Delta_{\mathrm{SC}}$ is the required energy to break a Cooper pair and create an excited state. An important prediction of the theory was that the superconducting gap at zero temperature, Δ_{SC}, is proportional the superconducting transition temperature T_c, via the relation $\Delta_{\mathrm{SC}} = 1.76 k_B T_c$.

Importantly, below the critical temperature T_c, a current can flow without dissipation in a superconductor, hence its name. To be more precise, a superconductor shows no resistance for oscillating currents whose frequency is much smaller than the superconducting gap, $\omega \ll 2\Delta_{\mathrm{SC}}/\hbar$. Therefore, a resonant superconducting circuit may exhibit large quality factor if its frequency is small compared to $\Delta_{\mathrm{SC}}/\hbar$. This is of course a good omen, since low energy dissipation rates are generally a synonym of longer-maintained quantum coherence, if any.

Another consequence of temperatures well below T_c is the exponential suppression of single-particle excitations. Conducting electrons near the Fermi level form Cooper pairs, behaving effectively as bosons, that are condensed into a single non-degenerate

macroscopic ground state. This clarifies the quantum-mechanical nature of macroscopic quantities such as the current or the charge. The latter are precisely the two dynamical degrees of freedom we aim to quantize in the resonant superconducting circuits we are dealing with.

In a resonant circuit, the charge and the current are conjugated degrees of freedom of electromagnetic modes and are related to a voltage (via a capacitance C) and a magnetic flux (via an inductance L) respectively. The excitation energy or level spacing of such electromagnetic modes is therefore approximately $\omega \simeq 1/\sqrt{LC}$. A condition for superconducting circuit to properly operate in the quantum regime is $k_B T \ll \hbar\omega \ll k_B T_c$. In this regime, dynamical variables such as the voltage of the magnetic flux are promoted to the rank of quantum mechanical operators.

A superconductor like aluminum has a superconducting transition temperature $T_c = 1.2$ K ($\Delta_{\mathrm{Al}} = 0.17$ meV). Due to their size and geometry, superconducting qubits and quantum buses have resonance frequencies in the microwave domain, of the order of 10 GHz (~ 0.5 K), much smaller than the superconducting gap in aluminum, $2\Delta_{\mathrm{Al}}/h \simeq 82$ GHz, or niobium $2\Delta_{\mathrm{Nb}}/h \simeq 740$ GHz. For these reasons, superconducting circuits are operated at low temperatures, around 10-30 mK ($\sim$ 0.2-0.6 GHz), generally in dilution refrigerators.

2.1.2 Coulomb interaction and plasma oscillations

According to the BCS theory of superconductivity, only the single-particle excitations are gapped. However, other types of collective excitation are present in an interacting electron gas. The Coulomb interaction plays an essential role in limiting the number of low-energy collective degrees of freedom in superconducting circuits.

The Coulomb interaction is long-ranged. In momentum space, its strength V_q is proportional to $1/q^2$ and it is clear that this interaction is more important for small momentum transfer q. It indeed plays a role for collective excitations known as plasma oscillations. Classically, plasma oscillations can be seen as charge density waves of the electron gas over the ionic background. We give hereafter a simple description of these collective excitations.

We define the electron charge density as $\rho_e(\mathbf{r}, t) = -e[n_e + \delta n(\mathbf{r}, t)]$, where $-e$ is the electron charge, n_e describes the average electron number density compensating the positively charged ionic background, and δn the fluctuations around n_e. If $\mathbf{v}(\mathbf{r}, t)$ is the velocity field of the electrons, the current density can be approximated by $\mathbf{j} = -en_e\mathbf{v}$. We further assume that the motion of the electrons satisfy Newton's law $m_e\dot{\mathbf{v}} = -e\mathbf{E}$ and the electrical field Gauss's law $\nabla \cdot \mathbf{E} = -e\delta n/\epsilon$, where m_e is the electron mass and ϵ the permittivity of the medium. The current $\mathbf{j}$ and charge fluctuation δn can be related through the continuity equation $\nabla \cdot \mathbf{j} - e\delta\dot{n} = 0$. We obtain an equation of motion for δn of the form

$$\delta\ddot{n} + \omega_p^2 \delta n = 0, \tag{2.1}$$

where $\omega_p = \sqrt{\frac{n_e e^2}{m_e \epsilon_0}}$ is the bulk plasma frequency.

This model is of course very incomplete. A quantum mechanical treatment of the interacting electron gas, using the random-phase approximation, leads to the gapped dispersion relation [Bruus04]

$$\omega(q) = \omega_p \left[1 + \frac{3}{10}\left(\frac{q v_F}{\omega_p}\right)^2\right], \tag{2.2}$$

where v_F is the Fermi velocity. Quantum mechanically, $\hbar\omega(q)$ is the energy required to create an elementary excitation with wave vector q of this collective plasma mode. Such a quasiparticle is usually called a bulk plasmon.

In aluminum we have for instance $\hbar\omega_p \simeq 14.7$ eV (corresponding to $1.7 \times 10^5 K$ or 3.57×10^6 GHz). Hence, at low temperatures down to the Kelvin range, bulk plasmon are completely absent in superconducting circuits. In conclusion, the Coulomb interaction is important to understand why superconducting circuits can be described with so few relevant quantized degrees of freedom. Bulk charge density fluctuations being frozen to their quantum-mechanical ground state, the remaining dynamical degrees of freedom are collective plasma excitations that are due to the finite size of superconducting circuit. These excitations are the resonant modes obtained from the lumped-element description of such superconducting circuits. They have frequencies in the gigahertz range and are the modes we aim to quantize, as we discuss in the next section.

2.2 Canonical quantization of an electrical circuit

Now that the basic mechanisms allowing us to understand why superconducting resonant circuit behave quantum-mechanically have been reviewed, we present the standard procedure of canonical quantization of such systems [Devoret97]. The first step is to describe these integrated circuits in terms of lumped elements. Then, we derive a classical Hamiltonian for variables such as the charge, the voltage, the current, or the magnetic flux. These variables are then promoted to the rank of operators, whose dynamics is governed by quantum mechanics.

2.2.1 Lumped-element description

The elementary components of a quantum information processor – qubits and quantum buses – made out of superconducting circuits can be described in terms of lumped elements. A quantum bus is modeled as a one-dimensional waveguide supporting stationary electromagnetic modes with harmonic energy spectrum. Its physical properties like its resonant frequency and its damping rate are understood from simple models involving only linear circuit elements: capacitors, inductors, and resistors. Superconducting qubits – our artificial atoms – are based on the non-dissipative Josephson junction element, which provides the nonlinearity required for an anharmonic energy spectrum. We briefly list the linear lumped elements used to describe superconducting circuits and specify our notation and convention. Josephson junctions will be discussed later in Sec. 2.4.1.

Capacitor

The application of a potential difference $V = V_2 - V_1$ across a capacitor produces a accumulation of charge $\pm Q$ on each plates of the capacitor. The capacitance C is a positive quantity relating Q and V,

$$Q = CV.$$

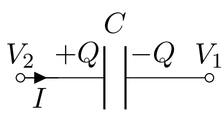

Notice that the current flowing across a capacitor is $I = \dot{Q} = C\dot{V}$.

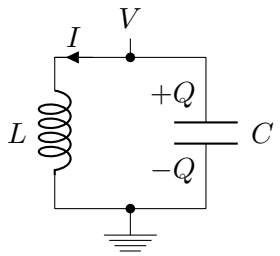

Figure 2.1: *Resonant LC circuit.* With the chosen convention, the current in the loop (flowing counterclockwise) and the charge on the capacitor plates are related through $\dot{Q} = -I$.

Inductor

The self-inductance L relates the voltage induced across a conductor $V = V_2 - V_1$ to the time-derivative of the current I,

$$V = L\dot{I}. \qquad \text{ 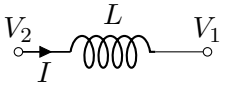 }$$

As we will see later, it turns out to be useful to define also the flux of any inductive element as $\Phi(t) = \int^t V(s)ds$. This quantity is proportional to the current and corresponds to the magnetic flux through the inductor, $\Phi = LI$. Since a magnetic flux is usually defined for a loop of current, Φ is sometimes called branch flux (or node flux) [Devoret04].

Resistor

The resistance R relates the current I and the voltage across the conductor V,

$$V = RI. \qquad \text{ 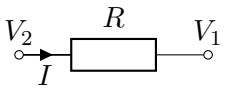 }$$

2.2.2 The LC resonator: a quantum harmonic oscillator

To illustrate the procedure of canonical quantization, we apply it to the LC resonator, shown in Fig. 2.1. For the moment, we forget about any resistive components in this ideal superconducting circuit, assuming there is no source of dissipation. In addition, since the supercurrent flows very rigidly, we can assume that the capacitor is the only place where charges can accumulate.

An obvious coordinate we may start with is of course the charge Q, related to the current by $I = -\dot{Q}$ (see Fig. 2.1). The Lagrangian of the system would be $\mathcal{L} = K - U$, where $K = L\dot{Q}^2/2$ is the kinetic inductive energy stored in the inductor, and $U = Q^2/(2C)$ the potential charging energy of the capacitor. The conjugate momentum of Q is $\Phi = \frac{\delta\mathcal{L}}{\delta\dot{Q}} = L\dot{Q} = -LI$, where LI is the magnetic flux through the inductor.

However, when considering circuits involving Josephson junctions, it turns out to be easier to use Φ instead of Q as the coordinate [Devoret97]. It can be conceptually understood as applying a canonical transformation that exchanges the role of coordinate and

momentum, $(Q, \Phi) \to (-\Phi, Q)$. In practice, the derivation of the Lagrangian in this new representation is done by defining the branch flux [Devoret04]

$$\Phi(t) = \int^t V(s)ds, \tag{2.3}$$

where V is the voltage at the upper node (see Fig. 2.1). The capacitive energy, $K = \frac{1}{2}CV^2 = \frac{1}{2}C\dot{\Phi}^2$ is now the kinetic energy and the inductive energy, $U = \frac{\Phi^2}{2L} = \frac{1}{2}LI^2$, the potential energy. The Euler-Lagrange equation is the equation of motion of a harmonic oscillator with resonance frequency $\Omega = 1/\sqrt{LC}$,

$$\ddot{\Phi} + \Omega^2\Phi = 0. \tag{2.4}$$

The conjugate momentum is $Q = \frac{\delta\mathcal{L}}{\delta\dot{\Phi}} = C\dot{\Phi} = CV$ and represents the charge of the capacitor. The classical Hamiltonian reads

$$\mathcal{H} = \dot{\Phi}Q - \mathcal{L} = \frac{Q^2}{2C} + \frac{\Phi^2}{2L}, \tag{2.5}$$

and the corresponding Hamilton equations of motion are

$$\dot{\Phi} = \frac{Q}{C}, \qquad \dot{Q} = -\frac{\Phi}{L}. \tag{2.6}$$

Obviously, those could have been readily obtained from the rules of circuit theory, $\dot{V} = -I/C$ and $V = L\dot{I}$.

The canonical quantization of the circuit is done as usual by promoting the coordinate Φ and the momentum Q to the rank of an operator. The flux $\hat{\Phi}$ and charge $\hat{Q}$ operators must satisfy the commutation relation

$$[\hat{\Phi}, \hat{Q}] = i\hbar. \tag{2.7}$$

Like for any other harmonic oscillator, the Hamiltonian can be expressed in terms of creation and annihilation operators, $\hat{a}^\dagger$ and $\hat{a}$,

$$\hat{H} = \hbar\Omega\left(\hat{a}^\dagger\hat{a} + \frac{1}{2}\right). \tag{2.8}$$

These operators $\hat{a}$ and $\hat{a}^\dagger$ satisfy the standard bosonic commutation relation $[\hat{a}, \hat{a}^\dagger] = 1$, and are related to $\hat{\Phi}$ and $\hat{Q}$ by

$$\hat{a} = \frac{1}{2}\left(\frac{\hat{\Phi}}{\Phi_{\text{zpf}}} + i\frac{\hat{Q}}{Q_{\text{zpf}}}\right), \qquad \hat{a}^\dagger = \frac{1}{2}\left(\frac{\hat{\Phi}}{\Phi_{\text{zpf}}} - i\frac{\hat{Q}}{Q_{\text{zpf}}}\right). \tag{2.9}$$

The flux and charge zero-point fluctuations depend on the characteristic impedance $Z = \sqrt{L/C}$,

$$\Phi_{\text{zpf}} = \sqrt{\frac{\hbar Z}{2}}, \qquad Q_{\text{zpf}} = \sqrt{\frac{\hbar}{2Z}}. \tag{2.10}$$

When the resonator is coupled to other systems, it is useful to define the voltage operator $\hat{V} = \hat{Q}/C$ and the current operator $\hat{I} = \hat{\Phi}/L$. The first one is relevant if we consider capacitive coupling to another system, while the second one is relevant in the case of inductive coupling.

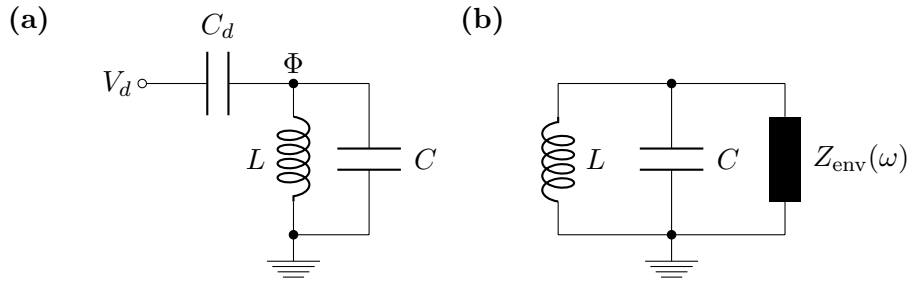

Figure 2.2: (a) Driven LC circuit. A time-dependent voltage $V_d(t)$ is applied to the LC resonator through the capacitance C_d. (b) LC resonator coupled to its environment. The electrical environment is modeled as frequency-dependent impedance $Z_{\mathrm{env}}(\omega)$.

Driven oscillator

We can now imagine that the LC resonator is coupled, through the capacitance C_d, to a time-dependent driving voltage $V_d(t)$, as illustrated in Fig. 2.2(a). The Lagrangian becomes

$$\mathcal{L} = \frac{1}{2}C\dot{\Phi}^2 + \frac{1}{2}C_d(V_d - \dot{\Phi})^2 - \frac{\Phi^2}{2L}. \tag{2.11}$$

The momentum $Q = \frac{\delta\mathcal{L}}{\delta\dot{\Phi}} = C\dot{\Phi} - C_d(V_d - \dot{\Phi})$ is the difference between the charges on the capacitors C and C_d. The corresponding Hamiltonian reads

$$\mathcal{H} = \frac{Q^2}{2C_\Sigma} + \frac{\Phi^2}{2L} + \frac{C_d}{C_\Sigma}V_d Q, \tag{2.12}$$

where $C_\Sigma = C + C_d$. This example shows how the resonance frequency $\Omega = 1/\sqrt{LC_\Sigma}$ is modified by the coupling to an external drive and how the charge couples to this external load. The Hamiltonian operator, expressed in terms of the creation and annihilation operators, is then

$$\hat{H} = \hbar\Omega\hat{a}^\dagger\hat{a} - i\hbar\epsilon(t)\left(\hat{a} - \hat{a}^\dagger\right), \tag{2.13}$$

where the driving amplitude is $\epsilon(t) = \frac{C_d}{C_\Sigma}\frac{Q_{\mathrm{zpf}}}{\hbar}V_d(t)$.

The Heisenberg equation of motion for the operator $\hat{a}(t)$ is

$$\dot{\hat{a}} = \frac{i}{\hbar}\left[\hat{H}, \hat{a}\right] = -i\Omega\hat{a} + \epsilon(t), \tag{2.14}$$

and describes the perfectly coherent and unitary evolution of the system. This comes from the implicit assumption we made in our derivation, we assumed the drive $V_d(t)$ to be perfectly classical, noiseless, and absolutely not influenced by the dynamics of the system. In reality, any external load or circuit has a finite impedance and carries noise of thermal or quantum origin. On one hand, it modifies the intrinsic properties of the quantum circuit and, on the other hand, it produces unavoidable dissipative effects, as we discuss below and later in Sec. 2.3.3.

Electrical environment

In practice, there are unavoidable sources of dissipation in any real circuit. The first source of dissipation we can think of is obviously some measurement apparatus coupled to the system or some applied electrical signal used to control or drive the system.

The energy dissipation resulting from the coupling between the quantum circuit and its environment produces a broadening of the energy levels. The magnitude of this broadening is characterized by $\hbar\kappa$, where κ is the ratio of the energy dissipation rate over the energy stored in the system. To give a concrete example, for the quantum LC oscillator, κ stands for the relaxation rate, at zero temperature, from the first excited state to the ground state. Also, the rate κ quantifies how strong the coupling between the quantum system and its environment is and how fast they can exchange energy.

Two important conditions must be satisfied for the flux Φ or the charge Q to be treated as quantum variables. An important parameter is obviously the temperature of the environment, i.e., the energy quantum associated with the resonance frequency Ω must be larger than the thermal fluctuation energy, $\hbar\Omega \gg k_B T$. Besides the temperature, another relevant quantity to determine to which extent a circuit is quantum is its quality factor. The latter is defined as $\mathcal{Q} = \Omega/\kappa$, i.e., the ratio of the resonance frequency over the dissipation rate. A necessary condition for a superconducting circuit to remain quantum when coupled to external loads is $\mathcal{Q} \gg 1$.

As shown in Fig. 2.2(b), the influence of the electrical environment can be modeled as an impedance $Z_{\rm env}(\omega)$ with unspecified frequency dependence, coupled in parallel to the LC resonator [Devoret97]. The impedance $Z_{\rm env}$ modifies the response of the circuit. The imaginary part of $Z_{\rm env}^{-1}$ changes the resonance frequency and the real part of $Z_{\rm env}^{-1}$ produces a broadening of the response, that is otherwise delta-peaked.

Assuming that the quality factor $\mathcal{Q}$ is large, the shift of the resonance frequency $\delta\Omega$ and the dissipation rate κ remain small compared to the bare resonance frequency $\Omega_0 = 1/\sqrt{LC}$. In this case, $\delta\Omega/\Omega_0$ and κ/Ω_0 can be approximated by

$$\frac{\delta\Omega}{\Omega_0} = \frac{1}{2}\mathrm{Im}\left(\frac{Z}{Z_{\rm env}(\Omega_0)}\right), \qquad \mathcal{Q}^{-1} = \frac{\kappa}{\Omega_0} = \mathrm{Re}\left(\frac{Z}{Z_{\rm env}(\Omega_0)}\right), \tag{2.15}$$

where $Z = \sqrt{L/C}$ is the characteristic impedance of the resonator only. These expressions are valid in the limit $Z/|Z_{\rm env}(\Omega_0)| \ll 1$. Moreover, it is implicitly assumed that the environment impedance $Z_{\rm env}(\omega)$ is nearly constant over the range of frequency where $|\omega - \Omega_0| \lesssim \kappa$.

The latter two assumptions turn out to be important when giving a quantum treatment of dissipation, the so-called quantum input-output theory. The impedance-mismatch condition, $|Z/Z_{\rm env}| \ll 1$, means that the system couples only weakly to its environment. The approximation $Z_{\rm env}(\omega) \sim Z_e(\Omega_0)$ suggests that the LC resonator mainly couples to environmental modes with frequency close to Ω_0. In addition it assumes that the coupling is nearly constant in this frequency range.

A more rigorous treatment of dissipation is given in Sec. 2.3.3, which treats superconducting transmission lines.

2.3 Superconducting transmission lines

A superconducting transmission line, as pictured in Fig. 2.3(a), is generally made of a conducting wire placed between two metallic ground planes, patterned by optical lithography on an insulating substrate such as single-crystal sapphire. When the central wire is of finite length, typically a few millimeters, such a transmission line forms a microwave resonator that can sustain photonic modes with high quality factors. In this configuration, the system is equivalent to an optical Fabry-Pérot cavity, but with resonance frequencies

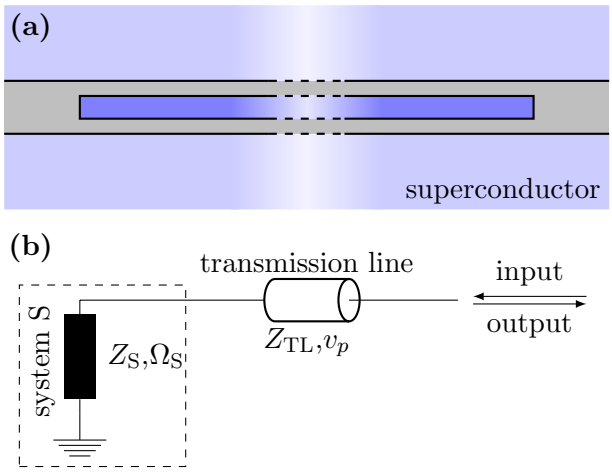

Figure 2.3: *Superconducting transmission line.* (a) Schematic representation of a superconducting transmission line resonator. The transmission line is formed by patterning a thin superconducting film (blue) on an insulating substrate (gray). The central wire (dark blue) is placed between two grounded planes (light blue). (b) Circuit diagrams showing a transmission line coupled to an arbitrary quantum system S. The transmission line is described by an impedance $Z_{\mathrm{TL}} = \sqrt{l/c}$ and a wave phase velocity $v_p = 1/\sqrt{lc}$, where l and c are its inductance and capacitance per unit length. From the transmission line perspective, the system is characterized by a generic impedance Z_{S} and a typical resonance frequency Ω_{S}.

in the gigahertz range. In this typical coplanar waveguide geometry, the electrical field is mainly confined in the gap between the wire and the ground planes, allowing strong capacitive coupling to other elements such as qubits.

A transmission line whose length is much longer can be used to measure or control some resonant circuits. The transmission line couples, at one of its ends, to a particular system of interest and is consider to be infinite on the other side. This type of transmission line no longer acts as a photonic resonator but rather as a waveguide that carries electromagnetic waves traveling towards or away from the system (see Fig. 2.3(b)). They are thought of as *semi-infinite* in the sense that energy leaving the system through the line never comes back. The 'infinite' end can be seen as being terminated by some environment, for instance a meter recording the signal coming out the line (output), or a signal generator that drives the system by sending waves down the line (input).

We proceed by first describing how to quantize the electromagnetic modes of finite-length superconducting transmission line resonator (TLR). Then we discuss semi-infinite transmission lines and their role in describing the dissipation and the coupling to external environment. Finally, we briefly present the input-output formalism, which can be conveniently derived in this framework even if its applicability goes beyond the scope of superconducting circuits.

2.3.1 Quantized modes of a transmission line resonator

A superconducting transmission line is modeled as a one-dimensional continuous chain of LC resonators, as shown in Fig. 2.4 [Blais04]. We denote its length by L_0, its capacitance per unit length by c, and its inductance per unit length by l. The current I and voltage

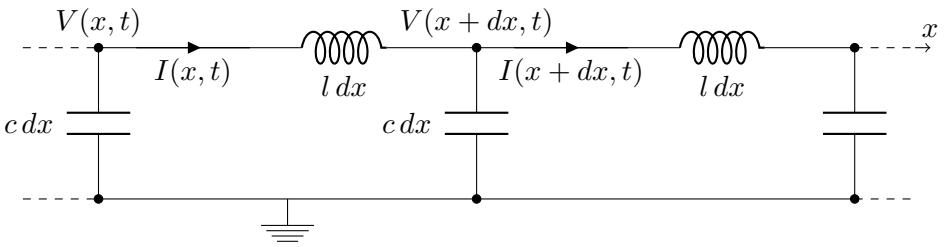

Figure 2.4: Continuous model of a transmission line resonator used to derive wave equations for the voltage $V(x,t)$ and the current $I(x,t)$. Capacitances are in parallel and inductances are in series, where c and l are the capacitance and inductance per unit of length respectively.

V are functions of the time t and the position $x \in [0, L_0]$. They are related through

$$\partial_x V(x,t) + l\partial_t I(x,t) = 0, \tag{2.16a}$$
$$\partial_x I(x,t) + c\partial_t V(x,t) = 0. \tag{2.16b}$$

The capacitive energy per unit length is $cV(x,t)^2/2$ and the inductive energy per unit length is $lI(x,t)^2/2$. As in the treatment of the LC-resonator, we prefer to use the flux variable $\Phi(x,t) = \int^t V(x,s)ds$. The definition of Φ and Eq. (2.16) lead to the following relations:

$$\partial_t \Phi(x,t) = V(x,t), \tag{2.17a}$$
$$\partial_x \Phi(x,t) = -lI(x,t). \tag{2.17b}$$

Defining the phase velocity $v_p = 1/\sqrt{lc}$, Eq. (2.16) translates to

$$v_p^2 \partial_x^2 \Phi(x,t) - \partial_t^2 \Phi(x,t) = 0, \tag{2.18}$$

which is the wave equation obtained from the Lagrangian

$$\mathcal{L} = \int_0^{L_0} dx \left\{ \frac{c}{2} \left[\partial_t \Phi(x,t)\right]^2 - \frac{1}{2l} \left[\partial_x \Phi(x,t)\right]^2 \right\}. \tag{2.19}$$

The conjugate momentum of the flux Φ is the linear charge density

$$q(x,t) = \frac{\delta \mathcal{L}}{\delta \left[\partial_t \Phi(x,t)\right]} = c\partial_t \Phi(x,t), \tag{2.20}$$

and the Hamiltonian is given by

$$\mathcal{H} = \int_0^{L_0} dx \left\{ \frac{1}{2c} \left[q(x,t)\right]^2 + \frac{1}{2l} \left[\partial_x \Phi(x,t)\right]^2 \right\}. \tag{2.21}$$

Before proceeding to the quantization of the Hamiltonian $\mathcal{H}$, we decompose the field $\Phi(x,t)$ into spatial normal modes $\phi_n(x)$,

$$\Phi(x,t) = \sum_{n \geq 0} \xi_n(t)\phi_n(x). \tag{2.22}$$

The arbitrary real functions $\xi_n(t)$ parametrize $\Phi(x,t)$ completely. The normal mode functions ϕ_n are given by

$$\phi_n(x) = \sqrt{\frac{2}{L_0}}\cos(k_n x - \varphi_n), \qquad k_n = \frac{n\pi}{L_0}, \tag{2.23}$$

for $n > 0$, while $\phi_0(x) = 1/\sqrt{L_0}$. The boundary conditions at $x = 0$ and $x = L_0$ set the value of the phases φ_n. For a transmission line resonator, we should consider open circuit boundary conditions, $I(0,t) = I(L_0,t) = 0$, which lead to $\varphi_n = 0$. For short circuit boundary conditions, $V(0,t) = V(L_0,t) = 0$, we would have instead $\varphi_n = \pi/2$, with the additional constraint of ξ_0 being constant. The normal mode functions ϕ_n satisfy

$$\int_0^{L_0} dx\ \phi_n(x)\phi_m(x) = \delta_{n,m}, \tag{2.24a}$$

$$\int_0^{L_0} dx\ \partial_x\phi_n(x)\partial_x\phi_m(x) = k_n^2\delta_{n,m}. \tag{2.24b}$$

The Lagrangian takes the form of a collection of independent harmonic oscillators with frequency $\omega_n = k_n v_p$

$$\mathcal{L} = \frac{1}{2}\sum_n c\dot{\xi}_n^2 - \frac{k_n^2}{l}\xi_n^2 = \frac{c}{2}\sum_n \dot{\xi}_n^2 - \omega_n^2\xi_n^2. \tag{2.25}$$

At this point, we can readily obtain the quantum version of the Hamiltonian in terms of position $\hat{\xi}_n$ and momentum $\hat{q}_n$ operators that satisfy the canonical commutation relation $[\hat{\xi}_n, \hat{q}_{n'}] = i\hbar\delta_{n,n'}$. We define the operators

$$\hat{a}_n = \sqrt{\frac{c\omega_n}{2\hbar}}\hat{\xi}_n + i\frac{1}{\sqrt{2\hbar c\omega_n}}\hat{q}_n, \tag{2.26a}$$

$$\hat{a}_n^\dagger = \sqrt{\frac{c\omega_n}{2\hbar}}\hat{\xi}_n - i\frac{1}{\sqrt{2\hbar c\omega_n}}\hat{q}_n, \tag{2.26b}$$

which annihilate or create a photon with energy $\hbar\omega_n$ in the corresponding n-th spatial mode. They satisfy the standard commutation relations $[\hat{a}_n, \hat{a}_{n'}^\dagger] = \delta_{n,n'}$. The Hamiltonian of the TLR reads

$$\hat{H} = \sum_{n>0}\frac{1}{2c}\hat{q}_n^2 - \frac{1}{2}c\omega_n^2\hat{\xi}_n^2 = \sum_{n>0}\hbar\omega_n\left(\hat{a}_n^\dagger\hat{a}_n + \frac{1}{2}\right). \tag{2.27}$$

Here, we have omitted the constant energy shift due to the zeroth mode ($n = 0$). Since $\omega_0 = 0$, the variable $\hat{\xi}_0$ has a particular status because its momentum is a constant of motion, $\dot{\hat{q}}_0 = 0$. As one can verify, it actually describes the effect of a uniform dc-voltage V_{dc}, $\hat{q}_0(t) = \sqrt{L_0}cV_{\mathrm{dc}}$.

The form of the Hamiltonian Eq. (2.27) indicates that a superconducting TLR of finite size can be seen as a one-dimensional microwave photonic cavity. The fundamental frequencies $\omega_1 = \pi v_p/L_0$ of such a superconducting resonator can be roughly estimated. It appears that $l \sim \nu_0$ (vacuum permeability) and $c \sim \epsilon_0$ (vacuum permittivity), and therefore, the wave phase velocity v_p is approximately the speed of light in vacuum. For a length $L_0 \simeq 10$ mm, it translates to a frequency $\omega_1/2\pi \simeq 15$ GHz. In practice, the exact

geometry of the TLR, the type of substrate, and the coupling to other elements influence the exact value of ω_1 significantly.

For the later discussion about semi-infinite TLRs and the coupling between superconducting qubits and a TLR, it is convenient to define the flux and charge density field operators $\hat{\Phi}(x)$ and $\hat{q}(x)$. The latter can be expressed in terms of the operators $\hat{x}_n$ and $\hat{q}_n$

$$\hat{\Phi}(x) = \sum_n \hat{\xi}_n \phi_n(x) = \sum_n \sqrt{\frac{\hbar}{2c\omega_n}} \left(\hat{a}_n + \hat{a}_n^\dagger\right) \phi_n(x), \tag{2.28a}$$

$$\hat{q}(x) = \sum_n \hat{q}_n \phi_n(x) = -i \sum_n \sqrt{\frac{\hbar c \omega_n}{2}} \left(\hat{a}_n - \hat{a}_n^\dagger\right) \phi_n(x). \tag{2.28b}$$

Using Eq. (2.28), we obtain the commutation relation

$$\left[\hat{\Phi}(x), \hat{q}(x')\right] = i\hbar \sum_n \phi_n(x)\phi_n(x') = i\hbar\delta(x - x'), \tag{2.29}$$

as well as the Hamiltonian

$$\hat{H} = \int_0^{L_0} dx \left\{ \frac{1}{2c}\hat{q}(x)^2 + \frac{1}{2l}\left[\partial_x \hat{\Phi}(x)\right]^2 \right\}. \tag{2.30}$$

Superconducting TLR can easily be coupled capacitively to some circuit elements placed between the central wire and the grounded planes. In this case, the voltage operator

$$\begin{aligned} \hat{V}(x) = \partial_t \hat{\Phi}(x) &= \frac{i}{\hbar}\left[\hat{H}, \hat{\Phi}(x)\right] = \frac{\hat{q}(x)}{c} \\ &= V_{\mathrm{dc}} - i \sum_{n>0} \sqrt{\frac{\hbar\omega_n}{2c}} \left(\hat{a}_n - \hat{a}_n^\dagger\right) \phi_n(x) \end{aligned} \tag{2.31}$$

couples to some charge degree of freedom.

2.3.2 Semi-infinite transmission line and classical input-output relation

We now extend our discussion to the case of semi-infinite superconducting transmission lines. First, we show how the voltage or the current field in an infinitely long transmission line can be decomposed into modes propagating toward the quantum system (incoming) and away from it [Clerk10]. Then, an example shows how this produces dissipation in the system.

Classical input-output theory

In a transmission line, the current-voltage relations Eq. (2.16) translates to the wave equations

$$\partial_t^2 V(x,t) - v_p^2 \partial_x^2 V(x,t) = 0, \tag{2.32a}$$

$$\partial_t^2 I(x,t) - v_p^2 \partial_x^2 I(x,t) = 0, \tag{2.32b}$$

Thus, the voltage and the current can be decomposed into incoming and outgoing modes

$$V(x,t) = V_{\text{out}}\left(t - \frac{x}{v_p}\right) + V_{\text{in}}\left(t + \frac{x}{v_p}\right), \tag{2.33a}$$

$$I(x,t) = \frac{1}{Z_c}\left[V_{\text{out}}\left(t - \frac{x}{v_p}\right) - V_{\text{in}}\left(t + \frac{x}{v_p}\right)\right], \tag{2.33b}$$

where $Z_c = \sqrt{l/c}$ is the impedance of the line. We assume that the line is terminated at its left side end ($x = 0$) by some system S (see Fig. 2.3(b)). The incoming V_{in} and outgoing V_{out} modes propagate toward and away from the system. Their shapes can in principle be arbitrary. From now on, we drop the position argument and assume that all the functions are taken at $x = 0$ and only depend on the time t. Thus, we can write

$$V_{\text{out}}(t) = V_{\text{in}}(t) + Z_{\text{TL}} I(t), \tag{2.34a}$$

$$V(t) = 2V_{\text{in}}(t) + Z_{\text{TL}} I(t), \tag{2.34b}$$

We emphasize that it only makes sense to speak about incoming and outgoing modes in the limit $L_0 \to \infty$, such that no other boundary conditions apply at the right side of the transmission line. In the limit of a semi-infinite transmission line, $V_{\text{in}}(t)$ and $V_{\text{out}}(t')$ are independent for $t > t'$. In other words, we assume the incoming mode V_{in} to be independent of the system dynamics. On the contrary, Eq. (2.34a) means that the outgoing mode V_{out} is the sum of the reflected incoming mode and an additional contribution $Z_{\text{TL}} I$ coming from the system dynamics.

If the transmission line is terminated by some system S, a boundary condition relates the voltage V and the current I. The boundary condition is better expressed in the frequency domain and reads

$$V(\omega) = -Z(\omega) I(\omega), \tag{2.35}$$

where $Z(\omega)$ is the frequency-dependent impedance of the system S. It yields a input-output relation between the incoming and outgoing modes

$$\frac{V_{\text{out}}(\omega)}{V_{\text{in}}(\omega)} = \frac{Z(\omega) - Z_{\text{TL}}}{Z(\omega) + Z_{\text{TL}}}. \tag{2.36}$$

In short, Eq. (2.36) expresses the relation between the output signal V_{out}, influenced by a system with impedance $Z(\omega)$, and the input signal V_{in}.

Semi-infinite line and dissipation

At the end of Sec. 2.2.2, we briefly discussed how to account for the dissipative effect of an electrical environment coupling to a quantized circuit. It appears that a semi-infinite transmission line appropriately models such an environment.

We briefly illustrate this mechanism in a classical framework, assuming that the system S is a LC-resonator (see Fig. 2.2(b)). The transmission line plays now the role of the electrical environment with impedance $Z_{\text{env}}(\omega) = Z_{\text{TL}}$.

We take the flux Φ, Eq. (2.3), as the dynamical variable. Using Eq. (2.34b), we obtain the equation of motion of a driven and damped oscillator

$$\ddot{\Phi} + \kappa\dot{\Phi} + \Omega_{\text{S}}^2 \Phi = \frac{2}{Z_{\text{TL}} C} V_{\text{in}}(t). \tag{2.37}$$

The damping rate is $\kappa = \Omega_S \frac{Z_S}{Z_{TL}}$, where $\Omega_S = 1/\sqrt{LC}$ is the unperturbed LC-resonator frequency and $Z_S = \sqrt{L/C}$ its characteristic impedance.

We notice how the LC resonator is damped via the coupling to the transmission line. In the absence of any input driving, $V_{in} = 0$, the transmission line acts as a resistance, $V = Z_{TL} I$, as it can be seen from Eq. (2.34b). Moreover, the damping rate of the system becomes large when its impedance matches the one of the transmission line, $Z_S \simeq Z_{TL}$, causing the system to easily lose energy by radiating through the line.

The characteristic impedance Z_S should not be confused with the frequency-dependent impedance $Z(\omega)$, which characterizes the system response to an external drive. For an LC resonator, we have $Z(\omega) = i\left[\omega C - 1/(\omega L)\right]^{-1}$.[1] The expression for $Z(\omega)$ can be simplified if the quality factor of the system is large, $\Omega_S \gg \kappa$. In this case, we have, for positive frequency ω,

$$\frac{Z(\omega)}{Z_{TL}} \simeq \frac{i}{2}\frac{Z_S}{Z_{TL}}\frac{\Omega_S}{\omega - \Omega_S} = \frac{i\kappa/2}{\omega - \Omega_S}. \tag{2.38}$$

The response of the system to the input is characterized by the response function $\chi(\omega)$, defined as

$$\chi(\omega) = \frac{V(\omega)}{V_{in}(\omega)} = \frac{2Z(\omega)}{Z(\omega) + Z_{TL}} = \frac{\kappa}{\kappa/2 - i(\omega - \Omega_S)}. \tag{2.39}$$

Eq. (2.39) shows that the system mainly responds the input modes with frequencies close to its resonance frequency, provided $\mathcal{Q} \gg 1$. As we will discuss in the next section, this narrow bandwidth response is a necessary assumption to derive the quantum version of the input-output relations.

Finally, for the LC resonator, the classical input-output relation, Eq. (2.36), becomes

$$\frac{V_{out}(\omega)}{V_{in}(\omega)} = \chi(\omega) - 1 = \frac{\kappa/2 + i(\omega - \Omega_S)}{\kappa/2 - i(\omega - \Omega_S)}. \tag{2.40}$$

Since the LC resonator contains no dissipative elements, $|V_{out}(\omega)/V_{in}(\omega)| = 1$. Its dynamics is contained in the relative phase between the input and output signals only.

2.3.3 Quantum input-output formalism

Our goal is to give a quantum description of some setup involving a semi-infinite transmission line together with a coupled system, as depicted in Fig. 2.3(b). Using the formulation given in Sec. 2.3.1, we show how the propagating modes of a single infinitely long transmission line are expressed as a continuous set of independent left and right-moving quantized modes. Finally, we introduce the so-called quantum input-output theory. This general model involves a quantum system coupled to an unspecified environment, represented as a large collection of harmonic oscillators. A possible interpretation of such a model is precisely a transmission line terminated by some quantum system. The environmental modes are expressed as propagating modes, which split into incoming modes, that drive the quantum system and carry noise, and outgoing modes, radiated by the quantum system into the environment.

[1] Here, we use the convention $f(\omega) = \int e^{i\omega t} f(t) dt$ for the Fourier transform. It follows that $-i\omega f(\omega) = \int e^{i\omega t} \dot{f}(t) dt$.

Quantized propagating modes of a transmission line.

The quantized photonic modes of the finite-length transmission line are actually standing-wave modes. This is a consequence of the boundary conditions which were set at both ends of the transmission line. To give a simplified picture, we consider the operator $\hat{a}_n^\dagger$, Eq. (2.26), which creates a photon with frequency ω_n in the spatial mode $\phi_n(x)$. The Heisenberg equation of motion of this operator is

$$\dot{\hat{a}}_n^\dagger(t) = i\omega_n \hat{a}_n^\dagger(t), \qquad \hat{a}_n^\dagger(t) = e^{i\omega_n t}\hat{a}_n^\dagger(0). \tag{2.41}$$

We notice that the term $\hat{a}_n^\dagger(t)\phi_n(x)$ contains both a right-moving component with negative wave vector, $e^{-ik_n(x-v_p t)}$, and a left-moving component with positive wave vector, $e^{ik_n(x+v_p t)}$. For $\hat{a}_n(t)\phi_n(x)$, the opposite is true. Therefore we need some reformulation if we want to decompose operators which contain both of these terms, such as the voltage $\hat{V}$, Eq. (2.31), into left and right-moving modes.

Assuming the classical flux $\Phi(x,t)$ and charge density $q(x,t)$ fields satisfy periodic boundary conditions, we write their most general solution in a form that anticipates the quantum version [Clerk10],

$$\Phi(x,t) = \frac{1}{\sqrt{L_0}} \sum_k \sqrt{\frac{\hbar}{2c\omega_k}} \left[b_k e^{i(kx-\omega_k t)} + b_k^* e^{-i(kx-\omega_k t)} \right], \tag{2.42a}$$

$$q(x,t) = \frac{-i}{\sqrt{L_0}} \sum_k \sqrt{\frac{\hbar c\omega_k}{2}} \left[b_k e^{i(kx-\omega_k t)} - b_k^* e^{-i(kx-\omega_k t)} \right], \tag{2.42b}$$

where the sum is taken over all $k = 2\pi m/L_0$, $m \in \mathbb{Z}$, and $\omega_k = v_p|k|$. The new mode index k is still discrete, but it can be either positive or negative, and replaces the previous index $n \in \mathbb{N}$. The above equation allows to clearly distinguish the right-moving components ($k > 0$) from the left-moving ones ($k < 0$). Note that since we have considered periodic boundary conditions, rather than open- or short-circuit terminations, the coefficients b_k and b_{-k} are completely independent, as we expect for an infinitely long transmission line.

It is clear how to decompose the Hamiltonian Eq. (2.30), written in terms of quantum field operators $\hat{\Phi}(x)$ and $\hat{q}(x)$, into modes propagating either to the left or to the right. For this purpose, we define the operators $\hat{b}_k$,

$$\hat{b}_k = \frac{1}{\sqrt{L_0}} \int_0^{L_0} dx\, e^{-ikx} \left[\sqrt{\frac{c\omega_k}{2\hbar}} \hat{\Phi}(x) + \frac{i}{\sqrt{2c\hbar\omega_k}} \hat{q}(x) \right]. \tag{2.43}$$

This leads to the following expressions for $\hat{\Phi}(x)$ and $\hat{q}(x)$:

$$\hat{\Phi}(x) = \frac{1}{\sqrt{L_0}} \sum_k \sqrt{\frac{\hbar}{2c\omega_k}} \left[\hat{b}_k e^{ikx} + \hat{b}_k^\dagger e^{-ikx} \right], \tag{2.44a}$$

$$\hat{q}(x,t) = \frac{-i}{\sqrt{L_0}} \sum_k \sqrt{\frac{\hbar c\omega_k}{2}} \left[\hat{b}_k e^{ikx} - \hat{b}_k^\dagger e^{-ikx} \right]. \tag{2.44b}$$

Using the commutation relation $[\hat{\Phi}(x), \hat{q}(x)] = i\hbar\delta(x-x')$, we obtain

$$[\hat{b}_k, \hat{b}_{k'}^\dagger] = \delta_{k,k'}. \tag{2.45}$$

The Hamiltonian, Eq. (2.30), takes the form

$$\hat{H} = \sum_k \hbar\omega_k \left(\hat{b}_k^\dagger \hat{b}_k + \frac{1}{2}\right). \tag{2.46}$$

Using Eq. (2.44), we can express the voltage operator $\hat{V} = \hat{q}/c$, taken at $x = 0$, as

$$\hat{V}(t) = \hat{V}^{\rightarrow}(t) + \hat{V}^{\leftarrow}(t) \tag{2.47}$$

$$\hat{V}^{\rightarrow}(t) = \frac{-i}{\sqrt{L_0}} \sum_{k>0} \sqrt{\frac{\hbar\omega_k}{2c}} \left(\hat{b}_k(t) - \hat{b}_k^\dagger(t)\right), \tag{2.48}$$

$$\hat{V}^{\leftarrow}(t) = \frac{-i}{\sqrt{L_0}} \sum_{k<0} \sqrt{\frac{\hbar\omega_k}{2c}} \left(\hat{b}_k(t) - \hat{b}_k^\dagger(t)\right). \tag{2.49}$$

The time dependence indicates that the operators are given in the Heisenberg representation,

$$\hat{b}_k(t) = e^{-i\omega_k}\hat{b}_k, \qquad \hat{b}_k^\dagger(t) = e^{i\omega_k}\hat{b}_k^\dagger. \tag{2.50}$$

We now formally let the length of the transmission line go to infinity and introduce a continuous indexing of the modes by their frequency ω,

$$\hat{b}^{\rightarrow}(\omega) = 2\pi\sqrt{\frac{v_p}{L_0}} \sum_{k>0} \hat{b}_k \delta(\omega - \omega_k), \tag{2.51a}$$

$$\hat{b}^{\leftarrow}(\omega) = 2\pi\sqrt{\frac{v_p}{L_0}} \sum_{k<0} \hat{b}_k \delta(\omega - \omega_k). \tag{2.51b}$$

Notice that these operators can be expressed as the Fourier transform operators of the temporal right and left-moving modes

$$\hat{b}^{\rightarrow}(t) = \sqrt{\frac{v_p}{L_0}} \sum_{k>0} \hat{b}_k(t), \tag{2.52a}$$

$$\hat{b}^{\leftarrow}(t) = \sqrt{\frac{v_p}{L_0}} \sum_{k<0} \hat{b}_k(t). \tag{2.52b}$$

The conjugated operators are defined as $\hat{b}^{\dagger\rightleftarrows}(t) = \left[\hat{b}^{\rightleftarrows}(t)\right]^\dagger$ and therefore, in the frequency domain, they satisfy $\hat{b}^{\dagger\rightleftarrows}(\omega) = \left[\hat{b}^{\rightleftarrows}(-\omega)\right]^\dagger$.[2] Changing the summation over the index k into an integral

$$\sum_{k>0} \quad \rightarrow \quad \frac{L_0}{2\pi}\int_0^\infty dk, \tag{2.53}$$

allows us to compute the relevant non-vanishing commutators between either the temporal or the frequency-resolved operators,

$$\left[\hat{b}^{\rightarrow}(\omega), \hat{b}^{\dagger\rightarrow}(\omega')\right] = \left[\hat{b}^{\leftarrow}(\omega), \hat{b}^{\dagger\leftarrow}(\omega')\right] = 2\pi\delta(\omega + \omega'), \tag{2.54a}$$

$$\left[\hat{b}^{\rightarrow}(t), \hat{b}^{\dagger\rightarrow}(t')\right] = \left[\hat{b}^{\leftarrow}(t), \hat{b}^{\dagger\leftarrow}(t')\right] = \delta(t - t'). \tag{2.54b}$$

[2] This is due to the following choice for the definition of Fourier-transformed operators: $\hat{o}(\omega) = \int dt\, e^{i\omega t}\hat{o}(t)$. Accordingly, $\hat{o}^\dagger(\omega) = \int dt\, e^{i\omega t}\hat{o}^\dagger(t) = [\hat{o}(-\omega)]^\dagger$.

Later, we will consider the coupling between a transmission line and some quantum system. For this purpose, it is important to consider the case of propagating modes having a finite temperature. If for instance the left-moving modes are in thermal equilibrium, we have

$$\left\langle \hat{b}^{\dagger\leftarrow}(\omega')\hat{b}^{\leftarrow}(\omega)\right\rangle = 2\pi\delta(\omega+\omega')n_{\mathrm{B}}(\hbar\omega), \tag{2.55a}$$

$$\left\langle \hat{b}^{\leftarrow}(\omega)\hat{b}^{\dagger\leftarrow}(\omega')\right\rangle = 2\pi\delta(\omega+\omega')\left[1+n_{\mathrm{B}}(\hbar\omega)\right], \tag{2.55b}$$

where n_{B} is the thermal occupation number given by the Bose-Einstein statistics,

$$n_{\mathrm{B}}(\hbar\omega) = \frac{1}{e^{\frac{\hbar\omega}{k_B T}}-1}. \tag{2.56}$$

Quantum input-output theory

Dissipation in a quantum system results from the coupling to an environmental bath. The latter is usually considered as a much larger system, more precisely larger in terms of the number of degrees of freedom. The system and its environment exchange energy and because of the large number of degrees of freedom, this exchange is incoherent and produces dissipation in the quantum system.

The available quantum description of transmission lines allows for a direct quantum treatment of environmental effects in electrical circuits. For convenience, we base the presentation of the quantum input-output formalism on this description of quantum circuits. However, we emphasize that this formalism applies to quantum systems and environment other than electrical circuits. Originally, it was derived in the context of quantum optics and this model actually encompasses several types of system described by bosonic operators, such as optical cavities or mechanical resonators.

Following standard references on the subject [Gardiner85, Gardiner04, Walls08], we define an Hamiltonian for the quantum system and the bath

$$\hat{H} = \hat{H}_{\mathrm{S}} + \hat{H}_{\mathrm{int}} + \hat{H}_{\mathrm{B}}. \tag{2.57}$$

The system Hamiltonian $\hat{H}_{\mathrm{S}}$ satisfies the following conditions. First, we assume that the system S has only a single degree of freedom with some characteristic resonance frequency Ω. Secondly, $\hat{H}_{\mathrm{S}}$ is expressed in terms of bosonic creation and annihilation operators, $\hat{a}^\dagger$ and $\hat{a}$, that oscillates approximately like $\hat{a}(t) \sim e^{-i\Omega t}$. The Hamiltonian of the bath is

$$\hat{H}_{\mathrm{B}} = \int_{-\infty}^{\infty} d\omega\, \hbar\omega\, \hat{b}_\omega^\dagger \hat{b}_\omega, \tag{2.58}$$

and the interaction between the system and the bath reads

$$\hat{H}_{\mathrm{int}} = \int_{-\infty}^{\infty} d\omega\, i\hbar\gamma(\omega)\left(\hat{b}_\omega^\dagger \hat{a} - \hat{b}_\omega \hat{a}^\dagger\right) \tag{2.59}$$

The operators of the bath satisfy $\left[\hat{b}_\omega, \hat{b}_{\omega'}^\dagger\right] = \delta(\omega-\omega')$. These operators should not be confused with the operators defined in the previous section, Eq. (2.51). In fact $\hat{H}_{\mathrm{B}}$ should rather be seen as the continuous version of an Hamiltonian like the one for a TLR, Eq. (2.27), with the mode frequency ω as a continuous index. When the bath, which might

be thought of as an infinitely long transmission line, is coupled to a quantum system, we cannot yet define independent counter-propagating modes.[3]

The form given for the bath Hamiltonian $\hat{H}_{\mathrm{B}}$ and the interaction $\hat{H}_{\mathrm{int}}$ already presupposes two important approximations. First, the rotating wave approximation (RWA) is made for the interaction, and secondly, the domain for the bath frequencies is $\omega \in (-\infty, \infty)$ rather than the more natural domain of positive frequency.

We consider a concrete example of electrical circuits to illustrate theses points. Imagine we capacitively couple a transmission line to an LC resonator. The coupling between a voltage, as given in Eq. (2.31), and a charge degree of freedom should involve terms like $\hat{b}_\omega \hat{a}$ and $\hat{b}_\omega^\dagger \hat{a}^\dagger$ and the frequency domain should be $(0, \infty)$. The RWA relies on the assumptions that the coupling rate $\gamma(\omega)$ is small, such that the dynamics of $\hat{a}$ is mainly governed by $\hat{H}_{\mathrm{S}}$. The neglected counter-rotating terms are oscillating rapidly with frequencies $\simeq \pm(\Omega + \omega)$. In the same way, we argue that the terms $\hat{b}_\omega \hat{a}^\dagger$ and $\hat{b}_\omega^\dagger \hat{a}$ are important for the dynamics of the system only near resonance, that is for bath frequencies ω close to Ω. This last point allows us to extend the domain of integration over ω to $(-\infty, \infty)$, because the added terms at negative bath frequencies are all non-resonant.

In the language of electrical circuitry, the approximation of small coupling rates translates to an impedance mismatch between the environment and the system, such that the latter exhibits a high quality factor $\mathcal{Q}$ as we discussed in Sec. 2.2.2. In addition, in the context of classical input-output theory (see Sec. 2.3.2), we have seen that a system with high $\mathcal{Q}$ is mainly sensitive to components of the input field with frequency close to Ω. In the same way, for the generic model given by $\hat{H}$, we understand that, if $\hat{H}_{\mathrm{int}}$ is small, the main influence on the system comes from the bath modes $\hat{b}_\omega$ with frequencies $\omega \sim \Omega$.

We now derive the quantum Langevin equations for the operator $\hat{a}$, starting from the Heisenberg equations of motion for the system and bath operators

$$\dot{\hat{a}} = \frac{i}{\hbar}\left[\hat{H}, \hat{a}\right] = \frac{i}{\hbar}\left[\hat{H}_{\mathrm{S}}, \hat{a}\right] - \int_{-\infty}^{\infty} d\omega\, \gamma(\omega)\, \hat{b}_\omega, \tag{2.60a}$$

$$\dot{\hat{b}}_\omega = \frac{i}{\hbar}\left[\hat{H}, \hat{b}_\omega\right] = -i\omega \hat{b}_\omega + \gamma(\omega)\, \hat{a}. \tag{2.60b}$$

The formal time-dependent solution of Eq. (2.60b) is

$$\hat{b}_\omega(t) = e^{-i\omega(t-t_0)} \hat{b}_\omega(t_0) + \gamma(\omega) \int_{t_0}^{t} ds\, e^{-i\omega(t-s)} \hat{a}(s) \tag{2.61}$$

where the time $t_0 < t$ sets the boundary condition in the past. This expression for $\hat{b}_\omega(t)$ can be inserted into Eq. (2.60a) to obtain

$$\begin{aligned} \dot{\hat{a}} =& \frac{i}{\hbar}\left[\hat{H}_{\mathrm{S}}, \hat{a}\right] - \int_{-\infty}^{\infty} d\omega\, \gamma(\omega)\, e^{-i\omega(t-t_0)} \hat{b}_\omega(t_0) \\ & - \int_{-\infty}^{\infty} d\omega\, \gamma(\omega)^2 \int_{t_0}^{t} ds e^{-i\omega(t-s)} \hat{a}(s). \end{aligned} \tag{2.62}$$

At this point, we make the Markov approximation which assumes that the coupling $\gamma(\omega)$ is constant over some range of frequency near the system frequency Ω. Therefore we can set

$$\gamma(\omega) = \sqrt{\frac{\kappa}{2\pi}}. \tag{2.63}$$

[3] Recall that this can be done only for a transmission line with periodic boundary conditions.

The above approximation is valid only when the system, even coupled to a bath, still has a well-defined resonance frequency Ω. In a sense, we can understand it as $\kappa \simeq 2\pi[\gamma(\Omega)]^2$. The broadening of the energy levels of the system, due to the energy exchange with this environment, should remain limited, which means that $\kappa \ll \Omega$. We can therefore make use of the relations

$$\int_{-\infty}^{\infty} \frac{d\omega}{2\pi}\, e^{-i\omega(t-s)} = \delta(t-s), \qquad \int_{t_0}^{t} ds\, \delta(t-s)\hat{a}(s) = \frac{1}{2}\hat{a}(t), \tag{2.64}$$

to simplify Eq. (2.62).

The input operator is now defined as

$$\hat{a}_{\rm in}(t) = \frac{1}{\sqrt{2\pi}} \int_{-\infty}^{\infty} d\omega\, e^{-i\omega(t-t_0)} \hat{b}_\omega(t_0). \tag{2.65}$$

The operator $\hat{a}_{\rm in}(t)$ express the free evolution of the bath modes until they interact with the system at time t. It is actually equivalent to the temporal left-moving modes $\hat{b}^{\leftarrow}(t)$, as defined for an infinitely long transmission line in Eq. (2.52), hence its name of input operator. The commutator

$$\left[\hat{a}_{\rm in}(t), \hat{a}_{\rm in}^\dagger(t')\right] = \delta(t-t') \tag{2.66}$$

can be compared to the one given in Eq. (2.54b). With these simplifications, the equation of motion for the system operator reads

$$\dot{\hat{a}} = \frac{i}{\hbar}\left[\hat{H}_{\rm S}, \hat{a}\right] - \frac{\kappa}{2}\hat{a} - \sqrt{\kappa}\hat{a}_{\rm in}(t), \tag{2.67}$$

and is referred to as *quantum Langevin equation*. The fact that the time t_0 is taken to be in the distant past, such that the system and the bath have not interacted yet, allows us to interpret $\hat{a}_{\rm in}$ as a driving term for the system. Since this driving is a superposition of quantum modes, it can be seen as a noisy drive carrying vacuum noise from the outside. The operator $\hat{a}_{\rm in}$ is therefore usually referred to as *quantum noise operator*. In addition, the emergence of a damping term proportional to κ in Eq. (2.67) shows how the opening of the quantum system to its surrounding environment produces energy dissipation.

The noise operators being delta-correlated, Eq. (2.66), indicates that such quantum noise is actually white noise. This is the consequence of the frequency range having been extend to $\omega \in (-\infty, \infty)$. This white noise is not physical but gives a good approximation over the range of frequency the system is mainly sensitive to, provided its quality factor is large.

If the system is a harmonic oscillator, $\hat{H}_{\rm S} = \hbar\Omega\hat{a}^\dagger\hat{a}$, we notice that Eq. (2.67) is the quantum analog of Eq. (2.37) which describes an LC-resonator driven and damped by a transmission line. Let $\hat{Q} = Q_{\rm zpf}(\hat{a} + \hat{a}^\dagger)$ be the charge operator of this LC-resonator, where $Q_{\rm zpf} = \sqrt{\hbar/2Z_{\rm S}}$ and $Z_{\rm S} = \sqrt{L/C}$. We assume that the charge $\hat{Q}$ couples to the voltage $\hat{V}$ at the end of some transmission line, Eq. (2.31),

$$\hat{V} = -i\sum_k \sqrt{\frac{\hbar\omega_k}{L_0 c}}\left(\hat{b}_k - \hat{b}_k^\dagger\right) = -i\int_0^\infty d\omega \sqrt{\frac{\hbar\omega Z_{\rm TL}}{\pi}}\left(\hat{b}_\omega - \hat{b}_\omega^\dagger\right). \tag{2.68}$$

The interaction $\hat{Q}\hat{V}$, within the RWA, leads to the frequency-dependent value of the coupling rate

$$\sqrt{2\pi}\gamma(\omega) = \sqrt{\frac{\omega Z_{\rm TL}}{Z_{\rm S}}}. \tag{2.69}$$

It yields a damping rate $\kappa = 2\pi[\gamma(\Omega)]^2 = \Omega\frac{Z_{\mathrm{TL}}}{Z_{\mathrm{S}}}$, which is the value expected from the classical analysis, where the transmission line acts like a resistance $R = Z_{\mathrm{TL}}$ for the LC resonator.

The example of the harmonic oscillator helps us to show that the system mainly responds to the bath modes with frequencies close to Ω. First we define the Fourier transformed input operator

$$\hat{a}_{\mathrm{in}}(\omega) = \int dt\, e^{i\omega t}\hat{a}_{\mathrm{in}}(t). \tag{2.70}$$

In the frequency domain, the quantum Langevin equation for the harmonic oscillator, Eq. (2.67), becomes

$$\hat{a}(\omega) = -\frac{\sqrt{\kappa}}{\kappa/2 - i(\omega-\Omega)}\hat{a}_{\mathrm{in}}(\omega) = -\frac{1}{\sqrt{\kappa}}\chi(\omega)\hat{a}_{\mathrm{in}}(\omega). \tag{2.71}$$

The system probes the bath only in a narrow frequency range around $\omega = \Omega$.

The noise carried by the bath or the transmission line to the system might be of pure quantum origin if the input modes are taken to be in their ground state. When considering a bath in equilibrium at temperature T, the input noise operator also contains noise of thermal origin and satisfies

$$\left\langle \hat{a}^\dagger_{\mathrm{in}}(t)\hat{a}_{\mathrm{in}}(t')\right\rangle = n_{\mathrm{th}}\delta(t-t'), \tag{2.72a}$$

$$\left\langle \hat{a}_{\mathrm{in}}(t)\hat{a}^\dagger_{\mathrm{in}}(t')\right\rangle = (n_{\mathrm{th}}+1)\delta(t-t'). \tag{2.72b}$$

The value of n_{th} expresses the thermal occupation number of the bath modes at the frequency of the system. It assumes a narrow frequency response around Ω. For the harmonic oscillator, one typically takes $n_{\mathrm{th}} = n_{\mathrm{B}}(\hbar\Omega)$. This is consistent with the similar equation we obtained for the propagating modes of a transmission line, Eq. (2.54a).

Finally, we can derive the quantum input-output relation. Solving Eq. (2.60b) for fixed boundary condition in the future $t_1 > t$, we end up with the so-called output operator

$$\hat{a}_{\mathrm{out}}(t) = \frac{1}{\sqrt{2\pi}}\int_{-\infty}^{\infty} d\omega\, e^{-i\omega(t-t_1)}\hat{b}_\omega(t_0), \tag{2.73}$$

together with the corresponding quantum Langevin equation

$$\dot{\hat{a}} = \frac{i}{\hbar}\left[\hat{H}_{\mathrm{S}}, \hat{a}\right] + \frac{\kappa}{2}\hat{a} - \sqrt{\kappa}\hat{a}_{\mathrm{out}}(t). \tag{2.74}$$

The output operator $\hat{a}_{\mathrm{out}}(t)$ expresses the free evolution of the bath modes after they interact with the system at time t. Comparing Eq. (2.67) and (2.74), we obtain the important *input-output relation*

$$\hat{a}_{\mathrm{out}}(t) = \hat{a}_{\mathrm{in}}(t) + \sqrt{\kappa}\hat{a}. \tag{2.75}$$

This equation is the quantum analog of the classical input-output relation that we obtain for a transmission line terminated by some arbitrary system, Eq. (2.34a). In contrast to a single transmission line, the incoming and outgoing modes are no longer independent but related to each other by the boundary conditions set by the presence of the system.

Remarks

The quantum input-output formalism allows to describe quantum-dissipative systems when a measurement is carried on the output fields. This particular situation requires the modes of the semi-infinite transmission line, or more generally the modes of the environment, to be effectively kept into the description as input and output noise operators. However, this formalism remains valid even in the absence of any measurement of the output fields and would describe dissipation through a bath of harmonic oscillators. In such a case, it allows to obtain information about the quantum system such as average quadrature amplitudes, average occupation numbers, or correlation functions. The quantum input-output formalism can be shown to be equivalent to other treatments where environmental degrees of freedom are traced out, like the standard Lindblad quantum master equation in particular [Gardiner04].

The description of the environment as a collection of harmonic oscillators is also reminiscent of other models used to characterize dissipative quantum systems. A close example is the quantum Brownian motion formalism, which get rids of the RWA and allows to consider systems with a low quality factor [Caldeira83a, Gardiner04]. Another prominent example to be mentioned is the spin-boson model for non-bosonic quantum systems such as two-level systems [Caldeira83b, Leggett87]. Results of the latter model will be discussed in Sec. 2.4.3, when considering decoherence effects affecting superconducting qubits.

2.4 Superconducting charge qubits

We show how resonant circuits can behave as artificial atoms with anharmonic spectrum, forming what we call superconducting qubits. We first discuss the properties of the Josephson junction, which is the essential nonlinear and dissipationless electrical element incorporated in any superconducting qubit. Secondly, we study a particular type of qubit implementation, the so-called Cooper pair box, as well as one of its improved design, the transmon qubit.

2.4.1 Josephson junction

The Josephson tunnel junctions encountered in superconducting circuits are made of a thin insulating barrier sandwiched between two superconducting metal pieces. The coherent tunneling of Cooper pairs through the junction produces a supercurrent whose intensity I is related to the superconducting phase difference $\phi = \varphi_2 - \varphi_1$ between the superconductors.[4] The equation relating I and ϕ is known as the first Josephson relation,

$$I = I_c \sin\phi. \tag{2.76}$$

The maximal tunneling current I_c depends on the geometry of the junction. It is proportional to the area and the transparency of the insulating barrier. When an voltage $V = V_2 - V_1$ is applied across the junction, the phase difference ϕ evolves according to the second Josephson relation,

$$\hbar\dot{\phi} = 2eV. \tag{2.77}$$

The convention for the direction of the current I, the sign of the phase difference ϕ and the voltage drop V is specified in Fig. 2.5.

[4] see e.g. [Tinkham96]

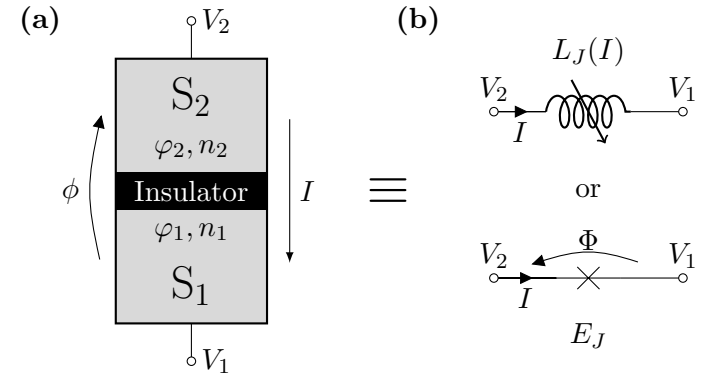

Figure 2.5: *Josephson junction.* (a) Josephson junction made of two superconducting metal leads, S_1 and S_2, separated by a thin insulating tunnel barrier. The important quantities entering the Josephson relations, Eqs. (2.76) and (2.77), are the superconducting phase difference, $\phi = \varphi_2 - \varphi_1$, the tunneling current I (positive when flowing from S_2 to S_1), and the potential difference $V = V_2 - V_1$. (b) Equivalent circuit representations of a Josephson junction, either by a nonlinear inductance $L_J(I)$ or by a cross with the associated Josephson energy E_J.

The Josephson junction acts as a nonlinear inductive element. Eqs. (2.76) and (2.77) can be combined into a single current-voltage relation similar to the one of a inductor, but with current-dependent inductance $L_J(I)$. This relation reads

$$V = L_J(I)\dot{I}, \qquad L_J(I) = \frac{\Phi_0}{2\pi\sqrt{I_c^2 - I^2}}, \tag{2.78}$$

where $\Phi_0 = h/(2e)$ denotes the magnetic quantum flux. The energy of the junction is

$$E = \int V I \, dt = \frac{\Phi_0 I_c}{2\pi} \int \sin\phi \, d\phi = -E_J \cos\phi, \tag{2.79}$$

where the quantity $E_J = \Phi_0 I_c/(2\pi)$ is known the Josephson energy.

It is often convenient to consider the superconducting phase difference as a dimensionless magnetic flux,

$$\phi = 2\pi\frac{\Phi}{\Phi_0}. \tag{2.80}$$

If we define Φ as a branch flux, like we did for the LC resonator, Eq. (2.3), then the second Josephson relation, Eq. (2.77) is automatically satisfied since $\dot{\Phi} = V$. The remaining constitutive equations for a Josephson junction are

$$I = I_c \sin\left(2\pi\frac{\Phi}{\Phi_0}\right), \qquad E = -E_J \cos\left(2\pi\frac{\Phi}{\Phi_0}\right). \tag{2.81}$$

Microscopic derivation of the Josephson relations

The periodic dependence of the current I on the flux Φ is a remarkable property of the Josephson junction. As we discuss below, such nonlinear behavior originates from a tunneling process that is simultaneously discrete and coherent.

The state of an homogeneous superconducting piece of metal at temperature $k_B T \ll \Delta_{SC}$ is usually considered as a macroscopic quantum state described by the wavefunction

$\Psi = \sqrt{\Delta_{\rm SC}} e^{i\varphi}$. The superconducting order parameter $\Delta_{\rm SC}$ appears in the wavefunction amplitude, while the phase φ, for an isolated superconductor, is undetermined. This comes from the fact that an isolated superconductor carries a well-defined number of Cooper pairs n. Since the number n and the phase φ are conjugated quantities, φ is completely undetermined if n is fixed. The phase becomes observable only when two superconductor can exchange charges, which is precisely the case in a Josephson junction. Hence, the gauge-invariant phase difference $\phi = \varphi_2 - \varphi_1$ is the relevant quantity entering the Josephson relations.

We consider two superconductors, denoted by S_1 and S_2, which can coherently exchange Cooper pairs through an insulating barrier, as shown in Fig. 2.5. We assume that each one is described by a state with a well-defined phase $|\varphi_j\rangle$. As stated previously, the phase and the number of Cooper pairs are conjugate variables. Therefore, we can define states with fixed number of Cooper pairs, denoted by $|n_j\rangle$, that are related to the states $|\varphi_j\rangle$ by

$$|n_j\rangle = \int_0^{2\pi} \frac{d\varphi_j}{2\pi}\, e^{-in_j\varphi_j} |\varphi_j\rangle, \tag{2.82}$$

$$|\varphi_j\rangle = \sum_{n_j} e^{in_j\varphi_j} |n_j\rangle. \tag{2.83}$$

With the above convention the number of Cooper pairs n_j is a position-like variable, while the phase φ_j is a momentum-like variable.

We can model a Josephson junction by the state $|\varphi_1, \varphi_2\rangle$ (equivalent to $|\varphi_1\rangle \otimes |\varphi_2\rangle$),

$$|\varphi_1, \varphi_2\rangle = \sum_{n_1, n_2} e^{i(n_1\varphi_1 + n_2\varphi_2)} |n_1, n_2\rangle. \tag{2.84}$$

But we have omitted the overall charge conservation, which requires that $n_1 + n_2 = N$ where N is a constant. When imposing this constraint on the state $|\varphi_1, \varphi_2\rangle$, we find that, up to an overall phase factor,

$$|\varphi_1, \varphi_2\rangle = \sum_n e^{in(\varphi_2 - \varphi_1)} |N - n, n\rangle. \tag{2.85}$$

We can therefore redefine the above number and phase states as $|n\rangle = |N - n, n\rangle$ and $|\phi\rangle = |\varphi_1, \phi + \varphi_1\rangle$, that is $\phi = \varphi_2 - \varphi_1$,

$$|\phi\rangle = \sum_n e^{in\phi} |n\rangle, \tag{2.86a}$$

$$|n\rangle = \int_0^{2\pi} \frac{d\phi}{2\pi} e^{-in\phi} |\phi\rangle. \tag{2.86b}$$

In addition, these states satisfy $\langle n|m\rangle = \delta_{n,m}$ and $\langle \phi|\phi'\rangle = 2\pi\delta(\phi - \phi')$. As we will show, the states with fixed superconducting phase difference $|\phi\rangle$ form a suitable basis to derive the Josephson relations. At this point, it might be useful to define the charge number $\hat{n}$ and phase $e^{i\hat{\phi}}$ operators as

$$\hat{n} = \sum_n |n\rangle n \langle n| = \int_0^{2\pi} \frac{d\phi}{2\pi}\, |\phi\rangle i \frac{\partial}{\partial \phi} \langle \phi| \tag{2.87a}$$

$$e^{i\hat{\phi}} = \int_0^{2\pi} \frac{d\phi}{2\pi}\, |\phi\rangle e^{i\phi} \langle \phi| = \sum_n |n\rangle\langle n+1|. \tag{2.87b}$$

The operators $e^{\pm i\hat{\phi}}$ are lowering and raising operators for the number state $|n\rangle$, as it can seen from the commutation relations

$$\left[e^{\pm i\hat{\phi}}, \hat{n}\right] = \pm e^{\pm i\hat{\phi}}. \tag{2.88}$$

We can now introduce a Hamiltonian for the discrete and coherent tunneling of Cooper pairs across the junction,

$$\hat{H}_T = -\frac{E_J}{2}\sum_n \left(|n+1\rangle\langle n| + |n\rangle\langle n+1|\right), \tag{2.89}$$

where E_J is the Josephson energy. It follows from Eq. (2.87) that $\hat{H}_T = -E_J\cos\hat{\phi}$. The state $|\phi\rangle$ is therefore an eigenstate of $\hat{H}_T$ with eigenvalue $E(\phi) = -E_J\cos\phi$.

The charge number operator $\hat{n}$ describes the charge configuration of the two superconductors, in units of Cooper pair charge. Thus, its time-derivative $\dot{\hat{n}}$ describes the charge transfer across the junction. According to our convention, an increase of $\hat{n}$ involves a transfer of negative charges from the first (S_1) to the second superconductor (S_2). We define the current operator as $\hat{I} = 2e\dot{\hat{n}}$. Notice that $\hat{I}$ gives the intensity of the current flowing from S_2 to S_1 (see Fig. 2.5) The Heisenberg equation of motion for $\hat{n}$ leads to

$$\hat{I} = 2e\dot{\hat{n}} = 2e\frac{i}{\hbar}\left[\hat{H}_T, \hat{n}\right] = I_c\sin\hat{\phi}. \tag{2.90}$$

We recognize here the Josephson current-phase relation, where we recover the relation between the critical current and the Josephson energy, $E_J = I_c\Phi_0/(2\pi)$.

To investigate the second Josephson relation we must include in the Hamiltonian the effect of an electrostatic potential applied across the junction. If we define $V = V_2 - V_1$ as the potential drop across the junction from S_2 to S_2, the total Hamiltonian, including the electrostatic energy, reads

$$\hat{H} = -E_J\cos\hat{\phi} - 2eV\hat{n}. \tag{2.91}$$

The Heisenberg equation of motion for the phase difference expresses the second Josephson relation

$$\hbar\dot{\hat{\phi}} = -i\frac{d}{dt}\left(e^{i\hat{\phi}}\right)e^{-i\hat{\phi}} = \left[\hat{H}, e^{i\hat{\phi}}\right]e^{-i\hat{\phi}} = 2eV. \tag{2.92}$$

We will later consider superconducting circuits involving Josephson junctions together with other linear elements. For this purpose, we define a flux operator, based on the phase operator, $\hat{\Phi} = \frac{\Phi_0}{2\pi}\hat{\phi}$. Any Josephson junction embedded in a larger circuit is assumed to have the following Hamiltonian:

$$\hat{H}_J = -E_J\cos\left(2\pi\frac{\hat{\Phi}}{\Phi_0}\right). \tag{2.93}$$

Accordingly, if the voltage across the junction is an operator, it will be given by $\hat{V} = \dot{\hat{\Phi}}$.

The nonlinear Hamiltonian $\hat{H}_J$ is the starting point to describe implementations of superconducting qubits, that is resonant circuits with anharmonic energy spectrum.

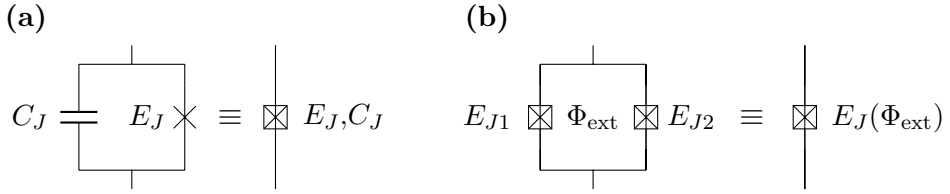

Figure 2.6: (a) Circuit diagram of a Josephson junction, formed by a nonlinear inductance (cross) with Josephson energy E_J, in parallel with a capacitance C_J. The combination of both elements is conventionally denoted by a box with a cross. (b) The split junction is formed by two Josephson junctions in parallel. This element is equivalent to a single junction whose Josephson energy $E_J(\Phi_{\text{ext}})$ can be tuned by applying an external magnetic field.

Junction capacitance

In the above discussion about the Josephson effect, we have omitted the effect of the junction capacitance. The thin insulating barrier forming the Josephson junction has a finite capacitance which cannot be neglected. A Josephson junction should therefore considered as a nonlinear inductance in parallel with a capacitance C_J, as shown in Fig. 2.6(a).

To derive an Hamiltonian for such a system, we must additionally include the electrostatic energy of the capacitance C_J. Classically, this energy is related to the voltage across the junction by $E = \frac{1}{2}C_J V^2$. We emphasize that this situation should not be confused with the case of an applied voltage, but rather corresponds to an isolated junction. The voltage V is due to the charge having formed on each side of the junction. Another way to see it is to consider the junction as an LC resonator with a nonlinear inductance.

Using the relation between the voltage and the phase difference, Eq. (2.77), we readily obtain the Lagrangian

$$\mathcal{L} = \frac{1}{2}C_J\left(\frac{\hbar}{2e}\dot{\phi}\right)^2 + E_J\cos\phi. \tag{2.94}$$

One can verify that the conjugate momentum $\frac{\delta\mathcal{L}}{\delta\dot{\phi}}$ is the charge on the capacitance C_J, in units of $2e$, multiplied by $\hbar$. We rather define the conjugate momentum n as

$$n = -\frac{1}{\hbar}\frac{\delta\mathcal{L}}{\delta\dot{\phi}} = -\frac{1}{\hbar}C_J\left(\frac{\hbar}{2e}\right)^2\dot{\phi} = \frac{C_J V}{-2e}. \tag{2.95}$$

The minus sign in the above definition comes from the negative charge of Cooper pairs. The corresponding quantum-mechanical operator is the charge number operator $\hat{n}$ we already encountered, Eq. (2.87). The Hamiltonian reads

$$\hat{H} = \frac{(2e)^2}{2C_J}\hat{n}^2 - E_J\cos\hat{\phi}. \tag{2.96}$$

Defining the canonically conjugated charge $\hat{Q} = -2e\hat{n}$ and flux operators $\hat{\Phi} = \frac{\Phi_0}{2\pi}\hat{\phi}$, the Hamiltonian can also be written as

$$\hat{H} = \frac{\hat{Q}^2}{2C_J} - E_J\cos\left(2\pi\frac{\hat{\Phi}}{\Phi_0}\right), \tag{2.97}$$

where $[\hat{\Phi}, \hat{Q}] = i\hbar$, like we obtained for the LC resonator. The Heisenberg equations of motion for $\hat{Q}$ and $\hat{\Phi}$ express the two Josephson relations,

$$\hat{I} = -\dot{\hat{Q}} = -\frac{i}{\hbar}\left[\hat{H}, \hat{Q}\right] = I_c \sin\left(2\pi\frac{\hat{\Phi}}{\Phi_0}\right), \tag{2.98a}$$

$$\dot{\hat{\Phi}} = \frac{i}{\hbar}\left[\hat{H}, \hat{\Phi}\right] = \frac{\hat{Q}}{C_J} = \hat{V}. \tag{2.98b}$$

The split Josephson junction

A split junction is formed by two Josephson junctions in parallel, as depicted in Fig 2.6(b). The two junctions are embedded in a SQUID-like ring which enclose an external magnetic flux Φ_{ext}. It effectively behaves as a single junction whose Josephson energy is tunable.

The energy of two junctions with Josephson energies E_{J1} and E_{J2} is given by

$$E = -E_{J1}\cos(\phi_1) - E_{J2}\cos(\phi_2), \tag{2.99}$$

where $\phi_{1,2}$ are the phase differences across each junctions. The quantization of the magnetic flux inside a superconducting loop sets the difference between ϕ_1 and ϕ_2,

$$\phi_2 - \phi_1 = 2\pi\frac{\Phi_{\text{ext}}}{\Phi_0} + 2k\pi, \qquad (k \in \mathbb{N}). \tag{2.100}$$

The value of the integer k is physically irrelevant and can be set to zero without loss of generality. The only effective degree of freedom is therefore the phase difference $\phi = \frac{1}{2}(\phi_1 + \phi_2)$. In terms of the corresponding operator $\hat{\phi}$, the Josephson Hamiltonian can be written as

$$\hat{H}_J = -E_J(\Phi_{\text{ext}})\cos\left(\hat{\phi} - \phi_0\right), \tag{2.101}$$

where the tunable energy $E_J(\Phi_{\text{ext}})$ and the phase shift ϕ_0 are given by

$$E_J(\Phi_{\text{ext}}) = \sqrt{E_{J1}^2 + E_{J2}^2 + 2E_{J1}E_{J2}\cos\left(2\pi\frac{\Phi_{\text{ext}}}{\Phi_0}\right)}, \tag{2.102}$$

$$\tan\phi_0 = \frac{E_{J2} - E_{J1}}{E_{J2} + E_{J1}}\tan\left(\pi\frac{\Phi_{\text{ext}}}{\Phi_0}\right). \tag{2.103}$$

The phase shift ϕ_0, if constant in time, can be eliminated by a displacement of the variable $\hat{\phi}$, that is by a gauge transformation $\hat{U} = e^{-i\hat{n}\phi_0}$,

$$\hat{U}\hat{H}_J\hat{U}^\dagger = -E_J(\Phi_{\text{ext}})\cos\hat{\phi}. \tag{2.104}$$

In case of a perfectly symmetric split junction, $E_{J1} = E_{J2}$, the flux-dependent Josephson energy takes the simpler form, $E_J(\Phi_{\text{ext}}) = 2E_{J1}\cos(\pi\Phi_{\text{ext}}/\Phi_0)$.

2.4.2 Cooper pair box

A Cooper pair box (CPB), or charge qubit, is one of the simplest quantum circuit involving a Josephson junction that can produce two-level physics. Its functioning was first described theoretically in [Büttiker87]. The first experimental realization was presented in [Bouchiat98], and the first demonstration of quantum coherent oscillations with superposition of energy eigenstates was reported in [Nakamura99].

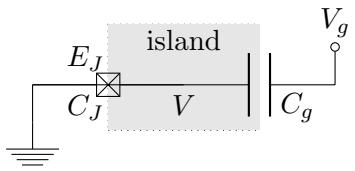

Figure 2.7: *Cooper pair box.* The superconducting island (gray) is connected to a voltage source V_g, via a capacitance C_g, and to the ground via a Josephson junction with energy E_J and capacitance C_J. The potential on the island is related to the phase difference across the junction by $V = \frac{\hbar\dot{\phi}}{2e}$

A CPB is formed by a superconducting island that is part of a tunnel junction with Josephson energy E_J and capacitance C_J (see Fig. 2.7). The island is biased by an additional gate voltage V_g applied in series with a gate capacitance C_g. The electrostatic energy required to place an electron e on the island is

$$E_C = \frac{e^2}{2C_\Sigma} \tag{2.105}$$

at zero voltage, where $C_\Sigma = C_J + C_g$ is the total capacitance of the island. The energy E_C is usually called *charging energy* or *Coulomb energy*. If the island, and therefore its capacitance C_Σ, are small enough, the energy E_C is much larger than the Josephson energy E_J. In the regime $E_C \gg E_J$, the number of Cooper-pair transferred to the island is a discrete variable exhibiting quantized behavior at low enough temperature. An environment with $T \simeq 1$ K typically requires $C_\Sigma \ll 1$ fF in order to satisfy $E_C \gg k_B T$ [Clarke08].

We are now rather familiar to the procedure used to obtain the Hamiltonian of such a circuit. Including the effect of the gate voltage V_g, the Lagrangian of the CPB is

$$\mathcal{L} = \frac{1}{2}C_\Sigma \left(\frac{\hbar\dot{\phi}}{2e} - \frac{C_g V_g}{C_\Sigma} \right)^2 + E_J \cos\phi. \tag{2.106}$$

The conjugate momentum to the phase difference across the junction ϕ is related to charge on the island, expressed as a number of Cooper pair n. To make this clear we use the simplification $V = \frac{\hbar\dot{\phi}}{2e}$, where V is the potential on the island. We have then

$$n = -\frac{1}{\hbar}\frac{\delta\mathcal{L}}{\delta\dot{\phi}} = -\frac{1}{2e}\left[C_J V - C_g(V_g - V)\right]. \tag{2.107}$$

Therefore, we can think of the variable n as the number of additional Cooper pairs on the island, with respect to the neutral configuration. As we have seen in the previous section treating the Josephson junction, the associated charge number operator $\hat{n}$ has a discrete spectrum, due to the 2π-periodicity of the phase variable ϕ. The Hamiltonian of the CPB is

$$\hat{H} = 4E_C\left(\hat{n} - n_g\right)^2 - E_J\cos\hat{\phi}, \tag{2.108}$$

where $n_g = \frac{C_g V_g}{2e}$ is the dimensionless gate charge.

The CPB box is a quantum circuit behaving like an artificial atom, with highly anharmonic spectrum. We now show that it can be approximated by a two-level system, when operated in the appropriate regime. This can be better seen if we write the Hamiltonian

in the discrete basis of eigenstates of the charge number operator $\hat{n}$. The different representations of the phase and charge number operators were given previously in Eq. (2.87). We obtain the Hamiltonian [Bouchiat98]

$$\hat{H} = \sum_n \left[4E_C(n-n_g)^2 |n\rangle\langle n| - \frac{E_J}{2}\big(|n\rangle\langle n+1| + |n+1\rangle\langle n|\big)\right]. \tag{2.109}$$

The spectrum of $\hat{H}$ is periodic for integer shift of the dimensionless gate charge n_g. Thus, for convenience, we can take n_g to be in the interval $[0,1)$ without loss of generality. Under this assumption, we see from the form of $\hat{H}$, that in the regime $E_C \gg E_J$, the low-energy physics is dominated by the states with charge number n close to zero.

If we completely neglect the influence of the Josephson Hamiltonian, setting $E_J = 0$, the charge number states $|n\rangle$ are energy eigenstates. If $0 < n_g < 1$, the two lowest energy eigenstates are $|0\rangle$ and $|1\rangle$. If $n_g = 0$, the ground state is $|0\rangle$, while $|\pm 1\rangle$ are the degenerate first excited states. In the particular case where $n_g = 1/2$, the states $|0\rangle$ and $|1\rangle$ are degenerate.

A finite Josephson energy E_J couples states with different charge number n. We notice that for finite, but small ratio E_J/E_C, the effect of coupling is only relevant near the point $n_g = 1/2$, where it lifts the degeneracy between the states $|0\rangle$ and $|1\rangle$. Away from this point the charging energy dominates and the energy eigenstates are well approximated by the charge number eigenstates $|n\rangle$.

The particular working point where the condition $n_g = 1/2$ is satisfied is called sweet spot or charge degeneracy point. Two-level physics can be realized near this particular working point of the CPB, since the states $|n \neq 0,1\rangle$ are well-separated in energy from the states $|0\rangle$ and $|1\rangle$ [You03b]. The energy splitting between the states $|0\rangle$ and $|1\rangle$ is of the order of E_J, while the other states have energies of at least E_C. Therefore, a large ratio E_C/E_J produces a very anharmonic energy spectrum, allowing us to truncate the Hamiltonian $\hat{H}$ to the low energy sector,

$$\hat{H} = 2E_C(1-2n_g)\big(|1\rangle\langle 1| - |0\rangle\langle 0|\big) - \frac{E_J}{2}\big(|0\rangle\langle 1| - |1\rangle\langle 0|\big). \tag{2.110}$$

If $n_g = 1/2$, the ground state is $|g\rangle = \frac{1}{\sqrt{2}}(|1\rangle + |0\rangle)$, and the first excited is $|e\rangle = \frac{1}{\sqrt{2}}(|1\rangle - |0\rangle)$. Expressed in terms of the Pauli matrices

$$\sigma_x = |g\rangle\langle e| + |e\rangle\langle g|, \tag{2.111a}$$
$$\sigma_y = i\big(|g\rangle\langle e| - |e\rangle\langle g|\big), \tag{2.111b}$$
$$\sigma_z = |e\rangle\langle e| - |g\rangle\langle g|, \tag{2.111c}$$

we obtain the Hamiltonian for a spin-1/2 particle

$$\hat{H} = \frac{\hbar\omega_{ge}}{2}\sigma_z + \frac{\hbar\Omega_x}{2}\sigma_x, \tag{2.112}$$

where $\omega_{ge} = E_J/\hbar$ and $\Omega_x = 4E_C(1-2n_g)/\hbar$. The form of $\hat{H}$ reminds us of the spin Hamiltonian in NMR, with the Josephson and charging energies playing the role of the Zeeman and transverse fields. At this point, we see that such an effective two-level structure allows us to really talk about a quantum bit, whose computational subspace is spanned by the states $|g\rangle$ and $|e\rangle$. The control field Ω_x and the energy splitting

$$\Delta E = \sqrt{E_J^2 + 16E_C^2(1-2n_g)^2} \tag{2.113}$$

are functions of the dimensionless gate charge n_g. This enables the manipulation and the preparation of arbitrary qubit states, by application of control voltage pulses $V_g(t)$. For the CPB and its derivatives, the control field couples to the charge degree of freedom, hence the name of charge qubit. This is the major distinction with the two other generic types of superconducting qubits that are phase and flux qubits, whose control fields are rather a current modulating the phase or an external magnetic flux, respectively.

The CPB is an example of artificial atom, which can be controlled and whose energy spectrum can be tuned by an external gate voltage. Its properties can be parametrized even further if the Josephson junction is replaced by a split junction. In this case, we have additional control on the Josephson energy, $E_J = E_J(\Phi_{\text{ext}})$, by applying an external magnetic field. As we will see, the CPB is quite sensitive to surrounding electrical noise. In the next section, we show how the noise in the control fields affects the qubit performance.

2.4.3 Effects of noise on the qubit performance

A qubit is never completely isolated and a coupling to uncontrolled environmental degrees of freedom cannot be avoided. This coupling leads to an exchange of energy between the qubit and its environment, causing relaxation, or produces fluctuations of the qubit transition frequency. As we know from the treatment of dissipation in linear resonant circuits, the energy dissipation produces a broadening of the energy levels and a loss of coherence. In the case of a two-level system, the decoherence effect splits up in two contributions. The first one is relaxation, the emission or absorption of energy by the qubit. The second one is dephasing, the loss of coherence in a superposition of two energy eigenstates.

The decoherence of a qubit is characterized by two timescales, the relaxation time T_1 and the dephasing time T_2. The state of a qubit, expressed with its density matrix $\hat{\rho}$, is expected to have the following time-dependence: off-diagonal elements decay at rate $1/T_2$, while diagonal elements relax to their equilibrium value at rate $1/T_1$. The diagonal elements of $\hat{\rho}$ are defined with respect to the energy eigenbasis, that is the basis in which the qubit Hamiltonian reads

$$\hat{H}_{\text{qb}} = \frac{\hbar\omega_{01}}{2}\sigma_z. \tag{2.114}$$

The relaxation and dephasing processes are exponential decays

$$\sigma_z(t) = \sigma_z(0)e^{-t/T_1} + \sigma_{\text{eq}}\left(1 - e^{-t/T_1}\right), \tag{2.115}$$

$$\sigma_\pm(t) = \sigma_\pm(0)e^{\pm i\omega_{01}t}e^{-t/T_2}, \tag{2.116}$$

where we have defined $\sigma_\pm = (\sigma_x \pm i\sigma_y)/2$. Here, $\sigma_i(t) = \text{Tr}\left[\hat{\rho}(t)\sigma_i\right]$.

In quantum-state engineering and quantum information processing, one generally needs to be able to control the dynamics of a qubit, i.e., apply quantum gates, before the coherence is lost. This requires both the coupling to the environment to be weak enough, and the temperature to be low enough, such that the evolution of the qubit state is nearly coherent and governed by its Hamiltonian on the timescale set by the gate time. The time required to perform a quantum gate is determined by a coupling energy J, to an external control field or between two qubits. The value of $JT_2/\hbar$ being appreciably much larger that unity is a minimal condition to allow efficient quantum-state manipulations.

The relaxation alone produces dephasing of the qubit. This can be illustrated as follows: if the qubit makes a transition form the excited state $|e\rangle$ to the ground state

$|g\rangle$, the coherent superposition of $|e\rangle$ and $|g\rangle$ is destroyed. One can show that the rate of such relaxation-induced dephasing is $(2T_1)^{-1}$. However, additional causes of decoherence, producing pure dephasing, might still be possible. We can distinguish the contributions to the total dephasing rate into pure dephasing, described by the rate T_φ^{-1}, and relaxation-induced dephasing. This distinction leads to the important relation

$$\frac{1}{T_2} = \frac{1}{2T_1} + \frac{1}{T_\varphi}. \tag{2.117}$$

We notice that, ultimately, when pure dephasing has been completely eliminated ($T_\varphi^{-1} = 0$), the coherence is limited by relaxation only. Such decomposition of the decoherence process in two distinct contributions coming from relaxation or pure dephasing is in general only possible if the temperature is low, $\hbar\omega_{01} \gg k_B T$, and the coupling to the environment weak [Makhlin01].

Pure dephasing is the consequence of fluctuations of the transition frequency ω_{01}. This process can be described by an environment that couples to the longitudinal component σ_z,

$$\hat{H} = \hat{H}_{\mathrm{qb}} + F_z(t)\sigma_z. \tag{2.118}$$

The random field F_z can be either considered as a classical or quantum noise term. For the moment, we focus on the first case and assume F_z to be a time-dependent random quantity. Evidently, the coupling cannot induce qubit transition, the longitudinal component $\sigma_z(t)$ is conserved, and such Hamiltonian shows pure dephasing only. To obtain an expression for the dephasing time T_φ, we consider the off-diagonal elements of the density matrix

$$\sigma_\pm(t) = \sigma_\pm(0) e^{\pm i\omega_{01} t} \left\langle e^{\pm i\varphi(t)} \right\rangle, \tag{2.119}$$

where the accumulated phase is $\varphi(t) = 2/\hbar \int_0^t ds\, F_z(s)$. If the noise is Gaussian with zero mean, it is fully characterized by its correlation function g or its power spectrum $S_{F_z F_z}$,

$$g(t-t') = \langle F_z(t) F_z(t') \rangle, \qquad S_{F_z F_z}(\omega) = \int d\tau\, e^{i\omega\tau} g(\tau). \tag{2.120}$$

In this case, the average can be carried out using the cumulant expansion,

$$\left\langle e^{i\varphi(t)} \right\rangle = e^{-\frac{1}{2}\langle \varphi(t)^2 \rangle} = \exp\left(-\frac{2}{\hbar^2} \int \frac{d\omega}{2\pi}\, S_{F_z F_z}(\omega) \frac{\sin^2(\omega t/2)}{(\omega/2)^2} \right). \tag{2.121}$$

Assuming the noise has a typical correlation time t_c such that $g(\tau) \sim e^{-|\tau|/t_c}$, one can show that that for $t \gg t_c$, Eq. (2.121) reduces to $\exp\left[-2|t| S_{F_z F_z}(\omega = 0)/\hbar^2\right]$. This expression directly gives an exponential decay law. The resulting dephasing time is

$$T_\varphi = \frac{\hbar^2}{2 S_{F_z F_z}(\omega = 0)}. \tag{2.122}$$

This situation corresponds to the case of homogeneous broadening and the above analysis holds only when the noise power spectrum is regular at low frequencies. More relevant experimentally is the case of $1/f$ noise, with a typical power spectrum

$$S_{F_z F_Z}(\omega) = \frac{A}{|\omega|}. \tag{2.123}$$

However, one needs to introduce a low-frequency cutoff $\omega_{\rm ir}$, which reflects the finite time of any measurement protocol. For $t \ll \omega_{\rm ir}^{-1}$, one obtains [Ithier05]

$$\frac{1}{2}\langle\varphi(t)^2\rangle = \frac{2A}{\pi\hbar^2}t^2|\ln(\omega_{\rm ir}t)|. \tag{2.124}$$

Since the decay of the off-diagonal components $\sigma_\pm(t)$ is not exponential, the pure dephasing time is approximated by the typical time needed for a decay by a factor e^{-1}. The dependence of T_φ on the frequency cutoff $\omega_{\rm ir}$ is only logarithmic. For $K = \frac{A}{\pi\hbar^2\omega_{\rm ir}^2} \gg 1$, we obtain

$$T_\varphi = \hbar\sqrt{\frac{\pi}{\ln KA}}\left[1 - \mathcal{O}\left(\frac{\ln(\ln K)}{\ln K}\right)\right]. \tag{2.125}$$

The numeric and logarithmic prefactors can generally be omitted. We end up with the approximate dephasing time

$$T_\varphi \simeq \frac{\hbar}{\sqrt{A}} \tag{2.126}$$

for $1/f$ noise.

To describe the effect of relaxation and obtain an expression for the relaxation time T_1, the model should include a coupling to the transversal component of the qubit. We now turn to the case of a quantum field $\hat{F}$ coupling to both the σ_x and σ_z components of the qubit,

$$\hat{H} = \frac{\hbar\omega_{01}}{2}\sigma_z + (\sin\theta\sigma_x + \cos\theta\sigma_z)\,\hat{F} + \hat{H}_{\rm B}. \tag{2.127}$$

The Hamiltonian $\hat{H}_B$ describes the evolution of the noise source only and commutes with the qubit operators.

In the case of pure dephasing ($\sin\theta$=0), the previous result for the time T_φ is recovered. Instead of the classical power spectrum, we need to consider the symmetrized power spectral density

$$\bar{S}_{FF}(\omega) = \frac{1}{2}\left[S_{FF}(\omega) + S_{FF}(-\omega)\right], \qquad S_{FF}(\omega) = \int dt e^{i\omega t}\langle\hat{F}(t)\hat{F}(0)\rangle. \tag{2.128}$$

The approximation of weak coupling means that the quantum expectation value $\langle\ldots\rangle$ is to be taken for the unperturbed environment alone.

If the noise source couples to the transverse component only ($\cos\theta$=0), it causes transitions between the ground state and the excited state of the qubit. The transition rates for emission $\Gamma_\downarrow$ and absorption $\Gamma_\uparrow$ of an excitation by the qubit can be evaluated using Fermi's Golden rule in the limit of weak-coupling and for short correlation time of the noise source. Under these approximations, we obtain

$$\Gamma_\downarrow = \frac{1}{\hbar^2}S_{FF}(\omega_{01}), \qquad \Gamma_\uparrow = \frac{1}{\hbar^2}S_{FF}(-\omega_{01}). \tag{2.129}$$

The positive-frequency part of the spectral density S_{FF} is a measure of the ability of the noise source to absorb energy, while the negative frequency part is a measure of the ability to emit energy. If the noise source is in thermal equilibrium at temperature $T \ll \hbar\omega_{01}/k_B$, the absorption rate is exponentially suppressed compared to the emission rate. The total relaxation rate of the qubit is then $T_1 = (\Gamma_\uparrow + \Gamma_\downarrow)^{-1}$ and the equilibrium value of $\sigma_z(t)$ becomes

$$\sigma_{\rm eq} = \frac{\Gamma_\uparrow - \Gamma_\downarrow}{\Gamma_\uparrow + \Gamma_\downarrow}. \tag{2.130}$$

If the noise source couples to both σ_x and σ_z, the contributions to relaxation and pure dephasing come from the high-frequency, respectively low-frequency, part of its power spectrum. Namely,

$$\frac{1}{T_1} = \sin^2\theta \frac{2\bar{S}_{FF}(\omega_{01})}{\hbar^2}, \tag{2.131a}$$

$$\frac{1}{T_\varphi} = \cos^2\theta \frac{2\bar{S}_{FF}(0)}{\hbar^2}, \tag{2.131b}$$

$$\frac{1}{T_2} = \frac{1}{2T_1} + \frac{1}{T_\varphi}, \tag{2.131c}$$

provided the noise power spectrum is regular at low frequencies.

Sensitivity of the CPB to charge noise

The fluctuations and offsets of the gate charge n_g are the dominating sources of relaxation and dephasing for the CPB. Since the gate voltage V_g is the main control parameter of such a qubit, the CPB is directly exposed to surrounding charge fluctuations and parasitic electrical fields, which causes relaxation of the qubit and fluctuations of its energy splitting ΔE.

As we have seen in the section treating semi-infinite transmission lines and the quantum input-output theory, the noise coming from the coupling to external control fields can be regarded as effectively produced by dissipative elements, such as resistors. For the CPB, the gate voltage can be decomposed into a dc-component and fluctuating term, $V_g = V_g^{\mathrm{dc}} + \hat{V}$. Dissipative behavior of the CPB can be investigate if one regards the operator $\hat{V}$ as the voltage at the end of a semi-infinite transmission line. Equivalently, one may think of the CPB being connected to a voltage source with a finite impedance $Z(\omega)$, microscopically modeled as collection of harmonic oscillators [Shnirman97].

We now derive the Hamiltonian for the coupled system in the two-level approximation. The interaction is obtained by replacing the gate charge n_g by $n_g + C_g\hat{V}/(2e)$ in Eq. (2.112). Reducing the CPB to an effective two-level system, we obtain, after an appropriate rotation of the qubit basis,

$$\hat{H} = \frac{\Delta E}{2}\sigma_z + \frac{C_g e}{C_\Sigma}\left(\sin\theta\sigma_x + \cos\theta\sigma_z\right)\hat{V} + \hat{H}_B, \tag{2.132}$$

where ΔE is given in Eq. (2.113) and $\cot\theta = 4E_C(1-2n_g)/E_J$. The voltage operator $\hat{V}$ and the bath Hamiltonian $\hat{H}_B$ for the transmission line were derived previously and read

$$\hat{V} = \sum_k \sqrt{\frac{\hbar\omega_k}{L_0 c}}\left(\hat{a}_k + \hat{a}_k^\dagger\right), \qquad \hat{H}_B = \sum_k \hbar\omega_k \hat{a}_k^\dagger \hat{a}_k. \tag{2.133}$$

Such microscopic model for the decoherence of the two-level system, known as the spin-boson model, as been studied extensively [Caldeira83b, Leggett87, Weiss08]. It has been successfully applied to different types of superconducting qubits for different noise channels [Makhlin01].

Here, the coupling strength to the k-th mode of the transmission line has a particular form, i.e., it is proportional to $\omega_k^{1/2}$. This corresponds to the case of Ohmic dissipation

and the fluctuations of the voltage source, taken to be in thermal equilibrium, have a Johnson-Nyquist power spectrum

$$S_{VV}(\omega) = 2Z_{\mathrm{TL}}\hbar|\omega|\Big[\Theta(\omega)\big(n_B(\hbar\omega)+1\big) + \Theta(-\omega)n_{\mathrm{B}}(\hbar|\omega|)\Big]. \tag{2.134}$$

In other words, the source impedance is taken to be purely resistive, $Z(\omega) = Z_{\mathrm{TL}}$. The relaxation and the dephasing times have been evaluated in the context of the spin-boson model and are given by [Makhlin01]

$$\frac{1}{T_1} = \lambda \sin^2\theta \frac{\Delta E}{\hbar} \coth\left(\frac{\Delta E}{2k_BT}\right), \tag{2.135}$$

$$\frac{1}{T_\varphi} = \lambda \cos^2\theta \frac{2k_BT}{\hbar}, \tag{2.136}$$

where $\lambda = \frac{2e^2}{\hbar} Z_{\mathrm{TL}} \left(\frac{C_g}{C_\Sigma}\right)^2$ is a dimensionless parameter expressing the strength of the coupling to the environment. These expressions are valid when the conditions $\lambda \ll 1$ and $\Delta E \gg \lambda k_BT$ are satisfied. They coincide with the expressions obtained in the previous section, Eq. (2.131), using the relation $\bar{S}_{FF} = (eC_g/C_\Sigma)^2 \bar{S}_{VV}$, where

$$\bar{S}_{VV}(\omega) = Z_{\mathrm{TL}}\hbar\omega\left[2n_{\mathrm{B}}(\hbar\omega)+1\right]. \tag{2.137}$$

Regarding the decoherence induced by dissipative elements, the CPB should exhibit longer T_φ when operated at the charge-degeneracy point, $\theta = \pi/2$. At the charge-degeneracy point, hence its name, the two low-energy eigenstates which form the qubit cannot be distinguished by their charge configuration. At first sight, this is obviously an advantage when the major source of decoherence is a noisy environment that couples to the charge degree of freedom. The dependence of the energy splitting ΔE to the dimensionless charge n_g, also called charge dispersion, has a minimum at the charge-degeneracy point.

However, other sources of noise such as fluctuations of the background charge might still affect the qubit coherence. They typically have $1/f$ power spectrum and mainly produce pure dephasing. Their contribution to the dephasing time T_φ can be evaluated using Eq. (2.126). Away from the charge-degeneracy point, it yields

$$T_\varphi \simeq \frac{2\hbar}{\sqrt{A}} \left|\frac{\partial \Delta E}{\partial n_g}\right|^{-1} \tag{2.138}$$

where A is the amplitude of the noise in the gate charge n_g, whose power spectrum is assumed to be given by $S_{n_gn_g}(\omega) = A/|\omega|$.

Sensitivity to charge noise with $1/f$ spectrum is reduced at the charge-degeneracy point. As can be seen from Eq. (2.113), ΔE is only sensitive to second-order fluctuations in the gate charge if $n_g = 1/2$ and fluctuations of the transition energy are reduced, hence the name of sweet spot. By operating at this particular point, the coherence time of the charge qubit was greatly improved [Vion02]. The dephasing time due to second-order effects for typical $1/f$ noise was calculated in [Ithier05],

$$T_\varphi \simeq \frac{2\hbar}{A\pi} \left|\frac{\partial^2 \Delta E(n_g = 1/2)}{\partial n_g^2}\right|^{-1} \simeq \frac{\hbar}{A\pi} \frac{E_J}{32E_C^2}. \tag{2.139}$$

The ratio E_C/E_J being large for the CPB, the second-order contribution of the charge noise is still the dominating cause of decoherence, as reported in Ref. [Metcalfe07].

The sensitivity against charge noise is precisely the weakness of the CPB that is tackled by the transmon design. As we will see, by reducing the ratio E_C/E_J, we can greatly suppress the charge dispersion while conserving enough anharmonicity in the energy spectrum.

2.4.4 Exact solutions of the charge qubit Hamiltonian

The exact energy spectrum and the corresponding eigenstates of the charge qubit Hamiltonian Eq. (2.108) can be obtained analytically in the phase representation [Cottet02]. These expressions turn out to be useful when discussing the properties of the system for smaller ratio E_C/E_J.

We first notice that the dimensionless gate charge n_g can be eliminated from the charge qubit Hamiltonian with the unitary transformation $\hat{U} = e^{in_g\hat{\phi}}$,

$$\hat{U}\hat{H}\hat{U}^\dagger = 4E_C\hat{n}^2 - E_J\cos\hat{\phi}. \tag{2.140}$$

Since the wave function $\psi(\phi) = \langle\phi|\psi\rangle$ is 2π-periodic, $\psi(\phi+2\pi) = \psi(\phi)$, we cannot strictly think of $\hat{U}$ as a gauge transformation, unless $n_g \in \mathbb{Z}$. In other words, the transformed wave function $\tilde{\psi}(\phi) = \langle\phi|\hat{U}|\psi\rangle$ satisfies new boundary conditions,

$$\tilde{\psi}(\phi + 2\pi) = e^{i2\pi n_g}\tilde{\psi}(\phi). \tag{2.141}$$

Using the phase representation of the charge number operator, $\hat{n} = i\frac{\partial}{\partial\phi}$, the Schrödinger equation reads

$$-\left(4E_c\frac{\partial^2}{\partial\phi^2} + E_J\cos\phi\right)\tilde{\psi}_k(\phi) = E_k\tilde{\psi}_k(\phi), \tag{2.142}$$

where k denotes the band index. This equation is reminiscent of the Schrödinger equation of a particle moving in periodic potential. Its Bloch solution is of the form $\tilde{\psi}_k(\phi) = e^{im_k\phi}u_k(\phi)$, where $u_k(\phi)$ must be 2π-periodic. Because of the periodicity of the wave function, only discrete 'particle' momenta m_k are allowed and $m_k - n_g \in \mathbb{Z}$. More precisely, the above differential equation has the canonical form of a Mathieu equation [Abramowitz70].

For vanishing Josephson energy, $E_J = 0$, the spectrum is given by the shifted parabolas, $E_k(n_g) = 4E_c[n_g - o(k, n_g)]^2$, where $o(k, n_g) \in \mathbb{Z}$ is an ordering function.[5] For finite E_J, the value of the eigenenergies are

$$E_k(n_g) = E_C\begin{cases} a_{2[n_g - o(k,n_g)]}\left(-\frac{E_J}{2E_C}\right), & 2n_g \notin \mathbb{Z}, \\ a_{k+(2n_g \bmod 2)}\left(-\frac{E_J}{2E_C}\right), & k \text{ even and } 2n_g \in \mathbb{Z}, \\ b_{k+(2n_g+1 \bmod 2)}\left(-\frac{E_J}{2E_C}\right), & k \text{ odd and } 2n_g \in \mathbb{Z}, \end{cases} \tag{2.143}$$

where $a_\nu(q)$ and $b_\nu(q)$ denotes the Mathieu characteristic values. The energy spectrum $E_k(n_g)$ for different values of the ratio E_J/E_C is shown in Fig. 2.8. For small values of E_J/E_C, we notice that the Josephson coupling produces an avoided crossing, as expected, between the two lowest eigenstates at the charge-degeneracy points $(n_g - \frac{1}{2}) \in \mathbb{Z}$, while leaving the spectrum almost unchanged in the other regions. When increasing the ratio E_J/E_C, the charge dispersion of the lowest energy eigenstates gets reduced.

[5] $o(k, n_g) = \lceil n_g \rceil + (-1)^{\lfloor 1+2n_g \rfloor \,(\bmod 2)}\big[\lfloor 1 + 2n_g \rfloor \,(\bmod 2) + (-1)^k \lceil k/2 \rceil\big]$

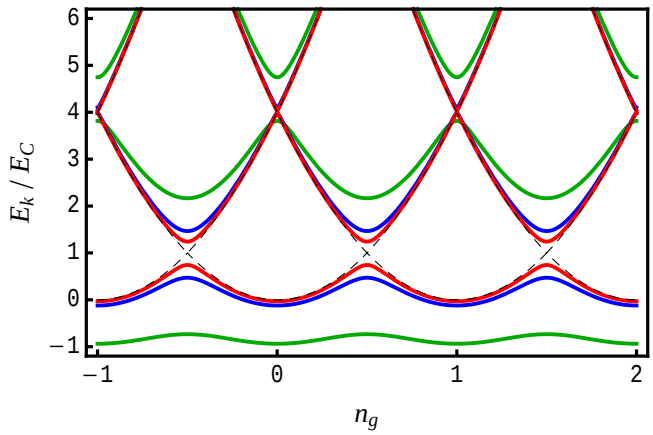

Figure 2.8: Energy spectrum of the CPB as a function of the dimensionless gate charge n_g. We show the first three energy levels E_k for the cases: $E_J/E_C = 0$ (black dashed), $E_J/E_C = 0.5$ (red), $E_J/E_C = 1$ (blue), $E_J/E_C = 3$ (green).

Denoting by $|k\rangle$ the eigenstates with energy E_k , its wave functions $\psi_k(\phi) = \langle\phi|k\rangle$ can be written in term of the Mathieu cosine and sine functions, M_c and M_s.[6] If $2n_g \notin \mathbb{Z}$, we have

$$\begin{aligned}\psi_k(\phi) = \mathcal{N} e^{-in_g\phi} M_c\left(\frac{E_k}{E_C}, -\frac{E_J}{2E_C}, \frac{\phi}{2}\right) \\ + i(-1)^{k+(\lfloor 2n_g \rfloor \bmod 2)} M_s\left(\frac{E_k}{E_C}, -\frac{E_J}{2E_C}, \frac{\phi}{2}\right),\end{aligned} \tag{2.144}$$

while if $2n_g \in \mathbb{Z}$,

$$\psi_k(\phi) = \mathcal{N} e^{-in_g\phi} \begin{cases} M_c\left(\frac{E_k}{E_C}, -\frac{E_J}{2E_C}, \frac{\phi}{2}\right), & k \text{ even}, \\ M_s\left(\frac{E_k}{E_C}, -\frac{E_J}{2E_C}, \frac{\phi}{2}\right), & k \text{ odd}. \end{cases} \tag{2.145}$$

Therefore we notice that the periodic Bloch function u_k have a well-defined parity given by $(-1)^k$ for $2n_g \in \mathbb{Z}$.

2.4.5 Transmon qubit

The transmon qubit is a charge qubit operated in the regime where the Josephson energy dominates over the charging energy. The consequences of such an operating regime are reduced charge dispersion and anharmonicity of the energy levels. On one hand, this is beneficial since it protects the qubit against charge noise and enhances its coherence time [Houck09]. On the other hand, the reduced anharmonicity requires particular precautions when applying control pulses, in order not to leak out of the computational subspace spanned by the lowest energy eigenstates.

The Hamiltonian of the transmon qubit is structurally the same as the CPB Hamiltonian, the main difference is that the Josephson junction is shunted, in parallel, by an additional large capacitance $C_B \gg C_J$ (see Fig. 2.9). The charging energy becomes $E_C = \frac{e^2}{2C_\Sigma}$, where $C_\Sigma = C_B + C_g + C_J$, and can be made small compared to the Josephson

[6] The functions $M_c(a, q, x)$ and $M_s(a, q, x)$ are defined as the even and odd solutions of the canonical Mathieu equation, $g''(x) + \big(a - \cos(2x)\big)g(x) = 0$.

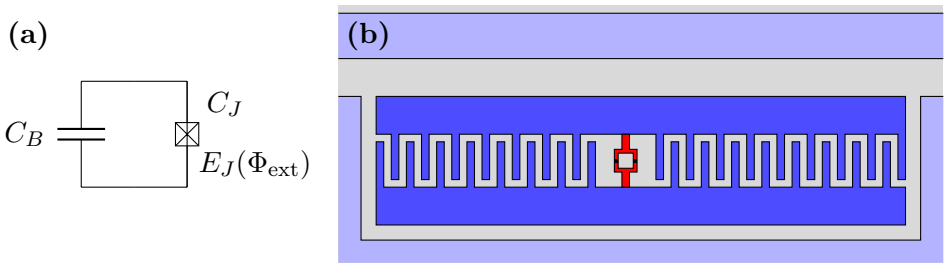

Figure 2.9: *Transmon qubit.* (a) Simplified circuit representation of the transmon qubit. The superconducting islands are connected by a split Josephson junction with tunable $E_J(\Phi_{\text{ext}})$ and an additional large capacitance C_B. (b) Actual planar geometry of the first generation of transmon qubits [Houck09], patterned by electron-beam lithography on single-crystal sapphire substrate. The dc-SQUID (red) is formed by two Josephson junction in parallel (black) and connects the two superconducting islands (blue).

energy, $E_C \ll E_J$. As we will see, the energy spectrum cannot be changed by an external static gate voltage. Therefore, they are generally made with a split junction, with tunable effective Josephson energy $E_J = E_J(\Phi_{\text{ext}})$. The external magnetic flux Φ_{ext} is a control parameter which makes possible to changes the level spacing.

Operated in the transmon regime, typically $E_J/E_C \sim 50-100$, a charge qubit exhibits a suppressed charge dispersion of the low-energy levels. This can already be seen for much smaller value of the ratio E_J/E_C, as shown in Fig. 2.8. For larger values of E_J/E_C, the energy bands $E_k(n_g)$ are nearly flat, as shown in Fig. 2.10(a). In addition, the anharmonicity of the low-energy spectrum is reduced when increasing E_J/E_C. The main benefit of such regime comes the fact that the charge dispersion is exponentially suppressed, while the loss in anharmonicity only follows a power law. The main properties and advantages of the transmon qubit were first theoretically predicted in Ref. [Koch07]. The experimental verification of these properties was reported in Refs. [Schreier08, Houck08], even if experiments involving such charge qubits with a ratio E_J/E_C well above unity had already been performed [Schuster07, Majer07].

The reduction of the charge dispersion and the weaker anharmonicity can be understood in the following way. The cosine Josephson potential becomes deeper when the Josephson energy is large. The low-energy eigenstates have their wave functions $\psi_k(\phi)$ exponentially suppressed for $\phi \to \pm\pi$, as illustrated in Fig. 2.10(b). The charge dispersion can be thought of as due to tunneling to adjacent cosine wells. Since the wave functions $\psi_k(\phi)$ gets localized around $\phi = 0$, they become less sensitive to the pseudo-periodic boundary conditions on the wave function, Eq. (2.141). Therefore, the energy bands $E_k(n_g)$ become flatter when E_J/E_C is increased. At the same time, the cosine potential gets closer to a parabolic potential for the low-energy states and their spectrum approaches the one of a harmonic oscillator in the limit $E_J/E_C \to \infty$.

Charge dispersion and increased coherence time

In the limit $E_J \gg E_C$, an approximation for the charge dispersion relation of the k-th energy band, ϵ_k, was derived in [Koch07],

$$\epsilon_k = \left|E_k(n_g = 1/2) - E_k(n_g = 0)\right| \simeq E_C \frac{2^{4k+5}}{k!}\sqrt{\frac{2}{\pi}}\left(\frac{E_J}{2E_C}\right)^{\frac{k}{2}+\frac{3}{4}} e^{-\sqrt{8E_J/E_C}}. \qquad (2.146)$$

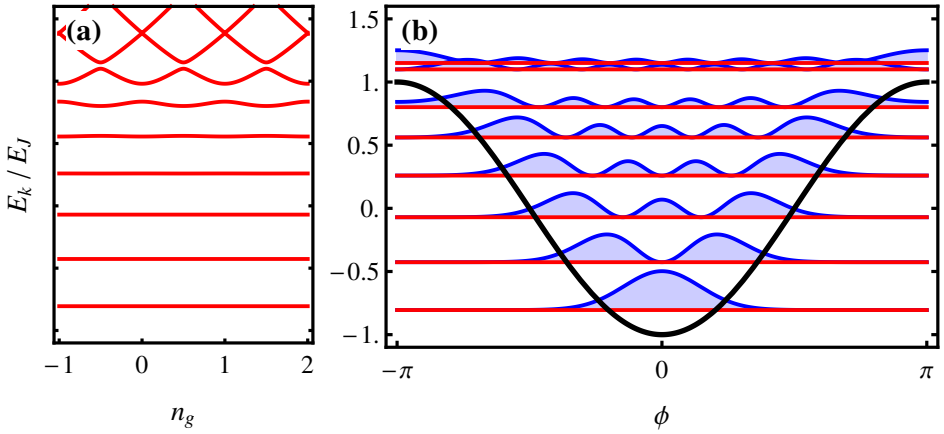

Figure 2.10: Energy spectrum and eigenstates of the charge qubit in the transmon regime. (a) Flat energy bands as a function of the dimensionless gate charge n_g, for $E_J/E_C = 50$, obtained from Eq. (2.143). (b) The energy levels (red) and modules of the wave function $|\psi_k(\phi)|^2$ (blue), obtained from the exact diagonalization of the charge qubit Hamiltonian, Eq. (2.145), are shown in the cosine Josephson potential (black) for $E_J/E_C = 50$ and $n_g = 0.5$.

The exponential suppression of the charge dispersion explains the robustness of the transmon qubit against charge noise. Actually, its transition energies becomes practically independent of the bias n_g, as shown in Fig. 2.11(b). The worst-case estimation for the dephasing time, due to charge noise only, is given by $T_2 \simeq \hbar/\epsilon_0$, which is extremely long for the typical parameters of transmon qubits. By going from $E_J/E_C = 1$ to 50, the expected improvement of T_2 is about six order of magnitudes [Houck09]. The limitation on the dephasing time would actually be set by other noise sources such as magnetic flux and critical current fluctuations, or quasiparticle tunneling [Koch07].

The first generation of transmon qubits, that is the standard planar geometry, patterned by electron-beam lithography on single-crystal sapphire substrate, as depicted in Fig. 2.9, reached dephasing times up to 3 μs and were mainly limited by relaxation, $T_2 = 2T_1$. The dominant source of decoherence was assumed to be critical current fluctuations in the Josephson junction. However, a more recent generation of transmon qubits [Paik11, Rigetti12] exhibiting surprisingly long dephasing times, up to 0.1 ms, seems to disprove the latter assumption.

An anharmonic quantum oscillator

In the transmon regime, a charge qubit can be described as a weakly anharmonic LC resonator. As we have seen previously, the phase fluctuations $\langle\hat{\phi}^2\rangle$ are small for the low-energy eigenstates (see Fig. 2.10). This allows us to neglect the effect of the gate charge n_g and to expand the Josephson cosine term of the charge qubit Hamiltonian, Eq. (2.108),

$$\hat{H} = 4E_c\hat{n}^2 - E_J\left(1 - \frac{\hat{\phi}^2}{2} + \frac{\hat{\phi}^4}{24}\right). \tag{2.147}$$

Without the fourth-order term, $\hat{H}$ is the Hamiltonian of a harmonic LC-resonator with capacitance C_Σ and inductance $L_J = E_J/I_c^2 = \left(\frac{\Phi_0}{2\pi}\right)^2 E_J^{-1}$. We usually refer to its resonance

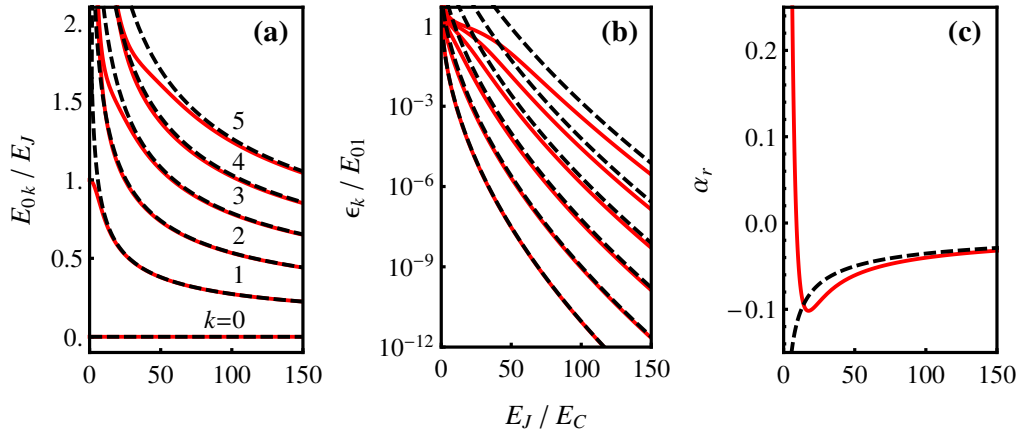

Figure 2.11: Transition energies $E_{0k} = E_k - E_0$ (a), charge dispersion ϵ_k (b), and relative anharmonicity α_r (c) of the charge qubit as a function of the ratio E_J/E_C. Exact values (red) are compared to the perturbative results given in Eqs. (2.146), (2.152), and (2.155) (dashed black).

frequency

$$\omega_p = \frac{1}{\sqrt{L_J C_\Sigma}} = \frac{\sqrt{8E_C E_J}}{\hbar} \tag{2.148}$$

as Josephson plasma frequency. The quartic term of $\hat{H}$ can be treated perturbatively to find approximate eigenenergies and eigenstates. We express $\hat{n}$ and $\hat{\phi}$ in terms of creation and annihilation operators, $\hat{c}^\dagger$ and $\hat{c}$,

$$\hat{n} = n_{\text{zpf}}\left(\hat{c} + \hat{c}^\dagger\right), \qquad n_{\text{zpf}} = \left(\frac{E_J}{32E_c}\right)^{1/4}, \tag{2.149}$$

$$\hat{\phi} = -i\phi_{\text{zpf}}\left(\hat{c} - \hat{c}^\dagger\right), \qquad \phi_{\text{zpf}} = \left(\frac{2E_C}{E_J}\right)^{1/4}. \tag{2.150}$$

The Hamiltonian becomes

$$\hat{H} = -E_J + \sqrt{8E_J E_C}\left(\hat{c}^\dagger\hat{c} + \frac{1}{2}\right) - \frac{E_C}{12}\left(\hat{c} - \hat{c}^\dagger\right)^4. \tag{2.151}$$

Using first-order perturbation theory, we obtain the approximate energy spectrum

$$E_k \simeq -E_J + \sqrt{8E_J E_C}\left(k + \frac{1}{2}\right) - \frac{E_C}{4}\left[2k(k+1) + 1\right]. \tag{2.152}$$

The above approximate energies are compared to the exact values in Fig. 2.11(a). The energy transition between to adjacent levels changes linearly with the band index k,

$$E_{k,k+1} = E_{k+1} - E_k = E_{01} - kE_C, \qquad E_{01} = \sqrt{8E_J E_C} - E_C. \tag{2.153}$$

The absolute anharmonicity of the transmon qubit is therefore negative and proportional to the charging energy,

$$\alpha = E_{12} - E_{01} \simeq -E_C. \tag{2.154}$$

From the above expression, we can find the scaling of the relative anharmonicity, defined as $\alpha_r = \alpha/E_{01}$,

$$\alpha_r \simeq -\left(\frac{E_C}{8E_J}\right)^{1/2}. \tag{2.155}$$

This approximate behavior is shown in Fig. 2.11(b) and compared to the exact solution of the full Hamiltonian.

A sufficient anharmonicity of the energy spectrum allows us to use such system as a qubit, where only the two lowest energy levels are addressed and form the computational basis states. However, the reduced anharmonicity imposes some constraint on the frequency bandwidth of control pulses used to manipulate the state of the qubit. In other words, it sets a lower bound on the pulse duration, typically of the order of $\hbar/\alpha$, in order not to excite higher energy states. Specific strategies have be developed and implemented to perform shorter control pulses with such weakly anharmonic qubit systems while avoiding leakage out of the computational subspace. They rely on the addition of a simultaneous second control whose optimal time-dependence is a function of the original control pulses to be performed [Motzoi09].

The perturbation theory also provides an approximation for the eigenstates of such a nonlinear resonator. They are conveniently expressed in the eigenbasis of the operator $\hat{c}^\dagger\hat{c}$, defined as the states $|k_0\rangle$, which satisfy

$$\hat{c}^\dagger\hat{c}|k_0\rangle = k_0|k_0\rangle, \qquad k_0 \in \mathbb{N}. \tag{2.156}$$

The k-th eigenstates of the transmon qubit, with the eigenenergy E_k given in Eq. (2.152), is approximately

$$|k\rangle \simeq |k_0\rangle - \frac{1}{48}\sqrt{\frac{E_C}{2E_J}}\sum_{m_0\neq k}\frac{\langle m_0|(\hat{c}-\hat{c}^\dagger)^4|k_0=k\rangle}{m_0-k}|m_0\rangle. \tag{2.157}$$

The quartic term of $\hat{H}$ produces a small mixing of $|k_0\rangle$ with the states $|k_0\pm 2\rangle$ and $|k_0\pm 4\rangle$. Defining the level frequencies as $\omega_k = E_k/\hbar$, the Hamiltonian of the transmon qubit reads

$$\hat{H} = \sum_k \hbar\omega_k|k\rangle\langle k|. \tag{2.158}$$

From now, unless otherwise specified, the sum over the level indices is taken over $k \geq 0$.

When considering the coupling of the transmon qubit to some external electrical field, it will be important to know the expression of the charge number operator $\hat{n}$ in terms of the eigenstates $|k\rangle$. For this purpose, we might examine the matrix elements $\langle k|\hat{c}|k+l\rangle$. Obviously, the leading order of the perturbation yields the terms with $l = 1$. The elements with even l vanish, and those with odd $l \neq 1$ are smaller by a factor $\sqrt{E_C/E_J}$ at least. Using the exact solution of the full Hamiltonian, one can actually show that the matrix elements $\langle k|\hat{n}|k+l\rangle$ decay algebraically in the small parameter E_C/E_J for odd $l > 0$, and fall off exponentially for even l [Koch07]. At the particular points where $2n_g \in \mathbb{Z}$, the matrix elements with even l are identically zero. This can be inferred from the parity of the wave functions $\psi_k(\phi) = \langle\phi|k\rangle$, Eq. (2.145).

Consequently we approximate the charge number operator by

$$\hat{n} \simeq \left(\frac{E_J}{32E_C}\right)^{1/4}\sum_k \sqrt{k+1}\big(|k+1\rangle\langle k| + |k\rangle\langle k+1|\big). \tag{2.159}$$

When restricting to the computational subspace ($|g\rangle = |0\rangle$ and $|e\rangle = |1\rangle$), the Hamiltonian Eq. (2.158) and the operator $\hat{n}$ can be expressed in terms of the standard Pauli matrices

$$\sigma_x = |0\rangle\langle 1| + |1\rangle\langle 0|, \tag{2.160a}$$
$$\sigma_y = i\left(|0\rangle\langle 1| - |1\rangle\langle 0|\right), \tag{2.160b}$$
$$\sigma_z = |1\rangle\langle 1| - |0\rangle\langle 0|. \tag{2.160c}$$

The charge operator becomes $\hat{n} \simeq (E_J/32E_C)^{1/4}\sigma_x$. Remarkably, the coupling to some electrical field is enhanced by a factor $(E_J/2E_C)^{1/4}$ in comparison to the CPB, where we had $\hat{n} = \frac{1}{2}\sigma_x$. This stronger coupling to a transverse field arises despite the level splitting begin almost independent of the gate voltage.

The expression for the charge number operator given in Eq. (2.159) turns out to be useful when discussing the coupling to a transmission line cavity, where the voltage is the one of a quantized microwave cavity mode. The system formed by one or several superconducting qubits and a TLR will be discussed in the next section and gives rise to the field known as circuit QED.

2.5 Circuit quantum electrodynamics

Circuit QED is an active field of research that considers superconducting qubits coupled to superconducting microwave cavities. This term was invented in analogy to the cavity QED [Raimond01, Mabuchi02], where atoms, placed in an optical cavity, couple to the electromagnetic modes via the dipole interaction. When the coupling to a particular cavity mode is strong, typically larger than the relaxation rates of the atom and the cavity, the latter can coherently exchange energy. The so-called regime of *strong coupling* between an effective two-level system and a single photonic modes gives rise to many interesting quantum effects that have been studied extensively in circuit QED experiments.

In circuit QED setups, the superconducting qubits – the artificial atoms – are placed inside an effective one-dimensional microwave cavity – the superconducting TLR we have considered previously – and realize an on-chip solid-state version of the Jaynes-Cummings Hamiltonian. This seminal idea was first proposed in Ref. [Blais04], but earlier suggestions of solid-state implementations of this Hamiltonian are worth mentioning [Marquardt01, You03a]. Charge qubits can naturally be coupled to the electrical mode of TLRs by placing them between the central wire and the ground planes, as shown in Fig. 2.12. In contrast to atomic cavity QED, the strong confinement of the electrical field in the circuit QED architecture already provides a big step towards the strong-coupling regime [Schoelkopf08].

We first present an Hamiltonian that describes the coupling between a single transmon qubit and a microwave cavity. Under appropriate conditions, this model can be effectively reduced to an conventional Jaynes-Cummings Hamiltonian involving only two levels of the qubit, akin to the one encountered in atomic QED. This model captures most of the effects arising in circuit QED and allows to discuss essential operations such as qubit readout and single-qubit rotations. Afterwards, we review some of the most notable quantum effects that have been observed in the strong-coupling regime of circuit QED. The straightforward generalization of the model to setups involving multiple qubits – the Tavis-Cummings Hamiltonian – is an important starting point in the description of many experiments and quantum information protocols. Postponing the presentation of this model to the next chapter, we conclude this chapter by giving some prominent examples of quantum information protocols that have been successfully implemented with this architecture.

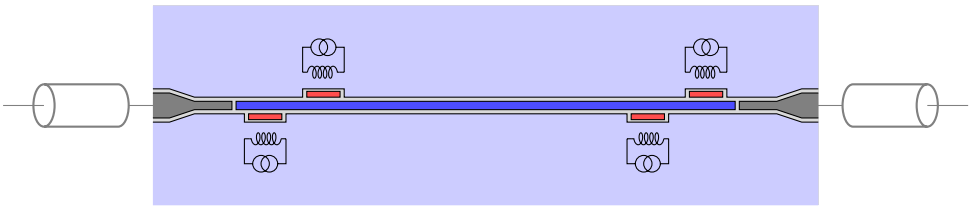

Figure 2.12: *Circuit QED setup with superconducting transmon qubits.* Schematic representation of the setup geometry consisting of four charge qubits (red), placed within the gap between the central wire (dark blue) and the ground planes (light blue) of a coplanar TLR (see Fig. 2.9(b) for an enlarged view). Input and output transmission lines (gray) couples to the TLR via gap capacitors and allow to probe the qubits-cavity system in transmission. External control lines (black) produces a local magnetic field that allows to tune the frequency of the qubits, provided the latter are made with a split Josephson junction.

2.5.1 Jaynes-Cummings Hamiltonian

We consider the situation where a single superconducting charge qubit is coupled capacitively to the electrical field between the central wire and the ground plane of a TLR. The full system Hamiltonian contains three terms: the charge qubit Hamiltonian, Eq. (2.108), the resonator Hamiltonian, Eq. (2.27), and a term describing the dipole coupling between the charge number operator of the qubit $\hat{n}$ and the voltage operator $\hat{V}(x)$ given in Eq. (2.31). Generally the system is only probed near a particular frequency, typically close to the qubit transition frequency and one specific cavity resonance. The qubit are designed to have frequency tunable close to the fundamental or first harmonic frequency of the TLR. This choice mainly depends on the qubit position along the TLR; if close to the ends, the qubit can couple to the fundamental mode, while this is not the case if the qubit is placed near the center of the resonator, where the voltage due to the fundamental mode is essentially zero. Thus, only one resonator mode is taken into account since the influence of other resonator modes, largely detuned from the qubit frequency, on the coherent dynamics of the qubit is negligible.

In principle, the exact expression for the dipole coupling requires a careful circuit analysis, however, an appropriate expression can be obtained by replacing the dimensionless gate n_g that appears in the qubit Hamiltonian by the sum of a dc-component n_g^{dc}, due to the overall biasing of the resonator, and a term proportional to the quantum voltage operator, $C_g\hat{V}(x)/(2e)$, due to the presence of photons in the resonator. The voltage operator, taken at the qubit position x_q, is written as

$$\hat{V}(x_q) = V_{\mathrm{rms}}\left(\hat{a}_m + \hat{a}_m^\dagger\right)\phi_m(x_q), \tag{2.161}$$

where $\hat{a}_m(\hat{a}_m^\dagger)$ is the annihilation (creation) operator of the relevant resonator mode with index m, $V_{\mathrm{rms}} = \sqrt{\frac{\hbar\omega_r}{2c}}$ the zero-point fluctuation of the voltage, $\omega_r = m\pi v_p/L_0$ the mode frequency, and ϕ_m the mode spatial distribution, with $\phi_m(x_q) = \sqrt{2/L_0}$ if the qubit position x_q matches an anti-node of the electrical field (see Sec. 2.3.1 for details). Since we only consider a single mode of the TLR, the index mode m will be dropped as from now. The Hamiltonian for the qubit and the cavity reads

$$\hat{H} = 4E_C\left(\hat{n} - n_g^{\mathrm{dc}}\right)^2 - E_J\cos\hat{\phi} + \hbar\omega_r\hat{a}^\dagger\hat{a} + 2\beta eV_{\mathrm{rms}}\hat{n}\left(\hat{a} + \hat{a}^\dagger\right), \tag{2.162}$$

where $\beta = C_g/C_\Sigma$.

The above Hamiltonian can be expressed in the qubit eigenbasis. We now focus on the case where the superconducting charge qubit is in the transmon regime, using the results from Sec. 2.4.5. In Eq. (2.159), an expression for the charge number operator $\hat{n}$ was derived. We can rewrite Eq. (2.162) in the form

$$\hat{H} = \sum_k \hbar\omega_k |k\rangle\langle k| + \hbar\omega_r \hat{a}^\dagger \hat{a} + \sum_k \hbar g_k \big(|k+1\rangle\langle k| + |k\rangle\langle k+1|\big)\left(\hat{a} + \hat{a}^\dagger\right). \tag{2.163}$$

Here, the frequency of the kth transmon level, $\omega_k = E_k/\hbar$, is obtained from the transmon eigenenergies given in Eq. (2.152). The coupling strengths are approximated by $g_k \simeq \sqrt{k+1}g_0$, where

$$\hbar g_0 = eV_{\mathrm{rms}} \frac{C_g}{C_\Sigma} \left(\frac{E_J}{32E_C}\right)^{1/4}. \tag{2.164}$$

If the transition frequency of the transmon qubit, $\omega_{k,k+1} = \omega_{k+1} - \omega_k$, is close to the resonator frequency ω_r and $\omega_r \gg g_k$, it is reasonable to invoke the RWA and drop the counter-rotating terms $\hat{a}\sigma_{k,-}$ and $\hat{a}^\dagger\sigma_{k,+}$. The resulting expression,

$$\hat{H} = \sum_k \hbar\omega_k |k\rangle\langle k| + \hbar\omega_r \hat{a}^\dagger \hat{a} + \sum_k \hbar g_k \left(\hat{a}|k+1\rangle\langle k| + \hat{a}^\dagger |k\rangle\langle k+1|\right), \tag{2.165}$$

has the form of a generalized Jaynes-Cummings Hamiltonian for a cavity coupled to a multilevel artificial atom. Eq. (2.165) is the starting point to many studies about circuit QED.

Two-level approximation

For the purpose of quantum information processing, it is obviously desirable that the transmon anharmonicity is sufficiently large for this qubit to be treated as an effective two-level system. When the transition frequency between the two lowest transmon levels is nearly resonant with the resonator frequency, $\omega_{01} \simeq \omega_r$, the influence of higher level can be neglected and Eq. (2.165) can be written as a conventional Jaynes-Cummings Hamiltonian [Jaynes63][7]

$$\hat{H} = \frac{\hbar\omega_{01}}{2}\sigma_z + \hbar\omega_r \hat{a}^\dagger \hat{a} + \hbar g_0 \left(\hat{a}\sigma_+ + \hat{a}^\dagger \sigma_-\right), \tag{2.166}$$

where $\sigma_+ = |1\rangle\langle 0|$ and $\sigma_- = |0\rangle\langle 1|$. While rather simple, the Jaynes-Cummings Hamiltonian is probably one of the most important model for understanding the light-matter interaction. This Hamiltonian, well-known from the field of cavity QED, contains highly non-trivial physics and captures various quantum effects.

In the dispersive regime, when the detuning between the qubit transition frequencies and the cavity resonance frequency, $\Delta_{k,k+1} = \omega_{k,k+1} - \omega_r$, is large compared to their coupling strength, $g_k \ll |\Delta_{k,k+1}|$, a two-level approximation can also be made. The standard procedure, when dealing with genuine two-level system, is to treat the interaction term in Eq. (2.166) perturbatively by making an unitary transformation $\hat{U}\hat{H}\hat{U}^\dagger$, where $\hat{U} = \exp[(g_0/\Delta_{01})(\hat{a}\sigma_+ + \hat{a}^\dagger\sigma_-)]$, and an expansion in the small parameter g_0/Δ_{01}. This results in a dynamical Stark shift $\frac{g_0^2}{\Delta_{01}}\sigma_z\hat{a}^\dagger\hat{a}$, which can be seen as shift of the cavity

[7] Details about the validity of such truncation of the Hilbert space can be found in Appendix A.1

frequency depending on the qubit state, or as a shift of the qubit frequency depending on the photon number.

However in circuit QED, when considering weakly anharmonic multilevel systems like transmon qubits, it is important to treat the interaction perturbatively at the level of the generalized Jaynes-Cummings Hamiltonian Eq. (2.165) before making the two-level approximation. Applying the unitary transformation $\hat{U} = \exp(\hat{S})$, where

$$\hat{S} = \sum_k \frac{g_k}{\Delta_{k,k+1}} \left(\hat{a}|k+1\rangle\langle k| - \hat{a}^\dagger |k\rangle\langle k+1| \right), \tag{2.167}$$

to Eq. (2.165) and expanding up to second order in $g_k/\Delta_{k,k+1}$, we obtain

$$\begin{aligned} \hat{U}\hat{H}\hat{U}^\dagger = {} & \hbar\omega_0 |0\rangle\langle 0| + \sum_{k\geq 1} \hbar \left(\omega_k + \chi_{k-1}\right) |k\rangle\langle k| \\ & + \left[\hbar\omega_r - \hbar\chi_0 |0\rangle\langle 0| + \sum_{k\geq 1} \hbar \left(\chi_{k-1} - \chi_k\right) |k\rangle\langle k| \right] \hat{a}^\dagger \hat{a} \\ & + \sum_k \hbar\eta_k \left(\hat{a}^2 |k+2\rangle\langle k| + \hat{a}^{\dagger 2} |k\rangle\langle k+2| \right). \end{aligned} \tag{2.168}$$

Here the generalized Stark shifts χ_k and two-photon transition rates η_k are given by

$$\chi_k = \frac{g_k^2}{\Delta_{k,k+1}}, \qquad \eta_k = \frac{1}{2} \frac{g_k g_{k+1}}{\Delta_{k,k+1}\Delta_{k+1,k+2}} \left(\omega_{k,k+1} - \omega_{k+1,k+2}\right). \tag{2.169}$$

In the two-level approximation, two-photons processes are neglected and the resulting dispersive Hamiltonian[8]

$$\hat{H} = \frac{\hbar\omega'_{01}}{2}\sigma_z + \hbar \left(\omega'_r + \chi\sigma_z\right) \hat{a}^\dagger \hat{a} \tag{2.170}$$

contains the dispersive ac-Stark shift $\chi = \chi_0 - \chi_1/2$, as well as Lamb-shifted qubit and resonator frequencies, $\omega'_{01} = \omega_{01} + \chi_0$ and $\omega'_r = \omega_r - \chi_1$.

The dispersive Hamiltonian Eq. (2.170) allows to understand how qubit readout can be performed in circuit QED by probing the cavity. The presence of the qubits cause a state-dependent shift χ of the cavity frequency, whose sign depends on the qubit state. When this frequency shift is comparable or larger than the cavity linewidth, it can be determined by driving the cavity close to its unperturbed resonance frequency. The frequency shift influences the measured amplitude and phase of the microwave field that is either reflected or transmitted from the cavity [Wallraff04, Schuster05, Wallraff05]. This measurement scheme is usually referred to as *dispersive readout*. When several qubits are dispersively coupled to the same microwave cavity, this scheme even allows to perform a joint qubit readout [Filipp09, Chow10b]. Importantly, the state of the qubit can be determined nondestructively. Since the interaction commutes with the free Hamiltonian, the dispersive readout is in principle a QND measurement scheme. It leaves the qubit into one of the σ_z eigenstates and does not affect later repetition of the measurement.

Driven Jaynes-Cummings Hamiltonian and single-qubit operations

We now want to show how single-qubit rotations can be performed with a microwave driving field acting on the TLR. The Hamiltonian

$$\hat{H}_d = \hbar \left[\epsilon^*(t) e^{i\omega_d t} \hat{a} + \epsilon(t) e^{-i\omega_d t} \hat{a}^\dagger \right] \tag{2.171}$$

[8] The validity of this approximation is discussed in Appendix A.2

models a coherent field with frequency ω_d and time-dependent amplitude $\epsilon(t)$ that drives the resonator mode. In the above expression, the RWA was made, assuming that the condition $|\epsilon| \ll \omega_r, \omega_d$ is satisfied. The Hamiltonian for the qubit-resonator system and the drive is

$$\hat{H} = \sum_k \hbar\omega_k |k\rangle\langle k| + \hbar\omega_r \hat{a}^\dagger \hat{a} + \sum_k \hbar g_k \left(\hat{a}|k+1\rangle\langle k| + \hat{a}^\dagger |k\rangle\langle k+1|\right) + \hat{H}_d. \tag{2.172}$$

It is more convenient to express the Hamiltonian in the rotating frame of the driving field by performing the unitary transformation $\hat{H}_{\text{new}} = \hat{U}\hat{H}\hat{U}^\dagger + i\hbar(\partial_t \hat{U})\hat{U}^\dagger$, where

$$\hat{U} = \exp\left[i\omega_d t \left(\hat{a}^\dagger \hat{a} + \sum_k |k\rangle k\langle k|\right)\right]. \tag{2.173}$$

The new Hamiltonian reads

$$\begin{aligned} \hat{H}_{\text{rot}} = &\sum_k \hbar\delta_k |k\rangle\langle k| + \hbar\delta_r \hat{a}^\dagger \hat{a} \\ &+ \sum_k \hbar g_k \left(\hat{a}|k+1\rangle\langle k| + \hat{a}^\dagger |k\rangle\langle k+1|\right) \\ &+ \hbar\left[\epsilon(t)\hat{a}^\dagger + \epsilon^*(t)\hat{a}\right], \end{aligned} \tag{2.174}$$

where $\delta_k = \omega_k - \omega_d$ and $\delta_r = \omega_r - \omega_d$.

When a coherent drive is applied, the resonator state is well described as the sum of a coherent state, with amplitude $\alpha(t)$, plus corrections. This coherent amplitude $\alpha(t)$ can be controlled by the driving field and allows to act on the qubit via the qubit-resonator interaction. To see how the driving term can act directly on the transmon operators, it is useful to write the Hamiltonian in a displaced frame. This can be done with the displacement operator

$$\hat{D} = \exp\left[\alpha^*(t)\hat{a} - \alpha(t)\hat{a}^\dagger\right] \tag{2.175}$$

which transforms the resonator mode operator as $\hat{D}\hat{a}\hat{D}^\dagger = \alpha(t) + \hat{a}$. If the displaced amplitude $\alpha(t)$ is chosen such that it satisfies the differential equation

$$\dot{\alpha}(t) = -i\left[\delta_r \alpha(t) + \epsilon(t)\right] \tag{2.176}$$

the displaced Hamiltonian, found from $\hat{D}\hat{H}_{\text{rot}}\hat{D}^\dagger + i\hbar(\partial_t \hat{D})\hat{D}^\dagger$, reads

$$\begin{aligned} \hat{H}_{\text{displ}} = &\sum_k \hbar\delta_k |k\rangle\langle k| + \hbar\delta_r \hat{a}^\dagger \hat{a} \\ &+ \sum_k \hbar g_k \left(\hat{a}|k+1\rangle\langle k| + \hat{a}^\dagger |k\rangle\langle k+1|\right) \\ &+ \sum_k \hbar g_k \left[\alpha(t)|k+1\rangle\langle k| + \alpha^*(t)|k\rangle\langle k+1|\right]. \end{aligned} \tag{2.177}$$

Examining the last term of $\hat{H}_{\text{displ}}$, it becomes clear that the microwave drive can be used to induce transition between different transmon levels.

In the dispersive regime, we can apply the transformation given in Eq. (2.167) to the Hamiltonian $\hat{H}_{\text{displ}}$ and truncate it to the two lowest transmon levels. We end up with the driven dispersive Hamiltonian in the rotating frame

$$\hat{H} = \frac{\hbar\delta'_{01}}{2}\sigma_z + \hbar\left(\delta'_r + \chi\sigma_z\right)\hat{a}^\dagger\hat{a} + \frac{\hbar}{2}\left[\Omega_0^*(t)\sigma_- + \Omega_0(t)\sigma_+\right], \tag{2.178}$$

where $\delta'_{01} = \omega'_{01} - \omega_d$ and $\delta'_r = \omega'_r - \omega_d$ are the detunings of the Lamb-shifted qubit and cavity frequencies with respect to the drive. In addition, we have introduced the Rabi frequency for the $0 \leftrightarrow 1$ transition $\Omega_0(t) = 2g_0\alpha(t)$. Eq.(2.178) shows that by choosing the phase of the drive, qubit rotations around any axis in the xy-plane can in principle be directly performed by applying microwave driving pulses with $\omega_d \simeq \omega'_{01}$.

In practice, well-controlled pulse shapes and careful calibration allow to perform such rotations with very high fidelities [Chow09]. Nevertheless, we should keep in mind that the microwave drive also couples to the $1 \leftrightarrow 2$ transition with a Rabi frequency $\Omega_1 = 2g_1\alpha(t)$. Due to their weak anharmonicity, of the order of E_C, this effect is particularly important for transmon qubits as it can produce leakage out of the computational subspace. The duration of control pulse cannot be made arbitrarily short and the time $\hbar/E_C$ sets a typical lower bound. This issue of weakly nonlinear artificial atoms was later reexamined and it was shown that specific pulse envelopes allow to reduce the leakage to higher states [Motzoi09, Gambetta11b]. This approach led to further improvements on single-qubit gate fidelities and durations for transmon qubits [Chow10a, Bianchetti10, Chow12] as well as for phase qubits [Lucero10].

2.5.2 Strong-coupling regime

The strong-coupling regime of cavity QED is reached when the atom-cavity coupling rate exceeds the relaxations rates of both the cavity and the atom. The quantum phenomena that can arise in this regime are diverse. If the energy splitting of the qubit match the resonance frequency of the cavity, the eigenstates of the coupled system are no longer purely photonic or atomic; in the language of quantum information, they are entangled. The degeneracy between the two states containing exactly one excitation of either atomic of photonic nature is lifted by the coupling. This effect, known as the vacuum Rabi mode splitting, was the first experimental demonstration of the strong-coupling regime in circuit QED. It was observed in 2004 both with charge qubits in the CPB regime [Wallraff04] and flux qubits [Chiorescu04]. In the strong-coupling regime, one energy quantum can be exchanged back and forth between the qubit and the cavity several times before it is lost. These so-called Rabi oscillations have been observed shortly after [Wallraff05].

As we have seen previously, the transmon regime further enhances the qubit-resonator interaction compared to CPB regime. This enhancement made possible the exploration of additional quantum effects. For instance, an important consequence of the strong-coupling regime is the anharmonic spectrum of the qubit-resonator system, also known as Jaynes-Cummings ladder, as revealed in a circuit QED setup [Fink08, Fink09]. This anharmonicity enables the observation of well-known quantum-optical effects such as photon number states [Schuster07, Houck07], or photon blockade [Lang11, Hoffman11b].

Another remarkable phenomenon exhibited in the resonant strong-coupling regime is the acceleration of the qubit decay, through the cavity mode, when the intrinsic qubit relaxation time is longer than the one the cavity. In contrast, when the qubit and cavity frequencies are detuned, the qubit has an improved lifetime as compared to the case where is couples to a continuum of vacuum modes. The cavity isolates the qubit and filters part of the vacuum noise that affects the qubit coherence. This enhancement or suppression of the qubit decay through the cavity modes is a well-know effect named after Purcell [Purcell46]. In the circuit QED architecture with transmon qubits, the Purcell decay is actually the main limiting effect for T_1 and is used to either implement a fast qubit reset or to limit qubit relaxation [Houck08, Reed10, Gambetta11a].

2.5.3 Realization of quantum information protocols and recent developments

The circuit QED architecture provides a number of features which make it a promising platform for the purpose of quantum information processing. We shall mention a few successful experiments that have implemented some of the important functionalities required to realize a quantum computer.

We already mentioned how the coupling to a microwave cavity turns out to be useful for the preparation, the control, and the readout of superconducting qubits. In addition, when several qubits are dispersively coupled to a common TLR, they can act as a small qubit register that can be addressed and on which quantum algorithms can be run. In this configuration, the resonator mediates effective dispersive interactions between the qubits and plays the role of a quantum bus, distributing quantum information among the qubits. These interactions, whose exact form will be specified in the next chapter, typically couple the transverse components of the qubits and, to some extent, their strength can be controlled by changing the qubit-resonator detunings. Importantly, the interaction between two qubits can be effectively turned on, by bringing these qubits on resonance (but still detuned from the resonator frequency), or switched off by setting large detunings between all components. These qubit-qubit interactions play a major role as they are required to implement entangling gates, i.e., gates that cannot be described as the product of local operations on each qubit, essential for any quantum algorithms.

The coupling of two transmon qubits via a quantum bus in a circuit QED setup has been reported in Ref. [Majer07]. Again, the development of superconducting transmon qubits has played an important role for the experimental demonstration of such effective qubit-qubit coupling. For the latter to be a coherent coupling, in other words to allow the coherent transfer of quantum information between qubits or to used for the implementation of two-qubit gates, its strength should exceed typical relaxation and dephasing rates. The dispersive coupling between two qubits directly depends on their bare individual couplings to the resonator. Therefore, transmon qubits, with their large capacitive coupling to the resonator, turn out to be particularly advantageous compared to the previous CPB qubit designs.

The implementation of qubit-qubit interaction, combined with high-fidelity single qubit operations, enables the realization of quantum information protocols. Circuit QED experiments with two transmon qubits have successfully achieved the creation of Bell states [Leek09, Filipp09, Chow10b], the realization of conditional two-qubit gates [DiCarlo09, Chow10b, Chow12], and the implementation of Grover search and Deutsch-Josza quantum algorithms [DiCarlo09]. The potential scalability of this architecture has made a step forward with experimental setups involving three transmon qubits and showing a high level of controllability. The generation of three-qubit entangled states [DiCarlo10, Mlynek12], the implementation of a three-qubit Toffoli gate [Fedorov12], as well as the first proof-of-principle demonstration of a quantum teleportation protocol have been reported [Baur12]. This last experiment has only demonstrated the coherent part of quantum teleportation, lacking the single-shot readout and feed-forward steps. These missing aspects have been implemented in a recent experiment where a complete quantum teleportation protocol has been realized [Steffen13].

Other remarkable achievements that are worth mentioning are the observation of Berry's phase in a Ramsey fringe interference experiment [Leek07], the realization of a transmon-like qubit with tunable qubit-resonator coupling [Srinivasan11, Hoffman11a],

and experiments involving higher transmon levels [Bianchetti10].

Regarding the readout of the qubit state, an important aspects of the measurement performance is the ability to realize a QND measurement. Such a measurement leaves the qubit in a definite eigenstate of the measured observable. In addition, it does not affect the qubit state if this one is already an eigenstate of the observable. Other important aspects are the ability to perform such a measurement in a single-shot fashion, i.e., to obtain a reliable outcome without the need for repeated measurement, and the rate at which such a readout can be carried out. QND measurements are of utmost importance to envision the realization of QEC schemes. To detect and correct errors, their occurrence should happen at a much slower rate than the rate at which successive qubit readouts can be performed. For the ultimate purpose of building a fault-tolerant quantum information processor, the qubit readout should therefore be a QND measurement, provide a single-shot record with a high fidelity, and be realizable at fast pace.

As we have mentioned previously, spectroscopic QND measurement of the qubit state can be performed in the standard circuit QED architecture with linear transmission line cavities by measuring the dispersive ac-Stark shift of the cavity resonance frequency [Schuster05, Wallraff05, Houck08]. This measurement scheme has been extended to experiments with several qubits were it serves as the main method to perform a joint qubit readout [Filipp09, Chow10b]. However, the latter implementations suffer from rather low single-shot fidelity. A single-shot qubit readout has been implemented in a slightly different architecture where a superconducting transmon qubit couples to a nonlinear resonator, demonstrating low back-action and good QND character [Mallet09], but the rate at which such readout could be performed was still comparable to the qubit relaxation rate. Recent experimental efforts to improve the readout techniques take advantage of nearly quantum-limited Josephson parametric amplifiers [Castellanos-Beltran08, Bergeal10b, Bergeal10a], whose use has significantly impacted the measurement performance. Using such amplifiers, fast and repeated single-shot dispersive QND measurements have been realized to monitor quantum jumps between qubit states [Vijay11], to apply a coherent feedback in order to perform a fast qubit reset [Ristè12a], or to stabilize Rabi [Vijay12, Campagne-Ibarcq13] and Ramsey oscillations [Campagne-Ibarcq13]. In addition, this advanced technique has been used for the initialization of two-qubit state by joint dispersive measurement [Ristè12b].

Finally, it is important to emphasize that the most recent experiments benefit from the improved coherence properties of a new circuit QED architecture design [Paik11, Rigetti12]. The latter replaces the on-chip coplanar waveguide resonator by a three-dimensional superconducting microwave cavity, hence the nickname 3D circuit QED. The actual geometry of the transmon qubits embedded in such cavities differs from the one we have presented in this chapter. They are a fabricated on a sapphire substrate that is mounted inside the hollow microwave cavity. Although the working principle remains unchanged, this type of transmon qubits exhibits dephasing time of some tens of microseconds [Paik11] up to nearly hundred microseconds [Rigetti12], representing an improvement of more than one order of magnitude with respect to original transmon qubits. Such transmon qubits are fabricated with significantly larger electrodes (they are made of nearly millimeter-scale superconducting islands) reducing their sensitivity to dielectric surface loss compared to the initial planar geometry [Paik11]. The larger electrodes also lead to an increased dipole moment and compensate the reduction of the electrical field, due to the larger mode volume of these three-dimensional cavities compared to one-dimensional transmission line cavities. The dipole coupling is still sufficiently large for these setups to

reach the strong-coupling regime of quantum electrodynamics.

Chapter 3

One-step deterministic generation of GHZ states

The present chapter essentially follows the line of our publication

> S. Aldana, Y.-D. Wang, and C. Bruder,
> *Greenberger-Horne-Zeilinger generation protocol for N superconducting transmon qubits capacitively coupled to a quantum bus,*
> Phys. Rev. B **84**, 134519 (2011).

Entangled quantum states are one of the essential resources for quantum information processing. They are necessary for the realization of quantum communication and the most important computational tasks [Nielsen00, Horodecki09]. Many efforts have been devoted to the elaboration of physical systems enabling to generate and control such states. In particular, different types of superconducting qubits are promising candidates to solve this problem.

In the previous chapter, we have discussed some properties of superconducting circuits, focusing in particular on the circuit QED architecture with charge qubits. A great deal of interest in these systems originates from their potential for quantum information processing tasks. So far, we have seen how these systems implement physical qubits and how to control them individually. In the present chapter, we explore the possibility to generate Greenberger-Horne-Zeilinger (GHZ) states [Greenberger90] with superconducting transmon qubits dispersively coupled to a microwave cavity, i.e., the circuit QED architecture realized in a number of experiments [Majer07, Houck08, Filipp09, DiCarlo09, DiCarlo10, Leek10, Chow10b, Baur12, Chow12, Fedorov12, Reed12].

Although the mathematical description of multipartite entanglement for more than three qubits is still being debated [Verstraete02, Lamata07, Borsten10], GHZ states remain paradigmatic states that are considered to be maximally entangled. These states are in particular useful for fault-tolerant quantum computing or quantum secret sharing [Hillery99, Gao05]. In addition, they are considered as optimal resource states for measurement-based computation [Anders09] and Heisenberg-limited measurement schemes [Bollinger96, Guillaume06, Giovannetti04, Giovannetti06]. Such highly entangled states have also received considerable attention in the context of violation of Bell-type inequalities [Mermin90a, Mermin90b, Cabello02].

This chapter is organized as follows: in Sec. 3.1, we briefly discuss several ways to generate GHZ states like successive application of single and two-qubit gates or probabilistic entangling schemes based on multi-qubit joint measurements. In particular, we

focus on the Mølmer-Sørensen scheme [Mølmer99], a multi-qubit entangling gate based on a pairwise exchange interaction between any pair of qubits. In Sec. 3.2 we consider on a system made of N transmon qubits homogeneously and dispersively coupled to a common microwave field. We derive an effective Hamiltonian, characterized by effective qubit interactions of the XY type that can be globally controlled. Sec. 3.3 shows how these interactions enable a solid-state implementation of the Mølmer-Sørensen idea. This procedure allows us to generate GHZ states in a one-step deterministic procedure, starting from a fully separable state. In Sec. 3.4, we discuss ways to confirm the N-partite nature of the entanglement in the generated states. Finally, in Sec. 3.5, we study how non-ideal physical parameters, such as inhomogeneities in the qubit-resonator coupling constants, thermal occupation of the microwave cavity, or weak transmon anharmonicity, might affect the generated state.

3.1 Generating GHZ states

GHZ states are maximally entangled states that involve at least three subsystems. For N qubits, they are defined as the quantum superposition of two product states, one with all qubits being in a particular state and one with all of them being in the orthogonal and fully distinguishable state. Up to single-qubit rotations, a GHZ state is commonly written as

$$|\mathrm{GHZ}\rangle = \frac{1}{\sqrt{2}}\left(\bigotimes_{q=1}^{N}|0_q\rangle + \bigotimes_{q=1}^{N}|1_q\rangle\right), \tag{3.1}$$

where the index q labels the qubits. In principle, any entangled state of several qubit can be created if a limited but universal set of single and two-qubit gates is available. For instance, a three-qubit GHZ state can be obtained, starting from the separable state of all qubits in their ground state, by the successive application of a Hadamard gate on the first qubit H_1, followed by two CNOT gates, controlled by qubit 1, on qubits 2 and 3, CNOT_{12} and CNOT_{13},

$$|000\rangle \xrightarrow{\mathrm{H}_1} \frac{1}{\sqrt{2}}\big(|000\rangle + |100\rangle\big) \tag{3.2}$$

$$\xrightarrow{\mathrm{CNOT}_{12}} \frac{1}{\sqrt{2}}\big(|000\rangle + |110\rangle\big) \tag{3.3}$$

$$\xrightarrow{\mathrm{CNOT}_{13}} \frac{1}{\sqrt{2}}\big(|000\rangle + |111\rangle\big). \tag{3.4}$$

In the circuit QED architecture with charge qubits, an effective qubit-qubit interaction is mediated by virtual excitations of the resonator in the dispersive regime [Majer07]. This interaction can be turned on and off via external control lines to realize two-qubit gates [DiCarlo09]. Entangling two-qubit gates have also been successfully realized with superconducting phase [Steffen06, Ansmann09] and flux qubits [Plantenberg07]. Based on these remarkable achievements, similar protocols involving a sequence of gates have been implemented to successfully entangle three qubits [DiCarlo10, Neeley10].

Such a procedure to produce highly entangled states might become tedious and technically difficult when the number of qubits increases. Alternative schemes have been proposed to generate such states in a different and possibly more efficient way. In particular, many proposals specifically address the question of GHZ state production in circuit QED setups [Tsomokos08, Helmer09, Hutchison09, Bishop09b, Galiautdinov09, Wang10].

Some measurement-based schemes are of a probabilistic nature, i.e., if a measurement on the N-qubit system has a specific result, the system is known to be in a GHZ state after the measurement [Helmer09, Hutchison09, Bishop09b]. These elegant schemes do not need the application of two-qubit gates and can therefore work in the absence of qubit-qubit interaction. Instead, the creation of entanglement requires the measurement to be a joint readout of several qubits. In circuit QED setups, such a multi-qubit measurement can be achieved with a dispersive readout [Filipp09, Chow10b]. It is also worth mentioning that these schemes allow for the generation of other type of entangled states, such as W states. These proposals extend an earlier and similar two-qubit entangling scheme [Sarovar05, Rodrigues08], that has been recently realized for the production of Bell states in a 3D circuit QED setup with two transmon qubits [Ristè13]. While particularly adapted to the current experimental situation, this promising type of state preparation suffers from its probabilistic nature. Indeed, the probability to achieve a GHZ state decreases exponentially with the number of qubits.

3.1.1 Mølmer-Sørensen scheme

A particular type of protocol considers the possibility to make use of a multi-qubit interaction to generate GHZ states in a deterministic way. It relies on the presence of an homogeneous effective exchange interaction between any pair of qubits. Named after Mølmer and Sørensen [Mølmer99, Sørensen00], this entangling technique was originally proposed to create GHZ states in ion traps and has proven to be remarkably efficient. Implementing this method, ion trap experiments were able to generate GHZ states with four [Sackett00], six [Leibfried05], and up to fourteen qubits [Monz11]. Later, it was suggested that this seminal idea could as well be employed to generate entangled states of Bose-Einstein condensed atoms [Helmerson01, You03b].

Any physical system where all the qubits are effectively coupled via a pairwise exchange interaction of the XY type, a situation we will refer to as a fully connected network of qubits, enables a direct implementation of the Mølmer-Sørensen idea [Tsomokos08, Galiautdinov09].

The protocol can be summarized as follows:

1. If the effective qubit-qubit interaction is homogeneous, the Hamiltonian is

$$\hat{H} = \frac{\hbar g}{4} \sum_{(q,q')} \left(\sigma_x^{(q)} \sigma_x^{(q')} + \sigma_y^{(q)} \sigma_y^{(q')} \right), \tag{3.5}$$

   where the sum runs over all possible qubit pairs. This Hamiltonian can be concisely written as $\hat{H} = -\hbar g \hat{J}_z^2$, where $\hat{J}_z$ is a shorthand notation to denote the total spin operator along the z direction.

2. The N qubits are initialized in a product state with all qubits oriented in a specific direction in the xy plane, characterized by the angle θ,

$$|\psi_0\rangle = \bigotimes_{q=1}^{N} \frac{|0_q\rangle + e^{i\theta}|1_q\rangle}{\sqrt{2}}. \tag{3.6}$$

3. Under the influence of $\hat{H}$, the state $|\psi_0\rangle$ coherently evolves, after a time $t = \pi/(2g)$,

to the state

$$|\psi\rangle = e^{i\frac{\pi}{2}\hat{J}_z^2}|\psi_0\rangle = \frac{1}{\sqrt{2}}\left(\bigotimes_{q=1}^{N}\frac{|0_q\rangle + e^{i\theta'}|1_q\rangle}{\sqrt{2}} + e^{i\phi}\bigotimes_{q=1}^{N}\frac{|0_q\rangle - e^{i\theta'}|1_q\rangle}{\sqrt{2}}\right), \tag{3.7}$$

which is a GHZ state, up to single-qubit rotations. Here, the phase angles θ' and ϕ depend on θ and N.

4. The final state $|\psi\rangle$ can then be transformed to a conventional GHZ state, in the sense of Eq. (3.1), by applying single-qubit rotations.

We notice that the duration of the step that produces entanglement between the qubits (step 3) does not depend on the number of qubits, highlighting the one-step nature of the protocol. The preparation of the qubit in the appropriate state $|\psi_0\rangle$, as well as the final step, still requires the application of N single-qubit gates each. Nevertheless, the latter can generally be realized much faster than two-qubit gates. For this reason, when N becomes large, the procedure might turn out to be more favorable than conventional approaches requiring typically N two-qubit gates.

In the context of quantum information processing with superconducting circuits, a possible realization of the Mølmer-Sørensen scheme with phase qubits was investigated in Ref. [Galiautdinov08], but no specific circuit design or details about physical implementations is provided. In Ref. [Wang10], a Mølmer-Sørensen type one-step scheme to generate GHZ states both for flux qubits or charge qubits coupled to a transmission line resonator (TLR) was proposed. A new design of charge and flux qubits is considered, where the qubit-resonator interaction commutes with the free Hamiltonian of the qubits. They authors show that the time-evolution operator takes the form of a Mølmer-Sørensen gate at stroboscopic times. The procedure is independent of the initial state of the resonator and works in the presence of multiple low-excitation modes. However, higher excitation modes of the resonator will introduce inhomogeneity because of the shorter wavelengths of the higher modes and decrease the GHZ fidelity. Moreover, uncontrolled dissipation might be coupled through the higher excitation modes and induce extra noise. It would be ideal to devise a GHZ generation scheme that, while keeping the one-step, deterministic nature, would involve only a single mode of the quantum bus mediating the qubit interaction.

In the following, we consider a circuit QED architecture with weakly anharmonic transmon qubits capacitively coupled to a single quantized mode of the field inside a microwave cavity. In the dispersive regime, the system is characterized by an effective qubit-qubit exchange interactions of the XY type, mediated by virtual excitations of the resonator. We show that the time evolution of the system is described by an effective Hamiltonian that allows a direct implementation of the Mølmer-Sørensen idea. This one-step deterministic generation protocol of GHZ states could potentially be implemented in the currently available circuit QED design.

3.2 Fully connected network of transmon qubits in the dispersive limit

We consider the superconducting circuit made of N transmon qubits capacitively coupled to a microwave cavity, for instance a TLR coupled at both ends to input and output lines as depicted in Fig. 2.12. In the dispersive regime, the resonator acts a quantum

bus, mediating interaction between the qubits. We derive an effective Hamiltonian for the system that exhibits the appropriate XY exchange interaction.

The properties of superconducting transmon qubits have been discussed in Sec. 2.4.5. We start by recalling their main features. Transmon qubits consist of a superconducting island connected to a superconducting electrode through a Josephson tunnel junction with capacitance C_J and an extra shunting capacitance C_B. A gate voltage V_g is applied to the island via a gate capacitance C_g, yielding to the definition of the dimensionless gate charge $n_g = C_g V_g/(2e)$. The system is characterized by the charging energy $E_C = e^2/(2C_\Sigma)$, where $C_\Sigma = C_g + C_J + C_B$ is the total capacitance of the island, and E_J is the Josephson energy of the tunnel junction.

Such Josephson junction based qubits behave effectively as quantum two-level systems in different regimes, categorized by the ratio E_J/E_C. We will focus on the so-called transmon regime, when $E_J/E_C \sim 50 - 100$. The Hamiltonian of a single transmon qubit has the form

$$\hat{H}_q = 4E_C(\hat{n} - n_g)^2 - E_J \cos\hat{\phi}\,. \tag{3.8}$$

In the following we assume that the Josephson junctions form a dc-SQUID i.e., E_J is tunable by an external applied magnetic flux Φ_{ext} allowing us to control independently the frequency of each qubit. In this case, $C_\Sigma = C_g + 2C_J^{(1)} + C_B$ and $E_J = 2\tilde{E}_J \cos(\pi\Phi_{\text{ext}}/\Phi_0)$, with $C_J^{(1)}$ and $\tilde{E}_J$ the capacitance and the Josephson energy of a single junction.

If a qubit is capacitively coupled to a superconducting transmission line cavity, C_g is now the capacitance between the superconducting island and the resonator. In that particular situation, the gate voltage involves a dc-part and an extra term depending on the state of the resonator,

$$V_g = V_g^{\text{dc}} + \hat{V}(x). \tag{3.9}$$

Therefore, the interaction with the resonator appears via the gate charge n_g, which implicitly includes the voltage $\hat{V}(x)$. In addition, we assume that each qubit can be controlled separately by microwave pulses applied through the transmission line in order to perform single-qubit quantum-gates.

For simplicity we consider the qubits to be coupled to a single mode of the resonator. This is a reasonable assumption if the qubits are nearly resonant with only one mode. Since higher modes have frequencies that are multiples of the fundamental frequency, we can tune the qubit transition frequencies such that the detuning with respect to one mode of the resonator is one order of magnitude smaller than the detuning to all the other modes. Under these conditions, we can realize the dispersive limit for a single mode of the resonator and neglect the influence of higher modes, as is the case in experiments using one transmon qubit [Bishop09a].

For instance, the qubits could be mainly coupled to the second mode if they are placed near the ends or the center of the resonator, that is, the positions where the electrical field amplitude is maximal. Such a possible geometry is sketched in Fig. 3.1. Following the procedure of canonical quantization of a (quasi-) one-dimensional superconducting resonator, the voltage across the resonator for this made is given by

$$\hat{V}(x) = \sqrt{\frac{\hbar\omega_r}{L_0 c}} \cos\left(\frac{2\pi x}{L_0}\right)\left(\hat{a} + \hat{a}^\dagger\right). \tag{3.10}$$

The length of the resonator is L_0 and its resonance frequency $\omega_r = 2\pi/\sqrt{L_0^2 lc}$ depends on its capacity c and inductance l per unit length. The position along the resonator is

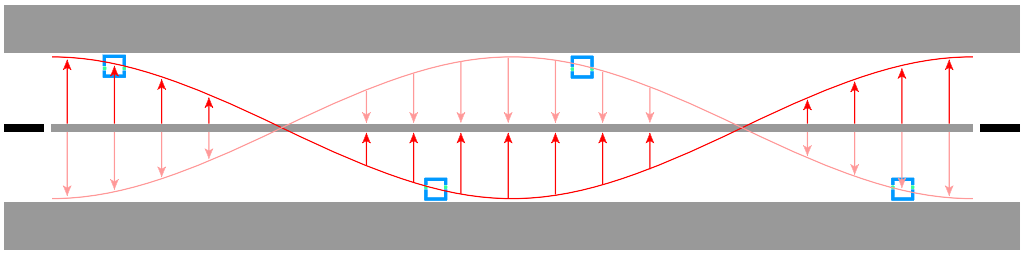

Figure 3.1: Sketch of a possible coplanar geometry for the proposed device with $N = 4$ qubits. Qubits (small blue squares) are placed around the maxima of the electrical field amplitude (red line), i.e., near the center and the ends of the one-dimensional resonator (gray strip). The second mode of the electrical field (red arrows) mediates the qubit-qubit interaction. Input and output ports of the resonator are drawn in black.

denoted by $x \in [-L_0/2, L_0/2]$, and $\hat{a}(\hat{a}^\dagger)$ represent bosonic annihilation (creation) field operators.

The system, composed of the resonator and N transmon qubits, can be described with a generalized Tavis-Cummings Hamiltonian, which is the Jaynes-Cummings given in Eq. (2.165), extended to more than one qubit. This Hamiltonian is expressed on the basis of transmon eigenstates $|j_q\rangle$, where the indices q label the transmon qubits,

$$\hat{H} = \hbar\omega_r \hat{a}^\dagger \hat{a} + \sum_{q=1}^{N} \sum_{j} \left[\hbar\omega_j^{(q)} |j_q\rangle\langle j_q| + \hbar g_j^{(q)} \left(\hat{a} \left| (j+1)_q \right\rangle\langle j_q| + \hat{a}^\dagger \left| j_q \right\rangle\langle (j+1)_q| \right) \right]. \quad (3.11)$$

The qubits frequencies $\omega_j^{(q)}$ are presumed to be tunable through external magnetic fields $\Phi_{\text{ext}}^{(q)}$, changing the effective Josephson energies of the qubits $E_J^{(q)} = 2\tilde{E}_J^{(q)} \cos(\pi\Phi_{\text{ext}}^{(q)}/\Phi_0)$, and the coupling frequencies $g_j^{(q)}$ depend on the position of the qubits. Invoking the rotating-wave approximation, we have neglected rapidly oscillating terms. In the transmon regime, we can only keep transmon-resonator coupling coefficients for neighboring levels, since terms like $|i_q\rangle\langle j_q|$ for $|i-j| > 1$ are comparatively small. Moreover, in the large E_J/E_C limit, an asymptotic expression has been be obtained for $\omega_j^{(q)}$ and $g_j^{(q)}$ in first-order perturbation theory,

$$\omega_j^{(q)} \simeq \frac{1}{\hbar}\sqrt{8E_C^{(q)}E_J^{(q)}}\left(j+\frac{1}{2}\right) - \frac{E_C^{(q)}}{12\hbar}(6j^2+6j+3), \quad (3.12a)$$

$$g_j^{(q)} \simeq g_0^{(q)}\sqrt{j+1}\cos\left(\frac{2\pi x_q}{L_0}\right), \quad (3.12b)$$

$$g_0^{(q)} \simeq \sqrt{\frac{\omega_r}{\hbar L_0 c}}\frac{eC_g^{(q)}}{C_\Sigma^{(q)}}\left(\frac{E_J^{(q)}}{2E_C^{(q)}}\right)^{1/4}. \quad (3.12c)$$

This form of the coupling frequencies $g_j^{(q)}$ describes the situation shown in Fig. 3.1. The amplitudes of these coupling coefficients $g_j^{(q)}$ can be assumed to be approximately homogeneous if the positions x_q of the qubits satisfy $|x_q/L_0| \simeq 0$ or $1/2$, since the electrical field amplitude decreases quadratically with the distance from its maxima and since the size of the qubits is typically much smaller than the resonator wavelength in realistic systems. However, even if they are close to the center or the ends of the resonator, the

qubits should be placed sufficiently far apart to reduce direct inductive or capacitive qubit-qubit coupling. There are also other positions in which the qubits can be placed (e.g. nodes of higher modes). However, the homogeneity of the coupling constants is important in our approach and should be taken care of.

In the so-called dispersive regime $|g_j^{(q)}/\Delta_{j,j+1}^{(q)}| \ll 1$, when transition frequencies of the transmon qubits $\omega_{j,j+1}^{(q)}$ are detuned from the resonator frequency ω_r, excitations of the resonator are virtual and the latter will rather act as a quantum bus mediating effective qubit-qubit interactions. The transition frequencies of the transmon qubits are defined as $\omega_{j,j+1}^{(q)} = \omega_{j+1}^{(q)} - \omega_j^{(q)}$ and their respective detuning as $\Delta_{j,j+1}^{(q)} = \omega_{j,j+1}^{(q)} - \omega_r$. In this regime, eliminating the direct interaction between resonator and transmon qubits to lowest order in $g_j^{(q)}/\Delta_{j,j+1}^{(q)}$, we exhibit an effective qubit-qubit interaction. This can be seen by performing the canonical transformation $e^{\hat{S}}\hat{H}e^{\hat{S}^\dagger}$, where

$$\hat{S} = \sum_{q=1}^{N}\sum_{j}\frac{g_j^{(q)}}{\Delta_{j,j+1}^{(q)}}\left(\hat{a}\,|(j+1)_q\rangle\langle j_q| - \hat{a}^\dagger\,|j_q\rangle\langle(j+1)_q|\right). \tag{3.13}$$

Keeping terms up to second order in $g_j/\Delta_{j,j+1}$, we obtain.

$$\begin{aligned}
\hat{U}\hat{H}\hat{U}^\dagger \simeq \hbar\left(\omega_r + \sum_{q=1}^{N}\left[-\chi_0^{(q)}|0_q\rangle\langle 0_q| + \sum_{j\geq 1}\left(\chi_{j-1}^{(q)} - \chi_j^{(q)}\right)|j_q\rangle\langle j_q|\right]\right)\hat{a}^\dagger\hat{a} \\
+ \sum_{q=1}^{N}\left[\hbar\omega_0^{(q)}|0_q\rangle\langle 0_q| + \sum_{j\geq 1}\hbar\left(\omega_j^{(q)} + \chi_{j-1}^{(q)}\right)|j_q\rangle\langle j_q|\right] \\
+ \sum_{q=1}^{N}\sum_{j}\hbar\eta_j^{(q)}\left(\hat{a}^2|(j+2)_q\rangle\langle j_q| + \hat{a}^{\dagger 2}|j_q\rangle\langle(j+2)_q|\right) \\
+ \sum_{q\neq q'}\sum_{j,j'}\frac{\hbar\tilde{g}_{jj'}^{(qq')}}{2}\Big(\left|(j+1)_q, j'_{q'}\right\rangle\left\langle j_q, (j'+1)_{q'}\right| \\
+ \left|j_q, (j'+1)_{q'}\right\rangle\left\langle (j+1)_q, j'_{q'}\right|\Big).
\end{aligned} \tag{3.14}$$

Here the dispersive shifts $\chi_j^{(q)}$, the two-photon transition rates $\eta_j^{(q)}$, and the effective qubit-qubit coupling coefficient $\tilde{g}_{jj'}^{(qq')}$ are given by

$$\chi_j^{(q)} = \frac{\left(g_j^{(q)}\right)^2}{\Delta_{j,j+1}^{(q)}}, \tag{3.15}$$

$$\eta_j^{(q)} = \frac{1}{2}\frac{g_j^{(q)}g_{j+1}^{(q)}}{\Delta_{j,j+1}^{(q)}\Delta_{j+1,j+2}^{(q)}}\left(\omega_{j,j+1}^{(q)} - \omega_{j+1,j+2}^{(q)}\right), \tag{3.16}$$

$$\tilde{g}_{jj'}^{(qq')} = g_j^{(q)}g_{j'}^{(q')}\frac{\Delta_{j,j+1}^{(q)} + \Delta_{j',j'+1}^{(q')}}{2\Delta_{j,j+1}^{(q)}\Delta_{j',j'+1}^{(q')}}. \tag{3.17}$$

Two-photon transitions can be safely neglected since the parameters $\eta_j^{(q)}$ are small in the dispersive regime.[1] An effective Hamiltonian $\hat{H}_{\text{eff}}$ is now obtained by restricting our

[1] see Appendix A.2

Hilbert space to the computational subspace, that is the first two levels of each transmon qubit. In principle, the qubit-qubit interaction couples any states of the qubits with more than one excitation to states that do not belong to the computational subspace (e.g. for $N = 3$, the state $|110\rangle$ or $|111\rangle$ will be coupled to $|020\rangle$ or $|021\rangle$). However, the amplitudes for these mixing processes of computational states with such non-computational states are of order $g^2/(E_C\Delta)$ and will be neglected for the moment.[2] (This effect will be investigated in Sec. 3.5.4.) Under these conditions,

$$\hat{H}_{\text{eff}} = \hbar\left(\omega + \sum_q \chi^{(q)}\sigma_z^{(q)}\right) a^\dagger a + \sum_q \frac{\hbar\tilde{\omega}_{01}^{(q)}}{2}\sigma_z^{(q)} + \sum_{q,q'} \frac{\hbar\tilde{g}_{00}^{(qq')}}{4}\left(\sigma_x^{(q)}\sigma_x^{(q')} + \sigma_y^{(q)}\sigma_y^{(q')}\right), \tag{3.18}$$

where the ac-Stark shifts are $\chi^{(q)} = \chi_0^{(q)} - \chi_1^{(q)}/2$, and we introduce Lamb-shifted resonator and qubit frequencies $\omega = \omega_r - \sum_q \chi_1^{(q)}/2$ and $\tilde{\omega}_{01}^{(q)} = \omega_{01}^{(q)} + \chi_0^{(q)}$. The single-qubit Pauli matrices $\sigma^{(q)}$ are expressed in terms of computational transmon eigenstates, see Eq. (2.160).

The Hamiltonian $\hat{H}_{\text{eff}}$ has the desired XY-form, provided that all qubits have identical parameters: that is all qubit and coupling frequencies are homogeneous, $\tilde{\omega}_{01}^{(q)} = \Omega$, $|g_0^{(q)}| = g$, $\Delta_0^{(q)} = \Delta$, and $\tilde{g}_{00}^{(qq')} = \chi_0^{(q)} = \tilde{g} = g^2/\Delta$. Using Eq. (3.12), we infer that $\chi^{(q)} = \chi = -\tilde{g}E_C/(\Delta - E_C) < \tilde{g}$, where $E_C = \omega_{01} - \omega_{12}$ is the weak anharmonicity of the transmon qubits. As mentioned earlier, in Eq. (3.12) the qubit transition frequencies can be made homogeneous by tuning the flux biases $\Phi_{\text{ext}}^{(q)}$. From now on we assume the $g_j^{(q)}$ are homogeneous. This is motivated by a promising new transmon architectures with tunable coupling that has been proposed recently [Srinivasan11, Hoffman11a]. Inhomogeneous coupling constants will be discussed in Sec. 3.5.3.

Previous GHZ state generation protocols based on homodyne measurement of the transmission line neglected the effective exchange interaction because of the large differences in qubit frequencies [Helmer09, Hutchison09, Bishop09b]. In our case, the qubit frequencies $\omega_{01}^{(q)}$ are tuned to be identical using the flux biases, and this effective interaction plays a significant role in the generation of the GHZ state in a one-step procedure, as shown below.

If the qubit and coupling frequencies are homogeneous, the total spin operators

$$\hat{J}_i = \frac{1}{2}\sum_{q=1}^{N}\sigma_i^{(q)}, \qquad (i = x, y, z), \tag{3.19}$$

and their corresponding Casimir operator $\hat{J}^2 = \hat{J}_x^2 + \hat{J}_y^2 + \hat{J}_z^2$ can be used to write the effective Hamiltonian in a very convenient form,

$$\hat{H}_{\text{eff}} = \hbar\omega\hat{a}^\dagger\hat{a} + \hbar\tilde{g}\,\hat{J}^2 + \hbar(\Omega + 2\chi\hat{a}^\dagger\hat{a})\hat{J}_z - \hbar\tilde{g}\,\hat{J}_z^2. \tag{3.20}$$

Evidently, $\hat{H}_{\text{eff}}$ is diagonal in the basis $|J, J_z\rangle \otimes |n\rangle$, where $|n\rangle$ denotes a state of the resonator containing n excitations and the state $|J, J_z\rangle$, describing a state of the N qubits, is an eigenstate of the operators $\hat{J}^2$ and $\hat{J}_z$ with respective eigenvalues $J(J+1)$ and J_z. Since $[\hat{H}, \hat{J}^2] = 0$, any eigenstates of $\hat{J}^2$ will remain so under the action of this Hamiltonian. In the following, we will restrict ourselves to such states with $J = N/2$. For

[2] This can be seen by applying perturbation theory in $\tilde{g}_{jj'}^{(qq')}$ for $|j - j'| > 1$ to Eq. (3.14) [Koch11].

example states with all spins aligned in a particular direction belong to this type and are therefore an appropriate choice for the initial state. Setting $J = N/2$ in what follows, we denote $|J{=}N/2, J_z\rangle$ by $|J_z\rangle$. Thus, the eigenstates of $\hat{H}_{\text{eff}}$ are $|J_z\rangle \otimes |n\rangle$ with eigenvalues

$$E_{J_z,n} = \hbar\omega n + \hbar\tilde{g}\left(\frac{N}{2}+1\right)\frac{N}{2} + \hbar(\Omega + 2\chi n)J_z - \hbar\tilde{g}J_z^2. \tag{3.21}$$

3.3 Protocol for generating GHZ states

The effective Hamiltonian $\hat{H}_{\text{eff}}$ allows us to produce GHZ states by turning on the interaction for a definite duration t_{GHZ}. It was shown in Refs. [Mølmer99, Sørensen00] that a Hamiltonian of the type $\hbar\tilde{g}\hat{J}_x^2$ will produce a GHZ state after the time $\pi/(2\tilde{g})$, starting, for instance, from the fully separable state $|0\ldots0\rangle$. The multi-qubit gate $\exp(i\pi\hat{J}_x^2/2)$ is sometimes referred to as the Mølmer-Sørensen gate.

We conveniently choose an initial state with all the qubits aligned in the same direction, that is, the maximal superposition state

$$|\psi_0\rangle = \bigotimes_{q=1}^{N} \frac{|0_q\rangle + |1_q\rangle}{\sqrt{2}}. \tag{3.22}$$

We assume that the qubits and the resonator are initially in a product state and the state of the resonator at $t = 0$ is denoted ρ_{res},

$$\rho(t{=}0) = |\psi_0\rangle\langle\psi_0| \otimes \rho_{\text{res}}. \tag{3.23}$$

Moreover, $|\psi_0\rangle = |J_x{=}N/2\rangle$ and can be expressed as a linear superposition of the states $|J_z\rangle$,

$$|\psi_0\rangle = \frac{1}{\sqrt{2^N}}\sum_{k=0}^{N}\sqrt{\tbinom{N}{k}}\,|J_z{=}k{-}N/2\rangle. \tag{3.24}$$

where $\binom{N}{k}$ is a binomial coefficient.[3]

We define $\rho(t)$ as the density matrix evolving under the action of the time-evolution operator $U(t) = \exp(-i\hat{H}_{\text{eff}}t/\hbar)$, where $\hat{H}_{\text{eff}}$ is the effective Hamiltonian Eq. (3.20),

$$\rho(t) = U(t)\,\rho(t{=}0)\,U^\dagger(t). \tag{3.25}$$

We assumed that $g/\Delta \ll 1$ and therefore we have neglected the effect of the canonical transformation $e^{\hat{S}}$ on the state vector. This turns out to be particularly useful, since $U(t)$ is diagonal in the basis $|n\rangle$, thus we can describe directly the time evolution of the reduced density matrix of the qubits $\rho_{\text{qb}}(t)$, obtained by tracing over the resonator state,

$$\rho_{\text{qb}}(t) = \frac{1}{2^N}\sum_{n,k,k'}\langle n|\rho_{\text{res}}|n\rangle\sqrt{\tbinom{N}{k}\tbinom{N}{k'}}e^{-i[\varphi_{k,n}(t)-\varphi_{k',n}(t)]}|J_z{=}k{-}N/2\rangle\langle J_z{=}k'{-}N/2|, \tag{3.26}$$

where $\varphi_{k,n}(t) = k\,(\Omega t + 2\chi tn + \tilde{g}t(N-k))$.

The GHZ states we aim to produce are of the following form:

$$|\text{GHZ}^{\pm}\rangle = \frac{1}{\sqrt{2}}\left(\bigotimes_{q=1}^{N}\frac{|0_q\rangle + |1_q\rangle}{\sqrt{2}} \pm i\bigotimes_{q=1}^{N}\frac{|0_q\rangle - |1_q\rangle}{\sqrt{2}}\right), \tag{3.27}$$

[3] Details about such decomposition can be found in Appendix B.

which are standard GHZ states up to single-qubit rotations. These states can be expressed as a linear superposition of the states $|J_z\rangle$ as well,[3]

$$|\mathrm{GHZ}^{\pm}\rangle = \sum_{k=0}^{N} \frac{1 \pm i\, e^{i\pi k}}{\sqrt{2^N}\sqrt{2}} \sqrt{\tbinom{N}{k}} |J_z = k - N/2\rangle. \tag{3.28}$$

To see why a GHZ state is produced after some time t_{GHZ}, we consider the effects of either $\exp(i\tilde{g}t\hat{J}_z^2)$ or $\exp[i\tilde{g}t(\hat{J}_z^2 - \hat{J}_z)]$ (for N either even or odd) on the state $|J_z = k - N/2\rangle$. We establish that one of the two possible GHZ states Eq. (3.27) is produced when $\tilde{g}t = \pi/2$ by noticing that

$$\frac{1 + ie^{i\pi(k+\frac{N}{2}-1)}}{\sqrt{2}} = e^{-i\frac{\pi}{4} + i\frac{\pi}{2}(k-\frac{N}{2})^2}, \qquad (N \text{ even}), \tag{3.29}$$

$$\frac{1 + ie^{i\pi(k+\frac{N-1}{2})}}{\sqrt{2}} = e^{-i\frac{\pi}{8} + i\frac{\pi}{2}\left[(k-\frac{N}{2})^2 - (k-\frac{N}{2})\right]}, \qquad (N \text{ odd}). \tag{3.30}$$

The shortest preparation time is

$$t_{\mathrm{GHZ}} = \frac{\pi}{2\tilde{g}}, \tag{3.31}$$

but a GHZ state is produced for every odd multiple of time t_{GHZ}.

However, the remaining term of the effective Hamiltonian in Eq. (3.20), the one that is proportional to $\hat{J}_z$, induces a collective rotation of the final state. The rotation angle depends again on N and the state of the resonator. The state $\rho_{\mathrm{qb}}(t_{\mathrm{GHZ}})$ is,

$$\rho_{\mathrm{qb}}(t_{\mathrm{GHZ}}) = \sum_n \langle n|\rho_{\mathrm{res}}|n\rangle \, \big|\mathrm{GHZ}(\alpha_n)\big\rangle\big\langle\mathrm{GHZ}(\alpha_n)\big|. \tag{3.32}$$

Here,

$$\big|\mathrm{GHZ}(\alpha)\big\rangle = e^{-i\alpha\hat{J}_z} \frac{1}{\sqrt{2}} \left(\bigotimes_{q=1}^{N} \frac{|0_q\rangle + |1_q\rangle}{\sqrt{2}} + e^{i\pi\frac{N-1}{2}} \bigotimes_{q=1}^{N} \frac{|0_q\rangle - |1_q\rangle}{\sqrt{2}} \right), \tag{3.33}$$

and $2\alpha_n/\pi = (\Omega + 2n\chi)/\tilde{g}$ for N even. For N odd, $2\alpha_n/\pi = (\Omega + 2n\chi)/\tilde{g} - 1$, and the relative phase $\exp(i\pi(N-1)/2)$ in Eq. (3.33) is changed to $\exp(i\pi N/2)$.

We notice that the produced states $\rho(t_{\mathrm{GHZ}})$ is not exactly the state depicted in Eq. (3.27), and therefore certain constraints on the angles α_n in Eq. (3.32) are required to generate the proper state $|\mathrm{GHZ}^+\rangle$. At low temperature, only the ground state of the resonator is significantly populated and $\langle 0|\rho_{\mathrm{res}}|0\rangle \gg \langle n|\rho_{\mathrm{res}}|n\rangle$ for $n \geq 1$. Thus we can restrict our considerations to $\alpha_{n=0}$, and this translates to some condition on the ratio $\Omega/\tilde{g}$.

To illustrate this, we consider the resonator to be initially in its ground state $\rho_{\mathrm{res}} = |0\rangle\langle 0|$. The state $|\mathrm{GHZ}^+\rangle$ is indeed produced at t_{GHZ}, provided we can tune the frequencies Ω and $\tilde{g}$ such that

$$\frac{\Omega}{\tilde{g}} = 4m + 2 - N\,, \qquad m \in \mathbb{Z}\,. \tag{3.34}$$

If the above condition cannot be satisfied, some correcting pulse $\exp(i\delta_N\hat{J}_z)$ can be applied to the final state $\rho_{\mathrm{qb}}(t_{\mathrm{GHZ}})$ to obtain a proper $|\mathrm{GHZ}^+\rangle$ state. The appropriate pulse length δ_N depends on N and the ratio $\Omega/\tilde{g}$,

$$\delta_N = \frac{\pi}{2}\left[\left(\frac{\Omega}{\tilde{g}} + N - 2\right) \bmod 4\right]. \tag{3.35}$$

Furthermore, $\delta_N = 0$ implies Eq. (3.34).

If not only the ground state of the resonator is populated, higher photon numbers n produce rotated GHZ states, according to Eq. (3.32). We notice that

$$\langle \mathrm{GHZ}(\alpha_n)|\mathrm{GHZ}(\alpha_{n+k})\rangle = \cos^N\left(\frac{k\pi\chi}{2\tilde{g}}\right), \tag{3.36}$$

which means that if a $|\mathrm{GHZ}^+\rangle$ state is produced for excitation number n, a slightly rotated state $\exp(-i\pi\chi\hat{J}_z/\tilde{g})|\mathrm{GHZ}^+\rangle$ is produced for $n+1$ (since $\chi < \tilde{g}$). Assuming some correcting pulse $\exp(i\delta_N\hat{J}_z)$ has been applied, the reduced density matrix of the qubits ρ_{qb} is a mixture of rotated GHZ states with classical probabilities depending only on the initial state of the resonator,

$$\begin{aligned} &e^{i\delta_N\hat{J}_z}\rho_{\mathrm{qb}}(t_{\mathrm{GHZ}})e^{-i\delta_N\hat{J}_z} \\ &= \langle 0|\rho_{\mathrm{res}}|0\rangle|\mathrm{GHZ}^+\rangle\langle\mathrm{GHZ}^+| + \sum_{n>0}\langle n|\rho_{\mathrm{res}}|n\rangle e^{-i\pi n\frac{\chi}{\tilde{g}}\hat{J}_z}|\mathrm{GHZ}^+\rangle\langle\mathrm{GHZ}^+|e^{i\pi n\frac{\chi}{\tilde{g}}\hat{J}_z}\,. \end{aligned} \tag{3.37}$$

We will now show that it is possible to choose realistic physical parameters in agreement with our assumptions. We use parameters from a setup involving four transmon qubits [DiCarlo10], where the qubits have frequencies $\Omega/2\pi$ that are tunable in the range 6-11 GHz, the coplanar waveguide resonators (the quantum bus) has a frequency $\omega/2\pi \simeq 9$ GHz, the transmon-resonator coupling frequencies are $g/2\pi \simeq 220$ MHz. Detuning the qubits from the resonator such that $g/\Delta \simeq 1/10$ would lead to an effective qubit-qubit coupling $\tilde{g} = 22$ MHz and to a preparation time t_{GHZ} of approximately 11 ns, which is approximately 1 % of the dephasing time of the qubits.

3.4 Measuring the generated GHZ states

3.4.1 Bell-Mermin operator

The question of detecting and probing the states generated in our scheme naturally arises. For $N \geq 4$, there is no unique way to quantify entanglement. We will focus on a measurement of the Bell-Mermin operator [Mermin90a] defined as

$$\begin{aligned} \hat{B} &= \frac{e^{i\pi N}}{2i}\left[\bigotimes_{q=1}^{N}\left(\sigma_z^{(q)} - i\sigma_y^{(q)}\right) - \bigotimes_{q=1}^{N}\left(\sigma_z^{(q)} + i\sigma_y^{(q)}\right)\right] \\ &= 2^{N-1}\left(|\mathrm{GHZ}^+\rangle\langle\mathrm{GHZ}^+| - |\mathrm{GHZ}^-\rangle\langle\mathrm{GHZ}^-|\right), \end{aligned} \tag{3.38}$$

whose expectation value for N-qubit quantum states is bounded by $|\langle\hat{B}\rangle| \leq 2^{N-1}$, and the extremal values $\pm 2^{N-1}$ are reached for the states $|\mathrm{GHZ}^\pm\rangle$. The maximal value predicted by local hidden-variable theory is $\sqrt{2^N}$ ($\sqrt{2^{N-1}}$) for N even (odd)[Mermin90a], leading to an exponentially increasing violation for the states $|\mathrm{GHZ}^\pm\rangle$ with N, the number of qubits. Therefore, a measurement of the Bell-Mermin operator leading to a result greater than $\sqrt{2^N}$ ($\sqrt{2^{N-1}}$) indicates the non-local nature of the generated quantum states.

Detection scheme

The Bell-Mermin operator expectation value can, in principle, be obtained experimentally but it is in general not amenable to a direct measurement. This operator can be expressed

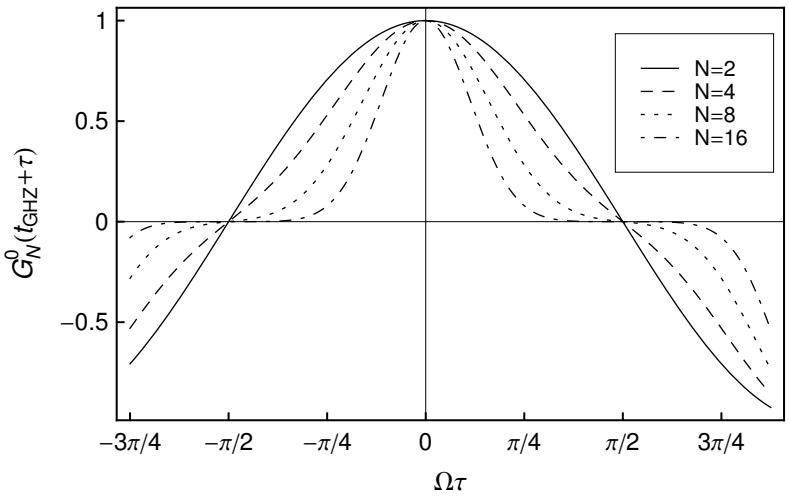

Figure 3.2: Behavior of the function $G_N^0(t_{\mathrm{GHZ}}+\tau)$ for different N, assuming for simplicity that $\delta_N = 0$.

as a sum of parity operators, which are more easily accessible by experiment, and inferring its expectation value would require 2^{N-1} parity measurements,

$$\langle \hat{B} \rangle = \sum_{l=1\,(\mathrm{odd})}^{N} \sum_{p} (-1)^{N-\frac{l+1}{2}} \left\langle \bigotimes_{q=1}^{N-l} \sigma_z^{p(q)} \bigotimes_{q'=N-l+1}^{N} \sigma_y^{p(q')} \right\rangle . \tag{3.39}$$

For each term, l is the number of factors σ_y and $\sum_p$ stands for the sum over the $\binom{N}{l}$ permutations p that give distinct products. The states $|\mathrm{GHZ}^{\pm}\rangle$ defined in Eq. (3.27) are those that give exactly ± 1 for each of the 2^{N-1} terms.

There are, therefore, 2^{N-1} parity measurements to realize which is possible only if one is able to generate GHZ states with high accuracy in a repeated way. Following Ref. [Hutchison09], these parity operators could be measured by dispersive readout. Since the resonator frequency is Stark-shifted, $\omega \to \omega + 2\chi \hat{J}_z$, it is possible to access the value of the operator $\hat{J}_z$. The value of the parity operator $\bigotimes_q \sigma_z^{(q)}$ can then be unambiguously deduced from $J_z = \langle \hat{J}_z \rangle$,

$$\left\langle \bigotimes_{q=1}^{N} \sigma_z^{(q)} \right\rangle = (-1)^{\frac{N}{2}-J_z} . \tag{3.40}$$

Hence, we can measure all the needed parities by rotating the operators $\sigma_y^{(q)}$ appearing in Eq. (3.39) to $\sigma_z^{(q)}$ using single-qubit rotations.

Time evolution of the Bell-Mermin operator

By means of Eq. (3.26), we can give an expression for the time evolution of the expectation value of the Bell-Mermin operator, $\langle \hat{B}(t) \rangle = \mathrm{Tr}\left[\hat{B}\rho_{\mathrm{qb}}(t)\right]$. For this purpose, we can express the matrix elements of $\hat{B}$ in the basis of the states $|J_z\rangle$, which diagonalizes the effective Hamiltonian,

$$\hat{B} = \sum_{k,k'=0}^{N} b_{k,k'} \, |J_z = k' - N/2\rangle\langle J_z = k - N/2| \, , \tag{3.41}$$

where

$$b_{k,k'} = \frac{1}{2i}\sqrt{\binom{N}{k}\binom{N}{k'}}\left[(-1)^k - (-1)^{k'}\right] . \tag{3.42}$$

Hence, $\langle \hat{B}(t)\rangle$ can be expressed as a sum of oscillating functions G_N^n, indexed by the photon number n,

$$\langle \hat{B}(t)\rangle = 2^{N-1}\sum_{n=0}^{\infty}\langle n|\rho_{\rm res}|n\rangle\; G_N^n(t)\,. \tag{3.43}$$

The functions G_N^n are Fourier series over a finite range of frequencies $\tilde{\omega}_{k,k'}^n$ defined as $\tilde{\omega}_{k,k'}^n = (k-k')\left[(k+k'-N)\tilde{g} - \Omega - 2n\chi\right]$,

$$G_N^n(t) = \sum_{k,k'=0}^{N} a_{k,k'}\sin(\tilde{\omega}_{k,k'}^n t)\,, \tag{3.44}$$

where $a_{k,k'} = 2^{-2N}\binom{N}{k}\binom{N}{k'}[(-1)^k - (-1)^{k'}]$.

Equation (3.43) shows that $\langle \hat{B}(t)\rangle$ is characterized by many oscillations on timescales of the order of $t_{\rm GHZ}$, since the $\tilde{\omega}_{k,k'}^n$ are of the same order as $\Omega \gg \tilde{g}, \chi$. However, the envelope indeed reaches its maximum at $t_{\rm GHZ}$, provided that only the ground state of the resonator is significantly populated. These fast oscillations are the manifestation of local rotations of the qubits, Eqs. (3.32-3.33). We have seen that this issue can be solved equivalently in two different ways and that the state $|{\rm GHZ}^+\rangle$ is indeed generated after $t_{\rm GHZ}$, either by applying some correcting pulse $\exp(i\delta_N \hat{J}_z)$, defined in Eq. (3.35), or by tuning the frequencies Ω and $\tilde{g}$ to satisfy the condition Eq. (3.34). Assuming for simplicity that $\delta_N = 0$, we have then

$$G_N^n(t_{\rm GHZ}) = \cos^{2N}\left(n\frac{\pi}{2}\frac{\chi}{\tilde{g}}\right) - \sin^{2N}\left(n\frac{\pi}{2}\frac{\chi}{\tilde{g}}\right). \tag{3.45}$$

The fast oscillations of $\langle \hat{B}(t)\rangle$ around $t_{\rm GHZ}$ become sharper as the number of qubits N increases, as shown in Fig. 3.2. In the simpler case $\delta_N = 0$, the behavior of G_N^0 around $t_{\rm GHZ}$ is given by

$$G_N^0(t_{\rm GHZ} + \tau) \simeq 1 - \tau^2\frac{N\Omega^2}{4}, \quad |\tau| \ll \frac{1}{\Omega}\,, \tag{3.46}$$

and that also means that we need a higher precision, for larger N, in controlling either the protocol time $t_{\rm GHZ}$ or the correcting pulse.

3.4.2 Detection of genuine N-partite entanglement

Other bounds than those predicted by local-hidden variable theory can actually be derived for the expectation value Bell-Mermin operator. For instance, it can easily be shown that any fully separable state ρ^S satisfies $|{\rm Tr}(\rho^S \hat{B})| \leq 1$. A significant bound can also be derived if the state is m-separable, i.e., describes a system that is partitioned in m subsystems that only share classical correlations. In other words, a pure state is called m-separable, for $1 < m \leq N$, if it can be written as a product of m states,

$$|\psi^{(m)}\rangle = \bigotimes_{i=1}^{m}|\psi_i\rangle_{P_i}, \tag{3.47}$$

where the $\{P_i\}$ describe a partition of the N qubits. Thus, a fully separable state in the traditional sense is N-separable. A mixed m-separable state $\rho^{(m)}$ is defined as a convex

sum of pure m-separable states, which might belong to different partitions [Gühne09]. Such an m-separable state satisfies

$$\mathrm{Tr}\left[\rho^{(m)}\hat{B}\right] \leq 2^{N-m}. \tag{3.48}$$

Thus, any measurement of the operator $\hat{B}$ with outcome above 2^{N-2} indicates that the state is not even biseparable (2-separable) and demonstrates the existence of genuine N-partite entanglement.

We now provide a derivation of the inequality Eq. (3.48). For this purpose, we define two distinct Bell-Mermin operators

$$\hat{M}_{\mathcal{S}_k} = 2^{k-1} i \left(\bigotimes_{q\in\mathcal{S}_k} |0_q\rangle\langle 1_q| - \bigotimes_{q\in\mathcal{S}_k} |1_q\rangle\langle 0_q| \right) \tag{3.49a}$$

$$\hat{M}'_{\mathcal{S}_k} = 2^{k-1} \left(\bigotimes_{q\in\mathcal{S}_k} |0_q\rangle\langle 1_q| + \bigotimes_{q\in\mathcal{S}_k} |1_q\rangle\langle 0_q| \right) \tag{3.49b}$$

that act on an arbitrary subset, denoted by $\mathcal{S}_k$, of k among N qubits. We denote the complementary subset of size $N-k$ by $\bar{\mathcal{S}}_k$. The Bell-Mermin operator acting on the complete set $\mathcal{S}_N$ can then be expressed as

$$\hat{M}_{\mathcal{S}_N} = \hat{M}_{\mathcal{S}_k}\hat{M}'_{\bar{\mathcal{S}}_k} + \hat{M}'_{\mathcal{S}_k}\hat{M}_{\bar{\mathcal{S}}_k}, \qquad (\forall\, 0 \leq k \leq N). \tag{3.50}$$

Importantly, this definition does not depend on the choice of the subset $\mathcal{S}_k$, neither on its size. One can easily verify that the operator $\hat{M}_{\mathcal{S}_N}$ is equivalent, up to local rotations of the qubit basis, to the operator $\hat{B}$ given in Eq. (3.38).[4] The subsets $\mathcal{S}_k$ and $\bar{\mathcal{S}}_k$ define a partition of the N qubits. Without loss of generality, we can partition the N qubit in a simple way, i.e., the subset $\mathcal{S}_k$ contains the qubits $q = 1, \ldots, k$ and $\bar{\mathcal{S}}_k$ the qubits $q = k+1, \ldots, N$.

Any pure biseparable N-qubit state $|\psi^{(2)}\rangle$, where the two subsets $\mathcal{S}_k$ and $\bar{\mathcal{S}}_k$ only share classical correlations, can be written as a product state

$$|\psi^{(2)}\rangle = |\psi_{\mathcal{S}_k}\rangle \otimes |\psi_{\bar{\mathcal{S}}_k}\rangle, \tag{3.51}$$

where $|\psi_{\mathcal{S}_k(\bar{\mathcal{S}}_k)}\rangle$ is a quantum state of k qubits ($N-k$ qubits) which can exhibit an arbitrary degree of entanglement. In addition, we notice that the only non-zero matrix elements of the operators $\hat{M}_{\mathcal{S}}$ and $\hat{M}'_{\mathcal{S}}$ involve states like $|0\ldots0\rangle$ and $|1\ldots1\rangle$. Therefore, we can infer the form of the state $|\psi^{(2)}\rangle$ that maximizes the value of the N-qubit Bell-Mermin operator $\hat{M}_{\mathcal{S}_N}$. It yields

$$|\psi_{\mathcal{S}_k}\rangle = \cos\theta_1 \bigotimes_{q=1}^{k} |0_q\rangle + e^{i\varphi_1}\sin\theta_1 \bigotimes_{q=1}^{k} |1_q\rangle, \tag{3.52a}$$

$$|\psi_{\bar{\mathcal{S}}_k}\rangle = \cos\theta_2 \bigotimes_{q=k+1}^{N} |0_q\rangle + e^{i\varphi_2}\sin\theta_2 \bigotimes_{q=k+1}^{N} |1_q\rangle. \tag{3.52b}$$

[4] The form of the operator $\hat{M}_{\mathcal{S}_N}$ actually corresponds to the one originally presented in Ref. [Mermin90a].

Using the relations

$$\langle\psi_{\mathcal{S}_k}|\hat{M}_{\mathcal{S}_k}|\psi_{\mathcal{S}_k}\rangle = 2^{k-1}\sin(2\theta_1)\cos\varphi_1, \tag{3.53a}$$

$$\langle\psi_{\mathcal{S}_k}|\hat{M}'_{\mathcal{S}_k}|\psi_{\mathcal{S}_k}\rangle = 2^{k-1}\sin(2\theta_1)\sin\varphi_1, \tag{3.53b}$$

we obtain

$$\langle\psi^{(2)}|\hat{M}_{\mathcal{S}_N}|\psi^{(2)}\rangle = 2^{N-2}\sin(2\theta_1)\sin(2\theta_2)\sin(\varphi_1+\varphi_2) < 2^{N-2}. \tag{3.54}$$

Thus, upper and lower bounds of the Bell-Mermin operator expectation value for pure biseparable states are $\pm 2^{N-2}$. The generalization to mixed states is straightforward and we conclude that any state ρ satisfying $|\mathrm{Tr}(\rho\hat{B})| > 2^{N-2}$ exhibits genuine N-partite entanglement.

In addition, we notice that the alternative N-qubit operator $\hat{M}'_{\mathcal{S}_N}$ is

$$\hat{M}'_{\mathcal{S}_N} = \hat{M}'_{\mathcal{S}_k}\hat{M}'_{\bar{\mathcal{S}}_k} - \hat{M}_{\mathcal{S}_k}\hat{M}_{\bar{\mathcal{S}}_k}, \tag{3.55}$$

which yields

$$\langle\psi^{(2)}|\hat{M}'_{\mathcal{S}_N}|\psi^{(2)}\rangle = 2^{N-2}\sin(2\theta_2)\sin(2\theta_2)\cos(\varphi_1+\varphi_2). \tag{3.56}$$

The argument to obtain an inequality for m-separable states, Eq. (3.48), goes as follows: for any partitioning of the N qubits into m subsets $\mathcal{S}_{k_1},\ldots,\mathcal{S}_{k_m}$, we can express the operator $\hat{M}_{\mathcal{S}_N}$ as a sum of 2^{m-1} products of m operators, each acting on the subset $\mathcal{S}_{k_m}$. In the case $m=3$, we have for instance

$$\hat{M}_{\mathcal{S}_N} = \hat{M}_{\mathcal{S}_{k_1}}\hat{M}'_{\mathcal{S}_{k_2}}\hat{M}'_{\mathcal{S}_{k_3}} - \hat{M}_{\mathcal{S}_{k_1}}\hat{M}_{\mathcal{S}_{k_2}}\hat{M}_{\mathcal{S}_{k_3}} + \hat{M}'_{\mathcal{S}_{k_1}}\hat{M}_{\mathcal{S}_{k_2}}\hat{M}'_{\mathcal{S}_{k_3}} + \hat{M}'_{\mathcal{S}_{k_1}}\hat{M}'_{\mathcal{S}_{k_2}}\hat{M}_{\mathcal{S}_{k_3}}, \tag{3.57}$$

where $(\mathcal{S}_{k_1},\mathcal{S}_{k_2},\mathcal{S}_{k_3})$ define a partition of the N qubits in three subsets of size k_1, k_2, and k_3 such that $k_1+k_2+k_3=N$. Using the same argument as before, the m-separable state that maximizes the value of the N-qubit Bell-Mermin operator has the form

$$|\psi^{(m)}\rangle = \bigotimes_{l=1}^{m}|\psi_{\mathcal{S}_{k_l}}\rangle, \tag{3.58}$$

where

$$|\psi_{\mathcal{S}_{k_l}}\rangle = \cos\theta_l \bigotimes_{q\in\mathcal{S}_{k_l}}|0_q\rangle + e^{i\varphi_l}\sin\theta_l \bigotimes_{q\in\mathcal{S}_{k_l}}|1_q\rangle. \tag{3.59}$$

Using such a decomposition of the N-qubit Bell-Mermin operator, one can show that

$$\langle\psi^{(m)}|\hat{M}_{\mathcal{S}_N}|\psi^{(m)}\rangle = 2^{N-m}\sin\left(\sum_{l=1}^{m}\varphi_l\right)\prod_{l=1}^{m}\sin(2\theta_l), \tag{3.60}$$

which, by generalizing to mixed states, proves Eq. (3.48).

Therefore, besides ruling out local-hidden variable theories, the Bell-Mermin operator can be used as an entanglement witness[5] that discriminates m-separable states from states exhibiting genuine $(m+1)$-partite entanglement, in the sense that a result $|\langle\hat{B}\rangle| > 2^{N-m}$ indicates that the state is not m-separable.

[5]Strictly speaking, an entanglement witness is an observable $\hat{W}$ such that $\mathrm{Tr}(\rho^S\hat{W}) \geq 0$ for all separable state ρ^S, and $\mathrm{Tr}(\rho^E\hat{W}) < 0$ for at least one entangled state ρ^E [Gühne09].

3.5 Undesirable effects

We investigate how non-ideal physical parameters might affect the generated state and the efficiency of the protocol. In particular, we study the effects related to a finite dispersive parameter g/Δ and thermal occupation of the resonator mode. We also discuss the consequences of inhomogeneous qubit-resonator coupling. Finally, we address the issue of weak anharmonicity of the transmon qubits.

3.5.1 Finite dispersive parameter g/Δ

The validity of the effective Hamiltonian Eq. (3.20) depends on how small the dispersive parameter g/Δ is. In the strong dispersive regime, when $g \ll \Delta$, the Hamiltonian $\hat{H}_{\text{eff}}$ is an accurate approximation to obtain the dynamics of the system. However the smaller is the parameter g/Δ, the longer it takes to create a GHZ state. Reducing the detuning in order to obtain a GHZ state in a shorter time cannot be done without investigations on how it affects the actual generated state.

To estimate whether our scheme remains valid for finite values of g/Δ, we investigate numerically the coherent dynamics of the system. To limit the effects caused by other types of non-ideal parameters, we assume that all qubits have the same transition frequency, that they couple homogeneously to the resonator, and that the resonator is initially in its ground state. In addition, we neglect the influence of higher transmon levels and truncate the Hamiltonian Eq. (3.11) to the two lowest levels. This should capture the main consequences of a finite dispersive parameter. The consequences of the weak anharmonicity of transmon qubits will be investigated in Sec. 3.5.4.

We consider the time-evolution of the Bell-Mermin operator due to the Hamiltonian

$$\hat{H}' = \hbar\omega_r \hat{a}^\dagger \hat{a} + \hbar\omega_{01} \hat{J}_z + \hbar g \left(\hat{a}\hat{J}_+ + \hat{a}^\dagger \hat{J}_- \right), \tag{3.61}$$

where $\hat{J}_\pm = \hat{J}_x \pm i\hat{J}_y$. In practice, we look at the time-dependent reduced density matrix of the qubits

$$\rho'_{\text{qb}}(t) = \sum_n \langle n | e^{-i\hat{H}'t/\hbar} \left(|\psi_0\rangle\langle\psi_0| \otimes \rho_{\text{res}} \right) e^{i\hat{H}'t/\hbar} | n \rangle. \tag{3.62}$$

The time-evolution of $\text{Tr}[\hat{B}\rho'_{\text{qb}}(t)]$ is characterized by many oscillations, at the qubits frequency, on the timescale t_{GHZ}. We rather consider the value of the operator $\hat{B}$ in a frame rotating at the frequency $\omega_{01} + g^2/\Delta$ (or ω_{01} for N odd), that is

$$\langle \hat{B}'(t) \rangle = \text{Tr}\left[\hat{B} e^{it(\omega_{01}+g^2/\Delta)\hat{J}_z} \rho'_{\text{qb}}(t) e^{-it(\omega_{01}+g^2/\Delta)\hat{J}_z} \right]. \tag{3.63}$$

This equivalently takes account of the correcting pulses that should be applied at $t \simeq t_{\text{GHZ}}$ in order to obtain exactly the state $|\text{GHZ}^+\rangle$ Eq. (3.27).

The value of $\langle \hat{B}'(t) \rangle$, obtained from Eq. (3.63) for $N = 4$ and $|g/\Delta|$ between 0.04 and 1, is shown in Fig. 3.3. The value of g/Δ is changed by tuning the qubits frequency $\omega_{01} = \Delta + \omega_r$ while the resonator frequency ω_r and the coupling strength g are kept constant. As expected, for very small values of the dispersive parameter, $|g/\Delta| < 0.05$, the Bell-Mermin operator is close to its ideal value $\pm 2^{N-1}$ at times close to odd multiple of t_{GHZ}, indicating that a GHZ states is produced. When increasing the dispersive parameter, around $|g/\Delta| \sim 0.1$, we observe that the value of $\langle \hat{B}'(t) \rangle$ is still close to maximal for $t \gtrsim t_{\text{GHZ}}$. The protocol efficiency is obviously affected when the detuning is further

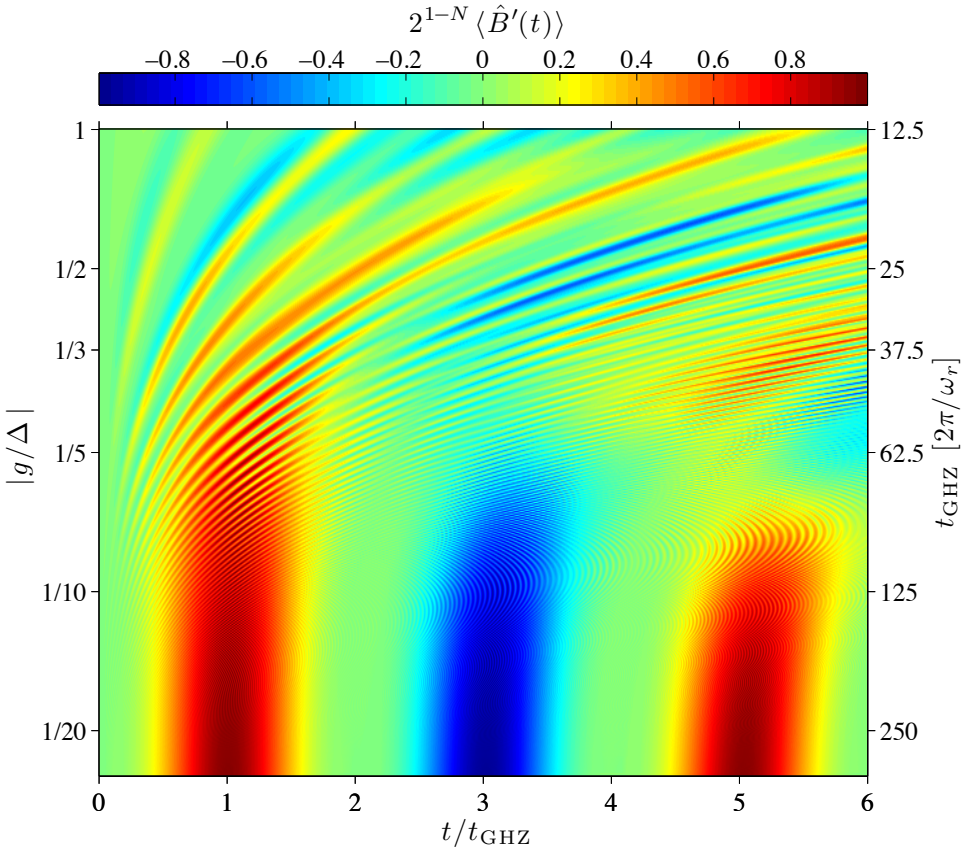

Figure 3.3: Coherent evolution of the Bell-Mermin operator expectation value as a function of the dispersive parameter g/Δ for identical two-level systems dispersively coupled to a common resonator mode. We show the time-evolution of the operator $\hat{B}$ in a frame rotating at the qubit frequency, obtained from Eq. (3.63). The time t (horizontal axis) is normalized for each value of g/Δ by the time t_{GHZ}, whose value is indicated on the right vertical axis. The value of g/Δ is changed by tuning the frequency of the qubits $\omega_{01} = \Delta + \omega_r$, while the resonator frequency ω_r and the coupling strength g are kept constant. The parameters are $N = 4$, $g/\omega_r = 0.02$, and $\Delta < 0$.

reduced. For $|g/\Delta| > 0.1$, additional structures in the time-dependence of $\langle\hat{B}'\rangle$ indicate that the dispersive Hamiltonian Eq. (3.20) is no longer a good approximation to describe the dynamics of the system and that contributions of higher order in g/Δ should be taken into account.

The maximally allowed value of the Bell-Mermin operator, both for biseparable states and according to local-hidden variable theory, is $2^{N/2} = 2^{N-2} = 4$ for $N = 4$. Values of $\langle\hat{B}'(t)\rangle$ above this limit are found for relatively small detuning, $|g/\Delta| \sim 0.3 - 0.5$, and even if we cannot make any conclusive remark about the state of the qubits, the latter clearly exhibits N-partite entanglement and violates local hidden-variable theory.

3.5.2 Thermal occupation of the quantum bus

The maximal value $\langle\hat{B}(t_{\mathrm{GHZ}})\rangle$ can reach also depends on the initial state of the resonator ρ_{res}. Provided the considerations about the ratio $\Omega/\tilde{g}$ or the correcting pulse angle δ_N

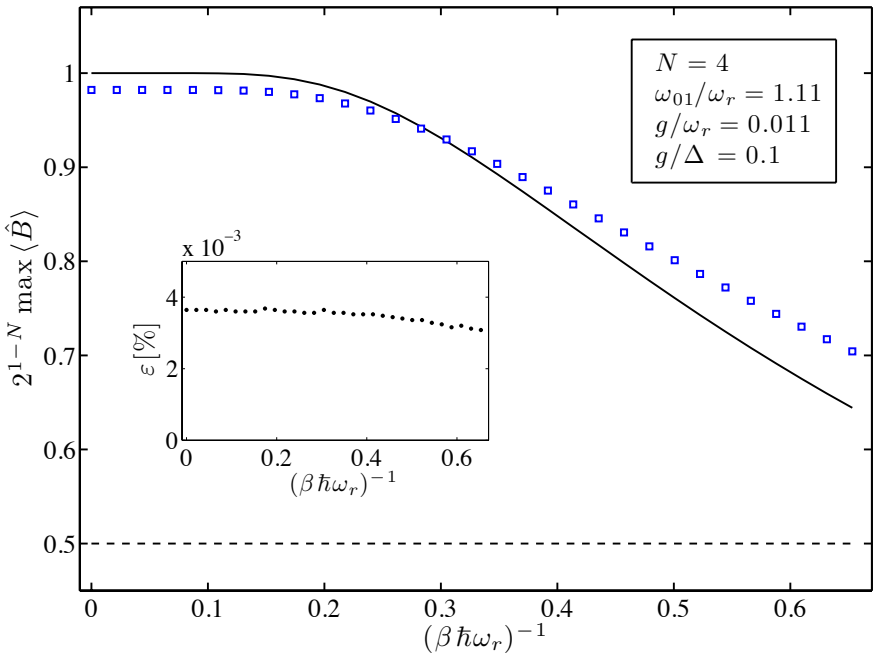

Figure 3.4: Temperature dependence of the maximal value reached by $\langle \hat{B}(t) \rangle$, denoted by $\max\langle \hat{B} \rangle$, for $t \sim t_{\mathrm{GHZ}}$ (blue squares) and normalized by 2^{N-1}. The solid line shows the theoretical bound $\tanh(\beta\hbar\omega)$ for a resonator initially in the thermal state Eq. (3.65). Inset: relative deviation $\varepsilon = t_{\max}/t_{\mathrm{GHZ}} - 1$ of the time $t_{\max}$ at which $\max\langle \hat{B} \rangle$ is realized compared to the predicted time $t_{\mathrm{GHZ}} = \pi/(2\tilde{g})$. Local hidden-variable theory only allows values of $\langle \hat{B} \rangle$ below the dashed line. For $N = 4$ this value also corresponds to the upper bound for biseparable states.

have been taken into account, uncontrolled excitations of the resonator might affect the final state of the qubits. Combining Eqs (3.37) and (3.38), we find that

$$\begin{aligned} &\mathrm{Tr}\left[\hat{B}(e^{i\delta_N \hat{J}_z}\rho_{\mathrm{qb}}(t_{\mathrm{GHZ}})e^{-i\delta_N \hat{J}_z})\right] \\ &\quad = 2^{N-1}\sum_{n=0}^{\infty}\langle n|\rho_{\mathrm{res}}|n\rangle\left[\cos^{2N}\left(n\frac{\pi}{2}\frac{\chi}{\tilde{g}}\right) - \sin^{2N}\left(n\frac{\pi}{2}\frac{\chi}{\tilde{g}}\right)\right]. \end{aligned} \tag{3.64}$$

For instance, we assume ρ_{res} to be a thermal state characterized by an inverse temperature $\beta = (k_B T)^{-1}$,

$$\rho_{\mathrm{res}} = \left(1 - e^{-\beta\hbar\omega}\right)\sum_n e^{-n\beta\hbar\omega}|n\rangle\langle n|\,. \tag{3.65}$$

In this simple case, the outcome of the Bell-Mermin operator measurement $\langle \hat{B}(t_{\mathrm{GHZ}}) \rangle$ should be at least $2^{N-1}\tanh(\beta\hbar\omega/2)$.

A numerical evaluation of $\langle \hat{B}(t) \rangle$, using the Tavis-Cummings Hamiltonian Eq. (3.61), shows good agreement with our simple estimate. We consider the ideal case of homogeneous qubit and coupling frequencies and we choose frequencies satisfying Eq. (3.34) such that no correcting pulse needs to be applied ($\delta_N = 0$). We look for the maximal value of $\langle \hat{B}(t) \rangle$ around t_{GHZ}, that is, for $|t - t_{\mathrm{GHZ}}| < \pi/(2\omega_{01})^{-1}$, and for the time $t_{\max}$ at which this maximal value is realized. The results for $N = 4$ qubits are shown in Fig. 3.4.

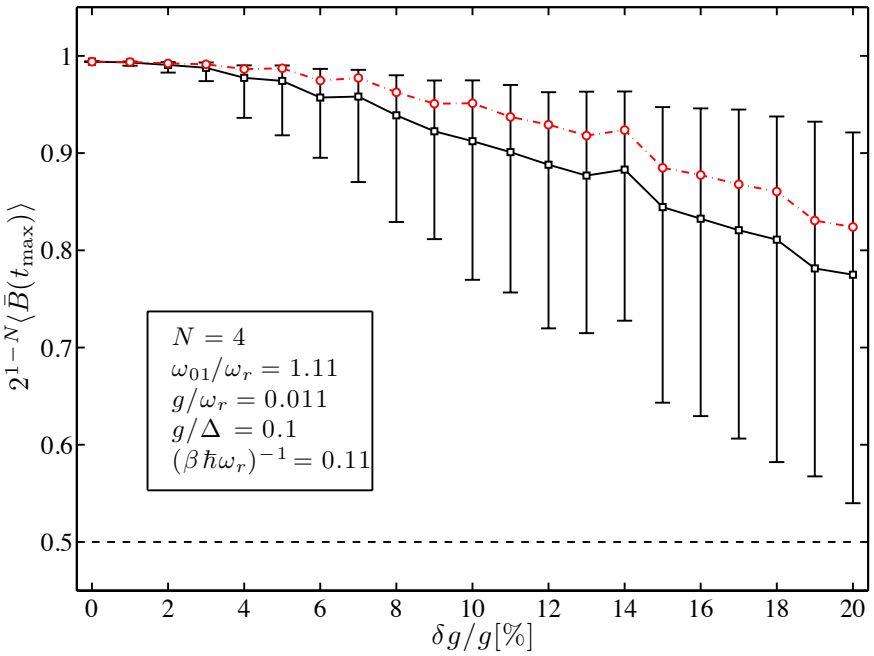

Figure 3.5: Effect of inhomogeneous coupling frequencies $g_0^{(q)}$ with mean g and standard deviation δg. We show the dependence of the maximal mean value $\langle \bar{B}(t_{\max})\rangle$ of $\langle \hat{B}(t)\rangle_{\{g_q\}}$ on $\delta g/g$ for $t \sim t_{\mathrm{GHZ}}$ (squares). The error bars show the standard deviation of $\langle \hat{B}(t_{\max})\rangle_{\{g_q\}}$ above and below the mean value. The median of $\langle \hat{B}(t_{\max})\rangle_{\{g_q\}}$ (red circles) is clearly above the mean value. Local hidden-variable theory only allows values of $\langle \hat{B}\rangle$ below the dashed line. For $N = 4$ this value also corresponds to the upper bound for biseparable states.

3.5.3 Inhomogeneous coupling frequencies

To estimate whether our scheme is robust against small random deviations in the physical parameters, we consider small inhomogeneities in the coupling strengths $g_j^{(q)}$. This effect will be investigated numerically, and for this purpose we compute the real-time evolution of the Bell-Mermin operator, using the Tavis-Cummings Hamiltonian Eq. (3.11), truncated to the two lowest levels of the transmon qubits. This should capture the main features of this effect, since in our effective description of the system Eq. (3.18), the third levels of the transmon qubits only affect the ac-Stark shifts $\chi^{(q)}$ and renormalize the resonator frequency. Assuming the qubit transition frequencies are still homogeneous, the inhomogeneity of the coupling frequencies $g_0^{(q)}$ produces inhomogeneous qubit-qubit couplings coefficients $\tilde{g}_{00}^{(qq')} = |g_0^{(q)} g_0^{(q')}|/\Delta$.

The coupling constants $g_0^{(q)}$ are assumed to be Gaussian distributed with mean g and standard deviation δg. The notation $\{g_q\}$ denotes a particular set of coupling frequencies $g_0^{(q)}$. The real-time evolution of the Bell-Mermin operator for one set of coupling frequencies $\{g_q\}$ is denoted $\langle \hat{B}(t)\rangle_{\{g_q\}}$.

For a given number n_r of random realizations $\{g_q\}$ (n_r around 200) with fixed δg, we

first calculate the mean value,

$$\langle \bar{B}(t) \rangle = \frac{1}{n_r} \sum_{\{g_q\}} \langle \hat{B}(t) \rangle_{\{g_q\}}. \tag{3.66}$$

Then, the maximal value $\langle \bar{B}(t_{\max}) \rangle$ defined by

$$\langle \bar{B}(t_{\max}) \rangle = \max_{t \geq 0} \langle \bar{B}(t) \rangle \tag{3.67}$$

is found. Finally the variances, above and below the maximal mean value $\langle \bar{B}(t_{\max}) \rangle$, of the particular set $\langle \hat{B}(t_{\max}) \rangle_{\{g_q\}}$ are calculated. The variances are calculated separately above and below, because the $\langle \hat{B}(t_{\max}) \rangle_{\{g_q\}}$ are not Gaussian-distributed. We also calculate the median among the $\langle \hat{B}(t_{\max}) \rangle_{\{g_q\}}$ and notice that the distribution is strongly asymmetric.

Results for $N = 4$ and $\delta g/g$ between 0 to 20 % are shown in Fig. 3.5. The time at which the maximum is attained is generally in good agreement with the predicted value $t_{\mathrm{GHZ}} = \pi/(2\tilde{g})$, as long as g/Δ is small. The value of $\langle \bar{B}(t_{\max}) \rangle$ remains close to the ideal one for $\delta g/g$ of the order of a few percents, and thus we notice that our scheme can tolerate some inhomogeneity in the coupling constants.

3.5.4 Influence of the weak transmon anharmonicity

Transmon qubits have a weakly anharmonic energy spectrum. As a consequence, leakage out of the computational subspace might affect the performance of our protocol. Examining the last term of the Hamiltonian Eq. (3.14), it is clear that the dispersive qubit-qubit interaction couples any transition between adjacent levels in one qubit to another transition in another qubit. Thus, any computational qubit state with more than one excitation is coupled to states that do not belong to the computational subspace (e.g., for $N = 3$, the state $|111\rangle$ is mixed with $|021\rangle$). Even if the anharmonicity is sufficiently large for these mixing amplitudes to be small, this might still affect the generated state. In order to test the robustness of our scheme against this effect, we compute the numerically exact coherent evolution of the Bell-Mermin operator, using the generalized Tavis-Cummings Hamiltonian $\hat{H}$ Eq. (3.11).

We consider the case of identical transmon qubits that are homogeneously coupled to the resonator. Their transition frequencies $\omega_{j,j+1} = \omega_{j+1} - \omega_j$ and coupling rates g_j are given in Eq. (3.12). We use typical transmon parameters leading to a relative anharmonicity

$$\alpha_r = \frac{\omega_{12} - \omega_{01}}{\omega_{01}} \tag{3.68}$$

which is negative and of the order of a few percent. In our protocol the qubits are initially prepared in a state involving up to N qubit excitations (the initial state $|\psi_0\rangle$ has a component $|1 \ldots 1\rangle$). The interaction Hamiltonian will mostly populate transmon levels with index $k \leq N$ and resonator states with $n \leq N$. This gives an indication on how many qubit and resonator levels should be included to obtain relevant information about the influence of the weak anharmonicity.

We compute the coherent evolution the operator $\hat{B}$ in a frame rotating at the frequency $\omega_{01} + \chi_0$ (for N even)

$$\langle \hat{B}'(t) \rangle = \mathrm{Tr} \left[\hat{B} e^{it(\omega_{01}+\chi_0)\hat{J}_z} \rho'_{qb}(t) e^{-it(\omega_{01}+\chi_0)\hat{J}_z} \right], \tag{3.69}$$

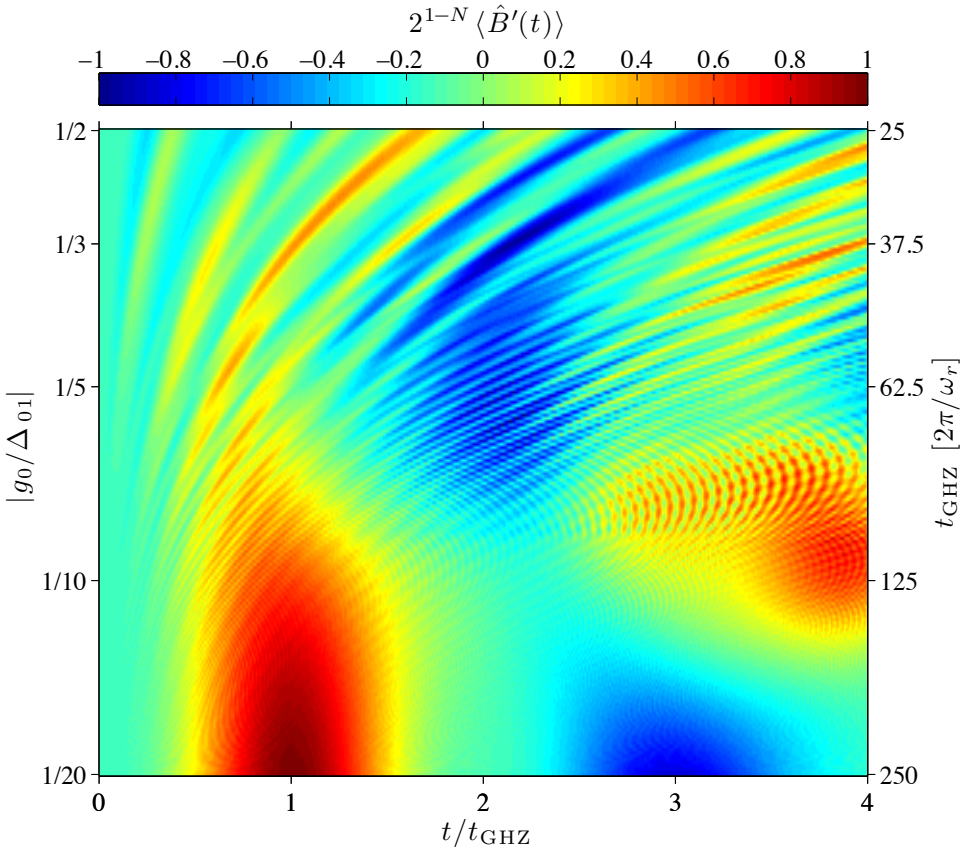

Figure 3.6: Time evolution of the Bell-Mermin operator as a function of the dispersive parameter g_0/Δ_{01} for $N = 4$ identical transmon qubits. We show the value of the operator $\hat{B}$ in a frame rotating at the qubit frequency, obtained from Eq. (3.69). Different values of g_0/Δ_{01} are obtained by changing the frequency of the qubits $\omega_{01} = \Delta_{01} + \omega_r$. We assume homogeneous qubit-resonator couplings $g_0/\omega_r = 0.02$ and $\Delta_{01} < 0$. The ratio $E_J/E_C = 50$ leads to a relative anharmonicity $\alpha_r = -5.3\%$ of the qubits' energy spectrum.

where $\rho'_{qb}(t)$ is the reduced density matrix of the qubits, obtained by tracing out both the resonator states and non-computational states of the transmon qubits, and $\hat{H}$ the Hamiltonian given in Eq.(3.11).

The results for $N = 4$ are shown in Fig. 3.6. We observe that the relatively weak anharmonic spectrum of transmon qubits imposes some constraints on the dispersive parameter g_0/Δ_{01}. Smaller values, of the order of $|g_0/\Delta_{01}| \sim 0.08$, are required to generate a GHZ state, at time $t = t_{\mathrm{GHZ}}$, with reasonably high fidelity. Importantly, we have observed that the sign of the detuning has an effect on the generated state. Leakage out of the computational subspace is reduced when the detuning Δ_{01} is negative. This effect is probably a consequence of the negative anharmonicity of transmon qubits ($\omega_{12} < \omega_{01}$). When $|\Delta_{12}| > |\Delta_{01}|$, the mixing to higher transmon levels is smaller, compared to the case $\Delta_{12} > \Delta_{01} > 0$, as it can be seen from a perturbative treatment of Eq. (3.14).

Surprisingly large values of $|\langle \hat{B}'(t)\rangle|$ are found for relatively small detuning and times larger than the ideal preparation time ($g_0/\Delta_{01} \sim 1/3$ and $t \sim 2.2t_{\mathrm{GHZ}}$). The reason why such a highly entangled state is generated in these conditions is not completely clear.

However it might indicate that a GHZ state could be produced in a relatively short time, recalling that $t_{\mathrm{GHZ}} \propto |\Delta_{01}/g_0^2|$.

3.6 Concluding remarks

To conclude, we have shown that it is possible to generate multipartite GHZ states on a set of transmon qubits in a circuit QED setup in a one-step deterministic protocol. In the dispersive limit $g \ll \Delta$, such a system behaves as a fully connected qubit network with exchange interactions proportional to $\tilde{g} = g^2/\Delta$. The preparation time of the protocol is inversely proportional to $\tilde{g}$. The non-local nature of the generated state can be investigated using a Bell-Mermin inequality. Moreover, we have derived and applied bounds on the expectation value of the Bell-Mermin operator as a detection criterion for genuine N-partite entanglement. We have shown that our scheme is robust against small inhomogeneities in the coupling frequencies. Finally, we have investigated the consequences of the weakly anharmonic spectrum of transmon qubits. The implementation proposed here looks like a promising way to generate GHZ states, and hopefully can be experimentally realized in a circuit QED setup.

Chapter 4

Cavity optomechanics

4.1 Hamiltonian of the optomechanical interaction

Since the 19th century and Maxwell's theory of electromagnetism, it is known that light can produce a radiation-pressure force. In the language of quantum theory, one can think of the radiation-pressure force as being exerted by photons carrying a momentum and bouncing off the reflective surface of an object. This effect is small and its experimental signatures have remained elusive for more than a century.[1] First observations of the radiation pressure were reported in Refs. [Lebedew01, Nichols01].

The radiation pressure exerted by a light beam with intensity I is $P_{\mathrm{rad}} = 2I/c$, where c is the speed of light. A mechanical object is therefore likely to experience the radiation-pressure force if it has a small mass or if the light intensity is particularly large. A way to reveal this effect is to use the strong confinement of the light field in a optical resonator. The density of states of the electromagnetic field is very particular in an optical cavity. The different standing modes have well-defined resonances whose frequencies depend on the length of the cavity. When a laser drive is applied near a resonance, one of these modes is populated and the light intensity increases. If one of the end mirrors is movable, the radiation-pressure force can displace it. The mirror motion changes the length of the cavity and thereby its resonance frequency, modifying the light intensity, and accordingly, the radiation pressure acting on the mirror varies. This mechanism, even if rather simple, leads to a wide variety of phenomena. The study of the effects arising from such coupling between a confined and resonant optical field and the motion a mechanical object is nowadays known as cavity optomechanics.

The generic optomechanical system, as depicted in Fig. 4.1, is described by two coupled bosonic modes: an optical mode and a mechanical resonator, whose position modulates the cavity resonance frequency. The physics of the system is captured by the Hamiltonian

$$\hat{H}_0 = \hbar\omega_c(\hat{x})\hat{a}^\dagger\hat{a} + \hbar\omega_m\hat{b}^\dagger\hat{b}, \tag{4.1}$$

where $\hat{a}$ and $\hat{b}$ are the creation operators for the optical and mechanical degrees of freedom, respectively. The position of the mechanical resonator is $\hat{x} = x_{\mathrm{zpf}}(\hat{b} + \hat{b}^\dagger)$, where $x_{\mathrm{zpf}} = \sqrt{\hbar/2m\omega_m}$ is the amplitude of the zero-point fluctuations, ω_m the mechanical frequency, and m its mass. For small resonator displacements, the dependence of the cavity resonance

[1] We should however mention here the notable Kepler's speculation on the comet tails being blown by a solar 'breeze'.

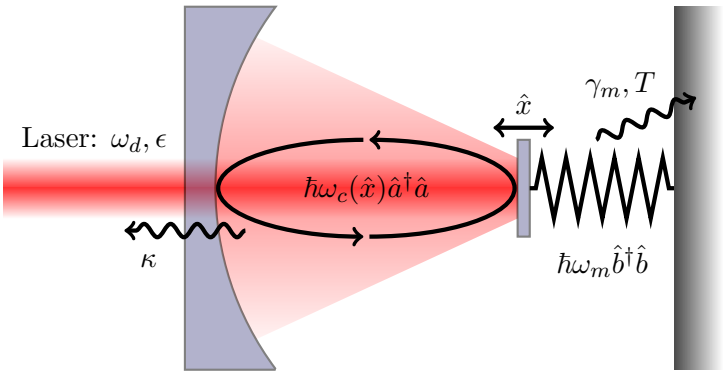

Figure 4.1: *Schematic optomechanical system.* The cavity consists of a fixed input mirror and a small movable end mirror harmonically coupled to a support. A laser with frequency ω_d and amplitude ϵ drives a cavity mode ($\hat{a}$) with resonance frequency ω_c. The light intensity stored inside the optical mode exerts a radiation-pressure force on the mechanics whose motion conversely changes the cavity resonance frequency via the mechanical displacement $\hat{x} = x_{\mathrm{zpf}}(\hat{b} + \hat{b}^\dagger)$. The finite transmission of the mirrors causes the decay, at rate κ, of the light intensity. The small mirror is described as an harmonic oscillator with frequency ω_m. The support act as a mechanical bath at temperature T and γ_m is the energy dissipation rate.

frequency on the position $\hat{x}$ is linearized around its unperturbed value,

$$\omega_c(\hat{x}) \simeq \omega_c - G\hat{x}. \tag{4.2}$$

The frequency pull parameter $G = -\partial\omega_c/\partial x$ describes the frequency shift of the cavity per displacement. It is defined with a minus sign such that $G > 0$, according to the fact that, when the cavity length increases, the resonance frequency decreases. For a cavity of length L, it is given by $G = \omega_c/L$. Now, we introduce the coupling rate of the optomechanical interaction, as $g_0 = Gx_{\mathrm{zpf}}$, which can be interpreted as the frequency shift per phonon. The optomechanical interaction

$$\hat{H}_{\mathrm{I}} = -\hbar g_0 \hat{a}^\dagger\hat{a}(\hat{b} + \hat{b}^\dagger) \tag{4.3}$$

is intrinsically nonlinear, as it contains the product of three field operators. The radiation-pressure force operator acting on the resonator is

$$\hat{F}_{\mathrm{rad}} = -\frac{\partial\hat{H}_{\mathrm{I}}}{\partial\hat{x}} = \frac{\hbar g_0}{x_{\mathrm{zpf}}}\hat{a}^\dagger\hat{a}. \tag{4.4}$$

Furthermore, we notice that the resonator displacement, induced by the presence of one photon in the cavity, is $2x_{\mathrm{zpf}}g_0/\omega_m$. The above expression for the interaction, $\hat{H}_I$, is a good starting point to study many effects in cavity optomechanics. For a more careful derivation of the optomechanical interaction, based on a classical nonrelativistic description and the subsequent canonical quantization of the optical and mechanical degrees of freedom, we refer the reader to the publication by Law [Law95].

The description of a cavity optomechanics experiment would be incomplete if we do not consider the effect of the driving field,

$$\hat{H}_d = i\hbar\epsilon\left(\hat{a}e^{i\omega_d t} - \hat{a}^\dagger e^{-i\omega_d t}\right). \tag{4.5}$$

The Hamiltonian $\hat{H}_d$ models a monochromatic coherent light field of frequency ω_d and amplitude ϵ that drives the optical mode. Generally, there are more than a single optical and mechanical mode in an optomechanical cavity. We can consider only one optical degree of freedom because the frequency of the drive selectively reveals the optomechanical interaction for a single cavity mode. In a high-finesse cavity, the driving near a particular resonance only populates the corresponding mode. The influence of other optical modes with frequencies much different from ω_d can be safely neglected. In addition, we focus on the case where the driven cavity mode interacts with a single mechanical mode. This assumption is mostly arbitrary and depends on the mechanical properties of the system at hand. This approximation is only valid if the different mechanical modes are decoupled and well-resolved in frequency. If several mechanical modes interact with the radiation field, their effect on the cavity frequency might still be described as a single harmonic mode with an effective mass and susceptibility [Pinard99].

The Hamiltonian is commonly written in a frame rotating at the frequency ω_d, such that the explicit time-dependence of the driving term $\hat{H}_d$ is eliminated. The new Hamiltonian is obtained from a unitary transformation, $\hat{H}_{\text{new}} = \hat{U}\hat{H}\hat{U}^\dagger + i\hbar(\partial_t\hat{U})\hat{U}^\dagger$, where $\hat{U} = e^{i\omega_d t\hat{a}^\dagger\hat{a}}$. The system and drive Hamiltonian now read

$$\hat{H}_0 = -\hbar\Delta_0\hat{a}^\dagger\hat{a} + \hbar\omega_m\hat{b}^\dagger\hat{b} - \hbar g_0\hat{a}^\dagger\hat{a}\left(\hat{b} + \hat{b}^\dagger\right), \tag{4.6}$$

$$\hat{H}_d = i\hbar\epsilon\left(\hat{a} - \hat{a}^\dagger\right), \tag{4.7}$$

where $\Delta_0 = \omega_d - \omega_c$ is the detuning of the drive from the unperturbed cavity resonance.

An optomechanical setup is an open quantum system. Its dynamics can be properly investigated only if we also consider the effects of dissipation. A photon inside the cavity decays due to the finite transmission of the end mirrors or by absorption. This decay process occurs at the rate κ and is the consequence of the coupling between the light field inside the cavity and the electromagnetic modes outside the cavity. The input modes carry some noise of either quantum or thermal origin. The cavity resonance frequency being generally larger than the temperature of the input modes we only consider quantum noise. The mechanical resonator, whose frequency is generally much smaller than the cavity frequency ω_c, is subject to damping. This effect is described by the coupling to an environmental bath of phonons with finite temperature T, that yields an energy damping rate γ_m. The coupling to the bath induces the emission, at rate $\gamma_m(n_{\text{th}} + 1)$, or the absorption, at rate $\gamma_m n_{\text{th}}$, of mechanical excitations into the bath. The parameter $n_{\text{th}} = n_{\text{B}}(\hbar\omega_m)$ is the thermal occupation of the bath, where n_{B} is the occupation number given by the Bose-Einstein statistics. If solely coupled to the environmental bath, the average energy of the mechanical mode is $\hbar\omega_m n_{\text{th}}$. The dissipative effects are included in the description by means of two additional terms in the Hamiltonian,

$$\hat{H} = \hat{H}_0 + \hat{H}_d + \hat{H}_\kappa + \hat{H}_{\gamma_m}. \tag{4.8}$$

In practice, the influence of the environment can be treated using standard Lindblad quantum master equations or in terms of quantum Langevin equations, using the quantum input-output formalism.

This prototypical model applies to many experimental situations and the optomechanical interaction gives rise to many interesting effects and practical applications. Cavity optomechanics has undergone a rapid development during the last years, both from experimental and theoretical perspectives. The optomechanical model has been widely

studied and a number of review articles has been published, covering the important features and most recent achievements [Aspelmeyer08, Kippenberg08, Marquardt09, Genes09, Milburn12, Meystre13, Aspelmeyer13].

4.2 Applicability and phenomenology of the model

Despite its apparent simplicity, the generic model of cavity optomechnanics, as described previously, gives rise to rich physics and applies to numerous physical systems. The radiation-pressure interaction describes the coupling of the light field to the mechanical motion of objects that range from clouds of ultracold atoms in submillimeter-long Fabry-Pérot cavities to massive mirrors of several kilograms in a kilometer-scale interferometer.

We can distinguish a few important steps in the development of this research field. One cannot talk about cavity optomechanics without evoking the pioneering work of Braginsky and coworkers, who studied and investigated the effects of the radiation-pressure force as early as the 1960s. The optical enhancement or reduction of mechanical damping was probably one of the first phenomena that has been studied and observed with a microwave cavity and a gram-scale mechanical oscillator [Braginsky67, Braginsky70].

The dynamical back-action of the light field enables the cooling or the amplification of the mechanical motion [Braginsky01, Braginsky02]. This effect has attracted much attention because of its important implications for sensitive force detection. Reducing the thermal motion of a mechanical object allows to determine its position more precisely. This potential cavity-assisted cooling was soon understood to be analogous to the laser cooling of ions [Neuhauser78] and atoms [Chu85, Aspect88, Lett88]. The quantum treatement of this passive sideband cooling scheme has been extended to optomechanical systems [Marquardt07, Wilson-Rae07]. In parallel, an alternative way to reduce the thermal motion of the oscillator has been proposed. It makes use of an active feedback loop that conditions the laser drive on the continuous monitoring of the mechanical position via homodyne detection [Mancini98]. This active scheme is often referred to as cold damping or feedback cooling. An insightful comparison of these cooling processes can be in found in Ref. [Genes08b].

The theoretical studies of Braginsky [Braginsky68, Braginsky75, Braginsky92], together with those of Caves [Caves80a, Caves80b, Caves81, Caves82], of the limitations that the quantum nature of light sets on sensitive position measurements, somehow encompassed in a more general theory of quantum measurements, paved the way for generations of physicists concerned with metrology. When trying to optically measure the displacement of a mechanical object, the fluctuations of the laser intensity, known as shot noise, induce a random motion of the object to be measured. This back-action noise might become the limiting source of imprecision if the laser power is large. The role of this quantum-measurement back-action has originally been studied in the context of interferometric gravitational-wave detection, but its great significance extends to the scope of all measurements or amplification processes limited by the effect of quantum noise (see [Clerk10] for a comprehensive review).

In the mid-1980s, experimental implementations of cavity optomechanics have observed the optical bistability induced by the radiation-pressure force of both optical [Dorsel83, Meystre85] and microwave light sources [Gozzini85] acting on truly macroscopic oscillators, with masses of tens of milligrams and resonance frequencies in the Hertz range. Similar results have recently been obtained with a torsion balance oscillator [Mueller08]. In addition, the stiffening or softening of the mechanical restoring force by the optical field,

referred to as optical-spring effect, was observed with a gram-scale mirror [Sheard04]. A similar setup was then used to perform active cavity-assisted cooling [Corbitt07].

For the purpose of gravitational wave detection [Abramovici92, Abbott09a], experimental investigations with even more massive mechanical objects have been carried on [Cuthbertson96]. Recently, the feedback cooling of a kilogram-scale mirror up to a thermal occupation number of two hundred mechanical quanta was achieved [Abbott09b], nearly facing the limitation set by the quantum back-action on the detection sensitivity.

In the last years, another trend was pursued with the miniaturization of the mechanical element. The advances in the design and the nanofabrication techniques of devices with large mechanical frequency and high quality factor have led to the exploration of a completely new territory: bringing cavity optomechanics to the quantum regime. Most of the recent setups realizing the optomechanical interaction are presented in Sec. 4.3. Beyond the usual prospects for quantum-limited measurements, these developments allow to envision completely new applications for optomechanical devices. The coherent control and manipulation of the quantum state of mechanical objects also makes conceivable tests of quantum mechanics in a unattainable regime of parameters up to now. A considerable amount of theoretical studies has appeared in the literature. From the most ambitious intents to create non-classical states of macroscopic objects [Mancini97, Bose97] and test foundational theories (wave function reduction models [Bose99, Marshall03, Romero-Isart11, Kaltenbaek12], quantum gravity [Pikovski12]), to the prospects of using nanomechanical systems for the purpose of quantum-state storage [Zhang03, Safavi-Naeini11b] or transfer [Stannigel10, Tian10, Wang12] in the context of quantum information processing, cavity optomechanics nowadays spans a large spectrum of experimental motivations.

4.2.1 Important parameters and operating regimes

The parameters $(\omega_m, g_0, \gamma_m, \kappa)$, that characterize cavity-optomechanics experiments, can be controlled in a wide range. Together with the additional parameters of the driving field, (Δ_0, ϵ), as well as the temperature of the mechanical bath T, a large variety of operating regimes is possible, leading to a rich phenomenology. Ratios of these parameters characterize the setup and determine if it can be used for one or another application. We review the most common of them and interpret them in simple physical terms.

Mechanical quality factor and thermal occupation number

The mechanical quality factor is defined as $Q_m = \omega_m/\gamma_m$, where γ_m is the mechanical energy dissipation rate. The rate γ_m describes the loss of mechanical energy and also quantifies the strength of the coupling to the mechanical bath. Another important quantity to describe the mechanical bath is the thermal occupation number $n_{\rm th} = n_{\rm B}(\hbar\omega_m)$. The majority of the recent implementations exhibit relatively high quality factors, at least $Q_m > 10^3$ (with the exception of ultracold atom cloud experiments). Another important quantity is the so-called *thermal decoherence rate* $n_{\rm th}\gamma_m$. It describes the rate at which a mechanical mode initially in the ground state heats up.

From a theoretical point of view, one can treat the mechanical dissipation with standard methods of quantum optics, such as the quantum input-output formalism or Lindblad quantum master equations, when the condition $Q_m \gg 1$ is satisfied. For low quality factors, one should resort to other methods like quantum Brownian motion [Caldeira83a, Gardiner04]. (See the remarks at the end of Sec. 2.3.3.)

Sideband resolution

The sideband parameter is defined as the ratio of the mechanical frequency over the cavity decay rate ω_m/κ. If the condition $\omega_m > \kappa$ is satisfied, the system is said to be in the *resolved-sideband regime* or *good-cavity limit*. In short, due to the harmonic motion of the end mirror (see Fig. 4.1), the light emitted by the cavity is phase-modulated. Consequently, the emission spectrum exhibits a series of sidebands at frequencies $\omega_c \pm k\omega_m$, where $k \in \mathbb{N}$. These peaks can only be resolved if the mechanical frequency ω_m is larger than the cavity linewidth κ.

In general, the good-cavity limit is a precondition for the observation of many interesting effects. In particular, the sideband parameter determines the ability to realize ground-state cooling of the mechanical mode. (A full quantum description of this effect can be found in Ref. [Marquardt07].)

Linear optomechanical coupling rate

In most of the current realizations of cavity optomechanics, the optomechanical coupling rate g_0 is small compared to the mechanical frequency ω_m and the cavity decay rate κ. To reveal the effects of the optomechanical interaction, the cavity is driven into a coherent state with large amplitude. In this case, we can split the cavity field into a steady-state amplitude $\bar{a}$ and a fluctuating term $\hat{d}$, that is $\hat{a} = \bar{a} + \hat{d}$. (Without loss of generality, we assume that $\bar{a}$ is real.) This transformation generates an interaction

$$\hat{H}_I = -\hbar g_0 \bar{a}^2(\hat{b} + \hat{b}^\dagger) - \hbar g_0 \bar{a}(\hat{d} + \hat{d}^\dagger)(\hat{b} + \hat{b}) - \hbar g_0 \hat{d}^\dagger \hat{d}(\hat{b} + \hat{b}^\dagger). \tag{4.9}$$

The first term represents a constant radiation-pressure force $\bar{F}_{\mathrm{rad}} = \hbar G \bar{a}^2$, causing a static displacement of the mechanical resonator $\bar{x} = 2x_{\mathrm{zpf}} g_0 \bar{a}^2/\omega_m$ that can be absorbed by shifting the reference frame for $\hat{x}$.[2] The second term describes the linear interaction between the mechanical mode and the quantum fluctuations of the optical field. If $\bar{a} \gg 1$, this term dominates over the nonlinear interaction (last term). The linearized Hamiltonian reads[3]

$$\hat{H}_0' = -\hbar\Delta \hat{a}^\dagger \hat{a} + \hbar\omega_m \hat{b}^\dagger \hat{b} - \hbar g(\hat{d} + \hat{d}^\dagger)(\hat{b} + \hat{b}^\dagger), \tag{4.10}$$

where $g = g_0\bar{a}$ denotes the *linear optomechanical coupling rate* and $\Delta = \Delta_0 - G\bar{x}$ is the effective detuning resulting from the displacement $\bar{x}$. This rate is often expressed as $g = g_0\sqrt{\bar{n}}$, where $\bar{n} = \bar{a}^2$ denotes the average number of photons circulating inside the cavity. The coupling strength g is sometimes referred to as *enhanced* or *parametric* optomechanical coupling rate since it depends on $\bar{n} \gg 1$ and can be modified by changing the driving strength and thereby the coherent amplitude $\bar{a}$.

If the system is in the resolved-sideband regime and if the coupling rate g exceeds both the mechanical and cavity decay rates, $g > \{\gamma_m, \kappa\}$, the system enters the so-called *strong-coupling regime*. In this regime, the driven optical mode and the mechanical modes hybridize to form two new modes with frequencies

$$\omega_\pm = \frac{\omega_m - \Delta}{2} \pm \sqrt{g^2 + \left(\frac{\omega_m + \Delta}{2}\right)^2}. \tag{4.11}$$

[2] However, for very large driving amplitudes this static displacement may significantly change the cavity line shape, resulting in a bistable behavior.

[3] The Hamiltonian $\hat{H}_0'$ is referred to as 'linearized' since the resulting coupled equations of motion for $\hat{d}$ and $\hat{b}$ are linear in this approximation.

The mechanical response splits into two peaks, an effect known as *normal-mode splitting*.

If, in addition, the linear coupling rate is larger than the thermal decoherence rate, $g > n_{\mathrm{th}}\gamma_m$, the interaction between the mechanical mode and the cavity field becomes *coherent*. This regime is a precondition for quantum state transfer between the optical mode and the mechanical mode.

Detuning

Depending on the value of the detuning Δ, we can distinguish three important regimes with respect to the optomechanical interaction, namely cooling, amplification, and position measurement of the mechanical resonator. In the following, we assume that the system is in the resolved-sideband regime such that we can make the rotating-wave approximation for the linearized optomechanical interaction

$$\hat{H}_I' = -\hbar g(\hat{d} + \hat{d}^\dagger)(\hat{b} + \hat{b}^\dagger). \tag{4.12}$$

Sideband cooling – For red-detuned driving frequency such that $\Delta \simeq -\omega_m$, the interaction becomes $-\hbar g(\hat{d}^\dagger\hat{b} + \hat{d}\hat{b}^\dagger)$. The process $\hat{d}^\dagger\hat{b}$ describes the absorption of a mechanical excitation by the optical mode and is enhanced by the cavity, which acts as a second zero-temperature bath for the mechanical mode. In particular, phonon numbers well below unity can be achieved if $\omega_m \gg \kappa$ [Marquardt07, Wilson-Rae07].

Amplification – If the driving field is injected on the upper sideband (blue detuning), $\Delta \simeq \omega_m$, the interaction takes the form $-\hbar g(\hat{d}^\dagger\hat{b}^\dagger + \hat{d}\hat{b})$. The cavity enhances the process $\hat{d}^\dagger\hat{b}^\dagger$, resulting in heating or parametric amplification [Clerk10] instead of cooling. If the amplification rate exceeds the intrinsic mechanical damping rate, the mechanical motion experiences a parametric instability [Marquardt06, Ludwig08].

Position measurement – If the cavity is driven on resonance, $\Delta = 0$, it works as an interferometer. The interaction Eq. (4.12) means that the mechanical position $\hat{x} = x_{\mathrm{zpf}}(\hat{b} + \hat{b}^\dagger)$ leads to a phase shift in the reflected (or transmitted) light. This mechanism is also evident when considering the nonlinear optomechanical interaction Eq. (4.3). Thus, a measurement of the mechanical motion can be obtained by monitoring this phase shift.

Driving strength

An important quantity involving the amplitude ϵ of the driving field is the input power launched into the cavity $P = \hbar\omega_d\epsilon^2/\kappa$. If the driving field is on resonance ($\Delta = 0$), the average number of photons circulating inside the cavity is given by $(2\epsilon/\kappa)^2$.

Single-photon coupling rate

Nonclassical effects can be revealed if the single-photon coupling rate g_0 becomes comparable to both the mechanical frequency ω_m or the cavity decay rate κ [Ludwig08, Nunnenkamp11, Rabl11, Qian12, Kronwald13]. Two important ratios involve the single-photon coupling rate g_0: the 'granularity parameter' g_0/κ [Murch08b] and the photon-blockade parameter $g_0^2/(\omega_m\kappa)$.

To interpret these ratios, we may consider the radiation-pressure force exerted by a single photon $\hbar g_0/x_{\mathrm{zpf}}$ (see Eq. (4.4)). A single photon passing through the cavity for a time κ^{-1} gives a momentum kick $2p_{\mathrm{zpf}}g_0/\kappa$ to the mechanical resonator, where $p_{\mathrm{zpf}} = \hbar/(2x_{\mathrm{zpf}})$ is the amplitude of the momentum zero-point fluctuations. The regime

$g_0/\kappa > 1$ allows to reveal the granularity of the light field and is usually referred to as *single-photon strong coupling regime*.

The force exerted by a single photon produces a displacement of the mechanical resonator $2x_{\mathrm{zpf}}g_0/\omega_m$ and thereby shifts the cavity resonance frequency by $2g_0^2/\omega_m$. If this shift is larger than the cavity linewidth, $g_0^2/(\omega_m\kappa) > 1$, a second photon cannot enter the cavity. This leads to the mechanically-induced photon-blockade regime, which additionally requires $\omega_m > \kappa$ [Rabl11].

4.3 Recent experimental implementations

The generic model of cavity optomechanics, as shown in Fig. 4.1, applies to a large variety of physical systems. We review the recent and most common experimental realizations of cavity optomechanics, give some typical regimes of parameters they can reach and their respective achievements so far. By no means we pretend to be exhaustive and the interested reader can find a detailed overview of experimental parameters in Refs. [Poot12, Aspelmeyer13].

4.3.1 Optical Fabry-Pérot cavities

The range of parameters encountered in this category of experiments spans a wide range of values. The devices most resembling the situation shown in Fig. 4.1 consist of an optical Fabry-Pérot cavity with one fixed mirror and one small movable mirror. The small mirror forms or is mounted on a flexible element like a cantilever, a suspended or clamped oscillator, or a mechanical beam. Many experiments have been conducted with setups in this configuration and we only mention a few remarkable achievements.

In one of the first experiments a silicon torsional oscillator was used. The thermal motion of the mechanical resonator could be observed [Tittonen99]. Experiments with cantilevers have successfully implemented active feedback cooling [Kleckner06, Poggio07], allowing to reach effective temperatures of the mechanical mode around 3 mK [Poggio07]. The mechanical frequency in these setups was rather low, in the kilohertz range, and the mechanical quality factors quite high, $Q_m \sim 10^4 - 10^5$.

Higher mechanical frequencies (several hundred kHz) and similar quality factors can for instance be reached with clamped micromechanical oscillators. An experiment with this type of optomechanical device has successfully implemented cavity-assisted feedback cooling and monitored the thermal motion of the resonator with a nearly quantum-limited sensitivity [Arcizet06b]. Two experiments have demonstrated passive cavity-assisted cooling with this type of setup as well [Gigan06, Arcizet06a]. In addition, parametric instabilities have been observed for blue-detuned laser frequency [Arcizet06a].

In general, optomechanical devices need to combine both good quality factors, i.e., high mechanical frequencies, and high optical finesse. The first point is typically achieved by reducing the size of the mechanical element but in return it unavoidably affects the optical properties of the cavity. Operating in the resolved-sideband regime ($\omega_m > \kappa$) is therefore particularly challenging with this 'standard' geometry. An experiment using a micro-mirror pad mounted a on mechanical beam with large resonance frequency ($\omega_m/2\pi \simeq 1$ MHz) has however reached this regime ($\omega_m/\kappa \simeq 5$). With this setup, sideband cooling up to a few tens of mechanical quanta was achieved [Groblacher09b]. Furthermore, this device entered the strong-coupling regime ($g \gtrsim \kappa$), exhibiting normal-mode splitting [Groblacher09a].

Finally, a series of experiments has been realized with an optomechanical system that separates the optical and the mechanical components, the so-called 'membrane-in-the-middle' setup [Thompson08]. In this setup, a thin dielectric silicon nitride membrane is inserted inside a Fabry-Pérot cavity with fixed end mirrors. Experimentally, this approach is beneficial as it allows to eliminate the optical losses that arise when using small mirrors. The membrane motion couples to the optical field through a dispersive interaction. A major achievement with this particular geometry was the first experimental observation of radiation-pressure shot noise on a macroscopic object [Purdy13a]. Shortly after, the same setup was able to generate squeezed light below the shot-noise level [Purdy13b]. These experiments operate in the unresolved-sideband regime, $\omega_m/\kappa \sim 0.3$, and the mechanical resonance frequency of the micromechanical membrane is of the order of 100 kHz.

4.3.2 Whispering gallery mode resonators

A relatively recent implementation of cavity optomechanics was realized with optical microresonators. These are silicon micrometer-scale structures where light is guided in whispering gallery modes [Vahala03]. They exist in three different geometries: microdisk resonators [Ding11], microsphere resonators [Park09, Fiore11, Dong12], and microtoroidal resonators [Carmon05, Schliesser06, Schliesser08, Schliesser09, Verhagen12]. In these structures, mechanical distortions influence the optical properties. In short, normal modes of vibrations can change the optical path length of the resonator, shifting the optical resonance frequency, thus producing an optomechanical coupling.

In general, the small size of these structures gives rise to high mechanical frequencies. Microdisk resonators exhibit very high mechanical frequencies in the gigahertz range and optomechanical coupling close to 1 MHz, but suffer from relatively high optical loss which prevents them to operate in the resolved sideband regime [Ding11]. Experiments with spherical and toroidal cavities achieve very high optical finesse, with decay rates $\kappa/2\pi \sim 10 - 40$ MHz, and mechanical frequencies around 100 MHz, thus showing high sideband resolutions.

Microtoroids and microspheres have been used to demonstrate several remarkable effects. The large sideband resolution of these setups allows to implement sideband cooling schemes [Schliesser08, Rivière11, Schliesser09], as well as nearly quantum-limited displacement sensitivity [Schliesser09]. An optomechanical dark mode was observed by coupling two optical modes to a common mechanical breathing mode. The three modes hybridize and one of the resulting modes is decoupled from the mechanical mode [Dong12]. A proof-of-principle experimental demonstration of storing the optical state into the mechanical mode was reported with a microsphere resonator [Fiore11]. However, this setup did not operate in the strong coupling regime ($g > \kappa$) that is required to coherently exchange optical and mechanical states. This regime has been reached in a experiment with a toroidal microcavity, demonstrating the transfer and retrieval of the optical quantum state[Verhagen12].

4.3.3 Circuit cavity electromechanics

A new class of optomechanical systems, based on microfabricated superconducting circuits, has emerged in the last few years, that had remarkably quickly gained ground and made his way to the quantum regime. The coupling of a mechanically compliant and electrically active element to the electromagnetic field of a resonant microwave circuit

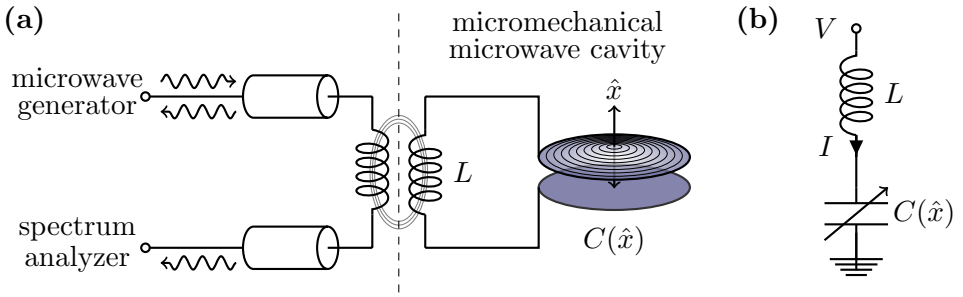

Figure 4.2: *Cavity optomechanics in the microwave domain.* An LC circuit forms a resonator for electromagnetic radiation in the microwave domain, i.e. $\omega_c/2\pi \sim$ GHz. A mechanical element is capacitively coupled to this microwave cavity and its motion results in a shift of the capacitance, and thereby of the cavity resonance frequency.

can be similar to the radiation-pressure interaction. Schematically, the optical Fabry-Pérot cavity of the generic optomechanical system is replaced by a microwave resonator. The cavity might be a stripline transmission line or a lumped-element LC resonator, and the coupling to the mechanical resonator is capacitive. The mechanical motion changes the capacitance $C(\hat{x})$ and thereby the resonance frequency of the microwave cavity $\omega_c(\hat{x}) = 1/\sqrt{LC(\hat{x})}$. The cavity resonance frequency ω_c typically lies in the gigahertz range and the use of a dilution refrigerator, to reach cryogenic temperature in the millikelvin range, is needed for the microwave input modes to be effectively at zero temperature. Nevertheless, these experiments profit from the available and highly accurate manipulation and readout techniques of microwave light, inherited from the related fields dealing with superconducting circuitry, such as nearly quantum-limited Josephson parametric amplifier [Castellanos-Beltran07, Castellanos-Beltran08, Bergeal10b, Bergeal10a]. This field, which investigates the coupling of mechanical resonator to the resonant modes of a microwave circuit in similar terms as 'standard' optomechanical experiments, has been nicknamed circuit cavity electromechanics.

First experiments in this direction have used a nanomechanical beam coupled to the center conductor of a superconducting stripline resonator [Regal08]. Similar setups have successfully implemented cooling close to the mechanical ground state [Rocheleau10]. Worth mentioning is also the first nearly back-action-evading measurement of mechanical motion [Hertzberg10], implementing an early scheme of quantum non-demolition measurement proposed in Ref. [Braginsky80]. These achievements rest upon the particularly good sideband resolution and the large enhanced optomechanical coupling rate $g = g_0\sqrt{\bar{n}}$. A similar experiment has lowered imprecision noise in the measurement of mechanical motion below the level of the standard quantum limit [Teufel09]. The latter device is formed by a lumped-element LC circuit instead of a transmission line resonator. The nanomechanical beam has been made longer, enhancing the optomechanical coupling at the expense of a lower mechanical frequency. Finally, another experiment has used a vibrating membrane as the capacitor of lumped-element LC resonator, as illustrated in Fig. 4.2(a). The latter setup exhibits a remarkably high optomechanical coupling rate, $g_0/2\pi \simeq 200$ MHz, and a sideband resolution among the highest, $\omega_m/\kappa \sim 50$. The parametric optomechanical coupling g could be made larger than the cavity decay rate κ, entering the strong-coupling regime [Teufel11b] and allowing sideband cooling of the mechanical motion with average phonon occupation well below unity [Teufel11a]. Lately, taking advantage of such a high

coupling, the same setup was used to coherently transfer the state of the incoming microwave field to the mechanical mode, and to retrieve it at later times [Palomaki13a]. Coherent coupling is an important prerequisite to exhibit truly quantum features and a major breakthrough was made by demonstrating entanglement between the itinerant microwave field and the mechanical motion [Palomaki13b].

Let us briefly mention the recent realization of a setup involving an optical cavity and a microwave resonator, both coupling to the same mechanical element [Andrews14]. This optomechanical device, interfacing two electromagnetic modes of widely different frequencies, was used as an optomechanical frequency converter between itinerant optical and microwave fields [Tsang11]. The remarkable performance achieved in both frequency upconversion and downconversion underlines the potential applications of optomechanical system for quantum-state transfer [Tian10, Safavi-Naeini11b, Barzanjeh12, Wang12], for instance between two different platforms like superconducting circuits and optical networks [McGee13].

Other types of devices aimed at measuring and controlling the mechanical motion of small resonators by electrical means have gained interests over the past years. These are refereed to as micro- and nano-electromechanical systems and implement coupling of a mechanical element to a single-electron transistor [LaHaye04], a quantum point contact [Cleland02] or a superconducting two-level system such as a Cooper-pair box [LaHaye09] or a phase qubit [O'Connell10] for instance. General reviews reporting experiments conducted with such systems are available in Refs. [Blencowe04, Schwab05, Poot12].

We give now a simple description of optomechanical systems where the mechanical resonator couples capacitively to a microwave cavity. A qualitative description of the setup can be obtained using a simple Lagrangian approach, similar to the one described in the chapter treating superconducting circuits. The microwave cavity is modeled as a simple LC resonator, as described in Sec. 2.2 and shown in Fig. 4.2(b). This description remains valid even if the cavity is actually a transmission line resonator, as long as only one mode is excited by the drive. The Lagrangian of the coupled system is simply obtained from the inductive and charging energies of the LC resonator, together with the kinetic and potential energies of the mechanical resonator

$$\mathcal{L} = \frac{1}{2}L\dot{Q}^2 + \frac{1}{2}m\dot{x}_m - \frac{Q^2}{2C(x_m)} - \frac{1}{2}m\omega_m x_m^2, \tag{4.13}$$

where m is an effective mass for the mechanical resonator and ω_m its frequency. The mechanical displacement being generally small, one can approximate the coupling to linear order,

$$\frac{1}{C(x_m)} \simeq \frac{1}{C_0} - \frac{C_0'}{C_0^2}\, x_m. \tag{4.14}$$

The quantum mechanical Hamiltonian associated to the Lagrangian is

$$\hat{H} = \frac{\hat{\Phi}^2}{2L} + \frac{\hat{Q}^2}{2C_0} + \frac{\hat{p}_m^2}{2m} + \frac{1}{2}m\omega_m^2\hat{x}_m^2 - \frac{C_0'}{2C_0^2}\hat{Q}^2\hat{x}_m, \tag{4.15}$$

where $[\hat{Q}, \hat{\Phi}] = [\hat{x}_m, \hat{p}_m] = i\hbar$. Introducing the corresponding optical ($\hat{a}$) and mechanical ($\hat{b}$) mode operators, one can rewrite the Hamiltonian as

$$\hat{H} = \hbar\omega_c\hat{a}^\dagger\hat{a} + \hbar\omega_m\hat{b}^\dagger\hat{b} - \frac{\hbar g_0}{2}(\hat{a} + \hat{a}^\dagger)^2(\hat{b} + \hat{b}^\dagger), \tag{4.16}$$

where the unperturbed cavity frequency $\omega_c = 1/\sqrt{LC_0}$ is in the GHz range. The optomechanical coupling rate is given by $g_0 = x_{\mathrm{zpf}}\omega_c C_0'/(2C_0)$. The usual form of the radiation-pressure interaction is recovered by neglecting the fast rotating terms $\hat{a}^2$ and $\hat{a}^{\dagger 2}$.

Having a large fraction of the overall capacitance responding to the mechanical motion is important to achieve large coupling rates g_0. This explains why the recent experiments using a flexural membrane, as depicted in Fig. 4.2(a), with a thin gap for the capacitance [Teufel11b, Teufel11a, Palomaki13a, Palomaki13b] can achieve a value of g_0 that is comparable to optomechanical devices in the optical domain.

4.3.4 Ultracold atom clouds

Recently, a particular branch of cavity optomechanics has developed where the solid-state mechanical resonator is replaced by a cloud of ultracold atoms [Botter09, Stamper-Kurn12]. The basic setup consists of two distinct components: a driven Fabry-Pérot resonator, whose length is $\sim 200\mu$m, and a cloud of atoms (see Fig. 4.3). The pioneering experiments conducted by the groups of Stamper-Kurn [Murch08b] and Esslinger [Brennecke08] use a gas of Rb atoms. In the first case, the atoms are kept in the cavity using far off-resonance optical trapping: a deep optical lattice is formed by a longitudinal laser beam that is largely detuned from the cavity resonance frequency. In the second case, the atom cloud, trapped by a transversal crossed-beam dipole trap, forms a Bose-Einstein condensate whose density fluctuations couple to the cavity light field and play the role of the mechanical resonator. In both these setups, the atoms were precooled before the interaction with the resonator light field was turned on. Successful observations of bistable behavior [Gupta07, Ritter09] and quantum-measurement back-action [Murch08b] have been reported. A similar experiment demonstrated motional cooling of a cloud of Cs atoms [Schleier-Smith11]. Lately, a remarkable achievement was the first observed signature of noise squeezing, caused by the mechanical motion, of the light coming out of the cavity [Brooks12].

We give a simplistic description of the setup used in [Gupta07, Murch08b], many details of which can be found in [Murch08a]. The dispersive interaction between atoms and the light field gives rise to an effective optomechanical coupling between the center of mass motion of the atomic cloud and the optical field. The ac-Stark shift of the cavity frequency, produced by the atoms absorbing and re-emitting photons into the cavity mode, depends on the position of the atoms. Hence, the atom cloud acts as a dielectric medium moving in the light field, collectively changing the refractive index of the cavity. We start by considering the Tavis-Cummings Hamiltonian,

$$\hat{H} = \hbar\omega_c \hat{a}^\dagger \hat{a} + \frac{\hbar\omega_a}{2}\sum_{i=1}^{N}\sigma_z^{(i)} + \hbar\sum_{i=1}^{N} g(\mathbf{r}_i)\left(\hat{a}\sigma_+^{(i)} + \hat{a}^\dagger\sigma_-^{(i)}\right) \tag{4.17}$$

which describes the dipole interaction, in the rotating-wave approximation, of N identical atoms with transition frequency ω_a, to a single mode of the cavity with frequency ω_c. Here, $\sigma_j^{(i)}$ $(j = z, \pm)$ denote the usual spin Pauli operators of the i-th atom, $\hat{a}(\hat{a}^\dagger)$ are the annihilation (creation) operators of the optical cavity mode. The coupling rate of each atom to the cavity field, $g(\mathbf{r}_i)$, depends on the atom position $\mathbf{r}_i$.

An effective Hamiltonian can be obtained in the dispersive limit, when the atom-cavity detuning $\Delta_{ac} = \omega_a - \omega_c$ is large compared to the coupling rate, $|g/\Delta_{ac}| \ll 1$. The effective

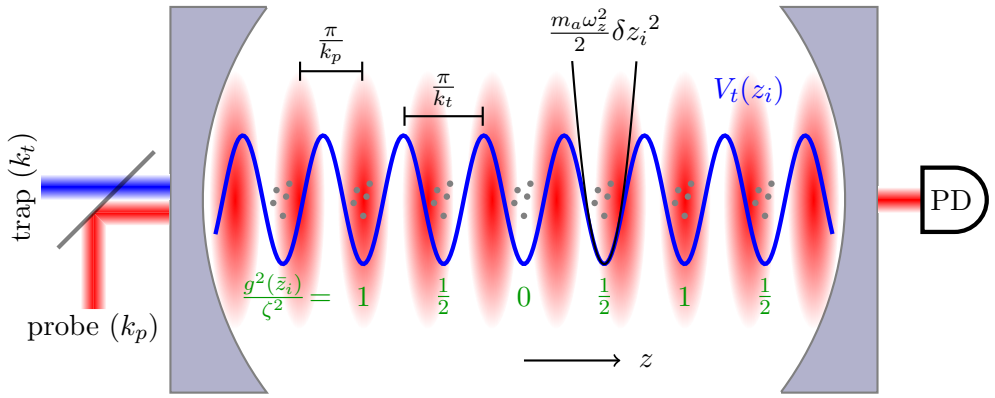

Figure 4.3: *Cavity optomechanics with ultracold atoms.* Schematic representation of the setup. The optical cavity is formed by two mirror (light purple). The probe laser, with wave vector k_p, excites a cavity mode (red) which interacts dispersively with the atoms (gray dots). The atoms are caught inside the cavity by an optical trap, formed by a second off-resonant longitudinal laser at k_t. This dipole trap is shown as a lattice potential (blue), which is approximated by an harmonic potential, $V_t(z_i) = \frac{1}{2}m_a\omega_z^2(z_i - \bar{z}_i)^2$, (black parabola) near the atom equilibrium positions $\bar{z}_i$. The dipole coupling of each atom to the probe field varies, from 0 to ζ, between the sites of the optical lattice (green). The cavity mode is probed in transmission.

Hamiltonian is found from the unitary transformation $\hat{U} = e^{\hat{S}}$, where

$$\hat{S} = \sum_{i=1}^{N} \frac{g(\mathbf{r_i})}{\Delta_{ac}} \left(\hat{a}\sigma_+^{(i)} - \hat{a}^\dagger \sigma_-^{(i)} \right). \tag{4.18}$$

To second-order in g/Δ_{ac} we obtain

$$\begin{aligned} \hat{U}\hat{H}\hat{U}^\dagger =& \hbar \left(\omega_c + \sum_{i=1}^{N} \frac{g^2(\mathbf{r}_i)}{\Delta_{ac}} \sigma_z^{(i)} \right) \hat{a}^\dagger \hat{a} + \frac{\hbar}{2} \sum_{i=1}^{N} \left(\omega_a + \frac{g^2(\mathbf{r}_i)}{\Delta_{ac}} \right) \sigma_z^{(i)} \\ &+ \hbar \sum_{i,j} \frac{g(\mathbf{r}_i) g(\mathbf{r}_j)}{\Delta_{ac}} \left(\sigma_+^{(i)} \sigma_-^{(j)} + \sigma_-^{(i)} \sigma_+^{(j)} \right) + \mathcal{O}\left(\frac{\hbar g^3}{\Delta_{ac}^2} \right). \end{aligned} \tag{4.19}$$

Far from resonance, atomic transitions are suppressed, provided Δ_{ac} is much larger than both the dipole coupling rate and the linewidth of the atomic transition. In this case, the atomic degrees of freedom are effectively frozen and the virtual absorption and re-emission of a photon by the atoms produces an ac-Stark shift of the cavity frequency,

$$\omega_c' = \omega_c - \sum_{i=1}^{N} \frac{g^2(\mathbf{r}_i)}{\Delta_{ac}}. \tag{4.20}$$

The coupling rate g depends on the spatial distribution of the electrical field inside the cavity. Neglecting transversal variations, it can be approximated by $g(\mathbf{r}_i) = \zeta \sin(k_p z_i)$, where z_i denotes the atom position along the cavity axis, and k_p the wavevector of the cavity mode used to probe the atomic motion. The positions are written as $z_i = \bar{z}_i + \delta z_i$, where $\bar{z}_i$ is the equilibrium position, mainly fixed by the deep trapping potential of the

optical trap $V_t(\bar{z}_i)$, and δz_i describes fluctuations. Around $\bar{z}_i$, the optical lattice is approximated by an harmonic potential $V_t(z_i) \simeq m_a\omega_z^2 {\delta z_i}^2/2$ (see Fig. 4.3). This assumption is valid in the Lamb-Dicke regime, $\omega_z \gg \hbar k_p^2/(2m_a)$, and for low temperature, $\hbar\omega_z \gg k_B T$. In this regime, the atoms most likely stay in their motional ground state and the condition $k\delta z_i \ll 1$ is satisfied, yielding

$$\omega_c' \simeq \omega_c - \Delta_N - G\,Z. \tag{4.21}$$

Here Δ_N is the static contribution to the frequency shift produced by all the atoms sitting at their equilibrium position, G is a frequency shift per unit displacement, and Z is a collective displacement variable, namely

$$\Delta_N = \sum_{i=1}^{N} \frac{g^2(\bar{z}_i)}{\Delta_{ac}}, \tag{4.22}$$

$$G = N_{\text{eff}} k \frac{\zeta^2}{\Delta_{ac}}, \tag{4.23}$$

$$Z = \frac{1}{N_{\text{eff}}} \sum_{i=1}^{N} \delta z_i \, \sin(2k_p \bar{z}_i). \tag{4.24}$$

The effective number of atoms, whose motion couples to the probe field, is given by

$$N_{\text{eff}} = \sum_{i=1}^{N} \sin^2(2k_p \bar{z}_i). \tag{4.25}$$

The collective variable Z is approximately a center of mass coordinate for the mass $M = N_{\text{eff}} m_a$, whose motion is relevant for the optical mode frequency shift. The mass M feels an effective harmonic potential characterized by the trapping frequency ω_z. The coordinate Z is treated as the position operator of a vibrational harmonic mode,

$$Z = \sqrt{\frac{\hbar}{2M\omega_z}} \left(\hat{b} + \hat{b}^\dagger\right). \tag{4.26}$$

Including the mechanical energy and neglecting the internal atomic degrees of freedom, the Hamiltonian finally reads

$$\hat{H} = \hbar(\omega_c - \Delta_N)\hat{a}^\dagger\hat{a} + \hbar\omega_z \hat{b}^\dagger\hat{b} - \hbar g_0 \hat{a}^\dagger\hat{a}\left(\hat{b} + \hat{b}^\dagger\right), \tag{4.27}$$

and we recognize the generic form of the radiation pressure-interaction. The optomechanical coupling rate g_0 for this setup is given by

$$g_0 = N_{\text{eff}} \frac{\zeta^2}{\Delta_{ac}} k \sqrt{\frac{\hbar}{2M\omega_z}}. \tag{4.28}$$

Experiments implementing cavity optomechanics with a cloud of ultracold atoms operate almost in the single-photon strong coupling regime $g_0/\kappa \sim 1$. The large dispersive coupling of the atoms to the light field, the effective number of atoms $N_{\text{eff}} \sim 10^5$, and most importantly the small effective mass M (resulting in large zero-point fluctuations) explain the large value of the single-photon coupling rate ($g_0/2\pi \sim 1$ MHz). Such a high ratio g_0/κ allows to explore nonlinear optical effects at low photon number and is at the moment only encountered in this particular implementation of cavity optomechanics. However, in these setups the small sideband resolution generally precludes the observation of quantum features of the collective mechanical mode.

4.3.5 Optomechanical crystals

Optomechanical crystals are one of the most recent designs of cavity optomechanics. In these systems, based on photonic crystal cavities [Vahala04], the light field is confined in a periodic in-plane silicon nanostructure. The photonic crystal simultaneously supports vibrational modes, whose motion modulates optical properties and therefore couples to the light field. Such optomechanical crystals have been realized in one-dimensional configurations [Eichenfield09, Safavi-Naeini10], where the photonic and phononic modes are localized in a small volume and couple strongly. In these setups, the mechanical resonance frequency can be as high as a few gigahertz. Optomechanical crystals combine both high mechanical quality factors and large sideband resolution. Remarkable experiments have been conducted, demonstrating cooling to the mechanical ground state [Chan11], mechanically-induced transparency [Agarwal10, Safavi-Naeini11a], frequency conversion between two different optical modes [Hill12], and ultimately generation of squeezed light [Safavi-Naeini13]. In addition, optomechanical coupling rates among the highest so far, of the order of MHz, and reaching a considerable fraction of cavity decay rate compared to other solid-state device ($g_0/\kappa \sim 0.25\%$) have been reported [Safavi-Naeini12]. In consequence, this type of optomechanical system is a strong candidate for the observation of quantum nonlinear effects.

Chapter 5

Equivalence between an optomechanical system and a Kerr medium

This chapter has been published in essentially the form presented here in

S. Aldana, C. Bruder, and A. Nunnenkamp
Equivalence between an optomechanical system and a Kerr medium,
Phys. Rev. A **88**, 043826 (2013).

Photons are ideal carriers of quantum information. They can propagate large distances in optical fibers before being absorbed, and their polarization has been used for quantum communication and quantum information applications [O'Brien07, O'Brien09]. However, photons barely interact, and thus it is difficult to implement the quantum two-qubit gates needed for universal quantum computation. This situation changes in an optical medium where the photons can inherit an effective interaction, often modeled as a Kerr nonlinearity. This is why so-called Kerr media are important for quantum technology based on photons [Milburn89, Chuang95, Chuang96, Hutchinson04].

Recently, it was suggested that optomechanical systems operated in the single-photon strong-coupling regime offer strong effective photon-photon interactions [Nunnenkamp11, Rabl11]. In optomechanical systems the position of a mechanical oscillator modulates the properties and (most commonly) the frequency of the optical cavity mode. The radiation pressure interaction is intrinsically nonlinear. It induces many interesting effects and enables many applications, e.g. sideband cooling [Wilson-Rae07, Marquardt07], radiation-pressure shot noise [Caves81, Braginsky92, Børkje10, Purdy13a], photon blockade [Rabl11], non-Poissonian photon statistics and multiphoton transitions [Kronwald13], and non-Gaussian and nonclassical mechanical states [Mancini97, Bose97, Nunnenkamp11, Qian12].

In this chapter, we will focus on the phenomenon of optical bistability, produced by the radiation pressure, and neglect other nonlinear effects such as the photothermal effect [Braginsky89, Fomin05, Marino11, Marino13] or a mechanical Duffing nonlinearity. Under certain conditions and sufficiently strong driving there are two classically stable equilibrium positions for the mechanical oscillator and correspondingly for the optical cavity. Optical bistability in optomechanical systems has been discussed in the context of ponderomotive squeezing [Fabre94, Mancini94] and entanglement [Ghobadi11], and led to one of the first experimental observations of optomechanical coupling [Dorsel83, Gozzini85]. Optical

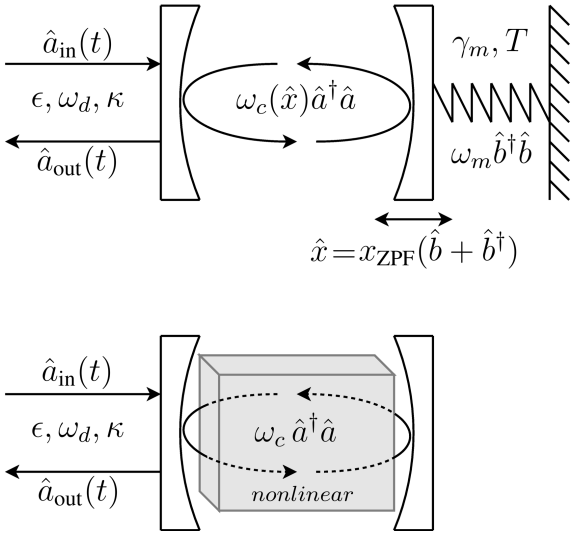

Figure 5.1: Schematic representations of an optomechanical setup (upper panel) and a Kerr medium in a cavity (lower panel). This chapter investigates in detail whether and in which way the two systems are equivalent.

bistability has also been discussed widely in the context of a Kerr medium [Drummond80, Walls08]. This raises the question whether and in which way the optomechanical system and the Kerr medium in a cavity can be considered to be equivalent, see Fig. 5.1 that shows both of these systems schematically. In the following we will investigate in detail the similarities and differences between optical bistability in an optomechanical system and a Kerr medium.

This chapter is organized as follows. In Sec. 5.1 we introduce the standard model of optomechanics – a cavity whose frequency is modulated by the position of a mechanical oscillator. We briefly introduce the steady-state mean-field equations of the system and the quantum Langevin description of quantum and thermal fluctuations for a linearized radiation-pressure interaction. In Sec. 5.2 we show that the mean-field equation for the optical mode is identical to the one for a Kerr medium, with a lower, a middle and an upper branch. In the optomechanical system, fluctuations of the mechanical mode change the picture. A study of the stability of the different mean-field solutions against fluctuations reveals a feature that is absent from the Kerr medium: the upper branch becomes unstable for certain parameters. We derive conditions on the parameters for this upper branch to remain stable. The stability requires the system to be in the resolved sideband regime with a mechanical quality factor that is not too large. In this case we expect the mechanical resonator to act as an effective Kerr medium for the optical mode, even in the quantum regime. This is confirmed in Sec. 5.3, where we compare the quantum steady states of both the optomechanical system and the Kerr medium, obtained from numerical solutions of the quantum master equations in the low-temperature limit. The optomechanical system exhibits the expected characteristic quantum signatures proving that it can be regarded as an effective Kerr medium.

5.1 Models for the optomechanical system and the Kerr medium

We first recall the standard model of optomechanics where the resonance frequency of an optical cavity is modulated by the position of a mechanical resonator (dispersive coupling). A monochromatic coherent light field with frequency ω_d and amplitude ϵ drives the optical mode. The full Hamiltonian, accounting for driving and dissipation, is $\hat{H} = \hat{H}_0 + \hat{H}_d + \hat{H}_\kappa + \hat{H}_{\gamma_m}$, where, in the rotating frame of the driving,

$$\hat{H}_0 = \hbar\omega_m \hat{b}^\dagger \hat{b} - \hbar\Delta_0 \hat{a}^\dagger \hat{a} - \hbar g_0 \hat{a}^\dagger \hat{a}(\hat{b} + \hat{b}^\dagger) \,, \tag{5.1}$$

and $\hat{H}_d = i\hbar\epsilon(\hat{a} - \hat{a}^\dagger)$. Here, $\hat{a}$ and $\hat{b}$ are the bosonic operators for the optical and mechanical modes, $\Delta_0 = \omega_d - \omega_c$ is the detuning of the drive from the unperturbed cavity resonance frequency ω_c, and ω_m the resonance frequency of the mechanical mode. The optomechanical coupling is given by $g_0 = -x_{\rm ZPF}(\partial\omega_c/\partial x)$, where $x_{\rm ZPF} = (2M\omega_m/\hbar)^{-1/2}$ is the zero-point fluctuation amplitude of the mechanical resonator, M its mass, and $(\partial\omega_c/\partial x)$ is the derivative of the cavity frequency with respect to the resonator position $\hat{x} = x_{\rm ZPF}(\hat{b} + \hat{b}^\dagger)$. The term $\hat{H}_\kappa$ describes the damping of the optical cavity at rate κ, and $\hat{H}_{\gamma_m}$ the damping of the mechanical resonator at rate γ_m. This leads to the definition of two important ratios, the sideband parameter ω_m/κ and the mechanical quality factor $Q_m = \omega_m/\gamma_m$.

Using the input-output formalism [Walls08, Clerk10], the dissipative dynamics of the system is described by the quantum Langevin equations (QLEs)

$$\dot{\hat{a}} = \left(i\Delta_0 - \frac{\kappa}{2}\right)\hat{a} + ig_0\hat{a}(\hat{b} + \hat{b}^\dagger) - \sqrt{\kappa}\,\hat{a}_{\rm in} \,, \tag{5.2a}$$

$$\dot{\hat{b}} = -\left(i\omega_m + \frac{\gamma_m}{2}\right)\hat{b} + ig_0\hat{a}^\dagger\hat{a} - \sqrt{\gamma_m}\,\hat{\eta} \,, \tag{5.2b}$$

where $\hat{a}_{\rm in}(t) = \bar{a}_{\rm in} + \hat{\xi}(t)$ consists of a coherent driving amplitude $\bar{a}_{\rm in} = \epsilon/\sqrt{\kappa}$ and a vacuum noise operator $\hat{\xi}$ which satisfies $\langle\hat{\xi}(t)\hat{\xi}^\dagger(t')\rangle = \delta(t-t')$ and $\langle\hat{\xi}^\dagger(t)\hat{\xi}(t')\rangle = 0$. Similarly, the noise operator $\hat{\eta}$ describes coupling to a Markovian bath at temperature T, i.e., $\langle\hat{\eta}(t)\hat{\eta}^\dagger(t')\rangle = (n_{\rm th}+1)\delta(t-t')$ and $\langle\hat{\eta}^\dagger(t)\hat{\eta}(t')\rangle = n_{\rm th}\delta(t-t')$. In the absence of any other coupling, the bath gives rise to a thermal state with mean occupation number $n_{\rm th} = [\exp(\hbar\omega_m/k_BT) - 1]^{-1}$ for the mechanical oscillator. This treatment of the mechanical dissipation in the form of a QLE for the mechanical amplitude $\hat{b}$, rather than for the displacement $\hat{x}$, is correct as long as $Q_m \gg 1$.

The optical and mechanical field operators can be split into a coherent mean-field amplitude and fluctuations: $\hat{a}(t) = \bar{a} + \hat{d}(t)$ and $\hat{b}(t) = \bar{b} + \hat{c}(t)$. Inserting these expressions in the QLEs (5.2), we obtain two coupled mean-field equations (MFEs) for the amplitudes $\bar{a}$ and $\bar{b}$. In steady state they read

$$0 = \left[i\Delta_0 + ig_0\left(\bar{b} + \bar{b}^*\right) - \frac{\kappa}{2}\right]\bar{a} - \epsilon \,, \tag{5.3a}$$

$$0 = -\left(i\omega_m + \frac{\gamma_m}{2}\right)\bar{b} + ig_0|\bar{a}|^2 \,. \tag{5.3b}$$

The coherent amplitude of the optical field $\bar{a}$ corresponds to a mean cavity occupation $\bar{n} = |\bar{a}|^2$ and produces a static radiation-pressure force $g_0\,\bar{n}/x_{\rm ZPF}$ on the resonator, displacing its equilibrium position by an amount $x_{\rm ZPF}(\bar{b} + \bar{b}^*)$. Proceeding this way we eliminate

the coherent drive ϵ from the QLEs for the operators $\hat{c}$ and $\hat{d}$ which describe thermal and quantum fluctuations around the mean-field values.

For large optical mean-field amplitudes $|\bar{a}| \gg 1$ and small coupling $g_0 \ll \kappa, \omega_m$, we can neglect the nonlinear terms like $\hat{d}^\dagger\hat{d}$ or $\hat{d}\hat{c}$ in the QLEs. As a result, the optomechanical interaction becomes bilinear: $g_0\hat{a}^\dagger\hat{a}(\hat{b}+\hat{b}^\dagger) \rightarrow g_0(\bar{a}^*\hat{d}+\bar{a}\,\hat{d}^\dagger)(\hat{c}+\hat{c}^\dagger)$. Introducing the convenient vector notation $\hat{\boldsymbol{u}} = (\hat{d}^\dagger, \hat{d}, \hat{c}^\dagger, \hat{c})^T$ and $\hat{\boldsymbol{u}}_{\rm in} = (\sqrt{\kappa}\hat{\xi}^\dagger, \sqrt{\kappa}\hat{\xi}, \sqrt{\gamma_m}\hat{\eta}^\dagger, \sqrt{\gamma_m}\hat{\eta})^T$, we can write the linearized QLEs in matrix form,

$$\frac{d}{dt}\hat{\boldsymbol{u}}(t) = -\boldsymbol{A}\cdot\hat{\boldsymbol{u}}(t) - \hat{\boldsymbol{u}}_{\rm in}(t)\,, \tag{5.4}$$

where $\boldsymbol{A}$ reads

$$\boldsymbol{A} = \begin{pmatrix} \frac{\kappa}{2}+i\Delta & 0 & ig^* & ig^* \\ 0 & \frac{\kappa}{2}-i\Delta & -ig & -ig \\ ig & ig^* & \frac{\gamma_m}{2}-i\omega_m & 0 \\ -ig & -ig^* & 0 & \frac{\gamma_m}{2}+i\omega_m \end{pmatrix}. \tag{5.5}$$

The new parameters entering the matrix $\boldsymbol{A}$ are the enhanced optomechanical coupling $g = g_0\bar{a}$ and the effective detuning $\Delta = \Delta_0 + g_0(\bar{b}+\bar{b}^*) = \Delta_0 + 2\bar{n}g_0^2/\omega_m$.

The Kerr medium [Drummond80, Walls08], to which we aim to compare the optomechanical system, is described by the Hamiltonian $\hat{H}' = \hat{H}_K + \hat{H}_d + \hat{H}_\kappa$, where, in the rotating frame of the driving,

$$\hat{H}_K = -\hbar\Delta_0\hat{a}^\dagger\hat{a} - \hbar\frac{g_0^2}{\omega_m}\left(\hat{a}^\dagger\hat{a}\right)^2\,, \tag{5.6a}$$

$$\hat{H}_d = i\hbar\epsilon(\hat{a}-\hat{a}^\dagger)\,, \tag{5.6b}$$

and $\hat{H}_\kappa$ describes again the damping of the optical cavity at rate κ. The QLE for this optical mode $\hat{a}$ is

$$\dot{\hat{a}} = \left[i\left(\Delta_0 + \frac{g_0^2}{\omega_m}\right) - \frac{\kappa}{2}\right]\hat{a} + 2i\frac{g_0^2}{\omega_m}\hat{a}^\dagger\hat{a}^2 - \sqrt{\kappa}\hat{a}_{\rm in}\,, \tag{5.7}$$

where the input operator $\hat{a}_{\rm in}(t)$ is the same as for the optomechanical system. The steady-state equation for the mean-field amplitude $\bar{a}$ is

$$0 = \left[i\left(\Delta_0 + \frac{g_0^2}{\omega_m}\right) - \frac{\kappa}{2}\right]\bar{a} + 2i\frac{g_0^2}{\omega_m}|\bar{a}|^2\bar{a} - \epsilon\,. \tag{5.8}$$

Replacing Δ_0 by $\Delta_0 - g_0^2/\omega_m$ in Eq. (5.8) yields the equation for the optical mean-field amplitude $\bar{a}$ of the optomechanical system obtained from Eq. (5.3) by eliminating the mechanical mean-field amplitude $\bar{b}$. This frequency shift of the detuning Δ_0 is consistent with the fact that $\hat{H}_0$ and $\hat{H}_K$ are connected by the canonical (polaron) transformation $\hat{U} = \exp[(g_0/\omega_m)(\hat{b}-\hat{b}^\dagger)\hat{a}^\dagger\hat{a}]$. Applying $\hat{U}$ to the optomechanical Hamiltonian $\hat{H}_0$, Eq. (5.1), we obtain $\hat{U}\hat{H}_0\hat{U}^\dagger = \hat{H}_K + \omega_n\hat{b}^\dagger\hat{b}$. In this frame, the optomechanical interaction is eliminated and the optical mode acquires a Kerr nonlinearity of the form of Eq. (5.6a) [Nunnenkamp11, Rabl11].

5.2 Optical bistability in the semiclassical regime

In the following, we will first show that the optomechanical system has MFEs with three solutions in a certain range of driving frequency and driving amplitude, just as the Kerr

medium does. After discussing the characteristic behavior of the mean-field solutions in the regime of optical bistability, we study the stability of the mean-field solutions against fluctuations of both the optical and mechanical mode and point out the differences with the Kerr medium. Finally, we find parameters for which the optomechanical system is accurately described by an effective Kerr medium.

5.2.1 Bistability at the mean-field level

We briefly review the origin of bistability in the mean-field equations of the optomechanical system [Meystre85, Meystre07, Gozzini85, Fabre94, Mancini94].

To simplify the notation we define the dimensionless nonlinearity parameter χ, detuning y, and driving power z by

$$\chi = \frac{g_0^2}{\omega_m \kappa} , \tag{5.9}$$

$$y = -\frac{\Delta_0}{\kappa} , \tag{5.10}$$

$$z = \chi \left(\frac{\epsilon}{\kappa}\right)^2 . \tag{5.11}$$

Combining Eqs. (5.3a) and (5.3b) we obtain a third-order polynomial root equation for the mean-field cavity occupation, $p(\chi\bar{n}) = 0$, where

$$p(\lambda) = 4\lambda^3 - 4y\lambda^2 + \left(y^2 + \frac{1}{4}\right)\lambda - z . \tag{5.12}$$

The MFE for the Kerr medium, Eq. (5.8), leads to the same equation for $\bar{n}$, provided we replace y by $y - \chi$ in Eq. (5.12).

Equation (5.12) indicates that the MFEs can have either one or three solutions, depending on the number of real roots of the polynomial. The three roots depend on the dimensionless detuning y and driving power z. Since the mean-field cavity occupation $\bar{n}$ follows from $p(\chi\bar{n}) = 0$, the nonlinearity parameter χ determines whether optical bistability occurs at small or large driving power and photon number.

The optical mean-field amplitude is $\bar{a} = -e^{i\varphi}\sqrt{\lambda/\chi}$, where $\varphi = \arctan(4\lambda - 2y)$. If the detuning y and driving power z are such that the equation $p(\lambda) = 0$ has three real roots, the smaller χ, the more distant in phase space are the different optical mean-field amplitudes $\bar{a}$. A similar observation can be made concerning the mechanical resonator: the equation $p(\lambda) = 0$ also holds for $\lambda = \sqrt{\chi\omega_m/(4\kappa)}(\bar{b}+\bar{b}^*)$, where $\bar{b}+\bar{b}^*$ is the equilibrium position of the mechanical resonator in units of x_{ZPF}. Therefore, the smaller χ and the sideband parameter ω_m/κ, the more distant are the different equilibrium positions.

We now examine some characteristic features of the MFEs, which occur both in an optomechanical system (5.3) and a Kerr medium (5.8). To this end, we find the conditions on the detuning y and the driving power z for the MFEs to have three solutions, and illustrate them with a few examples.

First we observe that the equation $p(\lambda) = 0$ can have three real roots only if the detuning y and the driving power z exceed some threshold value $\tilde{y}$ and $\tilde{z}$ [Risken87, Vogel89, Fabre94, Mancini94],

$$y > \tilde{y} \;=\; \frac{\sqrt{3}}{2} \simeq 0.87 , \tag{5.13a}$$

$$z > \tilde{z} \;=\; \frac{1}{6\sqrt{3}} \simeq 0.1 . \tag{5.13b}$$

Therefore, optical bistability can only be found for red-detuned driving frequencies. In addition, the three roots are real only if

$$z_-(y) < z < z_+(y)\,, \tag{5.14}$$

where

$$z_\pm(y) = \frac{1}{27}\left[y(y^2+3\tilde{y}^2) \pm (y^2-\tilde{y}^2)^{3/2}\right]\,. \tag{5.15}$$

The region in (y,z)-parameter space where Eqs. (5.13) and (5.14) are satisfied is shown in Fig. 5.2(c) with the labels *II* (blue) and *III* (purple). In this region the three mean-field occupations satisfy $\bar{n}_1 < n_- < \bar{n}_2 < n_+ < \bar{n}_3$, where $n_\pm$ are found from $p'(\chi n_\pm) = 0$ and read

$$\chi n_\pm(y) = \frac{1}{6}\left[2y \pm (y^2-\tilde{y}^2)^{1/2}\right]. \tag{5.16}$$

In the following, we refer to $\bar{n}_1$, $\bar{n}_2$, and $\bar{n}_3$ as the lower, middle, and upper branch of the MFEs.

In Fig. 5.2(a) we show the mean-field occupation $\chi\bar{n}$ as a function of the driving power z for fixed detuning y. For an increasing driving power z and a detuning above the threshold $y > \tilde{y}$, the three branches of the mean-field occupation $\bar{n}$ form a characteristic S-shaped curve. The lower branch starts from the origin and ends at the turning point given by (z_+, n_-) where the middle branch starts. The upper branch starts from the second turning (z_-, n_+), where the middle branch ends, and increases further.

In Fig. 5.2(b) we plot the mean-field occupation $\chi\bar{n}$ as a function of the detuning y for fixed driving power z. The cavity line shape is approximately Lorentzian if the driving power is far below the threshold $z \ll \tilde{z}$ (not shown). For larger and larger z it becomes more and more asymmetric and tilts until for $z = \tilde{z}$, it has an infinite slope at $y = \tilde{y}$. For a driving power beyond this threshold the cavity line-shape has three branches in the range of detuning y determined by Eq. (5.14).

According to these considerations, the optomechanical system and the Kerr medium are equivalent at the level of the steady-state MFEs. Our next goal is to discuss the stability of the different branches of the MFEs. The existence of three solutions to the MFEs indicates that the optomechanical system may be in a regime of bistability, with stable lower and upper branches, as well as an unstable middle branch. While for the Kerr medium this is always true [Drummond80], a stability analysis leads to different conclusions in the case of the optomechanical system. In addition, if the detuning y and driving power z lead to a unique solution for the mean-field cavity occupation $\bar{n}$, this solution is always stable for the Kerr medium, but not necessarily so for the optomechanical system.

5.2.2 Stability analysis of the mean-field solutions

The upper and lower branches are always stable for the Kerr medium. To find the range of parameters where the optomechanical system reproduces this behavior, we analyze the stability of the different branches of the MFEs (5.3) against fluctuations of both the optical and mechanical modes.

The stability of a point in any of the branches of the MFEs is established, if the linear QLEs (5.4), describing the fluctuations around this point, are stable. This in turn is ensured if all the eigenvalues of the matrix $\boldsymbol{A}$ given in Eq. (5.5), derived from the corresponding mean-field amplitudes $\bar{a}$ and $\bar{b}$, have positive real parts. This has to be verified even if the MFEs have only one solution.

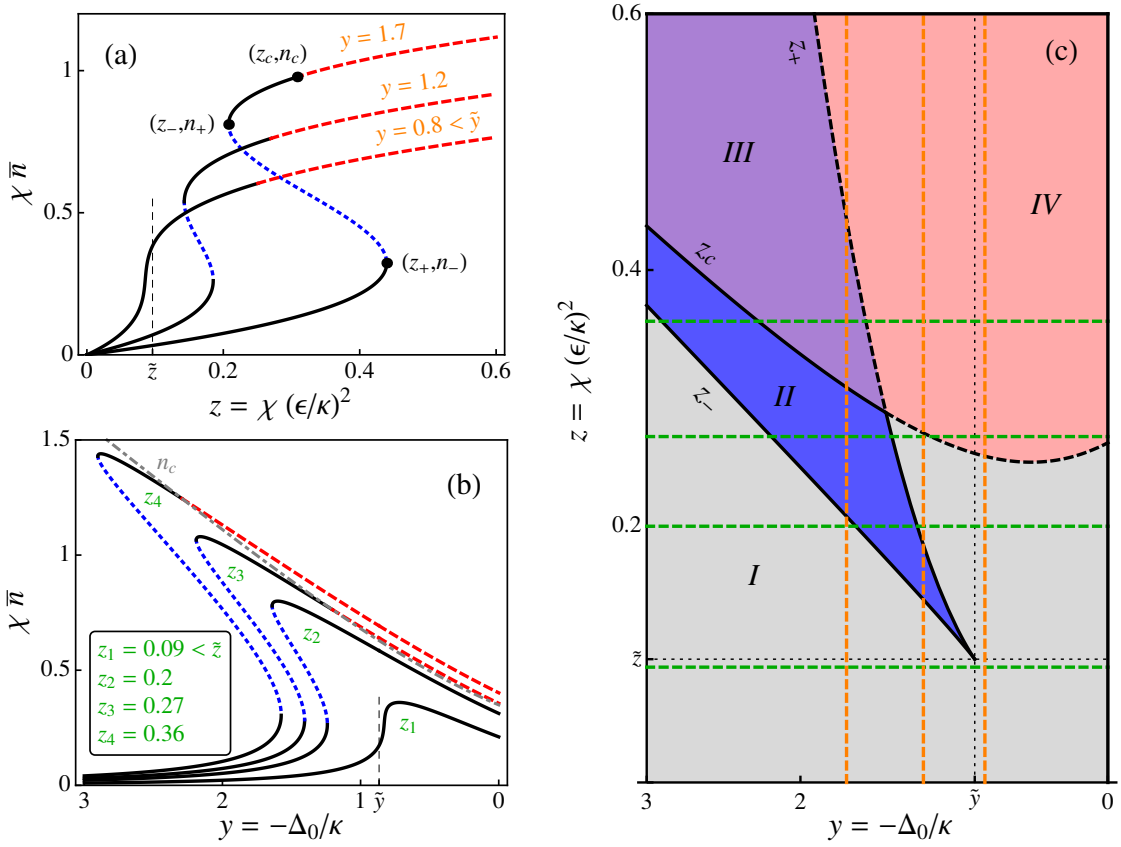

Figure 5.2: *Optical bistability in the semiclassical regime.* Typical curves for the mean-field cavity occupation $\bar{n}$ as a function of the dimensionless driving power z (a) and the dimensionless detuning y (b), obtained from the condition $p(\chi\bar{n}) = 0$ [see Eq. (5.12)]. According to the stability criteria $c_{1,2} > 0$ [see Eqs. (5.17)], Gaussian fluctuations lead to stable (solid black) or unstable (dotted blue and dashed red) mean-field solutions. As in the case of the Kerr medium, the first criterion $c_1 > 0$ always yields an unstable middle branch (dotted blue), while the additional criterion for the optomechanical system $c_2 > 0$ can turn part of the upper or only branch unstable (dashed red). In (b) we also show the critical mean-field occupation n_c (dash-dotted gray) obtained from the condition $c_2 = 0$. In (c) we summarize the behavior of the mean-field solution as a function of the parameters y and z. In regions II and III, between the curves z_- and z_+, Eqs. (5.13) and (5.14) are satisfied and there are three distinct mean-field solutions; the middle branch is always unstable. In region II (blue) the lower and upper branches are stable. In region III (purple) the second stability criterion shows the upper branch to be unstable ($c_2 < 0$) and only the lower branch is stable. In regions I and IV the mean-field equations (MFEs) have only one solution. Below the z_c curve in region I (gray) this unique branch is stable, while in region IV (red) the second criterion again shows that this solution is unstable ($c_2 < 0$). The values of the detuning y and driving power z used in (a) and (b) are indicated by the orange and green dashed lines. Note that none of these features depends on the nonlinearity parameter χ, due to appropriate scaling of the axes. The threshold detuning $\tilde{y}$ and driving power $\tilde{z}$ indicate the minimal values of y and z needed for the MFEs to have three solutions. The sideband parameter and mechanical quality factor chosen to show the influence of the second stability criterion $c_2 > 0$ are $\omega_m/\kappa = 10$ and $Q_m = 1000$.

Branch		Kerr medium	Optomechanical system	
No.	Type			
3	Lower	Stable	Stable	
	Middle	Unstable	Unstable	
	Upper	Stable	Stable $\bar{n} < n_c$	Unstable $\bar{n} > n_c$
1	-	stable	stable $\bar{n} < n_c$	unstable $\bar{n} > n_c$

Table 5.1: Stability for the different branches in an optomechanical system and a Kerr medium determined from the QLEs (5.4) and (5.7). The critical mean-field occupation n_c is found from the stability criterion, Eq. (5.17b), and depends on the detuning $y = -\Delta_0/\kappa$, the sideband parameter ω_m/κ, and the mechanical quality factor Q_m.

The differences and similarities between the optomechanical system and the Kerr medium are summarized in Table 5.1.

The difference between the two systems is explained by the parametric instability in the optomechanical system [Marquardt06, Ludwig08] that occurs at a mean-field occupation $\bar{n}$ above some critical value n_c. Around such a mean-field solution, the linear dynamics of optical and mechanical fluctuations becomes unstable. This particular feature of the optomechanical system is illustrated in Fig. 5.2; it is absent for the Kerr medium.

In Figs. 5.2(a) and 5.2(b), we indicate the unstable segments of the branches where $\bar{n} > n_c$. In case the MFEs have three branches, this critical value for the mean-field occupation n_c systematically lies in the upper branch or in its extension to the region where there is only one branch.

In Fig. 5.2(a), for a fixed detuning above threshold $y > \tilde{y}$, the upper branch is stable only in a finite segment near the second turning point n_+ at the beginning of the upper branch. The size of this stable segment diminishes as the detuning y increases, and shrinks to a single point in the limit of a far red-detuned driving frequency. The same effect is seen in Fig. 5.2(b). With increasing driving power z the stability in the upper branch is confined to a smaller and smaller segment near the maximum of the cavity line shape.

In Fig. 5.2(c), the regions in (y, z)-parameter space where the upper or only branch turns unstable are labeled by *III* and *IV*. These are the regions where the driving power z is larger than the critical value z_c, found by solving the equation $p\,(\chi n_c) = 0$ for z, where p is given in Eq. (5.12). The range of detuning y or driving power z at which bistability is observed shrinks with increasing y or z.

We now characterize the regime leading to optical bistability in the optomechanical system, and therefore examine how the stability of the branches depends on the parameters. To this end, we apply the Routh-Hurwitz criterion [DeJesus87] to the linear QLEs (5.4). Two conditions have to be satisfied for a particular mean-field solution to be

stable, $c_{1,2} > 0$, where [1]

$$c_1 = 4|g|^2\Delta + \omega_m\left(\Delta^2 + \frac{\kappa^2}{4}\right), \tag{5.17a}$$

$$c_2 = \kappa\,\gamma_m\left[\left(\Delta^2 - \omega_m^2\right)^2 + \frac{1}{2}\left(\Delta^2 + \omega_m^2\right)(\kappa+\gamma_m)^2 + \frac{1}{16}(\kappa+\gamma_m)^4\right] - 4|g|^2\Delta\,\omega_m\,(\kappa+\gamma_m)^2\,. \tag{5.17b}$$

The identification of the parameter regime leading to $c_{1,2} > 0$ is done as follows. We replace $|g|^2$ and Δ by their $\bar{n}$-dependent expressions,

$$|g|^2 = \kappa\omega_m\,\chi\bar{n}\,, \tag{5.18}$$

$$\Delta = \kappa(2\chi\bar{n} - y)\,, \tag{5.19}$$

in Eqs. (5.17), and express $c_{1,2}$ as functions of the rescaled mean-field occupation $\chi\bar{n}$, the detuning y, the sideband parameter ω_m/κ, and the mechanical quality factor $Q_m = \omega_m/\gamma_m$.

From the condition $c_1 < 0$ we conclude that the middle branch is unstable [Meystre85, Meystre07, Fabre94, Mancini94]. This follows from $\mathrm{sgn}(c_1) = \mathrm{sgn}\left[(n_+ - \bar{n})(n_- - \bar{n})\right]$, where $n_\pm$, Eq. (5.16), are the values of the mean-field cavity occupation at the lower and upper limits of the middle branch. The physical interpretation of this condition is simple. In the middle branch, the modification of the mechanical frequency due to radiation pressure, also known as the optical spring effect, is such that the modified mechanical force is no longer a restoring force.

In the Kerr medium, the same stability condition, $c_1 > 0$, is found from the linear QLEs, obtained by substituting $\hat{a} = \bar{a} + \hat{d}$ in Eq. (5.7) and neglecting second- and third-order terms in $\hat{d}$, $\hat{d}^\dagger$. No other criteria are needed to establish the stability of the system, and therefore the lower and upper branches are always stable.

The condition $c_2 = 0$ is equivalent to the relaxation rate of the system going to zero [Genes08a]. In a stable system, this relaxation rate is the real part of the eigenvalue of $\boldsymbol{A}$ closest to zero. Above the critical mean-field occupation, $\bar{n} > n_c$, this relaxation rate becomes negative, $c_2 < 0$, and the branch turns unstable. If in addition $\bar{n}$ is the only mean-field solution, the system is parametrically unstable. We find n_c by solving the equation $c_2 = 0$ for $\bar{n}$, as a function of the detuning y, the sideband parameter ω_m/κ, and the mechanical quality factor Q_m.

It turns out that n_c always lies in the upper branch or in its extension to the region with only one branch. This can be seen as follows. Since the condition $c_2 > 0$ is automatically satisfied for negative *effective* detuning, $\Delta \leq 0$, we find a lower bound for the critical occupation,

$$n_c \;\geq\; n_\Delta = \frac{y}{2\chi}\,. \tag{5.20}$$

In addition, the effective detuning Δ always turns positive in the upper branch, since $n_\Delta \geq n_+$. Thus the upper branch is only stable in the range $n_+ < \bar{n} < n_c$. This stable portion can be very small, e.g., in the extreme case $-\Delta_0 \gg \kappa$ and $\gamma_m = 0$, we have $n_c = n_\Delta \simeq n_+$.

[1] In Refs. [Genes08a, Vitali07a, Vitali07b, Genes08b], similar criteria have been obtained using a quantum Brownian motion approach to treat mechanical dissipation. Their criteria are equivalent to $c_{1,2}$ in the limit $Q_m \gg 1$.

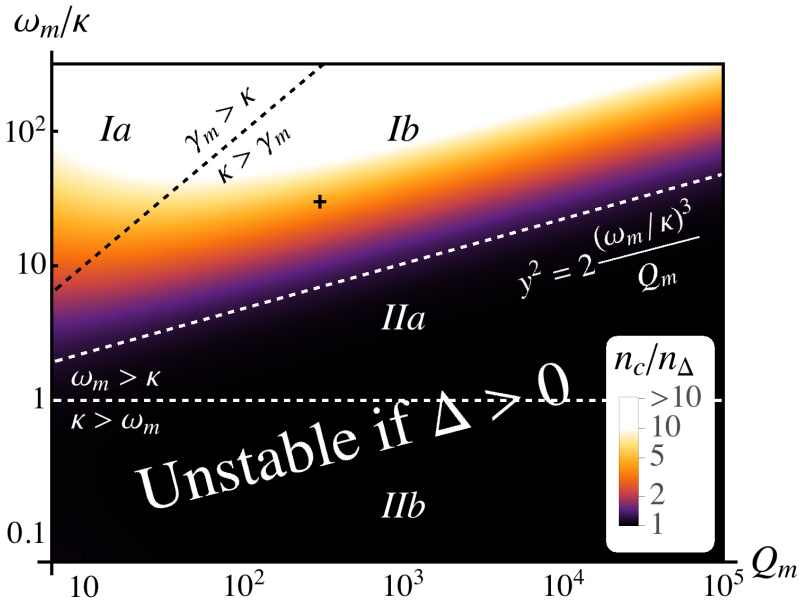

Figure 5.3: Critical cavity occupation n_c in units of n_Δ, as a function of the sideband parameter ω_m/κ and the mechanical quality factor Q_m. At n_c the mean-field solution $\bar{n}$ leads to unstable linear dynamics for the optomechanical system. The cavity occupation $n_\Delta = y/(2\chi)$ marks the point at which the effective detuning Δ becomes positive. We find n_c from the second stability criterion, Eq. (5.17b). The bare detuning is $y = -\Delta_0/\kappa = 1.5$. Note that the ratio n_c/n_Δ does not depend on the nonlinearity parameter χ. The black cross indicates the parameters used in Fig. 5.4.

In Fig. 5.3 we compare the critical mean-field cavity occupation n_c to the occupation n_Δ at which Δ changes sign. The ratio n_c/n_Δ is shown as a function of ω_m/κ and Q_m. If n_c/n_Δ is large, the upper branch is stable beyond the parameter range leading to bistability, $n_c \gg n_+$, mimicking the behavior of the Kerr medium. On the contrary, if $n_c/n_\Delta \simeq 1$, the upper branch turns unstable for $\Delta > 0$ and is only stable on a finite segment near its beginning.

We can distinguish four parameter regimes which encompass most experimental situations.

Resolved sideband and large mechanical damping (Ia)

For extremely low cavity damping, $\omega_m > \gamma_m > \kappa$, the critical occupation n_c is approximately

$$\chi n_c = \frac{1}{4}\left(y + \sqrt{y^2 + 2\,Q_m\frac{\omega_m}{\kappa}}\right) . \tag{5.21}$$

In the case of a fixed detuning satisfying $y^2 \ll 2Q_m\omega_m/\kappa$, we have $n_c \gg n_\Delta$ and the upper branch is stable on a considerable segment, extending up to driving powers z and mean-field occupations $\bar{n}$ that are much larger than those needed for bistable MFEs, i.e., $z_c \gg z_+$ and $n_c \gg n_+$. We recall that z_c is found by solving the equation $p(\chi n_c) = 0$, with p defined in Eq. (5.12). Therefore, the mean-field behavior of the optomechanical system is equivalent to the behavior of a Kerr medium in the regime of bistability. In Ref. [Kronwald13], the optomechanical system was compared to the Kerr medium in terms of the full counting statistics of photons. Although the two systems can behave differently

in some regime of parameters, the authors demonstrate that the influence of the mechanical resonator reduces to an effective Kerr nonlinearity when $\gamma_m \sim \kappa$, in particular with $y = \omega_m/\kappa$.

Resolved sideband and small mechanical damping (Ib and IIa)

In the regime characterized by $\omega_m > \kappa > \gamma_m$, the critical mean-field cavity occupation is found to be approximately

$$\chi n_c = \frac{1}{4}\left(y + \sqrt{y^2 + 2\,\frac{(\omega_m/\kappa)^3}{Q_m}}\right). \tag{5.22}$$

In this case, the parameter $(\omega_m/\kappa)^3/Q_m$ plays an important role to characterize the mean-field behavior.

If $Q_m > (\omega_m/\kappa)^3$, we obtain $n_c \simeq n_\Delta$ for a detuning above the bistability threshold $y > \tilde{y}$. In this case, the upper branch turns unstable if the effective detuning is positive, $\Delta > 0$. In addition, this means that if the detuning is negative and large, such that $-\Delta_0 \gg \kappa$, the stable segment is small, as $n_\Delta \simeq n_+$.

In the opposite limit, $Q_m \ll (\omega_m/\kappa)^3$, we can have $n_c \gg n_\Delta$ as in the previous case ($\gamma_m > \kappa$), provided the detuning y satisfies $y^2 \ll (\omega_m/\kappa)^3/Q_m$. The same conclusions then apply, i.e., $z_c \gg z_+$ and $n_c \gg n_+$, and the mean-field behavior of the optomechanical system and the Kerr medium is equivalent in the parameter regime of bistability.

Using the exact expression for n_c, we see in Fig. 5.3 that the border between the region where the optomechanical system experiences a parametric instability as soon as $\Delta > 0$ (black region), and the region where the system is still linearly stable for some positive effective detuning, $n_c > n_\Delta$, is approximately given by $y^2 = 2(\omega_m/\kappa)^3/Q_m$. Above this line, an optomechanical system driven to the regime of bistability behaves like a Kerr medium, as described by Eqs. (5.6) and (5.7). This will be confirmed in the next section by obtaining the quantum steady state of both systems numerically and showing that the states of the optical mode are similar.

Many experimental realizations of cavity optomechanics are in the resolved-sideband limit and fall into this category: coated micromechanical resonators [Groblacher09a], micromechanical microwave resonators [Regal08, Rocheleau10, Teufel11b, Massel11], photonic crystal cavities [Chan11], microspheres [Park09], and microtoroids [Schliesser08, Verhagen12].

Unresolved sideband and small mechanical damping (IIb)

The critical occupation n_c can be approximated in the limit of a small sideband parameter ω_m/κ and large enough mechanical quality factor, such that $1 > \omega_m/\kappa > 1/Q_m$, as

$$\chi n_c = \frac{1}{4}\left(y + \sqrt{y^2 + \frac{\kappa/\omega_m}{8\,Q_m}}\right). \tag{5.23}$$

If the bare detuning Δ_0 is negative and exceeds the threshold value for possible bistability, $y > \tilde{y}$, we obtain that $n_c \simeq n_\Delta$. The upper branch turns unstable as soon as the effective detuning Δ is positive, and for large bare red detuning, $-\Delta_0 \gg \kappa$, the upper branch is only stable on a small segment close to its beginning.

In this regime we find several experimental implementations of optomechanics: ultracold atoms [Murch08b, Schleier-Smith11, Brooks12], suspended membranes [Thompson08], and coated mechanical resonators [Arcizet06a, Kleckner11].

A simple interpretation of the critical mean-field occupation n_c in Eqs. (5.22) and (5.23) can be provided by considering the total mechanical damping $\gamma_{\rm tot} = \gamma_m + \Gamma_{\rm opt}$, where $\Gamma_{\rm opt}$ is the additional mechanical damping induced by coupling to the optical degree of freedom. In the weak-coupling limit of linearized optomechanics, i.e., $g, \gamma_m < \kappa$, this contribution is given by $\Gamma_{\rm opt} = -2\,\mathrm{Im}\,\Sigma(\omega_m)$ where $\Sigma(\omega) = -ig^2\left[\chi_c(\omega) - \chi_c^*(-\omega)\right]$ is the so-called optomechanical self-energy and $\chi_c(\omega) = \left[\kappa/2 - i(\Delta+\omega)\right]^{-1}$ the optical susceptibility [Marquardt07]. In this case, the condition $\bar{n} = n_c$ coincides with $\gamma_{\rm tot} = 0$ in both limits $\omega_m \lessgtr \kappa$.

Very small sideband parameter

In the regime where the sideband parameter is so small that $\omega_m/\kappa \ll 1/Q_m$, the situation is different. The upper branch is unconditionally stable as long as the detuning y is not too large, $y < \kappa/(\sqrt{32}Q_m\omega_m)$. For larger values of y, an unstable segment of the upper branch develops, from the second turning point n_+ up to some value n' of the mean-field cavity occupation given by

$$\chi n' = y\left(\frac{1}{2} + Q_m\frac{\omega_m}{\kappa} + \sqrt{\left(Q_m\frac{\omega_m}{\kappa}\right)^2 - \frac{1}{32y^2}}\right). \tag{5.24}$$

The dynamical timescales of the two modes are different in this limit. The optical mode adiabatically follows the mechanical motion and produces an effective mechanical potential with two stable equilibrium positions. However, as we have seen in the previous paragraph, this picture holds only if Q_m is not too large compared to κ/ω_m.

In this parameter regime, early experiments with hertz-scale mechanical resonance frequencies enabled the first observations of optical bistability and the related hysteresis cycle both in the optical [Dorsel83] and the microwave domain [Gozzini85].

In low-finesse cavities, the optical field can create several stable minima in the mechanical potential, a phenomenon sometimes referred to as multistability [Meystre85, Meystre07]. It has recently been observed with a torsion balance oscillator acting as the moving mirror [Mueller08]. This effect should not be confused with dynamical multistability [Marquardt06], where mechanical limit-cycle orbits of stable amplitudes arise due to parametric instability.

5.3 Optical bistability in the quantum regime

So far we have focused on the semiclassical regime, considering the mean-field solutions as well as the effect of fluctuations around them, and have identified the regime of parameters where the optomechanical system and the Kerr medium exhibit similar behavior. In the remainder, we want to confirm that the conclusions of this approach also hold in the quantum limit. To this end, we compare the quantum steady states of the optomechanical system and the Kerr medium, obtained from numerical solutions of the quantum master equations.

5.3.1 Quantum master equations description of dissipation

An alternative description of either the optomechanical system or the Kerr medium can be given in the form of quantum master equations, which describe the dynamics of their density operators $\hat{\rho}$, respectively $\hat{\rho}_K$. This treatment is equivalent to the quantum Langevin description given by Eqs. (5.2) and (5.7). Instead of using input noise operators $\hat{\xi}$ or $\hat{\eta}$, dissipation is taken into account with Lindblad dissipative terms.

The quantum master equation for the optomechanical system reads

$$\frac{d\hat{\rho}}{dt} = \mathcal{L}\left[\hat{\rho}\right] = \frac{-i}{\hbar}\left[\hat{H}_0 + \hat{H}_d, \hat{\rho}\right] + \kappa\,\mathcal{D}_{\hat{a}}\left[\hat{\rho}\right] + (n_{\mathrm{th}}+1)\gamma_m\,\mathcal{D}_{\hat{b}}\left[\hat{\rho}\right] + n_{\mathrm{th}}\gamma_m\,\mathcal{D}_{\hat{b}^\dagger}\left[\hat{\rho}\right], \tag{5.25}$$

where the dissipative terms have the standard form, $\mathcal{D}_{\hat{o}}[\hat{\rho}] = \hat{o}\,\hat{\rho}\,\hat{o}^\dagger - \frac{1}{2}\left(\hat{o}^\dagger\hat{o}\,\hat{\rho} + \hat{\rho}\,\hat{o}^\dagger\hat{o}\right)$.

In the same way, the quantum master equation for the equivalent Kerr medium is given by

$$\frac{d\hat{\rho}_K}{dt} = \mathcal{L}_K\left[\hat{\rho}_K\right] = \frac{-i}{\hbar}\left[\hat{H}_K + \hat{H}_d, \hat{\rho}_K\right] + \kappa\mathcal{D}_{\hat{a}}\left[\hat{\rho}_K\right]. \tag{5.26}$$

The steady-state density operators are found from the numerical solutions of $\mathcal{L}[\hat{\rho}] = 0$ and $\mathcal{L}_K[\hat{\rho}_K] = 0$, respectively.

5.3.2 Comparison of the quantum steady states

To corroborate the fact that the optomechanical system behaves like an effective Kerr medium, we compare the quantum steady states of both systems for parameters that lead to bistable behavior. To this end, we calculate the photon number $\langle\hat{a}^\dagger\hat{a}\rangle$, the cavity amplitude $|\langle\hat{a}\rangle|^2$, and the second-order correlation function

$$g^{(2)}(0) = \frac{\langle\hat{a}^\dagger\hat{a}^\dagger\hat{a}\hat{a}\rangle}{\langle\hat{a}^\dagger\hat{a}\rangle^2}\,, \tag{5.27}$$

which describes fluctuations in the photon number. We also characterize the similarity between the optomechanical system and the Kerr medium with the help of the overlap

$$F\left(\hat{\rho}_{\mathrm{opt}}, \hat{\rho}_K\right) = \mathrm{Tr}\left[\sqrt{\sqrt{\hat{\rho}_K}\,\hat{\rho}_{\mathrm{opt}}\,\sqrt{\hat{\rho}_K}}\right], \tag{5.28}$$

where $\hat{\rho}_{\mathrm{opt}}$ is the reduced density matrix of the system, obtained by tracing out the mechanical degree of freedom from $\hat{\rho}$. Finally, we investigate the Wigner distribution function of the optical mode, which reads

$$W_{\mathrm{opt}}(\alpha) = \frac{1}{\pi^2}\int d^2\lambda\,\mathrm{Tr}\left[\hat{\rho}_{\mathrm{opt}}\,e^{\lambda(\hat{a}^\dagger-\alpha^*)-\lambda^*(\hat{a}-\alpha)}\right]. \tag{5.29}$$

The steady states of both systems are compared for a constant detuning above the bistability threshold, $y > \tilde{y}$, and as a function of the driving power z. In this configuration the mean-field cavity occupation $\bar{n}$ forms a characteristic S-shaped curve.

The results are presented in Figs. 5.4 and 5.5. In Fig. 5.4, we show the mean-field cavity occupation $\bar{n}$, the photon number $\langle\hat{a}^\dagger\hat{a}\rangle$, and the cavity amplitude $|\langle\hat{a}\rangle|^2$ for both the optomechanical system, with zero and finite temperature of the mechanical bath, as well as for the equivalent Kerr medium. The two insets show the second-order correlation $g^{(2)}(0)$ and the overlap $F\left(\hat{\rho}_{\mathrm{opt}}, \hat{\rho}_K\right)$. In Fig. 5.5, we show the optical Wigner density function of the optomechanical system.

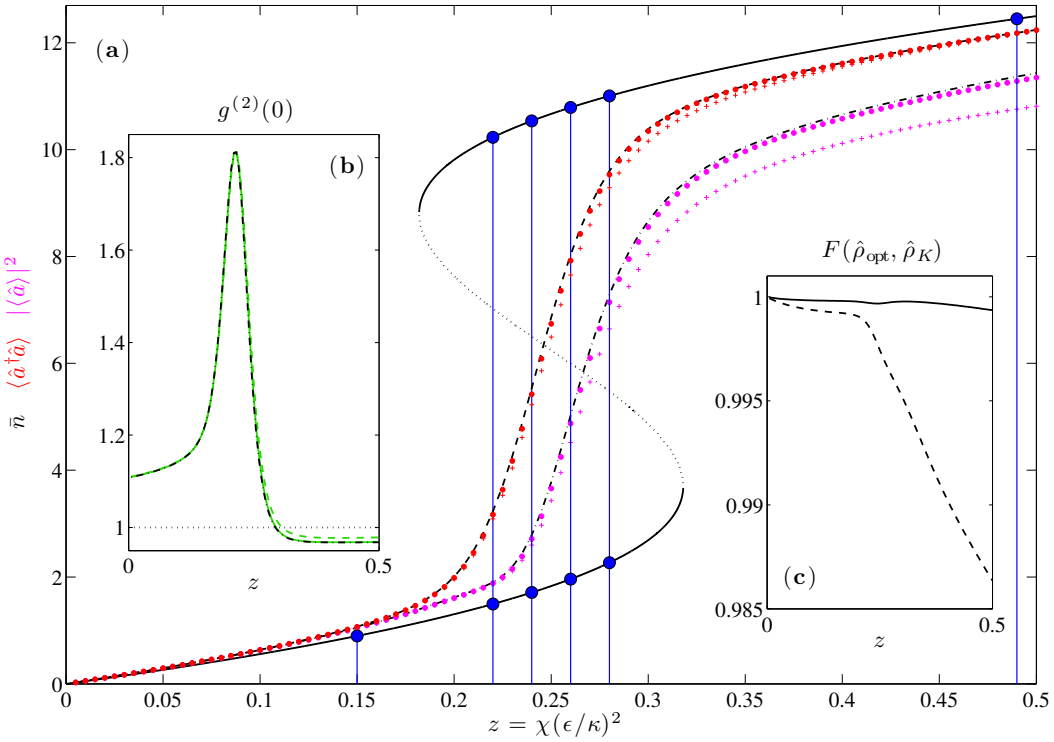

Figure 5.4: *Optical bistability in the quantum regime.* (a) Mean-field cavity occupation $\bar{n}$, with stable (black solid line) and unstable (black dotted line) branches, steady-state photon number $\langle\hat{a}^\dagger\hat{a}\rangle$ (red), and cavity amplitude $|\langle\hat{a}\rangle|^2$ (purple) of the optomechanical system, as a function of the dimensionless driving power z. The upper branch turns unstable outside the range of z parameters we plot, beyond $z_c \simeq 92$ and $n_c \simeq 42$. For comparison we also show $\langle\hat{a}^\dagger\hat{a}\rangle$ (black dashed line) and $|\langle\hat{a}\rangle|^2$ (black dash-dotted line) for the equivalent Kerr medium. For both systems, $y = -\Delta_0/\kappa = 1.5$ and $\chi = 0.08$. The parameters of the optomechanical system are $\omega_m/\kappa = 30$, $Q_m = 300$ (indicated by the black cross in Fig. 5.3), and $k_BT = 0$ (dots) or $k_BT = \hbar\omega_m$ (crosses). Inset (b) shows the second-order correlation function $g^{(2)}(0) = \langle\hat{a}^\dagger\hat{a}^\dagger\hat{a}\hat{a}\rangle/\langle\hat{a}^\dagger\hat{a}\rangle^2$ for the optomechanical system with $k_BT = 0$ (green solid line) as well as $k_BT = \hbar\omega_m$ (green dashed line) and for the Kerr medium (black dash-dotted line). The first and third curves are indistinguishable. Inset (c) shows the overlap $F(\hat{\rho}_{\rm opt}, \hat{\rho}_K)$, as defined in Eq. (5.28), between the density matrices of the pure Kerr medium $\hat{\rho}_K$ and the reduced density matrix of the optomechanical system $\hat{\rho}_{\rm opt}$, obtained by tracing out the mechanical degree of freedom from $\hat{\rho}$. The temperatures chosen are $k_BT = 0$ (solid line) and $k_BT = \hbar\omega_m$ (dashed line).

At low driving power before entering the region of bistability, $z < z_-$, the state of the optical mode is rather well described by a coherent state in both systems, as $\langle\hat{a}^\dagger\hat{a}\rangle = |\langle\hat{a}\rangle|^2 \simeq \bar{n}$.

In the range of driving power where two stable mean-field solutions exist, $z_- < z < z_+$, the master equations (5.25) and (5.26) have *unique* quantum steady states. Thus, instead of any bistable behavior, a transition of $\langle\hat{a}^\dagger\hat{a}\rangle$ and $|\langle\hat{a}\rangle|^2$, from the lower to the upper branch, occurs, as the driving power z increases. Simultaneously, both systems show large fluctuations in the photon number, $g^{(2)}(0) > 1$. Such behavior, in the regime where the MFEs lead to bistability, is well-known from the Kerr medium [Drummond80].

In this regime, the Wigner function $W_{\rm opt}(\alpha)$, shown in Fig. 5.5, exhibits two separate

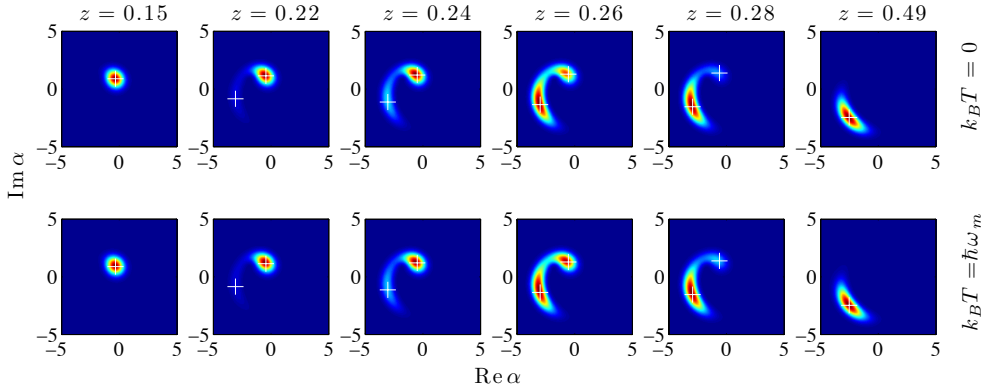

Figure 5.5: Wigner function $W_{\mathrm{opt}}(\alpha)$ of the optical mode of the optomechanical system for six different driving powers z and two different temperatures. The white crosses indicate the mean-field amplitudes $\bar{a}$ of the stable branches. The values of z are indicated by blue dots and lines in Fig. 5.4(a).

lobes peaked at the mean-field amplitudes, $\alpha \simeq \bar{a}$. This is another well-known feature of the Kerr medium [Risken87, Vogel89, Vogel90] and shows how classical bistability persists in the quantum regime. The two lobes are distinguishable if the phase-space separation of the two stable mean-field amplitudes $\bar{a}$ is larger than the fluctuations around them, which is satisfied here since $\chi \ll 1$. Since $W_{\mathrm{opt}} > 0$ everywhere, the optical mode can be regarded as an incoherent statistical mixture of two states with different amplitudes and non-Gaussian fluctuations. As the driving power z increases from z_- to z_+, the relative weights of the lobes continuously change from the lower branch to the upper one, describing the shift in probability for the system to be found in one or the other. This effect is robust to finite temperature of the mechanical environment.

The particular situation where the two stable branches are approximately equally likely ($z \simeq 0.26$ for $k_BT = \omega_m$) would enable the observation of noise-induced switching between both branches [Rigo97, Kerckhoff11] and constitute a clear signature of the nonlinear interaction between the optical and mechanical mode.

At higher driving power, $z > z_+$, when the MFEs have only one solution, both the optomechanical system and the Kerr medium exhibit sub-Poissionian statistics, $g^{(2)}(0) < 1$. Photon blockade in optomechanical systems has already been predicted for $\chi > 1$ [Rabl11]. In our case, photon blockade is not very pronounced: we chose $\chi \ll 1$ to have bistable mean-field solutions that are appreciably distant in phase space. For the parameters of Fig. 5.4, this effect is slightly suppressed even further due to the finite-temperature bath, $n_{\mathrm{th}} > 0$.

At various points of this chapter, we have already demonstrated that the optomechanical system can be regarded as an effective Kerr medium in some range of parameters that we have specified. In particular, in the present section we have shown numerically that both systems exhibit the same features. For example, the photon number and the second-order photon correlation function follow the same parameter dependence, the Wigner function has a two-lobe structure, and both systems show photon blockade. As a further strong confirmation of this equivalence, we compare the states $\hat{\rho}_{\mathrm{opt}}$ and $\hat{\rho}_K$ of the optical field in both systems. As can be seen in inset (c) of Fig. 5.4, their overlap F is close to 1 even at a finite thermal occupation of the mechanical mode. All of these calculations clearly establish the equivalence of the optomechanical system and a Kerr medium in the

appropriate parameter range.

5.4 Concluding remarks

The mean-field equations for the optical mode of a dispersively coupled optomechanical system agree with those of a Kerr medium, a paradigmatic quantum optics system whose nonlinearity induces optical bistability. This raises the question of whether and under which conditions the two systems can be considered to be equivalent. We have therefore compared the optical bistability in an optomechanical system and a Kerr medium. A stability analysis of the mean-field solutions reveals differences between the two systems: the upper branch of an optomechanical system can become unstable due to position fluctuations of the mechanical degree of freedom. We have identified the regime of parameters where the two systems are equivalent. Corroborating this semiclassical approach, we have shown that the (optical) quantum steady states of both systems, obtained numerically, show large overlap. These results help to clarify when an optomechanical system can be used as a Kerr nonlinearity in applications of quantum optics and quantum information.

Chapter 6

Conclusions

In this thesis, we have investigated quantum effects associated with two rather different physical systems with possible applications for quantum information processing and sensing technologies.

In the first part of this thesis, we have reviewed how superconducting circuits are currently used for the implementation of quantum information processing tasks. We have seen how the quantum state of qubits can be manipulated and measured and how the interaction between qubits – essential for the realization of quantum gates – is implemented.

In particular, we have discussed how highly entangled GHZ states can be generated in a circuit QED setup with transmon qubits. The entanglement protocol that we have proposed relies on a pairwise exchange interaction between qubits which could effectively be implemented by coupling dispersively and homogeneously several qubits to a single microwave mode. We have shown how the entangled nature of the GHZ state can be verified with a measurement of the Bell-Mermin operator, which we use as an entanglement witness. The necessary joint parity measurements are readily implemented in the current architecture. Finally, we have investigated the robustness of the entangling scheme against small inhomogeneities in the coupling frequencies and weak transmon anharmonicity. Using parameters of a recent experiment, we have found that the dispersive pairwise interaction could entangle the qubits in a time that is about one percent of the qubit dephasing time.

In the second part of this thesis, we have presented the generic model of cavity optomechanics and some of its recent implementations with micro-fabricated devices operating both in the optical and the microwave domain. Remarkable achievements like mechanical ground state cooling suggest that these devices might soon find practical applications for sensitive displacement detection.

In the future, optomechanical devices with large coupling constants could potentially implement the long-sought strong optical nonlinearities that are required for photonic quantum information processing. Understanding how optomechanical systems compare to optical nonlinear media is therefore of practical relevance for applications in nonlinear quantum optics. In our work, we have investigated the differences and similarities between an optomechanical cavity and a cavity filled with a Kerr medium with regard to optical bistability. We have found additional features in the stability diagram of optomechanical systems due to position fluctuations of the mechanical resonator. We have identified the parameter regime where both systems are equivalent and we have observed characteristic quantum features proving the optomechanical system can be regarded as an effective Kerr medium. Also, for large optomechanical coupling, this regime opens up the possibility to

explore other nonlinear quantum effects such as noise-induced switching between the two stable branches.

Finally, we would like to comment on the possibility to bring on a common playground the two types of systems we have been discussed throughout this thesis. The general development of the circuit QED architecture shows a very consistent trend where each advance has involved interconnected aspects: careful characterization of system parameters, robustness to noise from external control channels and improvement of the coherence time with proper circuit design, and development of accurate control techniques and sensitive readout schemes. The basic functionalities of a future quantum processor have been successfully implemented, but so far only within a relatively small qubit register. A first step towards the scalability of such devices probably relies on the ability to transfer quantum information between different qubit registers. Recently, it appears that optomechanical systems are particularly appealing for the transfer of quantum states between different frequency domains of light [Andrews14], in particular, microwave and optical photons. This would make possible to combine the fast gate times of superconducting circuits with the long coherence times of photonic qubits. One could therefore imagine that, in a not so distant future, combined systems taking advantage of each platform capabilities would make quantum information processing with superconducting circuits enter one of its most interesting phases of development.

Appendix A

Hilbert space truncation for weakly anharmonic transmon qubits

A.1 Two-level approximation in the resonant regime

We have obtained an effective two-level Jaynes-Cummings Hamiltonian, Eq. (2.166), by truncating the generalized Hamiltonian involving all transmon levels, Eq. (2.165), to the two lowest-lying energy levels forming the computational subspace. As we will show, this Hilbert space truncation is justified as long as the anharmonicity of the transmon spectrum is large enough, such that the mixing of computational basis states with higher energy states is small.

We start by writing Eq. (2.165) as the sum $\hat{H}_0 + \hat{H}_1$, where

$$\hat{H}_0 = \hbar\omega_r \hat{a}^\dagger \hat{a} + \sum_k \hbar\omega_{0k} |k\rangle\langle k| + \hbar g_0 \left(\hat{a}|1\rangle\langle 0| + \hat{a}^\dagger |0\rangle\langle 1| \right) \tag{A.1}$$

$$\hat{H}_1 = \sum_{k>0} \hbar g_k \left(\hat{a}|k+1\rangle\langle k| + \hat{a}^\dagger |k\rangle\langle k+1| \right). \tag{A.2}$$

Here $\omega_{kl} = \omega_l - \omega_k$ is the transition frequency between levels k and l and $|k\rangle$ denotes the transmon eigenstate with energy $\hbar\omega_k$. We denote product states of the coupled system by $|n, k\rangle$, where $|n\rangle$ is a resonator state with n photons. Using knowledge about the conventional Jaynes-Cummings Hamiltonian, the eigenstates and eigenenergies of $\hat{H}_0$ can readily be obtained. The ground state is simply $|0, 0\rangle$ with energy $E_{0,0} = 0$. The coupling term of $\hat{H}_0$ induces mixing of the states $|n-1, 1\rangle$ and $|n, 0\rangle$, for $n > 0$. Thus, eigenstates of $\hat{H}_0$ belonging to the computational subspace are

$$|n, +\rangle = \cos\theta_n |n-1, 1\rangle + \sin\theta_n |n, 0\rangle, \tag{A.3}$$

$$|n, -\rangle = \cos\theta_n |n, 0\rangle - \sin\theta_n |n-1, 1\rangle, \tag{A.4}$$

with eigenenergies

$$E_{n,\pm} = n\hbar\omega_r + \frac{\hbar\Delta_{01}}{2} \pm \frac{\hbar}{2}\sqrt{\Delta_{01}^2 + 4ng_0^2}. \tag{A.5}$$

Here, $\Delta_{01} = \omega_{01} - \omega_r$ is the qubit-cavity detuning and the angles θ_n are obtained from

$$\tan(2\theta_n) = \frac{2g_0\sqrt{n}}{\Delta_{01}}. \tag{A.6}$$

Eigenstates of $\hat{H}_0$ which do not belong to the computational subspace are all states $|n,k\rangle$ where $k>1$ and there eigenenergies are simply $E_{n,k}=\hbar(n\omega_r+\omega_{k0})$.

The Hamiltonian $\hat{H}_1$ causes mixing between states involving the non-computational third transmon level, $|n,2\rangle$, and computational states containing one qubit excitation and $n+1$ photonic excitations. For instance, the state $|n,\pm\rangle$ couples to the state $|n-2,2\rangle$. Using perturbation theory, we can evaluate the amplitude of such a mixing at resonance, $\Delta_{01}=0$. To leading order, the states $|n,\pm\rangle$ acquire a correction for $n\geq 2$

$$\widetilde{|n,\pm\rangle} \simeq |n,\pm\rangle + \frac{\sqrt{n-1}g_1}{\sqrt{n}g_0 \mp \alpha/\hbar}|n-2,2\rangle, \tag{A.7}$$

where $\alpha=\hbar(\omega_{01}-\omega_{12})$ is the absolute anharmonicity of the transmon qubit, typically of the order of the charging energy E_C. Thus, as long as the ratio $|\hbar g_0/\alpha|$ is sufficiently small, we may neglect this mixing to higher states. Finally, it is straightforward to see that there is no first-order correction to the eigenenergies $E_{n,\pm}$, hence the form of the truncated version of the generalized Jaynes-Cummings Hamiltonian given in Eq. (2.166).

A.2 Two-level approximation in the dispersive regime

In the dispersive regime, the truncation of the Hilbert space to the two lowest energy levels of the transmon qubit, as given in Eq. 2.170, can be justified with basically the same arguments that were given in Appendix A.1. Regarding the dispersive Hamiltonian with all transmon levels, a similar procedure can be carried out to show that the mixing of states with either zero or one qubit excitation with states that do not belong to the computational subspace is small provided the anharmonicity of the spectrum is large enough.

Two-photon processes (last term of Eq. 2.168) cause mixing of the states $|n,k\rangle$ and $|n-2,k+2\rangle$, and the amplitude of such mixing can be approximated by applying perturbation theory. We define the Hamiltonian

$$\hat{H}_0=\sum_{k\geq 1}\hbar\left(\omega_{0k}+\chi_{k-1}\right)|k\rangle\langle k| + \left[\hbar\omega_r-\hbar\chi_0|0\rangle\langle 0| + \sum_{k\geq 1}\hbar\left(\chi_{k-1}-\chi_k\right)|k\rangle\langle k|\right]\hat{a}^\dagger\hat{a}, \tag{A.8}$$

whose eigenstates are $|n,k\rangle$ with eigenenergies given by

$$E_{0,0}=0, \qquad E_{n,0}=n\hbar\left(\omega_r-\chi_0\right) \tag{A.9}$$

$$E_{n,k}=\hbar(\omega_{k0}-\chi_{k-1})+n\hbar\left(\omega_r+\chi_{k-1}-\chi_k\right), \qquad (k>0). \tag{A.10}$$

Two-photon processes

$$\hat{H}_1=\sum_k \hbar\eta_k\left(\hat{a}^2|k+2\rangle\langle k| + \hat{a}^{\dagger 2}|k\rangle\langle k+2|\right) \tag{A.11}$$

give no first-order corrections to the above energies, but lead to corrections for the states belonging to the computational basis,

$$\widetilde{|n,0\rangle} = |n,0\rangle + \frac{\hbar\eta_0\sqrt{n(n-1)}}{E_{n,0}-E_{n-2,2}}|n-2,2\rangle, \tag{A.12}$$

$$\widetilde{|n,1\rangle} = |n,1\rangle + \frac{\hbar\eta_1\sqrt{n(n-1)}}{E_{n,1}-E_{n-2,3}}|n-2,3\rangle. \tag{A.13}$$

The mixing amplitudes are $\sim \frac{g^2\alpha}{\hbar\Delta^3}$ and can be neglected if the transmon anharmonicity α is small compared to the qubit-cavity detuning. This allows to truncate $\hat{H}_0$ to the two lowest level of the transmon qubit and to take it as an approximation of Eq. (2.168).

Appendix B

Schwinger representation of total spin operators

We present briefly the Schwinger representation [Milburn97, Zheng01, You03b] of the total spin operators

$$\hat{J}_x = \frac{1}{2}\sum_{q=1}^{N}\sigma_x^{(q)}, \qquad \hat{J}_y = \frac{1}{2}\sum_{q=1}^{N}\sigma_y^{(q)}, \qquad \hat{J}_z = \frac{1}{2}\sum_{q=1}^{N}\sigma_z^{(q)}. \tag{B.1}$$

This turns out to be particularly useful for calculations in the subspace of $\hat{J}^2$-eigenstates with maximal eigenvalue $\frac{N}{2}\left(\frac{N}{2}+1\right)$, where N is the number of spins. From now on we set $J = N/2$ and denote the states $|J{=}N/2, J_i\rangle$ simply by $|J_i\rangle$ $(i = x, y, z)$.

States like $|J_z\rangle$ are sometimes referred to as Dicke states [Dicke54]. They form a complete basis of symmetric N-qubit states, i.e., states invariant under any permutation of qubits. We use for each qubit, labeled by q, the usual basis states $|0_q\rangle$ and $|1_q\rangle$ with the convention $\sigma_z^{(q)}|1_q\rangle = |1_q\rangle$ and $\sigma_z^{(q)}|0_q\rangle = -|0_q\rangle$. This yields

$$|J_z{=}k - N/2\rangle = \frac{1}{\sqrt{\binom{N}{k}}}\sum_p |1_{p(1)}\rangle\cdots|1_{p(k)}\rangle|0_{p(k+1)}\rangle\cdots|0_{p(N)}\rangle, \tag{B.2}$$

with $0 \le k \le N$ and where the sum is taken over the $\binom{N}{k} = \frac{N!}{k!(N-k)!}$ nonequivalent possible permutations p that give different product states.

The operators $\hat{J}_i$ are defined by means of two independent bosonic operators $\hat{a}$ and $\hat{b}$, with the usual commutation relations $[\hat{a}, \hat{a}^\dagger] = [\hat{b}, \hat{b}^\dagger] = 1$ and $[\hat{a}, \hat{b}] = [\hat{a}, \hat{b}^\dagger] = 0$,

$$\hat{J}_x = \frac{1}{2}(\hat{b}^\dagger\hat{a} + \hat{a}^\dagger\hat{b}), \tag{B.3}$$

$$\hat{J}_y = \frac{1}{2i}(\hat{b}^\dagger\hat{a} - \hat{a}^\dagger\hat{b}), \tag{B.4}$$

$$\hat{J}_z = \frac{1}{2}(\hat{b}^\dagger\hat{b} - \hat{a}^\dagger\hat{a}), \tag{B.5}$$

fulfilling the SU(2) algebra $[\hat{J}_l, \hat{J}_m] = i\epsilon_{lmn}\hat{J}_n$. Eigenstates of $\hat{J}_z$ can be expressed as

$$|J, J_z\rangle = \frac{\left(\hat{b}^\dagger\right)^{J+J_z}|\left(\hat{a}^\dagger\right)^{J-J_z}}{\sqrt{(J+J_z)!(J-J_z)!}}|n_a{=}0, n_b{=}0\rangle, \tag{B.6}$$

where $|n_a=0, n_b=0\rangle$ is the vacuum state of the operators $\hat{a}$ and $\hat{b}$. Since the choice of the operators $\hat{a}$ and $\hat{b}$ is not unique, we can equivalently introduce the operators $\hat{c} = (\hat{a}-\hat{b})/\sqrt{2}$ and $\hat{d} = (\hat{a}+\hat{b})/\sqrt{2}$, leading to $\hat{J}_x = \frac{1}{2}(\hat{d}^\dagger\hat{d} - \hat{c}^\dagger\hat{c})$ and

$$|J, J_x\rangle = \frac{\left(\hat{d}^\dagger\right)^{J+J_x}\left(\hat{c}^\dagger\right)^{J-J_x}}{\sqrt{(J+J_x)!(J-J_x)!}}|n_a=0, n_b=0\rangle. \tag{B.7}$$

We straightforwardly obtain the decomposition of the states $|J, J_x\rangle$ in terms of $|J, J_z\rangle$ and in particular

$$\begin{aligned} |J_x=\pm N/2\rangle &= \bigotimes_{q=1}^{N}\frac{|0_q\rangle \pm |1_q\rangle}{\sqrt{2}} \\ &= \frac{\left(\hat{a}^\dagger \pm \hat{b}^\dagger\right)^N}{\sqrt{2^N N!}}|n_a=0, n_b=0\rangle \\ &= \frac{1}{2^{N/2}}\sum_{k=0}^{N}(\pm 1)^k\sqrt{\tbinom{N}{k}}|J_z=k-N/2\rangle. \end{aligned} \tag{B.8}$$

Defining the ladder operators $\hat{J}_\pm = \hat{J}_x \pm i\hat{J}_y$ of the total spins, the Dicke states can also be expressed as

$$|J_z=k-N/2\rangle = \frac{\left(\hat{J}_+\right)^k}{k!\sqrt{\binom{N}{k}}}\bigotimes_{q=1}^{N}|0_q\rangle = \frac{\left(\hat{J}_-\right)^{N-k}}{(N-k)!\sqrt{\binom{N}{k}}}\bigotimes_{q=1}^{N}|1_q\rangle. \tag{B.9}$$

Bibliography

[Abbott09a] B. P. Abbott, R. Abbott, R. Adhikari, P. Ajith, B. Allen, *et al.*, *LIGO: the Laser Interferometer Gravitational-Wave Observatory*. Reports on Progress in Physics **72**, 076901 (2009).

[Abbott09b] B. P. Abbott, R. Abbott, R. Adhikari, P. Ajith, B. Allen, *et al.*, *Observation of a kilogram-scale oscillator near its quantum ground state*. New Journal of Physics **11**, 073032 (2009).

[Abramovici92] A. Abramovici, W. E. Althouse, R. W. P. Drever, Y. Gürsel, S. Kawamura, F. J. Raab, D. Shoemaker, L. Sievers, R. E. Spero, K. S. Thorne, R. E. Vogt, R. Weiss, S. E. Whitcomb, and M. E. Zucker, *LIGO: The Laser Interferometer Gravitational-Wave Observatory*. Science **256**, 325 (1992).

[Abramowitz70] M. Abramowitz and I. Stegun, *Handbook of mathematical functions*. Dover Publishing Inc. New York (1970).

[Agarwal10] G. S. Agarwal and S. Huang, *Electromagnetically induced transparency in mechanical effects of light*. Phys. Rev. A **81**, 041803 (2010).

[Anders09] J. Anders and D. E. Browne, *Computational Power of Correlations*. Phys. Rev. Lett. **102**, 050502 (2009).

[Andrews14] R. W. Andrews, R. W. Peterson, T. P. Purdy, K. Cicak, R. W. Simmonds, C. A. Regal, and K. W. Lehnert, *Bidirectional and efficient conversion between microwave and optical light*. Nat. Phys. **10**, 321 (2014).

[Ansmann09] M. Ansmann, H. Wang, R. C. Bialczak, M. Hofheinz, E. Lucero, M. Neeley, A. D. O'Connell, D. Sank, M. Weides, J. Wenner, A. N. Cleland, and J. M. Martinis, *Violation of Bell's inequality in Josephson phase qubits*. Nature **461**, 504 (2009).

[Arcizet06a] O. Arcizet, P.-F. Cohadon, T. Briant, M. Pinard, and A. Heidmann, *Radiation-pressure cooling and optomechanical instability of a micromirror*. Nature **444**, 71 (2006).

[Arcizet06b] O. Arcizet, P.-F. Cohadon, T. Briant, M. Pinard, A. Heidmann, J.-M. Mackowski, C. Michel, L. Pinard, O. Français, and

L. Rousseau, *High-Sensitivity Optical Monitoring of a Micromechanical Resonator with a Quantum-Limited Optomechanical Sensor*. Phys. Rev. Lett. **97**, 133601 (2006).

[Aspect88] A. Aspect, E. Arimondo, R. Kaiser, N. Vansteenkiste, and C. Cohen-Tannoudji, *Laser Cooling below the One-Photon Recoil Energy by Velocity-Selective Coherent Population Trapping*. Phys. Rev. Lett. **61**, 826 (1988).

[Aspelmeyer08] M. Aspelmeyer and K. Schwab, *Focus on mechanical systems at the quantum limit*. New Journal of Physics **10**, 095001 (2008).

[Aspelmeyer13] M. Aspelmeyer, T. J. Kippenberg, and F. Marquardt, *Cavity Optomechanics*. arXiv:1303.0733 (2013).

[Bardeen57] J. Bardeen, L. N. Cooper, and J. R. Schrieffer, *Theory of Superconductivity*. Phys. Rev. **108**, 1175 (1957).

[Barrett05] S. D. Barrett, P. Kok, K. Nemoto, R. G. Beausoleil, W. J. Munro, and T. P. Spiller, *Symmetry analyzer for nondestructive Bell-state detection using weak nonlinearities*. Phys. Rev. A **71**, 060302 (2005).

[Barzanjeh12] S. Barzanjeh, M. Abdi, G. J. Milburn, P. Tombesi, and D. Vitali, *Reversible Optical-to-Microwave Quantum Interface*. Phys. Rev. Lett. **109**, 130503 (2012).

[Baur12] M. Baur, A. Fedorov, L. Steffen, S. Filipp, M. P. da Silva, and A. Wallraff, *Benchmarking a Quantum Teleportation Protocol in Superconducting Circuits Using Tomography and an Entanglement Witness*. Phys. Rev. Lett. **108**, 040502 (2012).

[Bennett84] C. H. Bennett, G. Brassard, *et al.*, *Quantum cryptography: Public key distribution and coin tossing. Proceedings of IEEE International Conference on Computers, Systems and Signal Processing*, volume 175, New York (1984).

[Bennett00] C. H. Bennett and D. P. DiVincenzo, *Quantum information and computation*. Nature **404**, 247 (2000).

[Bergeal10a] N. Bergeal, F. Schackert, M. Metcalfe, R. Vijay, V. E. Manucharyan, L. Frunzio, D. E. Prober, R. J. Schoelkopf, S. M. Girvin, and M. H. Devoret, *Phase-preserving amplification near the quantum limit with a Josephson ring modulator*. Nature **465**, 64 (2010).

[Bergeal10b] N. Bergeal, R. Vijay, V. E. Manucharyan, I. Siddiqi, R. J. Schoelkopf, S. M. Girvin, and M. H. Devoret, *Analog information processing at the quantum limit with a Josephson ring modulator*. Nat. Phys. **6**, 296 (2010).

[Bianchetti10] R. Bianchetti, S. Filipp, M. Baur, J. M. Fink, C. Lang, L. Steffen, M. Boissonneault, A. Blais, and A. Wallraff, *Control and Tomography of a Three Level Superconducting Artificial Atom*. Phys. Rev. Lett. **105**, 223601 (2010).

[Birnbaum05] K. M. Birnbaum, A. Boca, R. Miller, A. D. Boozer, T. E. Northup, and H. J. Kimble, *Photon blockade in an optical cavity with one trapped atom*. Nature **436**, 87 (2005).

[Bishop09a] L. S. Bishop, J. M. Chow, J. Koch, A. A. Houck, M. H. Devoret, E. Thuneberg, S. M. Girvin, and R. J. Schoelkopf, *Nonlinear response of the vacuum Rabi resonance*. Nat. Phys. **5**, 105 (2009).

[Bishop09b] L. S. Bishop, L. Tornberg, D. Price, E. Ginossar, A. Nunnenkamp, A. A. Houck, J. M. Gambetta, J. Koch, G. Johansson, S. M. Girvin, and R. J. Schoelkopf, *Proposal for generating and detecting multi-qubit GHZ states in circuit QED*. New Journal of Physics **11**, 073040 (2009).

[Blais04] A. Blais, R.-S. Huang, A. Wallraff, S. M. Girvin, and R. J. Schoelkopf, *Cavity quantum electrodynamics for superconducting electrical circuits: An architecture for quantum computation*. Phys. Rev. A **69**, 062320 (2004).

[Blencowe04] M. Blencowe, *Quantum electromechanical systems*. Physics Reports **395**, 159 (2004).

[Bollinger96] J. J. Bollinger, W. M. Itano, D. J. Wineland, and D. J. Heinzen, *Optimal frequency measurements with maximally correlated states*. Phys. Rev. A **54**, R4649 (1996).

[Bondurant84] R. S. Bondurant and J. H. Shapiro, *Squeezed states in phase-sensing interferometers*. Phys. Rev. D **30**, 2548 (1984).

[Børkje10] K. Børkje, A. Nunnenkamp, B. M. Zwickl, C. Yang, J. G. E. Harris, and S. M. Girvin, *Observability of radiation-pressure shot noise in optomechanical systems*. Phys. Rev. A **82**, 013818 (2010).

[Borsten10] L. Borsten, D. Dahanayake, M. J. Duff, A. Marrani, and W. Rubens, *Four-Qubit Entanglement Classification from String Theory*. Phys. Rev. Lett. **105**, 100507 (2010).

[Bose97] S. Bose, K. Jacobs, and P. L. Knight, *Preparation of nonclassical states in cavities with a moving mirror*. Phys. Rev. A **56**, 4175 (1997).

[Bose99] S. Bose, K. Jacobs, and P. L. Knight, *Scheme to probe the decoherence of a macroscopic object*. Phys. Rev. A **59**, 3204 (1999).

[Botter09] T. Botter, D. Brooks, S. Gupta, Z.-Y. Ma, K. L. Moore, K. W. Murch, T. P. Purdy, and D. M. Stamper-Kurn, *Quantum Micro-Mechanics with Ultracold Atoms*. R. Côté, P. L. Gould, M. Rozman, and W. W. Smith, editors, *Pushing the Frontiers of Atomic Physics*, pp. 117–130, World Scientific (2009).

[Bouchiat98] V. Bouchiat, D. Vion, P. Joyez, D. Esteve, and M. H. Devoret, *Quantum coherence with a single Cooper pair*. Physica Scripta **1998**, 165 (1998).

[Braginsky67] V. Braginsky and A. B. Manukin, *Ponderomotive Effects of Electromagnetic Radiation*. Sov. Phys. JETP **25**, 653 (1967).

[Braginsky68] V. Braginsky, *Classical and Quantum Restrictions on the Detection of Weak Disturbances of a Macroscopic Oscillator*. Sov. Phys. JETP **26**, 831 (1968).

[Braginsky70] V. B. Braginsky, A. B. Manukin, and M. Y. Tikhonov, *Investigation of Dissipative Ponderomotive Effects of Electromagnetic Radiation*. Sov. Phys. JETP **31**, 829 (1970).

[Braginsky75] V. B. Braginsky and Y. I. Vorontsov, *Quantum-mechanical limitations in macroscopic experiments and modern experimental technique*. Soviet Physics Uspekhi **17**, 644 (1975).

[Braginsky80] V. B. Braginsky, Y. I. Vorontsov, and K. S. Thorne, *Quantum Nondemolition Measurements*. Science **209**, 547 (1980).

[Braginsky89] V. Braginsky, M. Gorodetsky, and V. Ilchenko, *Quality-factor and nonlinear properties of optical whispering-gallery modes*. Physics Letters A **137**, 393 (1989).

[Braginsky92] V. B. Braginsky and F. Y. Khalili, *Quantum measurement*. Cambridge University Press (1992).

[Braginsky01] V. Braginsky, S. Strigin, and S. Vyatchanin, *Parametric oscillatory instability in Fabry-Perot interferometer*. Physics Letters A **287**, 331 (2001).

[Braginsky02] V. Braginsky and S. Vyatchanin, *Low quantum noise tranquilizer for Fabry-Perot interferometer*. Physics Letters A **293**, 228 (2002).

[Brennecke08] F. Brennecke, S. Ritter, T. Donner, and T. Esslinger, *Cavity Optomechanics with a Bose-Einstein Condensate*. Science **322**, 235 (2008).

[Brooks12] D. W. C. Brooks, T. Botter, S. Schreppler, T. P. Purdy, N. Brahms, and D. M. Stamper-Kurn, *Non-classical light generated by quantum-noise-driven cavity optomechanics*. Nature **488**, 476 (2012).

[Bruus04] H. Bruus and K. Flensberg, *Many-Body Quantum Theory in Condensed Matter Physics: An Introduction*. 2nd edition, Oxford Graduate Texts, Oxford University Press (2004).

[Buluta09] I. Buluta and F. Nori, *Quantum Simulators*. Science **326**, 108 (2009).

[Büttiker87] M. Büttiker, *Zero-current persistent potential drop across small-capacitance Josephson junctions*. Phys. Rev. B **36**, 3548 (1987).

[Cabello02] A. Cabello, *Bell's theorem with and without inequalities for the three-qubit Greenberger-Horne-Zeilinger and W states*. Phys. Rev. A **65**, 032108 (2002).

[Caldeira83a] A. Caldeira and A. Leggett, *Path integral approach to quantum Brownian motion*. Physica A: Statistical Mechanics and its Applications **121**, 587 (1983).

[Caldeira83b] A. Caldeira and A. Leggett, *Quantum tunnelling in a dissipative system*. Annals of Physics **149**, 374 (1983).

[Campagne-Ibarcq13] P. Campagne-Ibarcq, E. Flurin, N. Roch, D. Darson, P. Morfin, M. Mirrahimi, M. H. Devoret, F. Mallet, and B. Huard, *Persistent Control of a Superconducting Qubit by Stroboscopic Measurement Feedback*. Phys. Rev. X **3**, 021008 (2013).

[Carmon05] T. Carmon, H. Rokhsari, L. Yang, T. J. Kippenberg, and K. J. Vahala, *Temporal Behavior of Radiation-Pressure-Induced Vibrations of an Optical Microcavity Phonon Mode*. Phys. Rev. Lett. **94**, 223902 (2005).

[Castellanos-Beltran07] M. A. Castellanos-Beltran and K. W. Lehnert, *Widely tunable parametric amplifier based on a superconducting quantum interference device array resonator*. Applied Physics Letters **91**, 083509 (2007).

[Castellanos-Beltran08] M. A. Castellanos-Beltran, K. D. Irwin, G. C. Hilton, L. R. Vale, and K. W. Lehnert, *Amplification and squeezing of quantum noise with a tunable Josephson metamaterial*. Nat. Phys. **4**, 929 (2008).

[Caves80a] C. M. Caves, *Quantum-Mechanical Radiation-Pressure Fluctuations in an Interferometer*. Phys. Rev. Lett. **45**, 75 (1980).

[Caves80b] C. M. Caves, K. S. Thorne, R. W. P. Drever, V. D. Sandberg, and M. Zimmermann, *On the measurement of a weak classical force coupled to a quantum-mechanical oscillator. I. Issues of principle*. Rev. Mod. Phys. **52**, 341 (1980).

[Caves81] C. M. Caves, *Quantum-mechanical noise in an interferometer*. Phys. Rev. D **23**, 1693 (1981).

[Caves82] C. M. Caves, *Quantum limits on noise in linear amplifiers*. Phys. Rev. D **26**, 1817 (1982).

[Chan11] J. Chan, T. P. M. Alegre, A. H. Safavi-Naeini, J. T. Hill, A. Krause, S. Groblacher, M. Aspelmeyer, and O. Painter, *Laser cooling of a nanomechanical oscillator into its quantum ground state*. Nature **478**, 89 (2011).

[Chan12] J. Chan, A. H. Safavi-Naeini, J. T. Hill, S. Meenehan, and O. Painter, *Optimized optomechanical crystal cavity with acoustic radiation shield*. Applied Physics Letters **101**, 081115 (2012).

[Chiorescu04] I. Chiorescu, P. Bertet, K. Semba, Y. Nakamura, C. J. P. M. Harmans, and J. E. Mooij, *Coherent dynamics of a flux qubit coupled to a harmonic oscillator*. Nature **431**, 159 (2004).

[Chow09] J. M. Chow, J. M. Gambetta, L. Tornberg, J. Koch, L. S. Bishop, A. A. Houck, B. R. Johnson, L. Frunzio, S. M. Girvin, and R. J. Schoelkopf, *Randomized Benchmarking and Process Tomography for Gate Errors in a Solid-State Qubit*. Phys. Rev. Lett. **102**, 090502 (2009).

[Chow10a] J. M. Chow, L. DiCarlo, J. M. Gambetta, F. Motzoi, L. Frunzio, S. M. Girvin, and R. J. Schoelkopf, *Optimized driving of superconducting artificial atoms for improved single-qubit gates*. Phys. Rev. A **82**, 040305 (2010).

[Chow10b] J. M. Chow, L. DiCarlo, J. M. Gambetta, A. Nunnenkamp, L. S. Bishop, L. Frunzio, M. H. Devoret, S. M. Girvin, and R. J. Schoelkopf, *Detecting highly entangled states with a joint qubit readout*. Phys. Rev. A **81**, 062325 (2010).

[Chow12] J. M. Chow, J. M. Gambetta, A. D. Córcoles, S. T. Merkel, J. A. Smolin, C. Rigetti, S. Poletto, G. A. Keefe, M. B. Rothwell, J. R. Rozen, M. B. Ketchen, and M. Steffen, *Universal Quantum Gate Set Approaching Fault-Tolerant Thresholds with Superconducting Qubits*. Phys. Rev. Lett. **109**, 060501 (2012).

[Chu85] S. Chu, L. Hollberg, J. E. Bjorkholm, A. Cable, and A. Ashkin, *Three-dimensional viscous confinement and cooling of atoms by resonance radiation pressure*. Phys. Rev. Lett. **55**, 48 (1985).

[Chuang95] I. L. Chuang and Y. Yamamoto, *Simple quantum computer*. Phys. Rev. A **52**, 3489 (1995).

[Chuang96] I. L. Chuang and Y. Yamamoto, *Quantum Bit Regeneration*. Phys. Rev. Lett. **76**, 4281 (1996).

[Cirac12] J. I. Cirac and P. Zoller, *Goals and opportunities in quantum simulation*. Nat. Phys. **8**, 264 (2012).

[Clarke08] J. Clarke and F. K. Wilhelm, *Superconducting quantum bits*. Nature **453**, 1031 (2008).

[Cleland02] A. N. Cleland, J. S. Aldridge, D. C. Driscoll, and A. C. Gossard, *Nanomechanical displacement sensing using a quantum point contact*. Applied Physics Letters **81**, 1699 (2002).

[Clerk08] A. A. Clerk, F. Marquardt, and K. Jacobs, *Back-action evasion and squeezing of a mechanical resonator using a cavity detector*. New Journal of Physics **10**, 095010 (2008).

[Clerk10] A. A. Clerk, M. H. Devoret, S. M. Girvin, F. Marquardt, and R. J. Schoelkopf, *Introduction to quantum noise, measurement, and amplification*. Rev. Mod. Phys. **82**, 1155 (2010).

[Cohen13] J. D. Cohen, S. M. Meenehan, and O. Painter, *Optical coupling to nanoscale optomechanical cavities for near quantum-limited motion transduction*. Opt. Express **21**, 11227 (2013).

[Cooper56] L. N. Cooper, *Bound Electron Pairs in a Degenerate Fermi Gas*. Phys. Rev. **104**, 1189 (1956).

[Corbitt06] T. Corbitt, Y. Chen, F. Khalili, D. Ottaway, S. Vyatchanin, S. Whitcomb, and N. Mavalvala, *Squeezed-state source using radiation-pressure-induced rigidity*. Phys. Rev. A **73**, 023801 (2006).

[Corbitt07] T. Corbitt, C. Wipf, T. Bodiya, D. Ottaway, D. Sigg, N. Smith, S. Whitcomb, and N. Mavalvala, *Optical Dilution and Feedback Cooling of a Gram-Scale Oscillator to 6.9 mK*. Phys. Rev. Lett. **99**, 160801 (2007).

[Cottet02] A. Cottet, *Implementation of a quantum bit in superconducting circuit*. Ph.D. thesis, Université de Paris VI (2002).

[Cuthbertson96] B. D. Cuthbertson, M. E. Tobar, E. N. Ivanov, and D. G. Blair, *Parametric back-action effects in a high-Q cyrogenic sapphire transducer*. Review of Scientific Instruments **67**, 2435 (1996).

[DeJesus87] E. X. DeJesus and C. Kaufman, *Routh-Hurwitz criterion in the examination of eigenvalues of a system of nonlinear ordinary differential equations*. Phys. Rev. A **35**, 5288 (1987).

[Devoret97] M. H. Devoret, *Course 10 Quantum fluctuations in electrical circuits*. S. Reynaud, E. Giaconibo, and J. Zinn-Justin, editors, *Quantum Fluctuations École d'été de Physique des Houches Session LXIII*, *Les Houches*, volume 68, pp. 351–386, Elsevier (1997).

[Devoret04] M. H. Devoret and J. M. Martinis, *Course 12 Superconducting qubits*. J.-M. R. Daniel Estève and J. Dalibard, editors, *Quantum Entanglement and Information Processing École d'été de Physique des Houches Session LXXIX*, *Les Houches*, volume 79, pp. 443 – 485, Elsevier (2004).

[Devoret13] M. H. Devoret and R. J. Schoelkopf, *Superconducting Circuits for Quantum Information: An Outlook*. Science **339**, 1169 (2013).

[DiCarlo09] L. DiCarlo, J. M. Chow, J. M. Gambetta, L. S. Bishop, B. R. Johnson, D. I. Schuster, J. Majer, A. Blais, L. Frunzio, S. M. Girvin, and R. J. Schoelkopf, *Demonstration of two-qubit algorithms with a superconducting quantum processor*. Nature **460**, 240 (2009).

[DiCarlo10] L. DiCarlo, M. D. Reed, L. Sun, B. R. Johnson, J. M. Chow, J. M. Gambetta, L. Frunzio, S. M. Girvin, M. H. Devoret, and R. J. Schoelkopf, *Preparation and measurement of three-qubit entanglement in a superconducting circuit*. Nature **467**, 574 (2010).

[Dicke54] R. H. Dicke, *Coherence in Spontaneous Radiation Processes*. Phys. Rev. **93**, 99 (1954).

[Ding11] L. Ding, C. Baker, P. Senellart, A. Lemaitre, S. Ducci, G. Leo, and I. Favero, *Wavelength-sized GaAs optomechanical resonators with gigahertz frequency*. Applied Physics Letters **98**, 113108 (2011).

[DiVincenzo00] D. P. DiVincenzo, *The Physical Implementation of Quantum Computation*. Fortschritte der Physik **48**, 771 (2000).

[Dong12] C. Dong, V. Fiore, M. C. Kuzyk, and H. Wang, *Optomechanical Dark Mode*. Science **338**, 1609 (2012).

[Dorsel83] A. Dorsel, J. D. McCullen, P. Meystre, E. Vignes, and H. Walther, *Optical Bistability and Mirror Confinement Induced by Radiation Pressure*. Phys. Rev. Lett. **51**, 1550 (1983).

[Drummond80] P. D. Drummond and D. F. Walls, *Quantum theory of optical bistability. I. Nonlinear polarisability model*. J. Phys. A **13**, 725 (1980).

[Eichenfield09] M. Eichenfield, J. Chan, A. H. Safavi-Naeini, K. J. Vahala, and O. Painter, *Modeling dispersive coupling and losses of localized optical and mechanical modes in optomechanical crystals*. Opt. Express **17**, 20078 (2009).

[Ekert91] A. K. Ekert, *Quantum cryptography based on Bell's theorem*. Phys. Rev. Lett. **67**, 661 (1991).

[Fabre94] C. Fabre, M. Pinard, S. Bourzeix, A. Heidmann, E. Giacobino, and S. Reynaud, *Quantum-noise reduction using a cavity with a movable mirror*. Phys. Rev. A **49**, 1337 (1994).

[Fedorov12] A. Fedorov, L. Steffen, M. Baur, M. P. da Silva, and A. Wallraff, *Implementation of a Toffoli gate with superconducting circuits*. Nature **481**, 170 (2012).

[Feynman82] R. Feynman, *Simulating physics with computers*. International Journal of Theoretical Physics **21**, 467 (1982).

[Filipp09] S. Filipp, P. Maurer, P. J. Leek, M. Baur, R. Bianchetti, J. M. Fink, M. Göppl, L. Steffen, J. M. Gambetta, A. Blais, and A. Wallraff, *Two-Qubit State Tomography Using a Joint Dispersive Readout*. Phys. Rev. Lett. **102**, 200402 (2009).

[Fink08] J. M. Fink, M. Goppl, M. Baur, R. Bianchetti, P. J. Leek, A. Blais, and A. Wallraff, *Climbing the Jaynes-Cummings ladder and observing its nonlinearity in a cavity QED system*. Nature **454**, 315 (2008).

[Fink09] J. M. Fink, R. Bianchetti, M. Baur, M. Göppl, L. Steffen, S. Filipp, P. J. Leek, A. Blais, and A. Wallraff, *Dressed Collective Qubit States and the Tavis-Cummings Model in Circuit QED*. Phys. Rev. Lett. **103**, 083601 (2009).

[Fiore11] V. Fiore, Y. Yang, M. C. Kuzyk, R. Barbour, L. Tian, and H. Wang, *Storing Optical Information as a Mechanical Excitation in a Silica Optomechanical Resonator*. Phys. Rev. Lett. **107**, 133601 (2011).

[Fomin05] A. E. Fomin, M. L. Gorodetsky, I. S. Grudinin, and V. S. Ilchenko, *Nonstationary nonlinear effects in optical microspheres*. J. Opt. Soc. Am. B **22**, 459 (2005).

[Galiautdinov08] A. Galiautdinov and J. M. Martinis, *Maximally entangling tripartite protocols for Josephson phase qubits*. Phys. Rev. A **78**, 010305 (2008).

[Galiautdinov09] A. Galiautdinov, M. W. Coffey, and R. Deiotte, *Greenberger-Horne-Zeilinger state protocols for fully connected qubit networks*. Phys. Rev. A **80**, 062302 (2009).

[Gambetta11a] J. M. Gambetta, A. A. Houck, and A. Blais, *Superconducting Qubit with Purcell Protection and Tunable Coupling*. Phys. Rev. Lett. **106**, 030502 (2011).

[Gambetta11b] J. M. Gambetta, F. Motzoi, S. T. Merkel, and F. K. Wilhelm, *Analytic control methods for high-fidelity unitary operations in a weakly nonlinear oscillator*. Phys. Rev. A **83**, 012308 (2011).

[Gao05] T. Gao, F. L. Yan, and Z. X. Wang, *Deterministic secure direct communication using GHZ states and swapping quantum entanglement*. Journal of Physics A: Mathematical and General **38**, 5761 (2005).

[Gardiner85] C. W. Gardiner and M. J. Collett, *Input and output in damped quantum systems: Quantum stochastic differential equations and the master equation*. Phys. Rev. A **31**, 3761 (1985).

[Gardiner04] C. Gardiner and P. Zoller, *Quantum Noise: A Handbook of Markovian and Non-Markovian Quantum Stochastic Methods with Applications to Quantum Optics*. 3rd edition, Springer (2004).

[Genes08a] C. Genes, A. Mari, P. Tombesi, and D. Vitali, *Robust entanglement of a micromechanical resonator with output optical fields*. Phys. Rev. A **78**, 032316 (2008).

[Genes08b] C. Genes, D. Vitali, P. Tombesi, S. Gigan, and M. Aspelmeyer, *Ground-state cooling of a micromechanical oscillator: Comparing cold damping and cavity-assisted cooling schemes*. Phys. Rev. A **77**, 033804 (2008).

[Genes09] C. Genes, A. Mari, D. Vitali, and P. Tombesi, *Quantum Effects in Optomechanical Systems*. P. R. B. E. Arimondo and C. C. Lin, editors, *Advances in Atomic Molecular and Optical Physics*, volume 57, pp. 33 – 86, Academic Press (2009).

[Ghobadi11] R. Ghobadi, A. R. Bahrampour, and C. Simon, *Quantum optomechanics in the bistable regime*. Phys. Rev. A **84**, 033846 (2011).

[Gigan06] S. Gigan, H. R. Bohm, M. Paternostro, F. Blaser, G. Langer, J. B. Hertzberg, K. C. Schwab, D. Bauerle, M. Aspelmeyer, and A. Zeilinger, *Self-cooling of a micromirror by radiation pressure*. Nature **444**, 67 (2006).

[Giovannetti04] V. Giovannetti, S. Lloyd, and L. Maccone, *Quantum-Enhanced Measurements: Beating the Standard Quantum Limit*. Science **306**, 1330 (2004).

[Giovannetti06] V. Giovannetti, S. Lloyd, and L. Maccone, *Quantum Metrology*. Phys. Rev. Lett. **96**, 010401 (2006).

[Gisin02] N. Gisin, G. Ribordy, W. Tittel, and H. Zbinden, *Quantum cryptography*. Rev. Mod. Phys. **74**, 145 (2002).

[Gisin07] N. Gisin and R. Thew, *Quantum communication*. Nat. Photon. **1**, 165 (2007).

[Gozzini85] A. Gozzini, F. Maccarrone, F. Mango, I. Longo, and S. Barbarino, *Light-pressure bistability at microwave frequencies*. J. Opt. Soc. Am. B **2**, 1841 (1985).

[Greenberger90] D. M. Greenberger, M. A. Horne, A. Shimony, and A. Zeilinger, *Bell's theorem without inequalities*. American Journal of Physics **58**, 1131 (1990).

[Groblacher09a] S. Groblacher, K. Hammerer, M. R. Vanner, and M. Aspelmeyer, *Observation of strong coupling between a micromechanical resonator and an optical cavity field*. Nature **460**, 724 (2009).

[Groblacher09b] S. Groblacher, J. B. Hertzberg, M. R. Vanner, G. D. Cole, S. Gigan, K. C. Schwab, and M. Aspelmeyer, *Demonstration of an ultracold micro-optomechanical oscillator in a cryogenic cavity*. Nat. Phys. **5**, 485 (2009).

[Grover97] L. K. Grover, *Quantum Mechanics Helps in Searching for a Needle in a Haystack*. Phys. Rev. Lett. **79**, 325 (1997).

[Guillaume06] A. Guillaume and J. P. Dowling, *Heisenberg-limited measurements with superconducting circuits*. Phys. Rev. A **73**, 040304 (2006).

[Gupta07] S. Gupta, K. L. Moore, K. W. Murch, and D. M. Stamper-Kurn, *Cavity Nonlinear Optics at Low Photon Numbers from Collective Atomic Motion*. Phys. Rev. Lett. **99**, 213601 (2007).

[Gühne09] O. Gühne and G. Tóth, *Entanglement detection*. Physics Reports **474**, 1 (2009).

[Haroche06] S. Haroche and J.-M. Raimond, *Exploring the quantum: Atoms, cavities, and photons*. Oxford University Press (2006).

[Helmer09] F. Helmer and F. Marquardt, *Measurement-based synthesis of multiqubit entangled states in superconducting cavity QED*. Phys. Rev. A **79**, 052328 (2009).

[Helmerson01] K. Helmerson and L. You, *Creating Massive Entanglement of Bose-Einstein Condensed Atoms*. Phys. Rev. Lett. **87**, 170402 (2001).

[Hennessy07] K. Hennessy, A. Badolato, M. Winger, D. Gerace, M. Atature, S. Gulde, S. Falt, E. L. Hu, and A. Imamoglu, *Quantum nature of a strongly coupled single quantum dot-cavity system*. Nature **445**, 896 (2007).

[Hertzberg10] J. B. Hertzberg, T. Rocheleau, T. Ndukum, M. Savva, A. A. Clerk, and K. C. Schwab, *Back-action-evading measurements of nanomechanical motion*. Nat. Phys. **6**, 213 (2010).

[Hill12] J. T. Hill, A. H. Safavi-Naeini, J. Chan, and O. Painter, *Coherent optical wavelength conversion via cavity optomechanics*. Nat. Commun. **3**, 1196 (2012).

[Hillery99] M. Hillery, V. Bužek, and A. Berthiaume, *Quantum secret sharing*. Phys. Rev. A **59**, 1829 (1999).

[Hoffman11a] A. J. Hoffman, S. J. Srinivasan, J. M. Gambetta, and A. A. Houck, *Coherent control of a superconducting qubit with dynamically tunable qubit-cavity coupling*. Phys. Rev. B **84**, 184515 (2011).

[Hoffman11b] A. J. Hoffman, S. J. Srinivasan, S. Schmidt, L. Spietz, J. Aumentado, H. E. Türeci, and A. A. Houck, *Dispersive Photon Blockade in a Superconducting Circuit*. Phys. Rev. Lett. **107**, 053602 (2011).

[Horodecki09] R. Horodecki, P. Horodecki, M. Horodecki, and K. Horodecki, *Quantum entanglement*. Rev. Mod. Phys. **81**, 865 (2009).

[Houck07] A. A. Houck, D. I. Schuster, J. M. Gambetta, J. A. Schreier, B. R. Johnson, J. M. Chow, L. Frunzio, J. Majer, M. H. Devoret, S. M. Girvin, and R. J. Schoelkopf, *Generating single microwave photons in a circuit*. Nature **449**, 328 (2007).

[Houck08] A. A. Houck, J. A. Schreier, B. R. Johnson, J. M. Chow, J. Koch, J. M. Gambetta, D. I. Schuster, L. Frunzio, M. H. Devoret, S. M. Girvin, and R. J. Schoelkopf, *Controlling the Spontaneous Emission of a Superconducting Transmon Qubit*. Phys. Rev. Lett. **101**, 080502 (2008).

[Houck09] A. Houck, J. Koch, M. Devoret, S. Girvin, and R. Schoelkopf, *Life after charge noise: recent results with transmon qubits*. Quantum Information Processing **8**, 105 (2009).

[Huelga97] S. F. Huelga, C. Macchiavello, T. Pellizzari, A. K. Ekert, M. B. Plenio, and J. I. Cirac, *Improvement of Frequency Standards with Quantum Entanglement*. Phys. Rev. Lett. **79**, 3865 (1997).

[Hutchinson04] G. D. Hutchinson and G. J. Milburn, *Nonlinear quantum optical computing via measurement*. Journal of Modern Optics **51**, 1211 (2004).

[Hutchison09] C. L. Hutchison, J. M. Gambetta, A. Blais, and F. K. Wilhelm, *Quantum trajectory equation for multiple qubits in circuit QED: Generating entanglement by measurement*. Canadian Journal of Physics **87**, 225 (2009).

[Ithier05] G. Ithier, E. Collin, P. Joyez, P. J. Meeson, D. Vion, D. Esteve, F. Chiarello, A. Shnirman, Y. Makhlin, J. Schriefl, and G. Schön, *Decoherence in a superconducting quantum bit circuit*. Phys. Rev. B **72**, 134519 (2005).

[Iwasawa13] K. Iwasawa, K. Makino, H. Yonezawa, M. Tsang, A. Davidovic, E. Huntington, and A. Furusawa, *Quantum-Limited Mirror-Motion Estimation*. Phys. Rev. Lett. **111**, 163602 (2013).

[Jaynes63] E. Jaynes and F. Cummings, *Comparison of quantum and semi-classical radiation theories with application to the beam maser*. Proceedings of the IEEE **51**, 89 (1963).

[Kaltenbaek12] R. Kaltenbaek, G. Hechenblaikner, N. Kiesel, O. Romero-Isart, K. Schwab, U. Johann, and M. Aspelmeyer, *Macroscopic quantum resonators (MAQRO)*. Experimental Astronomy **34**, 123 (2012).

[Kerckhoff11] J. Kerckhoff, M. A. Armen, and H. Mabuchi, *Remnants of semi-classical bistability in the few-photon regime of cavity QED*. Opt. Express **19**, 24468 (2011).

[Kimble08] H. J. Kimble, *The quantum internet*. Nature **453**, 1023 (2008).

[Kippenberg08] T. J. Kippenberg and K. J. Vahala, *Cavity Optomechanics: Back-Action at the Mesoscale*. Science **321**, 1172 (2008).

[Kleckner06] D. Kleckner and D. Bouwmeester, *Sub-kelvin optical cooling of a micromechanical resonator*. Nature **444**, 75 (2006).

[Kleckner11] D. Kleckner, B. Pepper, E. Jeffrey, P. Sonin, S. M. Thon, and D. Bouwmeester, *Optomechanical trampoline resonators*. Opt. Express **19**, 19708 (2011).

[Knill97] E. Knill and R. Laflamme, *Theory of quantum error-correcting codes*. Phys. Rev. A **55**, 900 (1997).

[Knill01] E. Knill, R. Laflamme, and G. J. Milburn, *A scheme for efficient quantum computation with linear optics*. Nature **409**, 46 (2001).

[Koch07] J. Koch, T. M. Yu, J. Gambetta, A. A. Houck, D. I. Schuster, J. Majer, A. Blais, M. H. Devoret, S. M. Girvin, and R. J. Schoelkopf, *Charge-insensitive qubit design derived from the Cooper pair box*. Phys. Rev. A **76**, 042319 (2007).

[Koch11] J. Koch, *Personal discussion* (2011).

[Kok07] P. Kok, W. J. Munro, K. Nemoto, T. C. Ralph, J. P. Dowling, and G. J. Milburn, *Linear optical quantum computing with photonic qubits*. Rev. Mod. Phys. **79**, 135 (2007).

[Krause12] A. G. Krause, M. Winger, T. D. Blasius, Q. Lin, and O. Painter, *A high-resolution microchip optomechanical accelerometer*. Nat. Photon. **6**, 768 (2012).

[Kronwald13] A. Kronwald, M. Ludwig, and F. Marquardt, *Full photon statistics of a light beam transmitted through an optomechanical system*. Phys. Rev. A **87**, 013847 (2013).

[Ladd10] T. D. Ladd, F. Jelezko, R. Laflamme, Y. Nakamura, C. Monroe, and J. L. O'Brien, *Quantum computers*. Nature **464**, 45 (2010).

[LaHaye04] M. D. LaHaye, O. Buu, B. Camarota, and K. C. Schwab, *Approaching the Quantum Limit of a Nanomechanical Resonator*. Science **304**, 74 (2004).

[LaHaye09] M. D. LaHaye, J. Suh, P. M. Echternach, K. C. Schwab, and M. L. Roukes, *Nanomechanical measurements of a superconducting qubit*. Nature **459**, 960 (2009).

[Lamata07] L. Lamata, J. León, D. Salgado, and E. Solano, *Inductive entanglement classification of four qubits under stochastic local operations and classical communication*. Phys. Rev. A **75**, 022318 (2007).

[Lang11] C. Lang, D. Bozyigit, C. Eichler, L. Steffen, J. M. Fink, A. A. Abdumalikov, M. Baur, S. Filipp, M. P. da Silva, A. Blais, and A. Wallraff, *Observation of Resonant Photon Blockade at Microwave Frequencies Using Correlation Function Measurements*. Phys. Rev. Lett. **106**, 243601 (2011).

[Law95] C. K. Law, *Interaction between a moving mirror and radiation pressure: A Hamiltonian formulation*. Phys. Rev. A **51**, 2537 (1995).

[Lebedew01] P. Lebedew, *Untersuchungen über die Druckkräfte des Lichtes*. Annalen der Physik **311**, 433 (1901).

[Leek07] P. J. Leek, J. M. Fink, A. Blais, R. Bianchetti, M. Göppl, J. M. Gambetta, D. I. Schuster, L. Frunzio, R. J. Schoelkopf, and A. Wallraff, *Observation of Berry's Phase in a Solid-State Qubit*. Science **318**, 1889 (2007).

[Leek09] P. J. Leek, S. Filipp, P. Maurer, M. Baur, R. Bianchetti, J. M. Fink, M. Göppl, L. Steffen, and A. Wallraff, *Using sideband transitions for two-qubit operations in superconducting circuits*. Phys. Rev. B **79**, 180511 (2009).

[Leek10] P. J. Leek, M. Baur, J. M. Fink, R. Bianchetti, L. Steffen, S. Filipp, and A. Wallraff, *Cavity Quantum Electrodynamics with Separate Photon Storage and Qubit Readout Modes*. Phys. Rev. Lett. **104**, 100504 (2010).

[Leggett87] A. J. Leggett, S. Chakravarty, A. T. Dorsey, M. P. A. Fisher, A. Garg, and W. Zwerger, *Dynamics of the dissipative two-state system*. Rev. Mod. Phys. **59**, 1 (1987).

[Leibfried05] D. Leibfried, E. Knill, S. Seidelin, J. Britton, R. B. Blakestad, J. Chiaverini, D. B. Hume, W. M. Itano, J. D. Jost, C. Langer, R. Ozeri, R. Reichle, and D. J. Wineland, *Creation of a six-atom /'Schrodinger cat/' state*. Nature **438**, 639 (2005).

[Lett88] P. D. Lett, R. N. Watts, C. I. Westbrook, W. D. Phillips, P. L. Gould, and H. J. Metcalf, *Observation of Atoms Laser Cooled below the Doppler Limit*. Phys. Rev. Lett. **61**, 169 (1988).

[Lucero10] E. Lucero, J. Kelly, R. C. Bialczak, M. Lenander, M. Mariantoni, M. Neeley, A. D. O'Connell, D. Sank, H. Wang, M. Weides, J. Wenner, T. Yamamoto, A. N. Cleland, and J. M. Martinis, *Reduced phase error through optimized control of a superconducting qubit*. Phys. Rev. A **82**, 042339 (2010).

[Ludwig08] M. Ludwig, B. Kubala, and F. Marquardt, *The optomechanical instability in the quantum regime*. New Journal of Physics **10**, 095013 (2008).

[Ludwig12] M. Ludwig, A. H. Safavi-Naeini, O. Painter, and F. Marquardt, *Enhanced Quantum Nonlinearities in a Two-Mode Optomechanical System*. Phys. Rev. Lett. **109**, 063601 (2012).

[Mabuchi02] H. Mabuchi and A. C. Doherty, *Cavity Quantum Electrodynamics: Coherence in Context*. Science **298**, 1372 (2002).

[Majer07] J. Majer, J. M. Chow, J. M. Gambetta, J. Koch, B. R. Johnson, J. A. Schreier, L. Frunzio, D. I. Schuster, A. A. Houck, A. Wallraff, A. Blais, M. H. Devoret, S. M. Girvin, and R. J. Schoelkopf, *Coupling superconducting qubits via a cavity bus*. Nature **449**, 443 (2007).

[Makhlin01] Y. Makhlin, G. Schön, and A. Shnirman, *Quantum-state engineering with Josephson-junction devices*. Rev. Mod. Phys. **73**, 357 (2001).

[Mallet09] F. Mallet, F. R. Ong, A. Palacios-Laloy, F. Nguyen, P. Bertet, D. Vion, and D. Esteve, *Single-shot qubit readout in circuit quantum electrodynamics*. Nat. Phys. **5**, 791 (2009).

[Mancini94] S. Mancini and P. Tombesi, *Quantum noise reduction by radiation pressure*. Phys. Rev. A **49**, 4055 (1994).

[Mancini97] S. Mancini, V. I. Man'ko, and P. Tombesi, *Ponderomotive control of quantum macroscopic coherence*. Phys. Rev. A **55**, 3042 (1997).

[Mancini98] S. Mancini, D. Vitali, and P. Tombesi, *Optomechanical Cooling of a Macroscopic Oscillator by Homodyne Feedback*. Phys. Rev. Lett. **80**, 688 (1998).

[Marder10] M. Marder, *Condensed Matter Physics*. Wiley (2010).

[Mari09] A. Mari and J. Eisert, *Gently Modulating Optomechanical Systems*. Phys. Rev. Lett. **103**, 213603 (2009).

[Marino11] F. Marino and F. Marin, *Chaotically spiking attractors in suspended-mirror optical cavities*. Phys. Rev. E **83**, 015202 (2011).

[Marino13] F. Marino and F. Marin, *Coexisting attractors and chaotic canard explosions in a slow-fast optomechanical system*. Phys. Rev. E **87**, 052906 (2013).

[Marquardt01] F. Marquardt and C. Bruder, *Superposition of two mesoscopically distinct quantum states: Coupling a Cooper-pair box to a large superconducting island*. Phys. Rev. B **63**, 054514 (2001).

[Marquardt06] F. Marquardt, J. G. E. Harris, and S. M. Girvin, *Dynamical Multistability Induced by Radiation Pressure in High-Finesse Micromechanical Optical Cavities*. Phys. Rev. Lett. **96**, 103901 (2006).

[Marquardt07] F. Marquardt, J. P. Chen, A. A. Clerk, and S. M. Girvin, *Quantum Theory of Cavity-Assisted Sideband Cooling of Mechanical Motion*. Phys. Rev. Lett. **99**, 093902 (2007).

[Marquardt09] F. Marquardt and S. M. Girvin, *Optomechanics*. Physics **2**, 40 (2009).

[Marshall03] W. Marshall, C. Simon, R. Penrose, and D. Bouwmeester, *Towards Quantum Superpositions of a Mirror*. Phys. Rev. Lett. **91**, 130401 (2003).

[Massel11] F. Massel, T. T. Heikkila, J.-M. Pirkkalainen, S. U. Cho, H. Saloniemi, P. J. Hakonen, and M. A. Sillanpaa, *Microwave amplification with nanomechanical resonators*. Nature **480**, 351 (2011).

[McGee13] S. A. McGee, D. Meiser, C. A. Regal, K. W. Lehnert, and M. J. Holland, *Mechanical resonators for storage and transfer of electrical and optical quantum states*. Phys. Rev. A **87**, 053818 (2013).

[Mermin90a] N. D. Mermin, *Extreme quantum entanglement in a superposition of macroscopically distinct states*. Phys. Rev. Lett. **65**, 1838 (1990).

[Mermin90b] N. D. Mermin, *Quantum mysteries revisited*. American Journal of Physics **58**, 731 (1990).

[Metcalfe07] M. Metcalfe, E. Boaknin, V. Manucharyan, R. Vijay, I. Siddiqi, C. Rigetti, L. Frunzio, R. J. Schoelkopf, and M. H. Devoret, *Measuring the decoherence of a quantronium qubit with the cavity bifurcation amplifier*. Phys. Rev. B **76**, 174516 (2007).

[Meystre85] P. Meystre, E. M. Wright, J. D. McCullen, and E. Vignes, *Theory of radiation-pressure-driven interferometers*. J. Opt. Soc. Am. B **2**, 1830 (1985).

[Meystre07] P. Meystre and M. Sargent, *Elements of Quantum Optics*. Springer (2007).

[Meystre13] P. Meystre, *A short walk through quantum optomechanics*. Annalen der Physik **525**, 215 (2013).

[Milburn89] G. J. Milburn, *Quantum optical Fredkin gate*. Phys. Rev. Lett. **62**, 2124 (1989).

[Milburn97] G. J. Milburn, J. Corney, E. M. Wright, and D. F. Walls, *Quantum dynamics of an atomic Bose-Einstein condensate in a double-well potential*. Phys. Rev. A **55**, 4318 (1997).

[Milburn12] G. Milburn and M. Woolley, *An Introduction to Quantum Optomechanics*. Acta Physica Slovaca. Reviews and Tutorials. **61**, 483 (2012).

[Mlynek12] J. A. Mlynek, A. A. Abdumalikov, J. M. Fink, L. Steffen, M. Baur, C. Lang, A. F. van Loo, and A. Wallraff, *Demonstrating W-type entanglement of Dicke states in resonant cavity quantum electrodynamics*. Phys. Rev. A **86**, 053838 (2012).

[Mølmer99] K. Mølmer and A. Sørensen, *Multiparticle Entanglement of Hot Trapped Ions*. Phys. Rev. Lett. **82**, 1835 (1999).

[Monz11] T. Monz, P. Schindler, J. T. Barreiro, M. Chwalla, D. Nigg, W. A. Coish, M. Harlander, W. Hänsel, M. Hennrich, and R. Blatt, *14-Qubit Entanglement: Creation and Coherence*. Phys. Rev. Lett. **106**, 130506 (2011).

[Motzoi09] F. Motzoi, J. M. Gambetta, P. Rebentrost, and F. K. Wilhelm, *Simple Pulses for Elimination of Leakage in Weakly Nonlinear Qubits*. Phys. Rev. Lett. **103**, 110501 (2009).

[Mueller08] F. Mueller, S. Heugel, and L. J. Wang, *Observation of optomechanical multistability in a high-Q torsion balance oscillator*. Phys. Rev. A **77**, 031802 (2008).

[Munro05] W. J. Munro, K. Nemoto, and T. P. Spiller, *Weak nonlinearities: a new route to optical quantum computation*. New Journal of Physics **7**, 137 (2005).

[Murch08a] K. W. Murch, *Cavity Quantum Optomechanics with Ultracold Atoms*. Ph.D. thesis, University of California, Berkeley (2008).

[Murch08b] K. W. Murch, K. L. Moore, S. Gupta, and D. M. Stamper-Kurn, *Observation of quantum-measurement backaction with an ultracold atomic gas*. Nat. Phys. **4**, 561 (2008).

[Nakamura99] Y. Nakamura, Y. A. Pashkin, and J. S. Tsai, *Coherent control of macroscopic quantum states in a single-Cooper-pair box*. Nature **398**, 786 (1999).

[Neeley10] M. Neeley, R. C. Bialczak, M. Lenander, E. Lucero, M. Mariantoni, A. D. O'Connell, D. Sank, H. Wang, M. Weides, J. Wenner, Y. Yin, T. Yamamoto, A. N. Cleland, and J. M. Martinis, *Generation of three-qubit entangled states using superconducting phase qubits*. Nature **467**, 570 (2010).

[Nemoto04] K. Nemoto and W. J. Munro, *Nearly Deterministic Linear Optical Controlled-NOT Gate*. Phys. Rev. Lett. **93**, 250502 (2004).

[Neuhauser78] W. Neuhauser, M. Hohenstatt, P. Toschek, and H. Dehmelt, *Optical-Sideband Cooling of Visible Atom Cloud Confined in Parabolic Well*. Phys. Rev. Lett. **41**, 233 (1978).

[Nichols01] E. F. Nichols and G. F. Hull, *A Preliminary Communication on the Pressure of Heat and Light Radiation*. Phys. Rev. (Series I) **13**, 307 (1901).

[Nielsen00] M. A. Nielsen and I. L. Chuang, *Quantum computation and quantum information*. Cambridge university press (2000).

[Nunnenkamp11] A. Nunnenkamp, K. Børkje, and S. M. Girvin, *Single-Photon Optomechanics*. Phys. Rev. Lett. **107**, 063602 (2011).

[O'Brien07] J. L. O'Brien, *Optical Quantum Computing*. Science **318**, 1567 (2007).

[O'Brien09] J. L. O'Brien, A. Furusawa, and J. Vuckovic, *Photonic quantum technologies*. Nature Photon. **3**, 687 (2009).

[O'Connell10] A. D. O'Connell, M. Hofheinz, M. Ansmann, R. C. Bialczak, M. Lenander, E. Lucero, M. Neeley, D. Sank, H. Wang, M. Weides, J. Wenner, J. M. Martinis, and A. N. Cleland, *Quantum ground state and single-phonon control of a mechanical resonator*. Nature **464**, 697 (2010).

[Paik11] H. Paik, D. I. Schuster, L. S. Bishop, G. Kirchmair, G. Catelani, A. P. Sears, B. R. Johnson, M. J. Reagor, L. Frunzio, L. I. Glazman, S. M. Girvin, M. H. Devoret, and R. J. Schoelkopf, *Observation of High Coherence in Josephson Junction Qubits Measured in a Three-Dimensional Circuit QED Architecture*. Phys. Rev. Lett. **107**, 240501 (2011).

[Palomaki13a] T. A. Palomaki, J. W. Harlow, J. D. Teufel, R. W. Simmonds, and K. W. Lehnert, *Coherent state transfer between itinerant microwave fields and a mechanical oscillator*. Nature **495**, 210 (2013).

[Palomaki13b] T. A. Palomaki, J. D. Teufel, R. W. Simmonds, and K. W. Lehnert, *Entangling Mechanical Motion with Microwave Fields*. Science **342**, 710 (2013).

[Park09] Y.-S. Park and H. Wang, *Resolved-sideband and cryogenic cooling of an optomechanical resonator*. Nat. Phys. **5**, 489 (2009).

[Pikovski12] I. Pikovski, M. R. Vanner, M. Aspelmeyer, M. S. Kim, and C. Brukner, *Probing Planck-scale physics with quantum optics*. Nat. Phys. **8**, 393 (2012).

[Pinard95] M. Pinard, C. Fabre, and A. Heidmann, *Quantum-nondemolition measurement of light by a piezoelectric crystal*. Phys. Rev. A **51**, 2443 (1995).

[Pinard99] M. Pinard, Y. Hadjar, and A. Heidmann, *Effective mass in quantum effects of radiation pressure*. The European Physical Journal D - Atomic, Molecular, Optical and Plasma Physics **7**, 107 (1999).

[Plantenberg07] J. H. Plantenberg, P. C. de Groot, C. J. P. M. Harmans, and J. E. Mooij, *Demonstration of controlled-NOT quantum gates on a pair of superconducting quantum bits*. Nature **447**, 836 (2007).

[Poggio07] M. Poggio, C. L. Degen, H. J. Mamin, and D. Rugar, *Feedback Cooling of a Cantilever's Fundamental Mode below 5 mK*. Phys. Rev. Lett. **99**, 017201 (2007).

[Poot12] M. Poot and H. S. van der Zant, *Mechanical systems in the quantum regime*. Physics Reports **511**, 273 (2012).

[Preskill98] J. Preskill, *Fault-tolerant quantum computations*. *Introduction to Quantum Computation and Information*, pp. 213–269, World Scientific (1998).

[Purcell46] E. M. Purcell, *Spontaneous emission probabilities at radio frequencies*. Phys. Rev. **69**, 681 (1946).

[Purdy13a] T. P. Purdy, R. W. Peterson, and C. A. Regal, *Observation of Radiation Pressure Shot Noise on a Macroscopic Object*. Science **339**, 801 (2013).

[Purdy13b] T. P. Purdy, P.-L. Yu, R. W. Peterson, N. S. Kampel, and C. A. Regal, *Strong Optomechanical Squeezing of Light*. Phys. Rev. X **3**, 031012 (2013).

[Qian12] J. Qian, A. A. Clerk, K. Hammerer, and F. Marquardt, *Quantum Signatures of the Optomechanical Instability*. Phys. Rev. Lett. **109**, 253601 (2012).

[Rabl11] P. Rabl, *Photon Blockade Effect in Optomechanical Systems*. Phys. Rev. Lett. **107**, 063601 (2011).

[Raimond01] J. M. Raimond, M. Brune, and S. Haroche, *Manipulating quantum entanglement with atoms and photons in a cavity*. Rev. Mod. Phys. **73**, 565 (2001).

[Rauschenbeutel99] A. Rauschenbeutel, G. Nogues, S. Osnaghi, P. Bertet, M. Brune, J. M. Raimond, and S. Haroche, *Coherent Operation of a Tunable Quantum Phase Gate in Cavity QED*. Phys. Rev. Lett. **83**, 5166 (1999).

[Reed10] M. D. Reed, B. R. Johnson, A. A. Houck, L. DiCarlo, J. M. Chow, D. I. Schuster, L. Frunzio, and R. J. Schoelkopf, *Fast reset and suppressing spontaneous emission of a superconducting qubit*. Applied Physics Letters **96**, 203110 (2010).

[Reed12] M. D. Reed, L. DiCarlo, S. E. Nigg, L. Sun, L. Frunzio, S. M. Girvin, and R. J. Schoelkopf, *Realization of three-qubit quantum error correction with superconducting circuits*. Nature **482**, 382 (2012).

[Regal08] C. A. Regal, J. D. Teufel, and K. W. Lehnert, *Measuring nanomechanical motion with a microwave cavity interferometer*. Nat. Phys. **4**, 555 (2008).

[Rigetti12] C. Rigetti, J. M. Gambetta, S. Poletto, B. L. T. Plourde, J. M. Chow, A. D. Córcoles, J. A. Smolin, S. T. Merkel, J. R. Rozen, G. A. Keefe, M. B. Rothwell, M. B. Ketchen, and M. Steffen, *Superconducting qubit in a waveguide cavity with a coherence time approaching 0.1 ms*. Phys. Rev. B **86**, 100506 (2012).

[Rigo97] M. Rigo, G. Alber, F. Mota-Furtado, and P. F. O'Mahony, *Quantum-state diffusion model and the driven damped nonlinear oscillator*. Phys. Rev. A **55**, 1665 (1997).

[Risken87] H. Risken, C. Savage, F. Haake, and D. F. Walls, *Quantum tunneling in dispersive optical bistability*. Phys. Rev. A **35**, 1729 (1987).

[Ristè12a] D. Ristè, C. C. Bultink, K. W. Lehnert, and L. DiCarlo, *Feedback Control of a Solid-State Qubit Using High-Fidelity Projective Measurement*. Phys. Rev. Lett. **109**, 240502 (2012).

[Ristè12b] D. Ristè, J. G. van Leeuwen, H.-S. Ku, K. W. Lehnert, and L. DiCarlo, *Initialization by Measurement of a Superconducting Quantum Bit Circuit*. Phys. Rev. Lett. **109**, 050507 (2012).

[Ristè13] D. Ristè, M. Dukalski, C. A. Watson, G. de Lange, M. J. Tiggelman, Y. M. Blanter, K. W. Lehnert, R. N. Schouten, and L. DiCarlo, *Deterministic entanglement of superconducting qubits by parity measurement and feedback*. Nature **502**, 350 (2013).

[Ritter09] S. Ritter, F. Brennecke, K. Baumann, T. Donner, C. Guerlin, and T. Esslinger, *Dynamical coupling between a Bose-Einstein condensate and a cavity optical lattice*. Applied Physics B **95**, 213 (2009).

[Rivière11] R. Rivière, S. Deléglise, S. Weis, E. Gavartin, O. Arcizet, A. Schliesser, and T. J. Kippenberg, *Optomechanical sideband cooling of a micromechanical oscillator close to the quantum ground state*. Phys. Rev. A **83**, 063835 (2011).

[Rocheleau10] T. Rocheleau, T. Ndukum, C. Macklin, J. B. Hertzberg, A. A. Clerk, and K. C. Schwab, *Preparation and detection of a mechanical resonator near the ground state of motion*. Nature **463**, 72 (2010).

[Rodrigues08] D. A. Rodrigues, C. E. A. Jarvis, B. L. Györffy, T. P. Spiller, and J. F. Annett, *Entanglement of superconducting charge qubits by homodyne measurement*. Journal of Physics: Condensed Matter **20**, 075211 (2008).

[Romero-Isart11] O. Romero-Isart, *Quantum superposition of massive objects and collapse models*. Phys. Rev. A **84**, 052121 (2011).

[Sackett00] C. A. Sackett, D. Kielpinski, B. E. King, C. Langer, V. Meyer, C. J. Myatt, M. Rowe, Q. A. Turchette, W. M. Itano, D. J. Wineland, and C. Monroe, *Experimental entanglement of four particles*. Nature **404**, 256 (2000).

[Safavi-Naeini10] A. H. Safavi-Naeini and O. Painter, *Design of optomechanical cavities and waveguides on a simultaneous bandgap phononic-photonic crystal slab*. Opt. Express **18**, 14926 (2010).

[Safavi-Naeini11a] A. H. Safavi-Naeini, T. P. M. Alegre, J. Chan, M. Eichenfield, M. Winger, Q. Lin, J. T. Hill, D. E. Chang, and O. Painter, *Electromagnetically induced transparency and slow light with optomechanics*. Nature **472**, 69 (2011).

[Safavi-Naeini11b] A. H. Safavi-Naeini and O. Painter, *Proposal for an optomechanical traveling wave phonon-photon translator*. New Journal of Physics **13**, 013017 (2011).

[Safavi-Naeini12] A. H. Safavi-Naeini, J. Chan, J. T. Hill, T. P. M. Alegre, A. Krause, and O. Painter, *Observation of Quantum Motion of a Nanomechanical Resonator*. Phys. Rev. Lett. **108**, 033602 (2012).

[Safavi-Naeini13] A. H. Safavi-Naeini, S. Groblacher, J. T. Hill, J. Chan, M. Aspelmeyer, and O. Painter, *Squeezed light from a silicon micromechanical resonator*. Nature **500**, 185 (2013), letter.

[Sarovar05] M. Sarovar, H.-S. Goan, T. P. Spiller, and G. J. Milburn, *High-fidelity measurement and quantum feedback control in circuit QED*. Phys. Rev. A **72**, 062327 (2005).

[Scarani09] V. Scarani, H. Bechmann-Pasquinucci, N. J. Cerf, M. Dušek, N. Lütkenhaus, and M. Peev, *The security of practical quantum key distribution*. Rev. Mod. Phys. **81**, 1301 (2009).

[Schleier-Smith11] M. H. Schleier-Smith, I. D. Leroux, H. Zhang, M. A. Van Camp, and V. Vuletić, *Optomechanical Cavity Cooling of an Atomic Ensemble*. Phys. Rev. Lett. **107**, 143005 (2011).

[Schliesser06] A. Schliesser, P. Del'Haye, N. Nooshi, K. J. Vahala, and T. J. Kippenberg, *Radiation Pressure Cooling of a Micromechanical Oscillator Using Dynamical Backaction*. Phys. Rev. Lett. **97**, 243905 (2006).

[Schliesser08] A. Schliesser, R. Riviere, G. Anetsberger, O. Arcizet, and T. J. Kippenberg, *Resolved-sideband cooling of a micromechanical oscillator*. Nat. Phys. **4**, 415 (2008).

[Schliesser09] A. Schliesser, O. Arcizet, R. Riviere, G. Anetsberger, and T. J. Kippenberg, *Resolved-sideband cooling and position measurement of a micromechanical oscillator close to the Heisenberg uncertainty limit*. Nat. Phys. **5**, 509 (2009).

[Schoelkopf08] R. J. Schoelkopf and S. M. Girvin, *Wiring up quantum systems*. Nature **451**, 664 (2008).

[Schreier08] J. A. Schreier, A. A. Houck, J. Koch, D. I. Schuster, B. R. Johnson, J. M. Chow, J. M. Gambetta, J. Majer, L. Frunzio, M. H. Devoret, S. M. Girvin, and R. J. Schoelkopf, *Suppressing charge noise decoherence in superconducting charge qubits*. Phys. Rev. B **77**, 180502 (2008).

[Schuster05] D. I. Schuster, A. Wallraff, A. Blais, L. Frunzio, R.-S. Huang, J. Majer, S. M. Girvin, and R. J. Schoelkopf, *ac Stark Shift and Dephasing of a Superconducting Qubit Strongly Coupled to a Cavity Field*. Phys. Rev. Lett. **94**, 123602 (2005).

[Schuster07] D. I. Schuster, A. A. Houck, J. A. Schreier, A. Wallraff, J. M. Gambetta, A. Blais, L. Frunzio, J. Majer, B. Johnson, M. H. Devoret, S. M. Girvin, and R. J. Schoelkopf, *Resolving photon number states in a superconducting circuit*. Nature **445**, 515 (2007).

[Schwab05] K. C. Schwab and M. L. Roukes, *Putting mechanics into quantum mechanics*. Physics Today **58**, 36 (2005).

[Sheard04] B. S. Sheard, M. B. Gray, C. M. Mow-Lowry, D. E. McClelland, and S. E. Whitcomb, *Observation and characterization of an optical spring*. Phys. Rev. A **69**, 051801 (2004).

[Shnirman97] A. Shnirman, G. Schön, and Z. Hermon, *Quantum Manipulations of Small Josephson Junctions*. Phys. Rev. Lett. **79**, 2371 (1997).

[Shor95] P. W. Shor, *Scheme for reducing decoherence in quantum computer memory*. Phys. Rev. A **52**, R2493 (1995).

[Shor97] P. W. Shor, *Polynomial-time algorithms for prime factorization and discrete logarithms on a quantum computer*. SIAM journal on computing **26**, 1484 (1997).

[Slusher85] R. E. Slusher, L. W. Hollberg, B. Yurke, J. C. Mertz, and J. F. Valley, *Observation of Squeezed States Generated by Four-Wave Mixing in an Optical Cavity*. Phys. Rev. Lett. **55**, 2409 (1985).

[Sørensen00] A. Sørensen and K. Mølmer, *Entanglement and quantum computation with ions in thermal motion*. Phys. Rev. A **62**, 022311 (2000).

[Srinivasan11] S. J. Srinivasan, A. J. Hoffman, J. M. Gambetta, and A. A. Houck, *Tunable Coupling in Circuit Quantum Electrodynamics Using a Superconducting Charge Qubit with a V-Shaped Energy Level Diagram*. Phys. Rev. Lett. **106**, 083601 (2011).

[Stamper-Kurn12] D. M. Stamper-Kurn, *Cavity optomechanics with cold atoms*. arXiv:1204.4351 (2012).

[Stannigel10] K. Stannigel, P. Rabl, A. S. Sørensen, P. Zoller, and M. D. Lukin, *Optomechanical Transducers for Long-Distance Quantum Communication*. Phys. Rev. Lett. **105**, 220501 (2010).

[Steane96] A. Steane, *Multiple-Particle Interference and Quantum Error Correction*. Proceedings of the Royal Society of London. Series A: Mathematical, Physical and Engineering Sciences **452**, 2551 (1996).

[Steffen06] M. Steffen, M. Ansmann, R. C. Bialczak, N. Katz, E. Lucero, R. McDermott, M. Neeley, E. M. Weig, A. N. Cleland, and J. M. Martinis, *Measurement of the Entanglement of Two Superconducting Qubits via State Tomography*. Science **313**, 1423 (2006).

[Steffen13] L. Steffen, Y. Salathe, M. Oppliger, P. Kurpiers, M. Baur, C. Lang, C. Eichler, G. Puebla-Hellmann, A. Fedorov, and A. Wallraff, *Deterministic quantum teleportation with feedforward in a solid state system*. Nature **500**, 319 (2013).

[Teufel09] J. D. Teufel, T. Donner, M. A. Castellanos-Beltran, J. W. Harlow, and K. W. Lehnert, *Nanomechanical motion measured with an imprecision below that at the standard quantum limit*. Nat. Nano. **4**, 820 (2009).

[Teufel11a] J. D. Teufel, T. Donner, D. Li, J. W. Harlow, M. S. Allman, K. Cicak, A. J. Sirois, J. D. Whittaker, K. W. Lehnert, and R. W. Simmonds, *Sideband cooling of micromechanical motion to the quantum ground state*. Nature **475**, 359 (2011).

[Teufel11b] J. D. Teufel, D. Li, M. S. Allman, K. Cicak, A. J. Sirois, J. D. Whittaker, and R. W. Simmonds, *Circuit cavity electromechanics in the strong-coupling regime*. Nature **471**, 204 (2011).

[Thompson08] J. D. Thompson, B. M. Zwickl, A. M. Jayich, F. Marquardt, S. M. Girvin, and J. G. E. Harris, *Strong dispersive coupling of a high-finesse cavity to a micromechanical membrane*. Nature **452**, 72 (2008).

[Tian10] L. Tian and H. Wang, *Optical wavelength conversion of quantum states with optomechanics*. Phys. Rev. A **82**, 053806 (2010).

[Tinkham96] M. Tinkham, *Introduction to Superconductivity*. 2nd edition, McGraw-Hill (1996).

[Tittonen99] I. Tittonen, G. Breitenbach, T. Kalkbrenner, T. Müller, R. Conradt, S. Schiller, E. Steinsland, N. Blanc, and N. F. de Rooij, *Interferometric measurements of the position of a macroscopic body: Towards observation of quantum limits*. Phys. Rev. A **59**, 1038 (1999).

[Tsang11] M. Tsang, *Cavity quantum electro-optics. II. Input-output relations between traveling optical and microwave fields*. Phys. Rev. A **84**, 043845 (2011).

[Tsomokos08] D. I. Tsomokos, S. Ashhab, and F. Nori, *Fully connected network of superconducting qubits in a cavity*. New Journal of Physics **10**, 113020 (2008).

[Turchette95] Q. A. Turchette, C. J. Hood, W. Lange, H. Mabuchi, and H. J. Kimble, *Measurement of Conditional Phase Shifts for Quantum Logic*. Phys. Rev. Lett. **75**, 4710 (1995).

[Vahala03] K. J. Vahala, *Optical microcavities*. Nature **424**, 839 (2003).

[Vahala04] K. Vahala, *Optical Microcavities*. Advanced series in applied physics, World Scientific (2004).

[Verhagen12] E. Verhagen, S. Deléglise, S. Weis, A. Schliesser, and T. Kippenberg, *Quantum-coherent coupling of a mechanical oscillator to an optical cavity mode*. Nature **482**, 63 (2012).

[Verstraete02] F. Verstraete, J. Dehaene, B. De Moor, and H. Verschelde, *Four qubits can be entangled in nine different ways*. Phys. Rev. A **65**, 052112 (2002).

[Vijay11] R. Vijay, D. H. Slichter, and I. Siddiqi, *Observation of Quantum Jumps in a Superconducting Artificial Atom*. Phys. Rev. Lett. **106**, 110502 (2011).

[Vijay12] R. Vijay, C. Macklin, D. H. Slichter, S. J. Weber, K. W. Murch, R. Naik, A. N. Korotkov, and I. Siddiqi, *Stabilizing Rabi oscillations in a superconducting qubit using quantum feedback*. Nature **490**, 77 (2012).

[Vion02] D. Vion, A. Aassime, A. Cottet, P. Joyez, H. Pothier, C. Urbina, D. Esteve, and M. H. Devoret, *Manipulating the Quantum State of an Electrical Circuit*. Science **296**, 886 (2002).

[Vitali07a] D. Vitali, S. Gigan, A. Ferreira, H. R. Böhm, P. Tombesi, A. Guerreiro, V. Vedral, A. Zeilinger, and M. Aspelmeyer, *Optomechanical Entanglement between a Movable Mirror and a Cavity Field*. Phys. Rev. Lett. **98**, 030405 (2007).

[Vitali07b] D. Vitali, P. Tombesi, M. J. Woolley, A. C. Doherty, and G. J. Milburn, *Entangling a nanomechanical resonator and a superconducting microwave cavity*. Phys. Rev. A **76**, 042336 (2007).

[Vogel89] K. Vogel and H. Risken, *Quasiprobability distributions in dispersive optical bistability*. Phys. Rev. A **39**, 4675 (1989).

[Vogel90] K. Vogel and H. Risken, *Dispersive optical bistability for large photon numbers and low cavity damping*. Phys. Rev. A **42**, 627 (1990).

[Wallraff04] A. Wallraff, D. I. Schuster, A. Blais, L. Frunzio, R.-S. Huang, J. Majer, S. Kumar, S. M. Girvin, and R. J. Schoelkopf, *Strong coupling of a single photon to a superconducting qubit using circuit quantum electrodynamics*. Nature **431**, 162 (2004).

[Wallraff05] A. Wallraff, D. I. Schuster, A. Blais, L. Frunzio, J. Majer, M. H. Devoret, S. M. Girvin, and R. J. Schoelkopf, *Approaching Unit Visibility for Control of a Superconducting Qubit with Dispersive Readout*. Phys. Rev. Lett. **95**, 060501 (2005).

[Walls08] D. Walls and G. Milburn, *Quantum Optics*. 2nd edition, Springer (2008).

[Wang10] Y.-D. Wang, S. Chesi, D. Loss, and C. Bruder, *One-step multiqubit Greenberger-Horne-Zeilinger state generation in a circuit QED system*. Phys. Rev. B **81**, 104524 (2010).

[Wang12] Y.-D. Wang and A. A. Clerk, *Using Interference for High Fidelity Quantum State Transfer in Optomechanics*. Phys. Rev. Lett. **108**, 153603 (2012).

[Weiss08] U. Weiss, *Quantum Dissipative Systems*. Series in modern condensed matter physics, World Scientific (2008).

[Williams11] C. Williams, *Quantum Gates. Explorations in Quantum Computing*, pp. 51–122, Texts in Computer Science, Springer London (2011).

[Wilson-Rae07] I. Wilson-Rae, N. Nooshi, W. Zwerger, and T. J. Kippenberg, *Theory of Ground State Cooling of a Mechanical Oscillator Using Dynamical Backaction*. Phys. Rev. Lett. **99**, 093901 (2007).

[Winger11] M. Winger, T. D. Blasius, T. P. M. Alegre, A. H. Safavi-Naeini, S. Meenehan, J. Cohen, S. Stobbe, and O. Painter, *A chip-scale integrated cavity-electro-optomechanics platform*. Opt. Express **19**, 24905 (2011).

[Wu86] L.-A. Wu, H. J. Kimble, J. L. Hall, and H. Wu, *Generation of Squeezed States by Parametric Down Conversion*. Phys. Rev. Lett. **57**, 2520 (1986).

[Yoshie04] T. Yoshie, A. Scherer, J. Hendrickson, G. Khitrova, H. M. Gibbs, G. Rupper, C. Ell, O. B. Shchekin, and D. G. Deppe, *Vacuum Rabi splitting with a single quantum dot in a photonic crystal nanocavity*. Nature **432**, 200 (2004).

[You03a] J. Q. You and F. Nori, *Quantum information processing with superconducting qubits in a microwave field*. Phys. Rev. B **68**, 064509 (2003).

[You03b] L. You, *Creating Maximally Entangled Atomic States in a Bose-Einstein Condensate*. Phys. Rev. Lett. **90**, 030402 (2003).

[Zhang03] J. Zhang, K. Peng, and S. L. Braunstein, *Quantum-state transfer from light to macroscopic oscillators*. Phys. Rev. A **68**, 013808 (2003).

[Zheng01] S.-B. Zheng, *One-Step Synthesis of Multiatom Greenberger-Horne-Zeilinger States*. Phys. Rev. Lett. **87**, 230404 (2001).